PREPARATION OF HIGH-ASPECT-RATIO PARTICLES THROUGH THE HIGH TEMPERATURE GROWTH OF 2M-WOLLASTONITE CRYSTALS

by

Liangzhu Zhu

A dissertation submitted to the faculty of
The University of Utah
in partial fulfillment of the requirements for the degree of

Doctor of Philosophy

Department of Metallurgical Engineering

The University of Utah

December 2013

The University of Utah Graduate School

STATEMENT OF DISSERTATION APPROVAL

The dissertation of **Liangzhu Zhu**

has been approved by the following supervisory committee members:

Hong Yong Sohn	, Chair	**8/1/2013** Date Approved
Zhigang Zak Fang	, Member	**8/1/2013** Date Approved
K. S. Ravi Chandran	, Member	**8/1/2013** Date Approved
Moo Eob Choi	, Member	**8/1/2013** Date Approved
Erich U. Petersen	, Member	**8/1/2013** Date Approved

and by **Manoranjan Misra** , Chair/Dean of

the Department/College/School of **Metallurgical Engineering**

and by David B. Kieda, Dean of The Graduate School.

ABSTRACT

A polytype of wollastonite, 2M-wollastonite, that breaks into acicular particles under external forces is being synthesized through two different processes, namely a Partial Melting and Recrystallization Process (PMR Process) and a Flux Growth Process (FG Process).

The PMR Process combines the advantages of the solid state reaction and liquid phase reaction methods by creating a partially melted phase to maintain the original shape of the compacts of raw materials while melted regions form locally within the compacts, providing a favorable environment for the growth of alpha-wollastonite in the first step. The target crystal, 2M-wollastonite, nucleates and grows during the subsequent recrystallization stage. Using this process, effects of additives on the preparation of acicular wollastonite particles were investigated. It was found that B_2O_3 is one of the melting point depressing additives that can lower the melting point of the raw mixtures significantly in a small amount. Li_2O is one of the catalytic additives that promote the formation of acicular wollastonite particles.

The FG Process completely melt the raw mixtures in a suitable crucible at temperatures above 1400^{o}C, and then lets the melt solidify under a favorable cooling rate to allow the nucleation and growth of 2M-wollastotnite during this stage. It takes advantage of the heat transfer properties of the melt-crucible-furnace wall (MCF) system; a vertical temperature gradient is achieved to provide sites for the preferable nucleation of

2M-wollatonite crystals at the top melt surface. The solidified products contain nearly pure 2M-wollastonite crystals as the major component and an amorphous glass phase as the minor part.

Both the PMR and FG processes yielded high-aspect-ratio (HAR) particles. The crystals grown by the PMR process were small in size but large in number, and they grew randomly in the final products. The crystals grown by the FG process were aligned and they formed cellular and dendritic patterns. Such a growth behavior offers additional benefits for producing HAR wollastonite particles. When the two processes were compared, the FG process surpasses the PMR process in terms of efficiency.

Modeling and simulation work was done on the FG process that presented cellular and dendritic growth. Based on experimental studies, an empirical model was proposed that modified the existing models on predicting cellular and dendritic growth on a SiO_2-CaO-B_2O_3-Li_2O ceramic alloy under high temperature unsteady-state heat transfer. Using this new model, the growth rate and primary arm spacing were predicted well compared with experimental observations. Besides, the average growth front, solidification volume fraction, and mean aspect ratio were also simulated. The simulation work helped to understand and predict the growth of wollastonite crystals in a significant way.

TABLE OF CONTENTS

LIST OF TABLES

ACKNOWLEDGEMENTS

First and foremost, I would like to express my deepest gratitude to my academic advisor, Professor Hong Yong Sohn, for accepting me as one of his students. I would never have been able to finish my dissertation without his excellent guidance, patience, motivation, enthusiasm, immense knowledge, and especially the free atmosphere for doing research. Besides guiding me on how to do research, he was also teaching me from various aspects. For example, he spent a lot of time reviewing the double weekly or annual reports I submitted. He could always point out those major to minor mistakes I had made. As an international student, I used to have some grammar mistakes in my research reports; when those happened, he became my English teacher.

I am also grateful to the rest of my supervisory committee, Professor Zhigang Zak Fang, Professor K. S. Ravi Chandran, Dr. Moo Eob Choi, and Professor Erich U. Petersen, for their encouragement, insightful comments, and hard but good questions. Special thanks to Professor Zhigang Zak Fang, for allowing me to use the SEM and DSC equipment of his group.

This work was supported in part by the U.S.-Egypt Science and Technology Joint Fund in cooperation with U.S. National Science Foundation and the Academy of Scientific Research and Development of Egypt under NSF Grant No. OISE 0913513/MAN10011354-F1, I would like to express my gratitude to their support without which I would not have been able to finish this dissertation.

Thanks also to Professor Ayman El-Midany for his cooperation on this project. I received a scholarship from the China Scholarship Council during the course of this research; I would like to show my greatest appreciation for its financial support.

I wish to thank Mr. Salvatore LaRosa, Technical Marketing Manager of NYCO Minerals Inc., for supplying the natural wollastonite samples used in this research and providing comments regarding synthetic wollastonite products, which is gratefully acknowledged.

Professor Diego P. Fernandez from the Univeristy of Utah helped a lot on LA-ICP-MS analysis. Mr. Robert L. Virta, who is from the U.S. Geological Survey and has been writing annual reports for wollastonite for many years, has provided useful comments on natural wollastonite, which helped me to understand the behavior of wollastonite better. They are also appreciated in this dissertation.

I also wish to thank my friends Messrs. Tyler Bronson and Pei Sun for helpful technical discussion on SEM, Chai Ren and Meenakshisundaram Ramanathan for XRD, Yakun Zhu for SWLI, Xia Zhang for surface analysis, Chengshang Zhou for DSC, and Zhixue Yuan for some laboratory work.

My sincere thanks to Ms. Kay Argyle and Ms. Evelyn Wells, the Executive Secretary and Administrative Assistant of the Department of Metallurgical Engineering, respectively, for their help on purchasing research-related consumables.

Last but not the least, I would like to thank my family: my parents, Mr. Xianjun Zhu and Mrs. Dongju Xu, for giving birth to me and supporting me spiritually and financially throughout my life, and my wife, Hongyan Li, for her encouragement, support, and great love during the past few years.

CHAPTER 1

LITERATURE REVIEW ON WOLLASTONITE: ITS CRYSTAL STRUCTURE, APPLICATIONS, AND SYNTHESIS

1.1 Introduction

Wollastonite is a mineral that has a chemical formula of $CaSiO_3$ with a theoretical composition of 48 wt.% CaO and 52 wt.% SiO_2. Naturally occurring wollastonite may contain trace elements such as aluminum, iron, magnesium, manganese, potassium, and sodium. It is usually white with a hardness of 4.5 to 5.5 on the Mohs scale. Both iron and manganese affect its color.

Wollastonite has two polymorphs [1, 2]: α-wollastonite also called pseudo-wollastonite or cyclo-wollastonite that is stable at high temperatures, and β-wollastonite that is stable at low temperatures. The two polymorphs are further divided into different polytypes [3, 4]. According to Ymanaka and Mori [4], α-wollastonite has four-layer and six-layer polytypes based on the combination of different repeating layers. A unit of the repeating layers is made of a layer of Ca octahedrals and ternary rings of $[Si_3O_9]^{6-}$. For convenience, the four-layer polytype in this study is denoted as α-wollastonite-4A and six-layer polytype as α-wollastonite-6A accordingly, with A being a repeating layer. Since α-wollastonite-4A is the predominant polytype and is rarely found in synthetic wollastonite [4], hereafter, the terms of α-wollastonite, pseudo wollastonite, and α-wollastonite-4A refer to the same crystal structure in this study if no specific distinction

is made.

The β-wollastonite was further divided into six polytypes [1-6] , namely, 1T, 2M, 3T, 4T, 5T, and 7T, where M and T represent monoclinic and triclinic structure, respectively. The number here indicates the number of subcells in each unit cell of that particular polytype. Henmi et al. [6] listed two types of subcells. One is the normal 1T wollastonite unit cell (T) and the other is a unit cell related to T by a displacement of *b*/2. Hesse [7] suggested $d_{subcell} \approx 7.7$ Å for a unit subcell.

2M-wollastonite, which is also named para-wollastonite, has a unique structure because it has long chains of silicon tetrahedrons $[SiO_4]^{4-}$ parallel to its *b* axis, which results in its fibrous nature. Jefferson et al. [8] demonstrated this habit by high-resolution electron microscopy.

While the structures of wollastonite have been thoroughly studied, however, a very critical aspect that is missing from these studies is the lack of phase transformation temperatures. The only available transformation temperature is the beta to alpha wollastonite transformation as seen in a few studies [7, 9, 10]. However, these reported phase transformation temperatures are inconsistent with each other. They are 1125°C (Phillips et al. [9]), 1150°C (Hesse et al. [7]), and 1200°C (He et al. [11]). Meanwhile, to effectively synthesize 2M-wollasonite, it is necessary to determine the thermodynamically favorable temperature range for the formation of 2M-wollasonite. Lastly, the melting point for wollastonite has been reported as 1380°C [12], 1512°C [13], and 1544°C [9]. The inconsistency among these studies suggests that further experiments should be carried out to verify the actual melting point of wollastonite when this information becomes important.

The formation of naturally occurring wollastonite involves two different theories. The first involves the reaction between silica and limestone at intermediate temperatures provided by deep burial or igneous intrusion. The second is achieved by the recrystallization of magma. However, the origin of the magma is still controversial [14] .

1.2 Applications of Wollastonite

Wollastonite has some unique properties which make it useful in industry. The first property is its chemical inertness. The second is its brightness and whiteness, which lead to its use as white pigments. Besides these properties, wollastonite does not contain water of crystallization, as do talc, kaolin, mica, and a few other minerals that are used in ceramics. It also acts as a source of calcium, replacing calcium carbonate in some ceramics, so when it is fired, CO_2 is not generated; therefore, it can greatly eliminate gas dispersal problems during ceramic firing, and reduce firing time. Furthermore, wollastonite has high pH in water slurry, making it possible to stabilize the acidity and reduce the dissociation of polyvinyl acetate in paints. It is thermally stable up to 1120^{o}C, which makes it valuable in insulation applications such as replacing asbestos. The last and the most important property is its needle-like morphology after being crushed. Because of this property, high-aspect-ratio (HAR) wollastonite powders can be produced from bulk wollastonite. HAR wollastonite is used mainly because this morphology improves flexural modulus, reduces heat distortion, and improves impact resistance. The long, thin aspect of acicular wollastonite gives it a larger surface area for a given weight of product. With more surface area, there is more contact with the matrix than with low-aspect-ratio particles. This allows for improved adhesion. The HAR particles act like miniature reinforcing rods, stopping cracks that develop in the matrix, similar to the way

that reinforcing bars stop cracks that develop in concrete structure. Because of the properties mentioned above, wollastonite is used in products of plastics, paints, coatings, rubbers, ceramics, refractories, and adhesives.

Today, plastics, paint, and green ceramics are the main markets for high-aspect-ratio wollastonite, as seen in Figure 1.1. Within these broad markets are many end uses. More detailed information about its applications and market distribution is available from the websites of NYCO Mineral Inc. and R.T. Vanderbilt Company, Inc., which are the two major companies in the U.S. that mine and sell commercial natural wollastonite.

As shown in Figure 1.2a, worldwide annual wollastonite production has been increasing dramatically from about 40,000 metric tons in 1970 to approximately 600,000 metric tons in 2000. Since then, the production rate has remained relatively steady. Among the total worldwide wollastonite production, China is the largest producer, followed by India and the United States (Figure 1.2b).

1.3 Necessity of Synthetic Wollastonite

Wollastonite usually occurs in small amounts and is often contaminated by other minerals such as diopside, calcite, and garnet. As a consequence, it has to have beneficiation steps for producing commercially natural wollastonite. Since we can control the impurities and their amounts in synthetic wollastonite, this problem will be eliminated or at least greatly reduced. Meanwhile the properties of synthetic wollastonite will be more homogeneous compared with natural wollastonite even though the acicularity of the former may not be as good as the latter.

Being a mineral, wollastonite is a nonrenewable resource just like coal and fossil

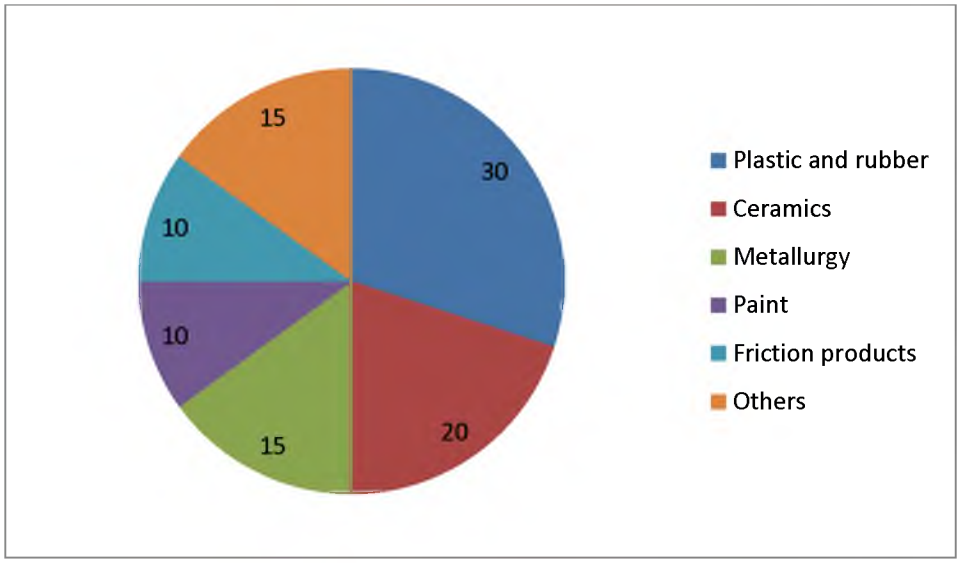

(a)

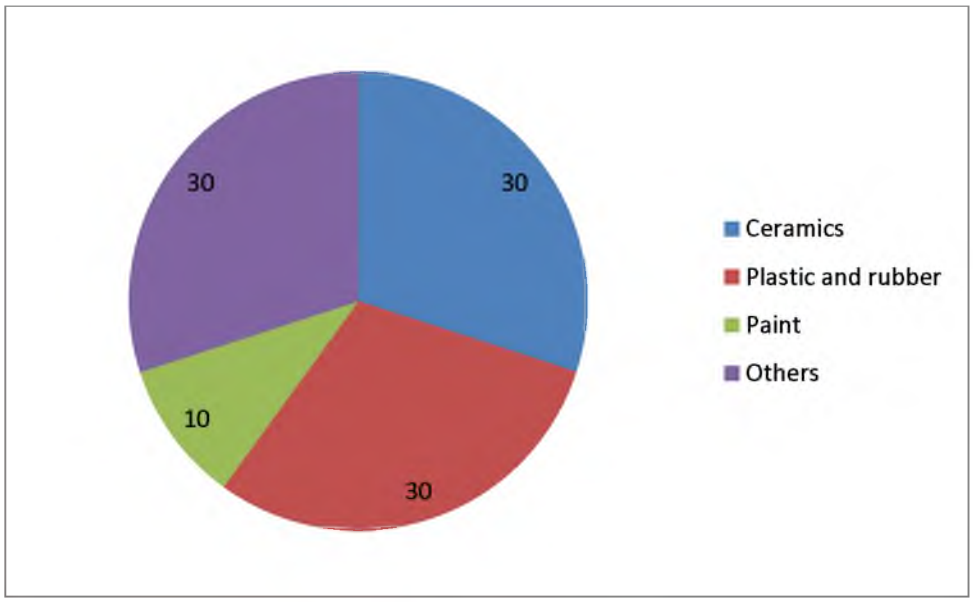

(b)

Figure 1.1 Wollastonite consumptions in various applications in 2010 within: (a) U.S., and (b) worldwide. Data from references [15, 16].

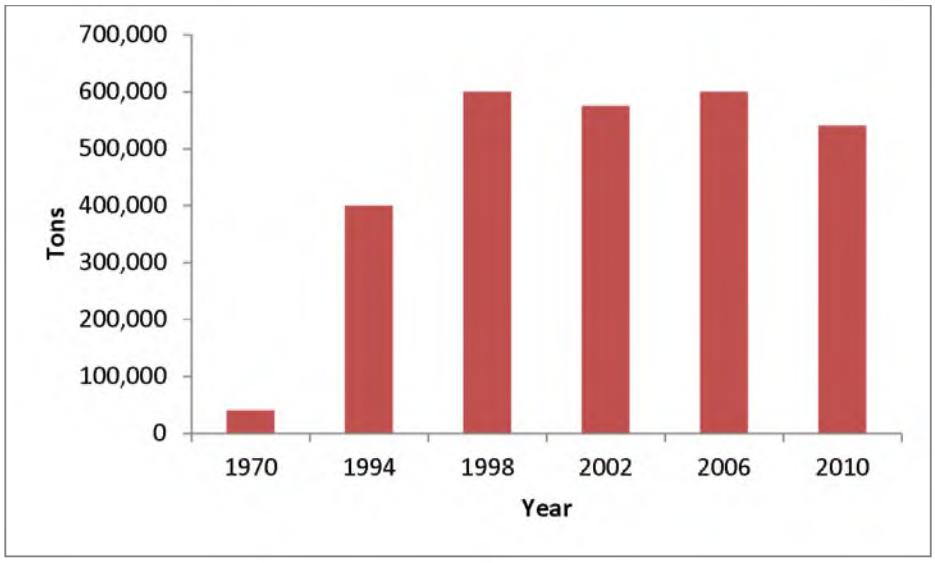

(a)

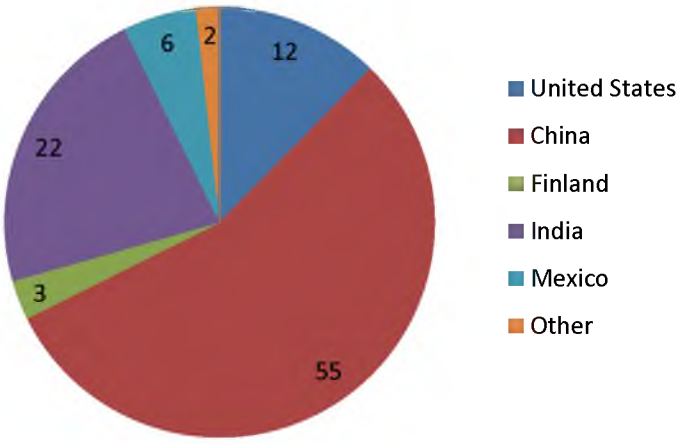

(b)

Figure 1.2 Wollastonite production in years 1970-2010 in the world (a) and approximate wollastonite production of individual countries in 2010 (b). Data from references [15, 16].

oil. Even if we still have natural wollastonite to mine at this moment, it is always good to think about alternative ways to slow down its consumption for future applications, which is similar to the research that is being carried out to find new ways to replace or preserve traditional energy resources.

Scientists have been working on finding new and effective approaches to recycle waste materials. Among these materials, some of them are actually the main raw materials for synthesizing wollastonite, such as marble cuttings, fumed silica, and blast furnace slag. They all contain a substantial amount of silica and lime. If they can be used to synthesize wollastonite, they will not only help to reduce the dependence on natural wollastonite but also contribute to recycling of waste materials. Therefore, it has aroused an interest in research to develop synthetic wollastonite, especially wollastonite powder with high-aspect-ratios in all of the aforementioned applications.

1. 4 Existing Research on Wollastonite Synthesis

Currently, there are three types of methods for synthesizing wollastonite: the wet methods [17-20], the solid state reaction methods [1, 12, 21-26], and the liquid phase reaction methods [27, 28]. Among these methods, the wet methods are usually performed at low temperatures (less than 200^{o}C), accompanied by a high pressure. They can be further divided into sol-gel processing, hydrothermal reaction, and colloid emulsion technique. The solid state reaction methods are based on the reaction of silica with calcium oxide or calcium carbonate above 800^{o}C. In the liquid phase reaction methods, starting mixtures are melted inside suitable crucibles at a composition close to wollastonite together with other oxides such as sodium oxide or boron oxide to lower the melting temperature. The liquid is solidified, sometimes cast into thin layers, followed by

various heat treatments.

The three existing methods listed above have their advantages and disadvantages. However, they were all proved to be unsuitable or limited to prepare HAR wollastonite in an effective way, especially when recycled materials are used as raw materials.

The wet methods can produce wollastonite of the highest aspect ratios among the three. However, they usually consume large amounts of high purity organic solvents and templates such as citric acid ($C_6H_8O_7.H_2O$), causing environmental and health issues [17], or rely on inorganic salts such as $Ca(NO_3)_2.4H_2O$ and $Na_2SiO_3.9H_2O$ as raw materials [18], making them relatively expensive and less flexible, and which does not allow the use of recycled materials. An example of wet methods is summarized in Figure 1.3.

The solid state reaction methods can utilize various raw materials such as silica fume, calcite, marble waste, natural siliceous carbonates, and tailing materials. But more often, they failed to produce acicular particles. None of the studies that used these methods reported product aspect ratios [25-32]. We repeated experiments under similar conditions to these methods. XRD analysis proved the formation of wollastonite in the products, but the powder did not show acicular shapes. When aspect ratio is not of significant interest, the solid state reaction methods are most efficient. An example of these methods is illustrated in Figure 1.4.

The liquid phase reaction methods can produce acicular wollastonite powder as well, but the working temperature (usually greater than 1400°C) is high; therefore, it needs stricter requirements on the experimental conditions. The liquid phase in this case is a mixture of acidic SiO_2 and basic CaO of 1:1 molar ratio, with some metal oxides added for various purposes. Since most refractory containers are also made of metal

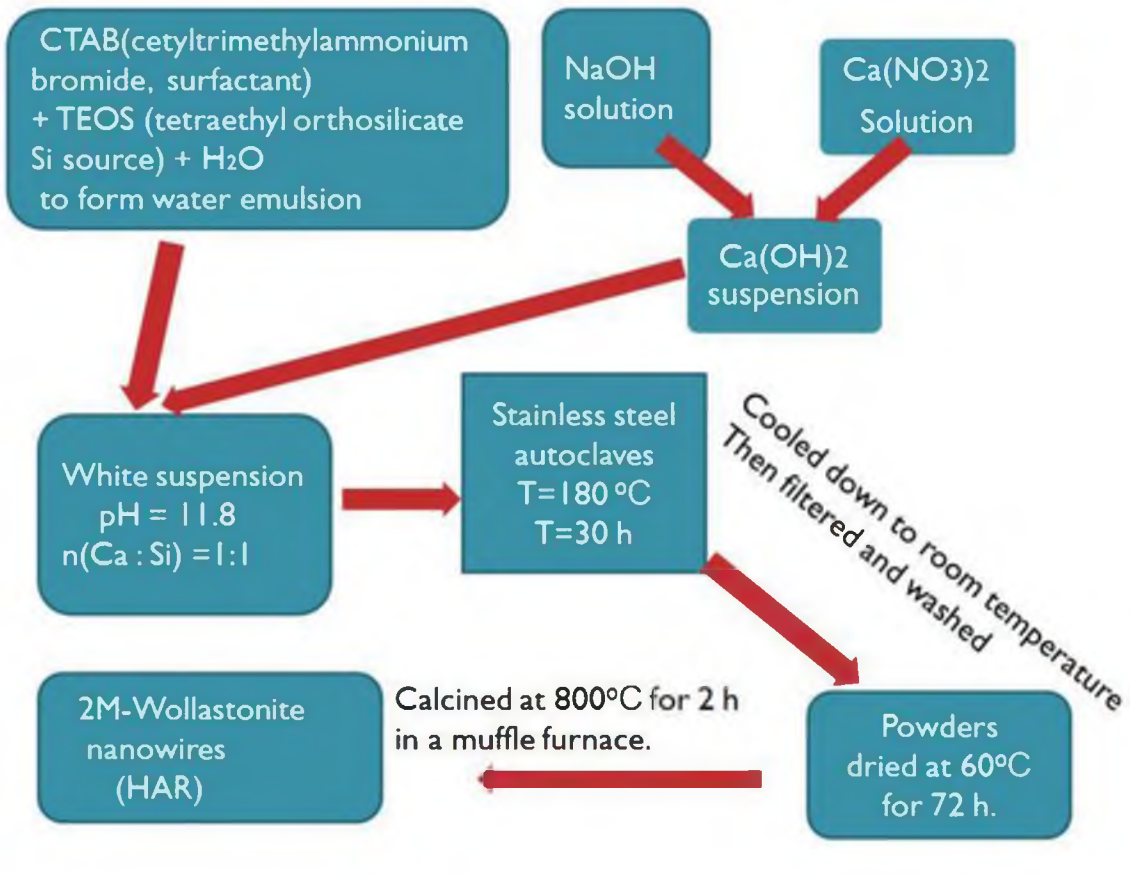

Figure 1.3 A typical example of wet methods sketched based on the Chang et al. study [19].

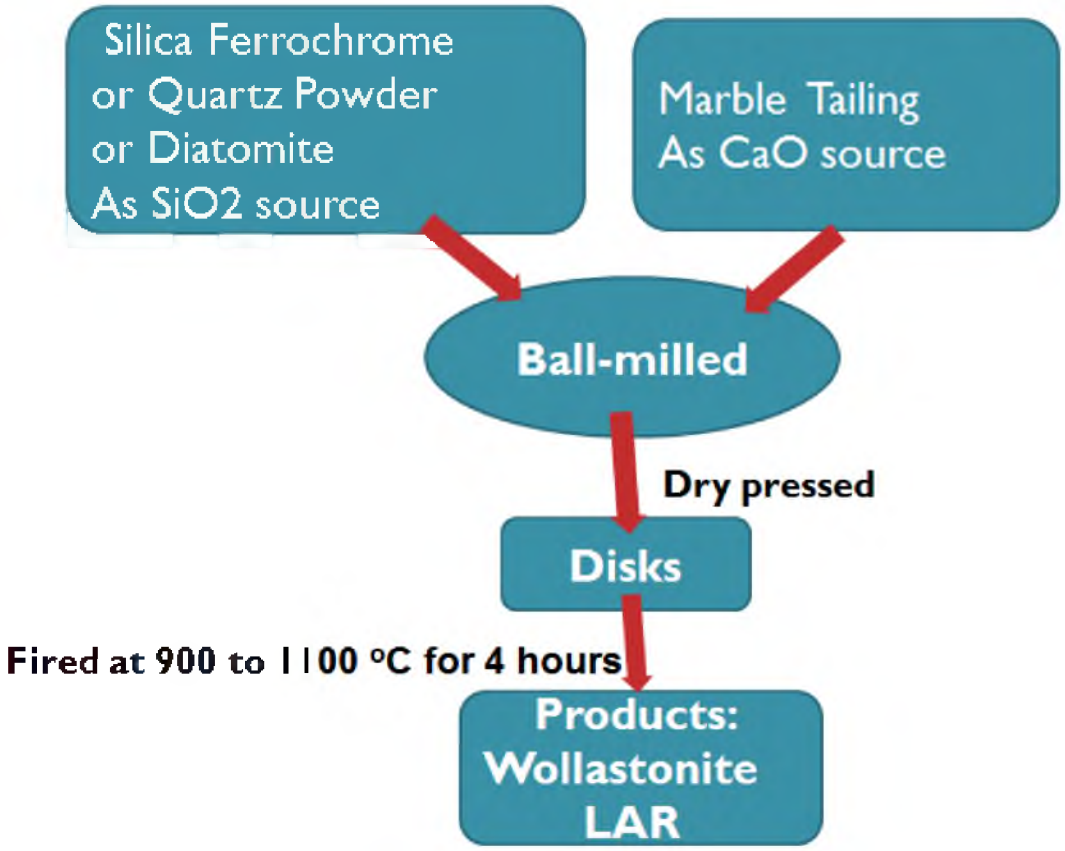

Figure 1.4 A typical example of solid state reaction methods sketched based on the Emrullahoğlu et al. study [23].

oxides, they tend to form complex compounds with the reactant mixture, resulting in both contamination and corrosion problems. A platinum crucible is therefore necessary to hold these types of mixtures at temperatures above 1400°C. Meanwhile, this type of method was usually more complicated than other types of nonmelting methods. However, since the liquid phase reaction methods are the most promising ones that can possibly be applied to preparing HAR wollastonite particles from recycled materials compared with those aforementioned nonmelting methods, two representative liquid phase reaction process examples are illustrated as follows.

Example 1 by Ohsato et al. [27]: the experiment was carried out by preparing a starting mixture having a composition of $K_2CaSi_2O_7$. The mixture was then melted at 1400°C and cooled slowly from 1400°C to 1060°C during a 24-hour period and was held at 1060°C for 20 hours in air. According to this study, the precipitation of wollastonite crystals seemed to occur from the melt by the evaporation of K_2O from the surface. The crystals formed were of 1-2 mm in length and 0.1-0.7 mm in cross-section, and were determined as beta- and para-wollastonite.

Example 2 by Maries et al. [29]: mixtures made of different oxides were prepared first. Since their objective was to make fibrous crystals having a silicate chain structure similar to that of wollastonite, those mixtures were not following a 1:1 molar ratio of SiO_2 and CaO, and contained large contents of additives such as 20% ZnO, 13% Al_2O_3, or 7.5% Na_2O. The mixtures were then melted to prepare glass rods with diameter of about 1 mm. The solidified glass rods were then passed slowly through a platinum heating coil that would locally melt the rod again. The temperature of the coil was controlled so that the glass was in molten phase within it. The maximum rate of drawing

a rod through the coil could not exceed 3 mm per minute. By this method, they produced β-$CaSiO_3$. Though they only mentioned the products had fibrous property without giving their aspect ratio information, the Mean Aspect Ratio of these crystallized products should be higher than other liquid phase processes because of the favorable crystallization environment. An illustration of this method is shown in Figure 1.5.

The two liquid phase reaction process examples, however, still have some limitations for preparation of HAR wollastonite from recycled materials for the following reasons. Firstly, in addition to the cost of platinum wares, the restrictions on using platinum wares at high temperatures, such as avoiding alkali oxides, iron oxides, and other unknown species, will make this method prohibitive for wollastonite production in industrial scale. Secondly and the most importantly, both of them have a low efficiency to produce wollastonite. The former needs long crystallization time at temperatures close to the molten phase temperature and also long holding time. The latter, which is often used to prepare single crystals, has a very low drawing rate even with only a 1 mm diameter rod and it becomes even lower if the diameter is increased because of the time needed for completely solidification.

Because of the limitations mentioned above, either an alternative method or an improvement on an existing method needs to be developed to produce wollastonite products that have high-aspect-ratios while keeping the process technically and practically acceptable.

1.5 Conclusions

Wollastonite is a versatile nonreusable material. While the current market relies greatly on natural wollastonite products, it is worthwhile to develop synthetic

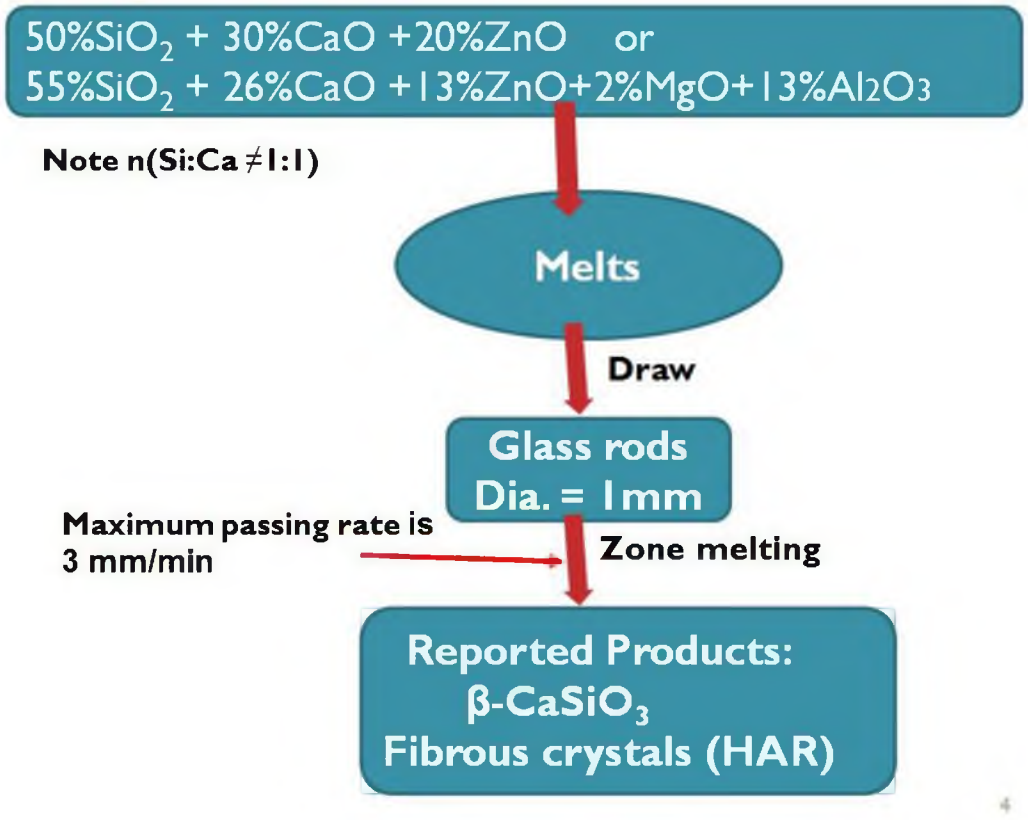

Figure 1.5 A typical example of liquid phase reaction methods sketched based on the Maries et al. study [29].

wollastonite to partially replace the natural resource.

Though current research has been done to synthesize wollastonite, it either failed to produce high-aspect-ratio wollastonite or did not produce acicular particles in an effective way. In order to produce high-aspect-ratio wollastonite effectively, we need to find either alternative methods or significant improvements on existing methods.

CHAPTER 2

DETERMINATION ON PHASE TRANSFORMATION TEMPERATURE OF WOLLASTONITE POLYMORPHS AND POLYTYPES

2.1 Introduction

Being a mineral, wollastonite is a type of silicate; therefore, it inherits most of the common properties seen in hundreds of silicates. One of these properties is their complex structures, resulting in their special polymorphism and polytypism. While polymorphism is used to describe the general relations among the several phases of the same substance, the polytypism is used to denote a special type of polymorphism in which the different structures assumed by a compound differ only in the order in which a two-dimensional layer is stacked [30].

In order to understand the structure of wollastonite, especially when some of its important properties are tightly related to its structure, it is important to introduce the general structure of silicates. The basic unit of silicates is silicon tetrahedron $[SiO_4]^{4-}$ (hereafter called tetrahedron) with Si^{4+} sitting in the center and surrounded by four O^{2-} at the four apices. Each of these tetrahedrons has a maximum of 4 apices, to be shared by other tetrahedrons. Based on different combinations of such tetrahedrons, there are five general groups (some references use slightly different classification [5, 30, 31].

Group 1 is island silicates: if the island is made of only one tetrahedron, it is also

named nesosilicates. In this subgroup, none of the apices is shared by other tetrahedrons, forming isolated tetrahedronsl islands. Olivine ($(Mg,Fe)_2SiO_4$) is a good example of this subgroup. If the island is made of two tetrahedrons, it is also called sorosilicates. In this group, one apex of a tetrahedron is shared by another tetrahedron, making a basic unit of $[Si_2O_7]^{6-}$. Group 2 is cyclosilicates. In this group, each tetrahedron shares two apices with others to make a ring structure. Therefore, they are also called ring silicates. Some common rings are $[Si_3O_9]^{6-}$, $[Si_4O_{12}]^{8-}$, and $[Si_6O_{18}]^{12-}$. Group 3 is inosilicates or chain silicates. In this group, if each tetrahedron shares two apices with other tetrahedrons but does not make rings, then it forms single chain silicates. If each tetrahedron is connected by three other tetrahedrons, then it forms double chain silicates. The basic unit for single chain and double chain silicates is $[Si_2O_6]^{4-}$ (or $[SiO_3]^{2-}$) and $[Si_4O_{11}]^{6-}$. If three apices of a tetrahedron are linked by other tetrahedrons to form infinite sheet layers, they belong to Group 4, that is phyllosilicates. A typical example of this group is mica. Group 5 is tectosilicates or framework silicates, in which all of the apices are shared by other tetrahedrons to form a 3D network frame. Since each Si^{4+} is surrounded by four O^{2-} that are also shared by adjacent Si^{4+}, the resulting formula becomes SiO_2, which is one of the major components in wollastonite synthesis. However, even if all apices of the tetrahedrons are linked by others in silica, they can still form different structures by varying the relative positions among these tetrahedrons, namely, low quartz, high quartz, low tridymite, middle tridymite, high tridymite, low cristobalite, and high critbolatite. These polymorphs transform into one another through four displacive and two reconstructive transformations at differention temperatures [30], which might directly account for the following polymorphism property of wollastonite.

With the above description on silicate structures, it is then easier to understand the structure of wollastonite. From the point of view of polymorphism, Balkevich et al. [1] and Kotsis et al. [2] defined that wollastonite has two polymorphs: α-wollastonite, also called pseudo-wollastonite or cyclo-wollastonite, which is stable at high temperatures, and β-wollastonite, which is stable at low temperatures. While the former belongs to cyclosilicates (Group 2), the later is a type of inosilicates (Group 3). The two polymorphs are further divided into different polytypes from the standing of polytypism [3, 4]. According to Ymanaka and Mori [4], α-wollastonite has four-layer and six-layer polytypes based on the combination of different repeating layers. A unit of the repeating layers is made of a layer of Ca octahedra and ternary rings of $[Si_3O_9]^{6-}$, as shown in Figure 2.1. For convenience, the four-layer polytype in this study is denoted as α-wollastonite-4A and six-layer polytype as α-wollastonite-6A accordingly, with "A" being a repeating layer. Since α-wollastonite-4A is the predominant polytype and is rarely found in synthetic wollastonite [4], hereafter, the terms of α-wollastonite, pseudowollastonite, and α-wollastonite-4A refer to the same crystal structure in this study if no specific distinction is made. A structure model of α-wollastonite-4A is shown in Figure 2.1.

The β-wollastonite was further divided into six polytypes [1-6] , namely, 1T, 2M, 3T, 4T, 5T, and 7T, where M and T represent monoclinic and triclinic structure, respectively. The number here indicates the number of subcells in each unit cell of that particular polytype. Henmi et al. [6] listed two types of subcells. One is the normal 1T wollastonite unit cell (T) and the other is a unit cell related to T by a displacement of $b/2$.

However, quite a few studies on wollastonite synthesis did not distinguish these

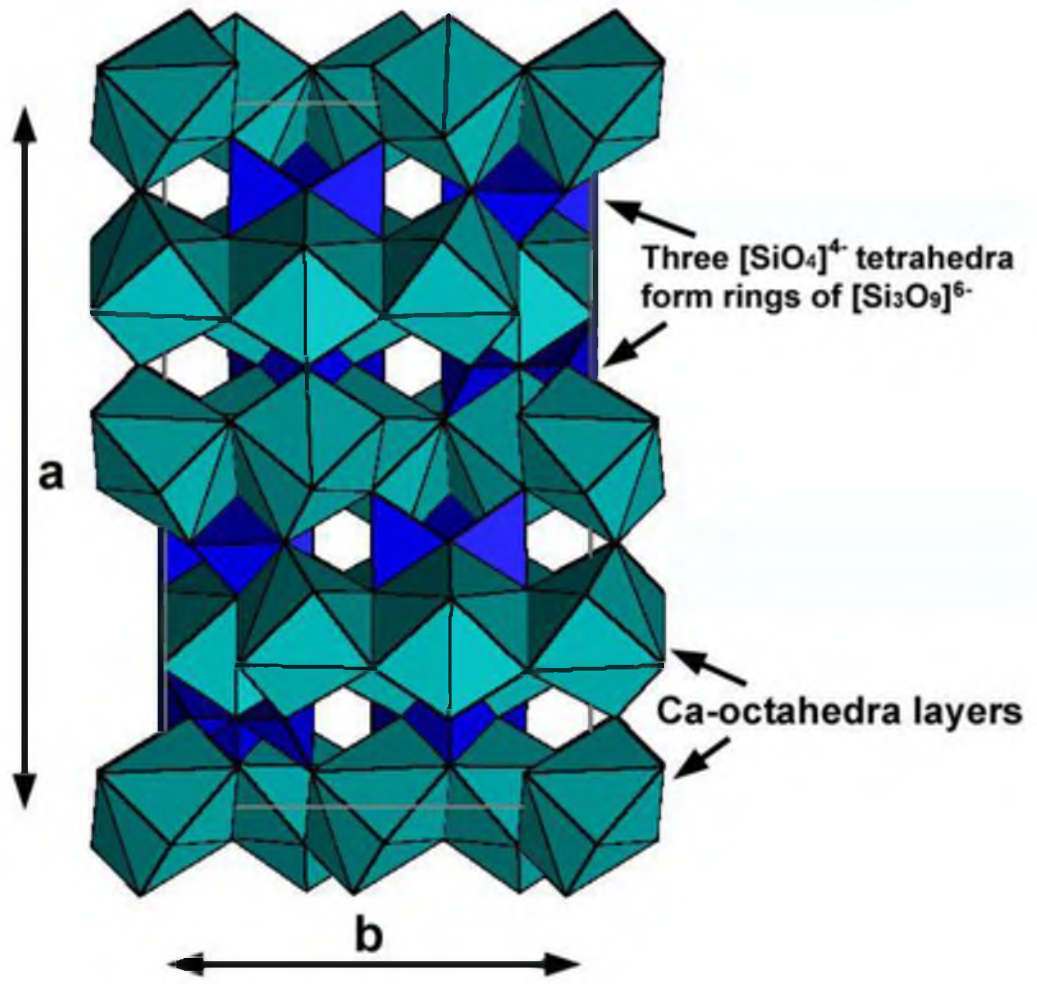

Figure 2.1. A unit cell of α-wollastonite-4A showing four layers of Ca octahedral and ternary rings made of three tetrahedrons. Repeating layers are along ***a*** direction. Lattice parameters: $a = 6.823\,\text{Å}$, $b = 11.895\,\text{Å}$, $c = 19.674\,\text{Å}$, $\alpha = 90.12^{\circ}$, $\beta = 90.55^{\circ}$, $\gamma = 90.00^{\circ}$. Atomic coordinates and lattice parameters are obtained from "The Structure and Polytypes α-CaSiO3 (Pseudowollastonite)" by Yamanaka et al. [4].

polymorphs and polytypes in their synthesis of wollastonite; they claimed wollastonite was synthesized by various methods [12, 21, 23] without providing further crystal structure information. A common phenomenon of these articles is that none of them reported their aspect ratios. When aspect ratio is not of a concern, it does not that matter how many polytypes wollastonite can have, but when aspect ratio, especially high-aspect-ratio, is desired for wollastonite products, one has to consider these different structures because of the following critical observation. Tolliday et al. [32] and others [8, 33] pointed out that among all the polymorphs and polytypes, 2M-wollastonite, which is also named para-wollastonite, has a unique structure because it has long chains of silicon tetrahedrons $[SiO_4]^{4-}$ parallel to its *b* axis, which results in its fibrous nature. Jefferson et al. [8] demonstrated this habit by high-resolution electron microscopy. A crystal structure model plotted from the atomic coordinates obtained by Troier et al. [33] using X-ray analysis presents the same chain structure, as seen in Figure 2.2. Therefore, the initial objective of preparing HAR wollastonite undoubtedly becomes the study of growing 2M-wollastonite crystals.

While the structures of wollastonite have been thoroughly studied, however, a very critical aspect that is missing from these studies is the lack of phase transformation temperatures. The only available transformation temperature is the beta to alpha wollastonite transformation as seen in a few studies [7, 9, 10]. However, these reported phase transformation temperatures are inconsistent. They are 1125°C by Phillips et al. [9], 1150°C by Hesse et al. [7], and 1200°C by He et al. [11]. If we neglect the possible errors in these studies, the question becomes whether we can assume the beta wollastonite reported as 2M-wollastonite polytype in these studies without further information.

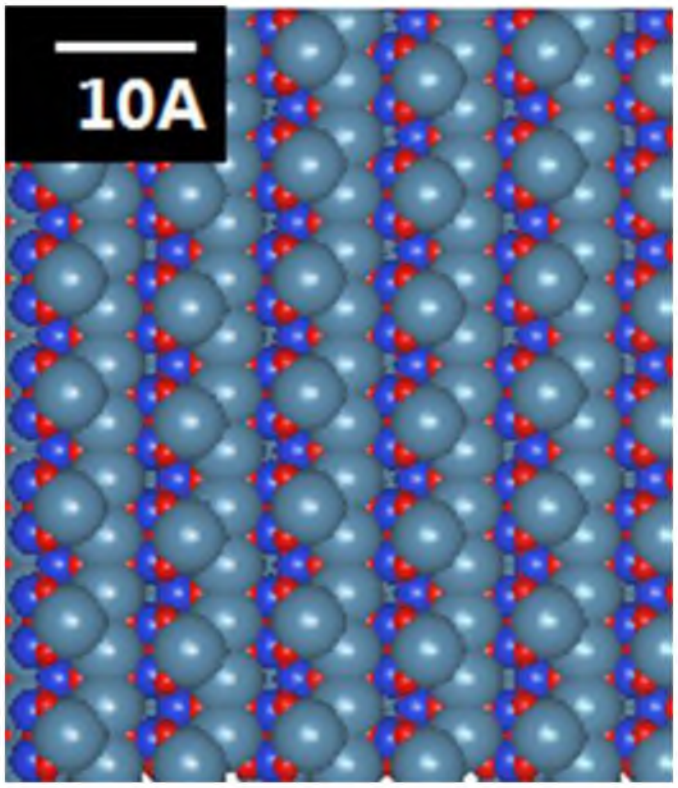

Figure 2.2. Structure of 2M-wollastonite viewing down ***c*** direction: a space filling structure model created using software VICS-II. Atomic coordinates are obtained from "The crystal structure of parawollastonite" by Trojer [33]. Each chain structure is made of two adjacent silicon tetrahedrons chains (red and blue atoms), only the left chain is exposed in the model, the right chain is hidden by the gray calcium atoms.

Meanwhile, to effectively synthesize 2M-wollasonite, it is necessary to determine the thermodynamically favorable temperature range for the formation of 2M-wollasonite.

Lastly, the melting point for wollastonite had been reported as 1380°C [12], 1512°C [13], and 1544°C [9]. The inconsistency among these studies suggests that further experiments should be carried out to verify the actual melting point of wollastonite when this information becomes important. With these uncertainties waiting to be solved, we designed the following experiment.

2.2 Experimental Procedure

Pure SiO_2 and CaO with a 1:1 molar ratio were thoroughly mixed and put into an alumina crucible. The mixture and the crucible were then preheated at 1000°C for half an hour in a muffle furnace and transferred to a vertical furnace at the end of preheating. The mixture was completely melted at 1560°C within 5 minutes, but an extra 10 minutes was added to yield a molten phase as homogeneous as possible. At the end of the homogenization stage, the crucible and the melt were taken out of the vertical furnace and quenched immediately in water at 20°C. Since the holding time at high temperature was relatively short, and meanwhile the obtained glass after quenching could be easily separated from the crucible wall, the contamination introduced by the crucible could be neglected.

The sample glass was then grounded into fine powder of below 200 mesh size, and dried for 24 hours at 150°C. Then, small amounts of such powder were heated at different temperatures for various times. After heat treatment, each sample was analyzed by XRD. The corresponding phase is then determined in the next section.

2.3 Results and Discussion

As can be seen in Figure 2.3a, when temperature is below 860°C, only amorphous phase was observed. From 860 °C to 1100 °C, only 2M-wollastonite phase was detected (see Figure 2.3b). At 1150°C, a mixture of α and 2M-wollastonite coexisted, which indicated that 1150°C is very close to the actual phase transformation temperature between the two phases. A more accurate temperature can be determined by inserting more temperatures between 1150°C and 1100°C. In this study, we will use the average between the two temperatures that is 1125°C as the phase transformation temperature. This temperature agrees with the α to β wollastonite transformation temperature (1125°C) reported by reference [9]. Furthermore, natural wollastonite that yielded high-aspect-ratio particles was analyzed under the same condition; the XRD pattern showed it had the same crystal structure with 2M-wollastonite at room temperature. Combining these results, it is therefore reasonable to say that 2M and β wollastonite represent the same crystal structure of wollastonite under most conditions at least when only powder diffraction is available. In this study, no distinction will be made between 2M- and β-wollastonite except with other polytypes that are to be found by future experiments.

By further increasing the temperature to between 1200 to 1400°C, only α wollastonite (4A) was detected, as shown in Figure 2.3c. When temperature was raised to 1500°C, the powder was no longer in crystalline phase; instead, it was amorphous. Neglecting the possible error of the thermocouple used, this XRD observation suggests that at this temperature, even wollastonite is not melted; it should have either become softened or amorphous prior to the reported melting point at 1544°C [9].

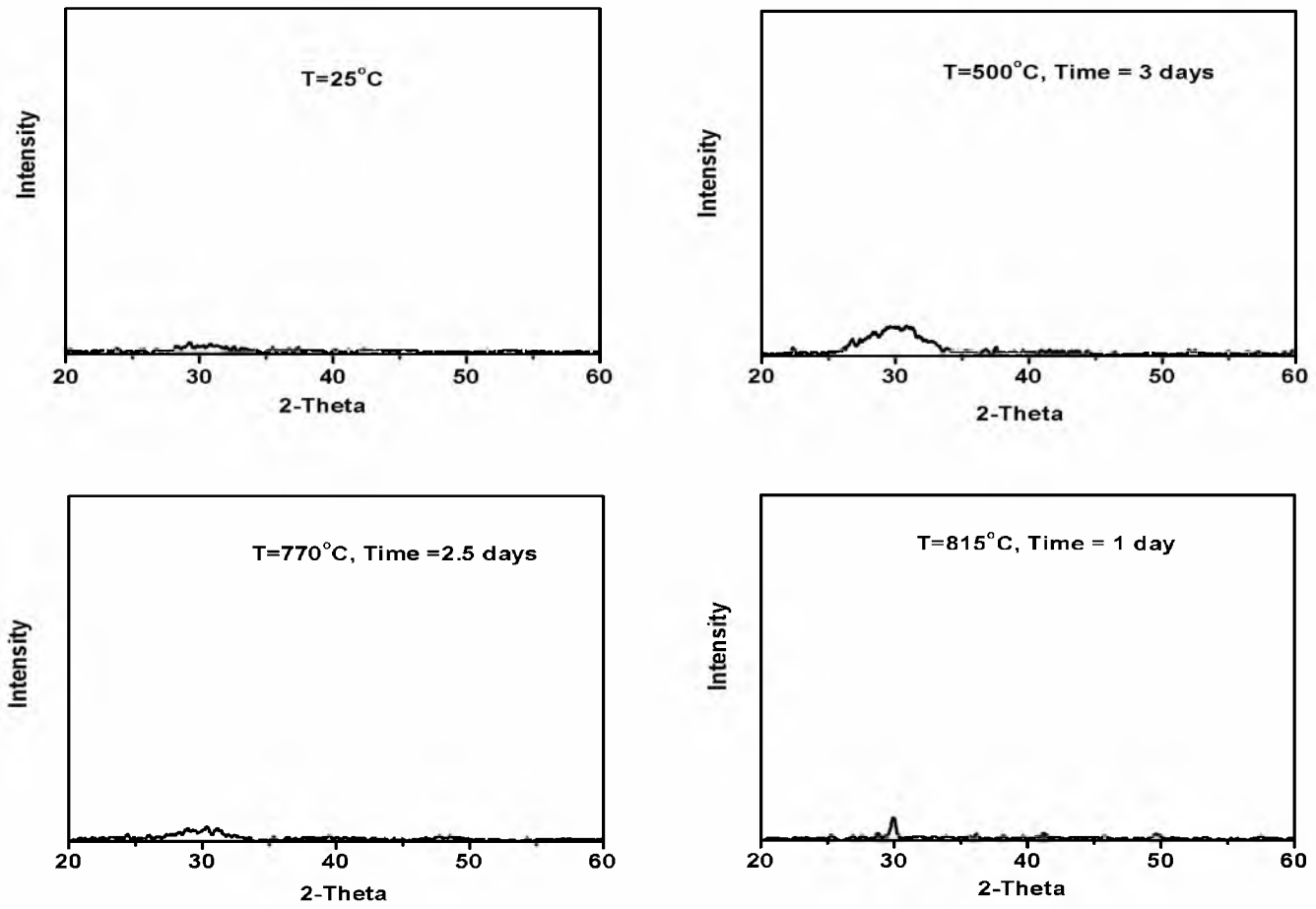

(a)

Figure 2.3 XRD patterns of samples heat treated at temperatures of: (a) 25 to 815°C, (b) 860 to 1150°C, (c) 1200 to 1500°.

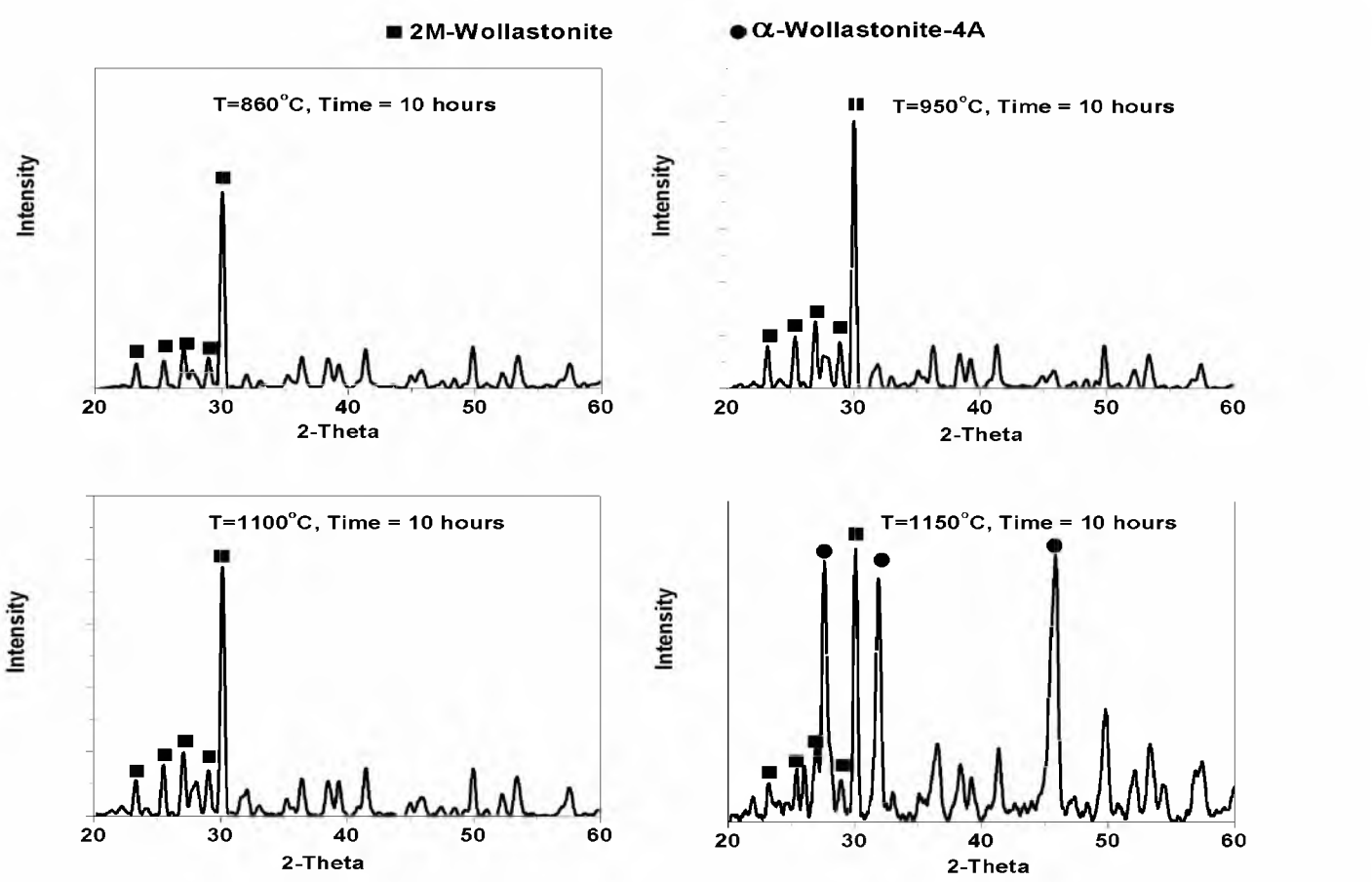

(b)

Figure 2.3 (Continued)

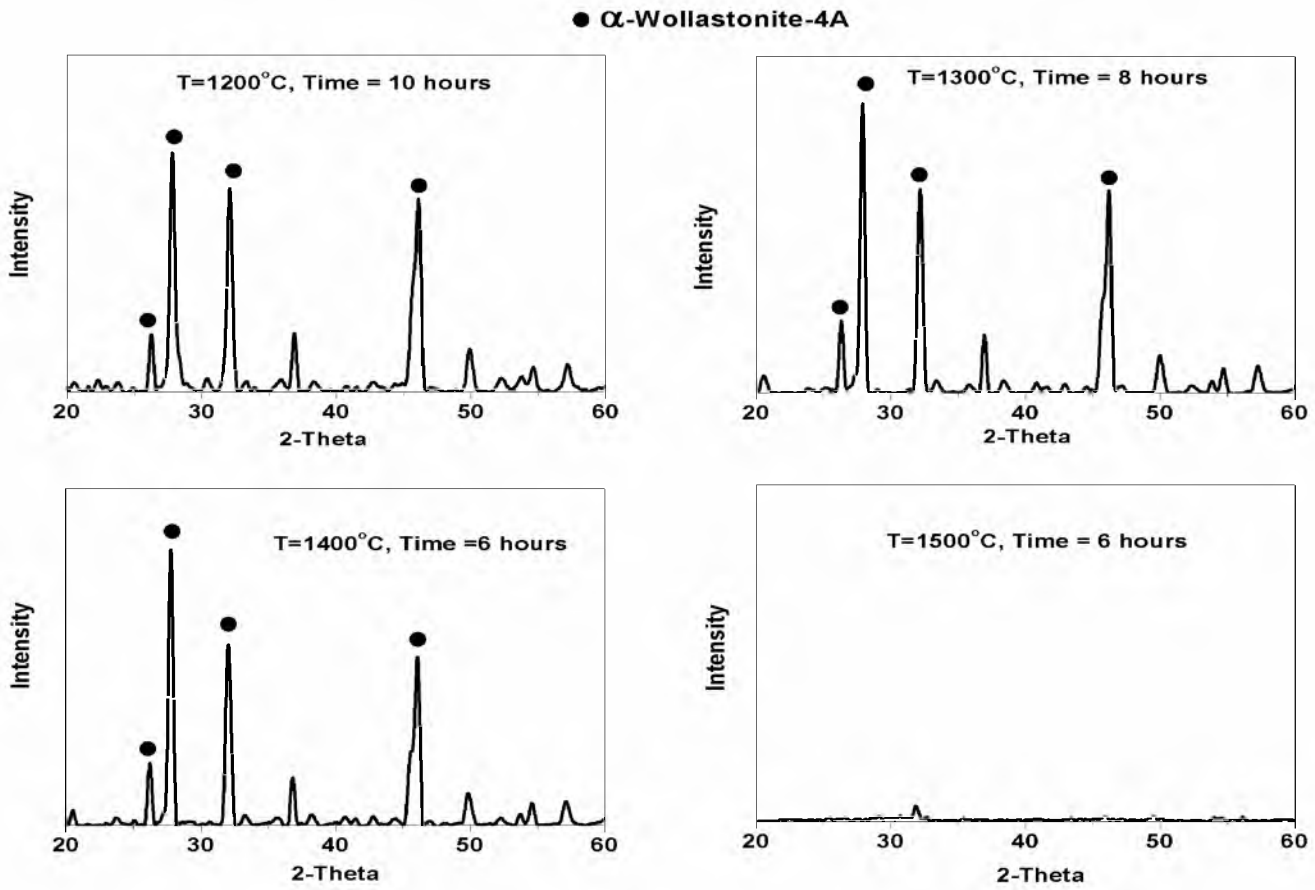

(c)

Figure 2.3 (Continued

From the Introduction, we have seen different polytypes of silica; now, we shall provide a possible explanation to the observed XRD results based on the transformation temperature of silica.

As previously mentioned, silica has two reconstructive transformations and four displacive transformations. The major difference between the two types is that there is no need to break Si-O bonds in the displacive transformations while Si-O has to be broken in the reconstructive transformation. In order to add other atoms, Ca as an example, to the silicate framework, some Si-O bonds have to be broken to accommodate Ca atoms.

The first reconstructive transformation for silica occurs at 860 ^{o}C where high quartz transforms to high tridymite. From the XRD results, 2M-wollastonite obviously began to form also at 860 ^{o}C. The second reconstructive transformation occurs at 1470^{o}C where high tridymite transfers to high cristobalite. Previously, it was determined that wollastonite became amorphous at 1500^{o}C. A possible explanation is that at 860^{o}C, a new configuration of Si-O bonds is more favorable; therefore, old bonds will break, and this will give the chance to adjacent Ca atoms to be reacted with the silica frame structure to form wollastonite ($CaSiO_3$); when temperature is reaching 1470^{o}C, a second type of Si-O bonding is even more favorable, so the Si-O bonds tends to break again. Without the presence of Ca atoms, a new frame structure can form until it reaches the melting point of silica (1723^{o}C); on the contrary, with Ca atoms, the melting point will be decreased. In the case of wollastonite, the melting point drops to 1544^{o}C; under this condition, the broken Si-O bonds may not have the chance to form a new ordered structure as seen in pure SiO_2; instead, a less ordered cluster of Si-O bonds together with Ca atoms may have a lower total free energy.

2.4 Conclusions

In order to grow 2M-wollastonite, experiments were done to determine its favorable nucleation and growth temperatures. Meanwhile, phase transformation of wollastonite($CaSiO_3$) in response to temperature was investigated. Compared with existing data, our results helped to clarify some inconsistences existing in order studies, and for the first time provided the direct information for the synthesis of 2M-wollasonite in the following way: 2M-wollastonite forms in an observable rate only when temperature exceeds 860^{o}C, and it transfers to α-wollastonite-4A around 1125^{o}C, so the latter becomes amorphous when temperature is above 1500^{o}C.

CHAPTER 3

GROWTH OF 2M-WOLLASTONITE CRYSTALS BY A PARTIAL MELTING AND RECRYSTALLIZATION PROCESS FOR THE PREPARATION OF HIGH-ASPECT-RATIO PARTICLES

3.1 Introduction

Currently, there are three types of methods for synthesizing wollastonite: the wet methods [17-20], the solid state reaction methods [1, 12, 21-26], and the liquid phase reaction methods [27, 28]. The three methods all have advantages and disadvantages that have been discussed and compared in detail in Chapter 1.

In this chapter, a method henceforth called the Partial Melting and Recrystallization Process was developed by combining the advantages of the solid state reaction and the liquid phase reaction methods. The purpose of creating a partially melted state is to maintain the original shape of the compacts of raw materials while melted regions form at certain points within the compacts, providing a favorable environment for the growth of wollastonite while obviating the need for a container that must withstand high temperature contact with a corrosive melt. Currently, the synthetic wollastonite accounts for less than 2 percent of world production of wollastonite and is mostly not of acicular type [16].

Among the processing conditions, additives (usually metal oxides) play important roles on the aspect ratio of synthetic wollastonite. Some oxides were reported as additives

for preparing acicular wollastonite, but the effects of those oxides were not well established. Therefore, up to 12 additives were tested in this study.

The products were analyzed by different methods. Under appropriate conditions, fine acicular particles with mean aspect ratios of greater than 5, including particles with aspect ratios of greater than 15, were obtained. These particles were 2M-wollastonite, which is of the same crystal structure as that of high-aspect-ratio natural wollastonite particles.

3.2 Experimental Procedure

3.2.1 Preparation of Raw Materials

Since wollastonite has a 1:1 molar ratio of SiO_2 to CaO, this ratio was adopted for the preparation of starting mixtures. The major raw materials were commercially available SiO_2 (99%) and CaO (99%). Various additives were tested in this study, namely, B_2O_3 (97.5%), Al_2O_3 (99.9%), Na_2O (88% Na_2O, 12% Na_2O_2), Li_2O (99.5%), ZnO (99.1%), Fe_2O_3 (99.9%), MgO (96%), MnO (99%), BaO (88-94%), Co_3O_4 (99.7%), TiO_2 (99.9%), and Na_2CO_3 (99.5%). Table 3.1 shows the compositions of the samples used in this study. The compositions of all other samples used to determine the effects of additives and processing conditions on wollastonite synthesis are presented in the subsections where they are discussed in detail. All the chemicals mentioned above but not listed in Table 3.1 were purchased from Alfa Aesar, Ward Hill, MA.

The aforementioned mixtures were hydraulically dry-pressed into discs at a uniaxial pressure of 300 MPa. Each disc had a diameter of 13 mm and a height of about 5 mm. To prevent the sample disc from reacting with the alumina crucible during heat

Table 3. 1 Composition of Samples 1 to 4 discussed in Chapter 3.

Sample #	Main components (wt.%)		Additives (wt.%)					
	[1]SiO_2	[2]CaO	[3]B_2O_3	[3]Na_2O	[3]Al_2O_3	[4]Na_2CO_3	[3]Li_2O	[2]ZnO
1	46.8	43.2	2.7	1.8	1.8	2.7	1.0	0.0
2	46.8	43.2	2.5	2.0	2.0	2.5	1.0	0.0
3, 4	46.8	43.2	3.0	2.0	1.0	0.0	1.5	2.5

[1]Fisher Scientific, Fair Lawn, NJ; [2]J.T. Baker, Phillipsburg, NJ; [3]Alfa Aesar, Ward Hill, MA; [4]Mallinchrodt Chemicals, Phillipsburg, NJ.

treatment in the furnace, it was put on a sintered SiC disc and then placed in the crucible. The SiC discs were prepared as follows: SiC powder (600 grit) mixed with a small amount of ethylene glycol (99%) was pressed into discs under a hydraulic pressure of 300 MPa. The green SiC discs were sintered at 1250^{o}C for 3 hours.

3.2.2 Heat Treatment

The raw materials were heat treated by following a typical schedule shown in Figure 3.1, except that in some experiments, the schedule was stopped at a certain point. In the schedule, T_S stands for the temperature at which the raw material was partially melted. Its value was determined based on the deformation of the sample during the initial heat-up stage. In order to achieve this, a simple device was fabricated. The working principle is shown schematically in Figure 3.2. A green filter, a monocular telescope, and a web camera with high resolution (8 MP) were placed in the order as illustrated. The web camera was connected to a computer to record the deformation of samples at different temperatures.

Using the system shown in Figure 3.2, the Ts of each type of mixture was determined as the temperature when its contour began to deform at an observable level, which is further divided into three stages. The first stage was when the sample had its corners gradually changing from right angles to curved shape. In the second stage, its contour tilted or bended to one side, and finally, in the last stage, the whole sample spread out or collapsed. The values of Ts were chosen as the temperature at which the samples were in the second stage. Figure 3.3 illustrates two mixtures with different B_2O_3 contents and how they responded to the temperature increase.

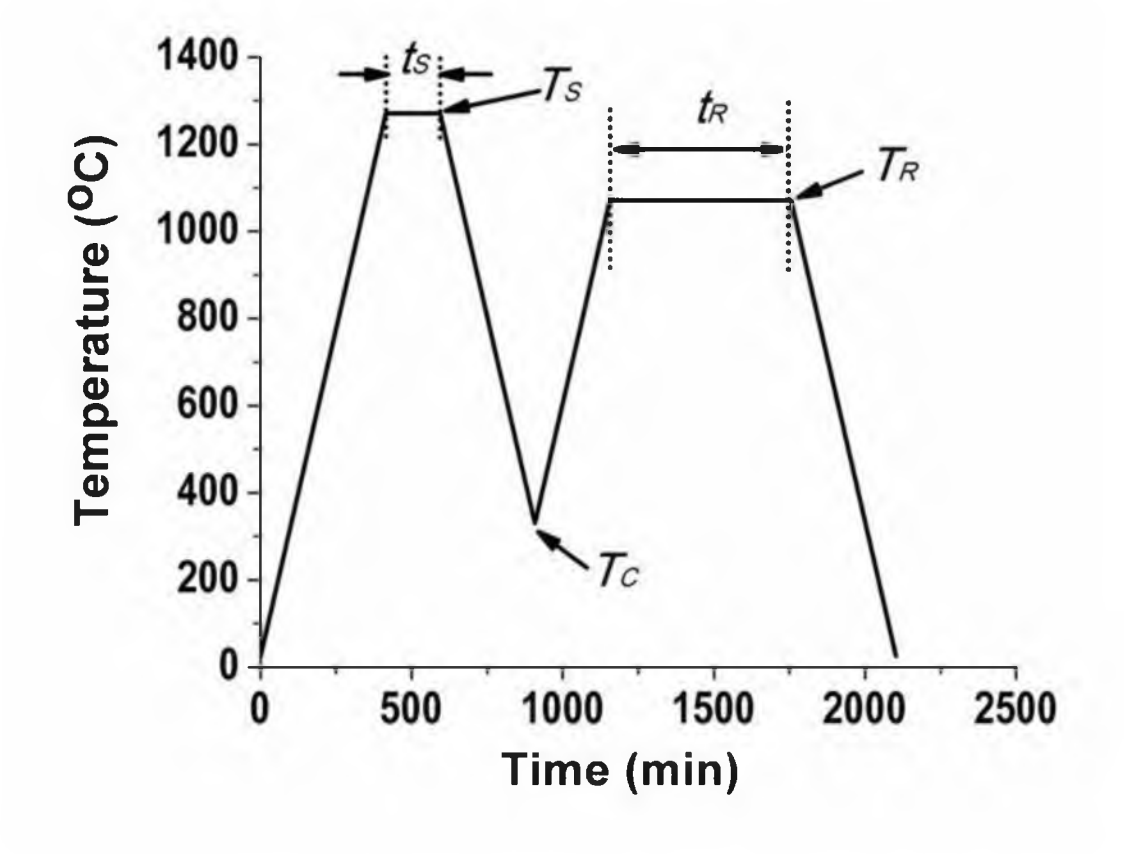

Figure 3.1 Typical heating schedule of the PMR process.

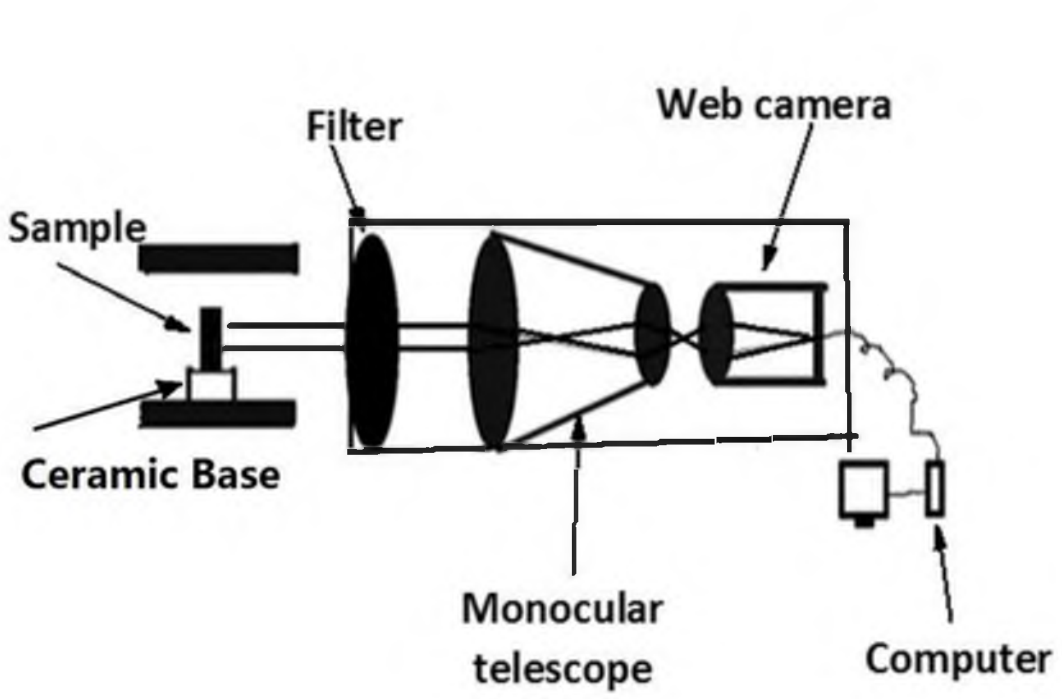

Figure 3.2 Working principle of the device used to measure optimum T_S.

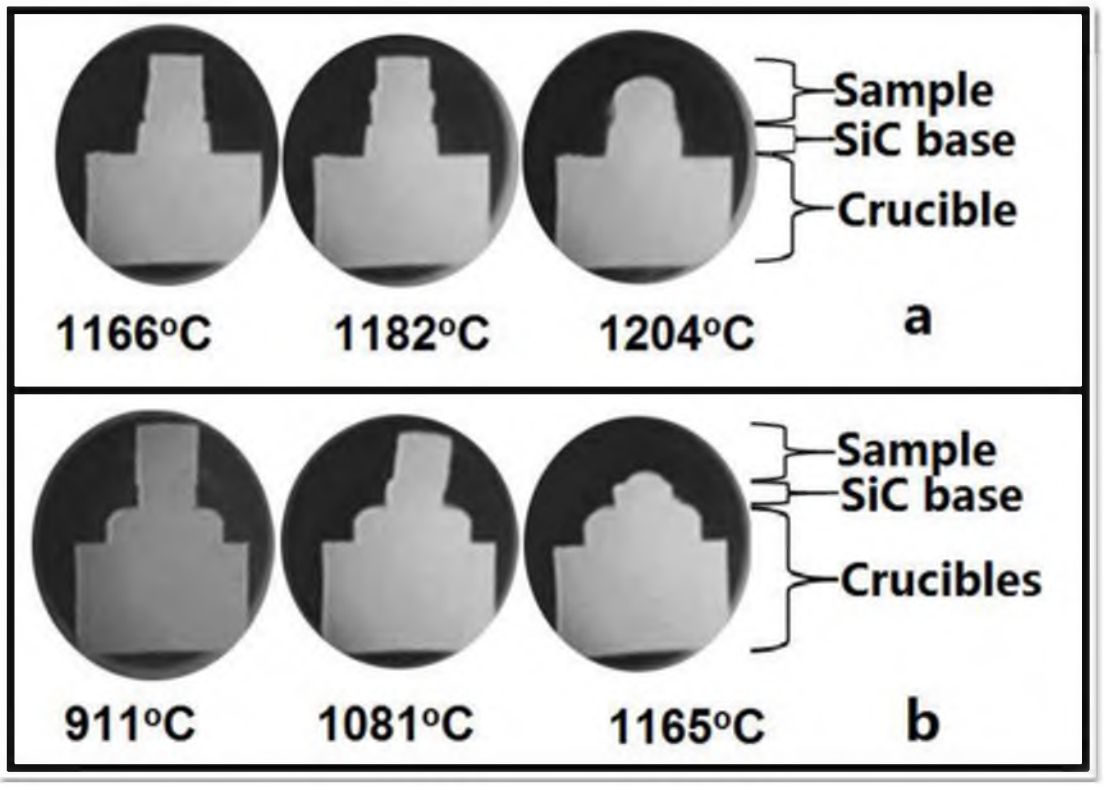

Figure 3.3 Determination of optimum Ts for two samples with different compositions based on their responses to temperature increase: (a) Ts ≈ 1180°C; (b) Ts ≈ 1081°C.

To determine the optimum heat treatment conditions, a detailed experimental procedure is designed, as shown in Figure 3.4.

3.2.3 Measurement of Aspect Ratio

After heat treatment, parts of the samples were crushed inside a cylindrical stainless steel mold by hydraulic pressure to a loose aggregate of < 1 mm size particles. These particles were then placed on a well-polished steel plate to form a thin layer of 0.5 to 1 mm thickness. A heavy cylindrical steel bar with a smooth surface was placed on top of the thin layer. A uniform force was then applied to the steel bar to roll it back and forth on the layer 10 times. The powder was collected and screened by a series of sieves. Particles that remained on the 100 mesh sieve were further ground to below 100 meshes. The aspect ratios of the particles falling in each size range were calculated by measuring the length and width of each particle using the digital images obtained from an optical microscope or SEM. In reality, particles have three-dimensional need-like or rod-like shapes with the two short dimensions having similar sizes, and therefore measurement from the 2D projection images gives an average value of the short dimension. The mean aspect ratio of a given wollastonite powder was measured from five random view fields.

The errors in the measurement were mainly caused by crushing as well as sieving procedure [34]. Other possible factors causing errors were overlapping of particles, irregular particle shapes, and uneven sampling.

3.2.4 Effects of Additives

In order to quantitatively study the effects of additives on the aspect ratio of synthetic wollastonite particles, 12 different candidates were tested. Since some

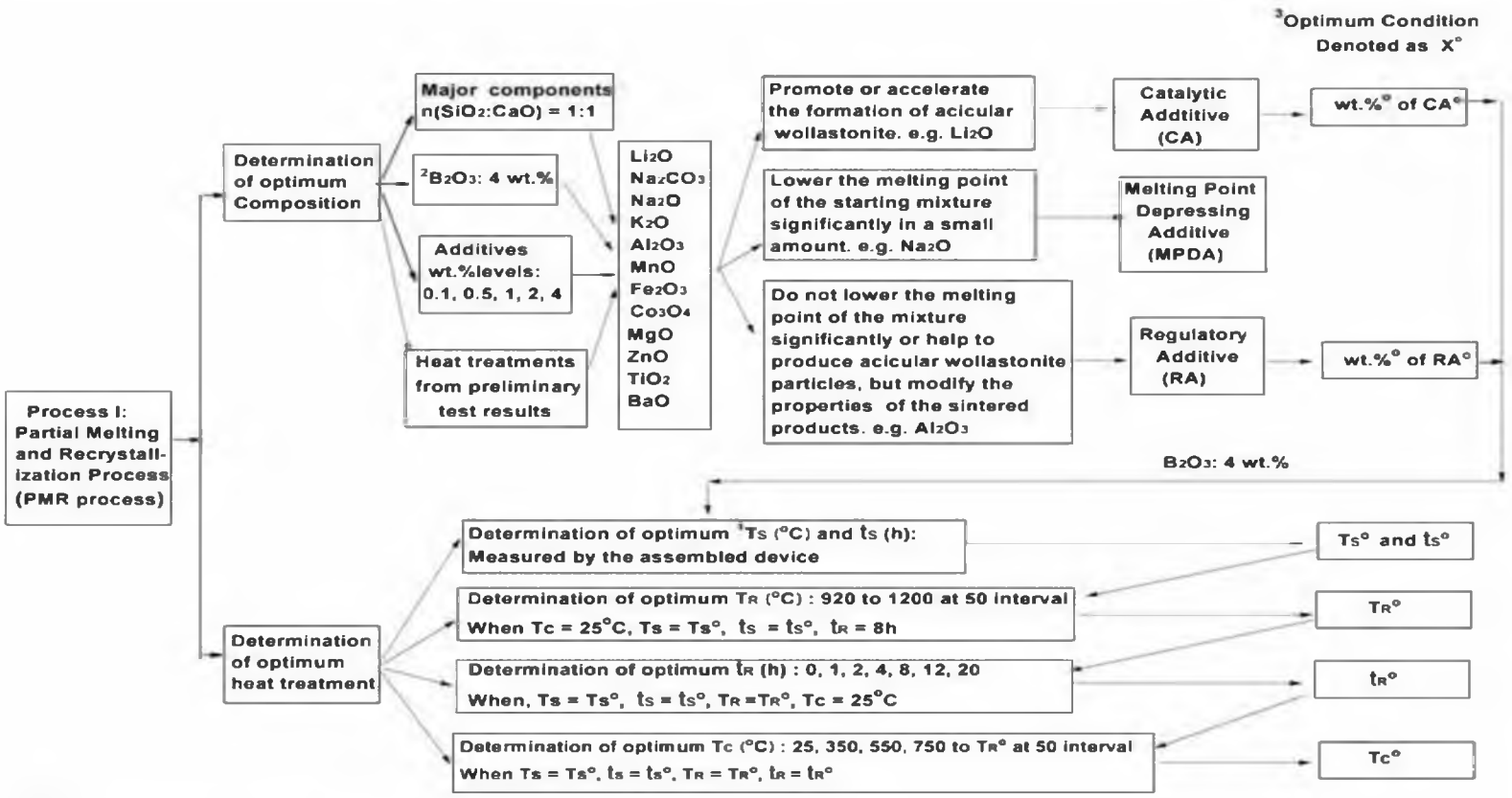

Note:
1: All symbls have been defined in the heating schedule corresponding to this process.
2: Additives are required to produce wollastonite ($CaSiO_3$), but all additives themselves are impurities, their contents are arbitrarily controlled to be lower than 4 wt.%. B_2O_3 has the lowest melting point among all of the additives. Therefore 4 wt.% B_2O_3. is selected as a basis.
3: The mutual effect among the individual optimum conditions is considered as negligbile to simplify the experimental procedures.

Figure 3.4 Experimental flow sheet for the determination of optimum processing conditions for the PMR process.

additives have higher melting points, such as MgO, and TiO_2, a higher temperature is needed to produce a partially melted phase compared with additives with lower melting points such as Na_2O. Therefore, an auxiliary additive has to be added to help generate a partially melted phase. After a few tests, B_2O_3 was determined to be the best auxiliary additive that meets the requirement, without itself promoting the formation of acicular wollastonite particles. The sintering temperature for the measurements of the effects of additives was fixed as 1270°C. At this temperature, the desired partial melting was produced for most samples with only 4 wt.% B_2O_3. For some samples containing relatively high-melting-point oxides, the content of B_2O_3 had to be increased to 6 wt.%. The first group contained 4 wt.% B_2O_3, an additive selected from Li_2O, Al_2O_3, Na_2CO_3, Na_2O, MnO, Fe_2O_3, or Co_3O_4, and a 1:1 molar ratio of SiO_2 and CaO. The second group contained 6 wt.% B_2O_3, an additive selected from ZnO, BaO, MgO, or TiO_2, and a 1:1 molar ratio of SiO_2 and CaO. Each additive was added from zero percent to a level beyond which the aspect ratio remained unchanged or decreased in some cases. T_C and T_R were fixed at 25°C and 1070°C, respectively, and t_S and t_R were fixed at 3 and 5 hours, respectively, which yield good results as discussed later.

In order to understand the mechanism of catalytic additives on the formation of 2M-Wollastonite crystals, three mixtures made of pure 1:1 molar ratio of SiO_2 to CaO (S5), a 1:1 molar ratio of SiO_2 to CaO balanced by 6 wt.% B_2O_3 (S6), and a 1:1 molar ratio of SiO_2 to CaO balanced by 4 wt.% B_2O_3 and 2 wt.% Li_2O (S7), were prepared. The mixtures were pressed into discs and sintered at a partial melting temperature of 1285°C for 3 hours. Part of each sintered-only sample after being cooled to room temperature was further recrystallized at 1070°C for 8 hours followed by being cooled to room

temperature again. The remaining part of each sintered-only sample was heated inside a differential scanning calorimetry (DSC) equipment to record heat gain or loss during the ramping up stage. Samples at different stages were also analyzed by XRD.

3.2.5 X-ray Diffraction

The crystal structure of synthesized products was determined by X-ray diffraction (XRD) using a Siemens D5000 X–ray diffractometer, with Cu-Kα radiation, 0.02° step size, and 0.4 second scan time interval. The working voltage and current were 40 KV and 20 mA. The 2-theta scan range was from 20° to 100°. The collected patterns were compared with α-wollastonite (JCPDS 10-486) and 2M-wollastonite (JCPDS 43-1460).

3.2.6 SEM and Optical Microscope

The morphology of individual particles and the microstructure and elemental distribution of polished wollastonite samples were investigated using scanning electron microscopy (SEM, TOPCON SM-300), and optical microscope (PME3 Inverted Metallurgical Microscope, Olympus). For polished samples, they were prepared by regular metallographic techniques and etched with 10 vol.% HF solution for 15~20 seconds.

3.3 Results and Discussion

3.3.1 XRD, SEM, and Optical Microscope Analysis

Figure 3.5 shows that the major crystalline phase in natural wollastonite (NW) particles that present high-aspect-ratios is 2M-wollastonite. The major phase in wollastonite product with sintering only (SW) is alpha-wollastonite. The major phase in the product with both sintering and recrystallization treatment (SRW) is 2M-wollastonite,

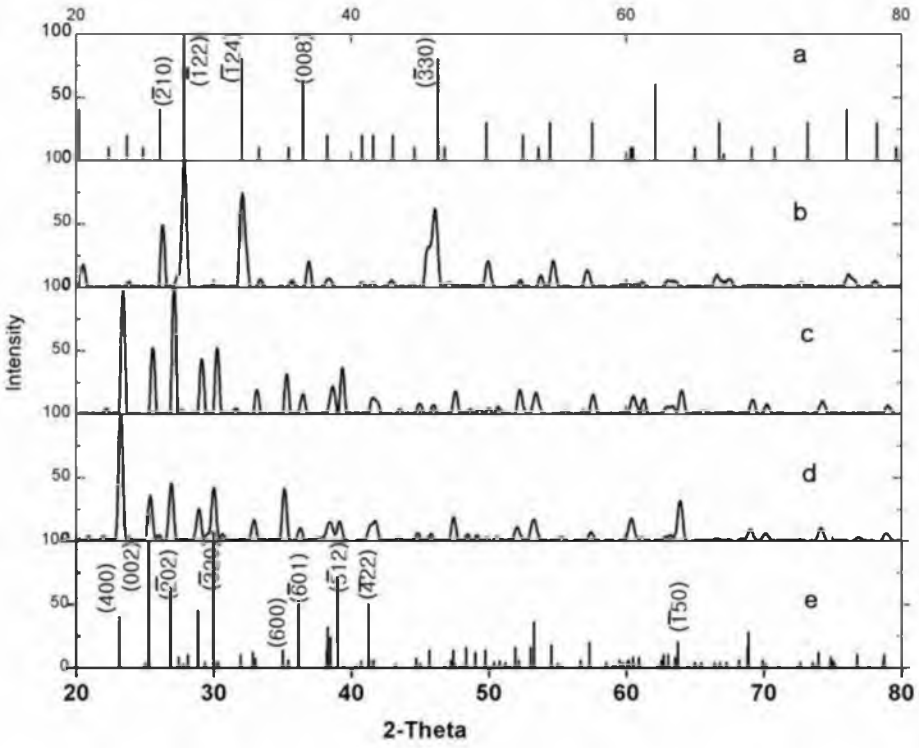

Figure 3.5 XRD patterns: (a) standard XRD pattern of alpha-wollastonite (also called cyclowollastonite, JCPDS 10-486); (b) product with sintering only (SW) - Sample 3; (c) product with both sintering and recrystallization treatments (SRW) - Sample 4; (d) natural wollastonite (NW) from NYCO Company (NYGLOS®12); (e) standard XRD pattern of 2M-wollastonite (JCPDS 43-1460).

which is the same as in natural wollastonite.

Corresponding to the difference in crystal structures, we found that the fracture surfaces of the SW and the SRW products also have different properties. The exposed fracture surfaces of the SW samples were relatively smooth, while the SRW samples had a rough facture surface, as shown in Figure 3.6.

Under the exposure to a light source with changing direction, the fracture surfaces of the SW products showed nearly even reflection of light from different areas. The fracture surfaces of the SRW products, however, showed that some areas were brighter than the surrounding areas, as seen in Figure 3.6. These brighter areas mostly had rectangular shapes with a maximum length of about 4 mm, and a maximum width of about 2 mm. These areas were either the crystal faces that were developed during the crystal growth stage or the planes created during special cleavage, as seen in Figure 3.7. By varying the incident light direction, new brighter spots were reflected, while the previous ones disappeared, one can even use tweezers to pick small crystals with the help of light reflection, as shown in Figure 3.8. Some preliminary explanation to this phenomenon is given as follows: 2M-wollastonite has good cleavage along certain planes just like mica. When exposed to incident light, these planes display directional reflection of the incident light because of their perfect smoothness. Compared with 2M-wollastonite, alpha wollastonite does not have planes with good cleavage. As a consequence, a beam of incident light will be reflected much weaker from such a fracture surface, making the reflection diffusive.

Knowing this difference can actually help to estimate the aspect ratios of particles obtained from an uncrushed product to a relatively good accuracy. If no shining crystals

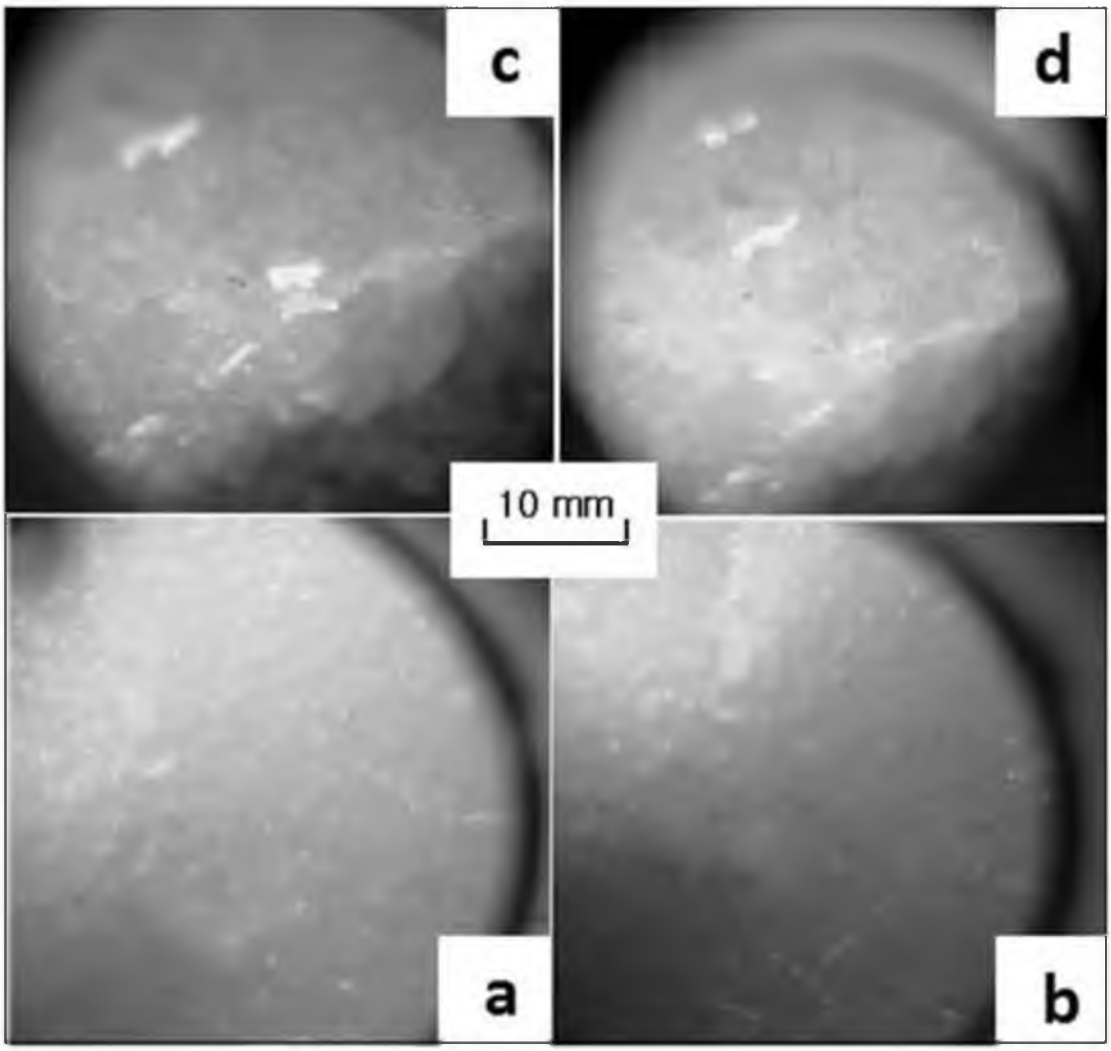

Figure 3.6 Reflection of incident light from fracture surfaces of: (a and b) a product with sintering treatment only (SW) - Sample 3 (The entire surface displays diffuse reflection); (c and d) a product with both sintering and recrystallization treatments (SRW) - Sample 40 (Lighter areas show directional reflection from either the cleavage planes or crystal faces).

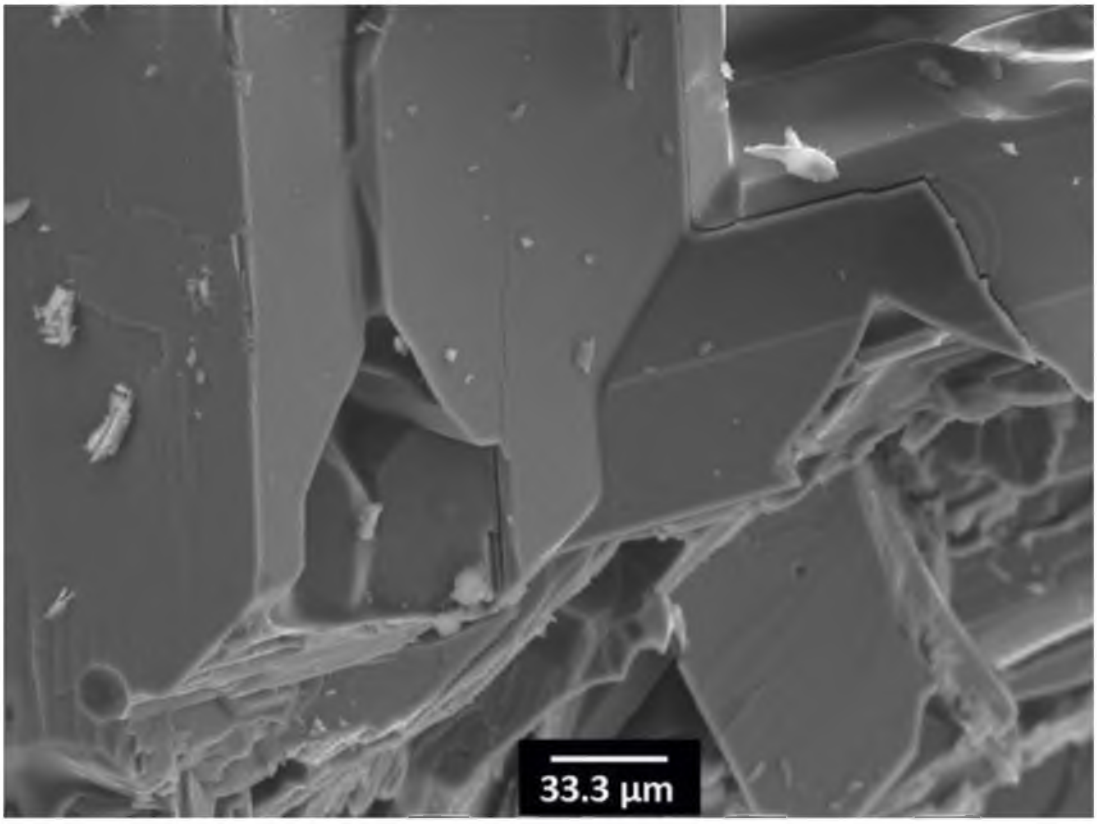

Figure 3.7 Demonstration of flat crystal faces or cleavage planes that act as perfect planes for mirror reflection.

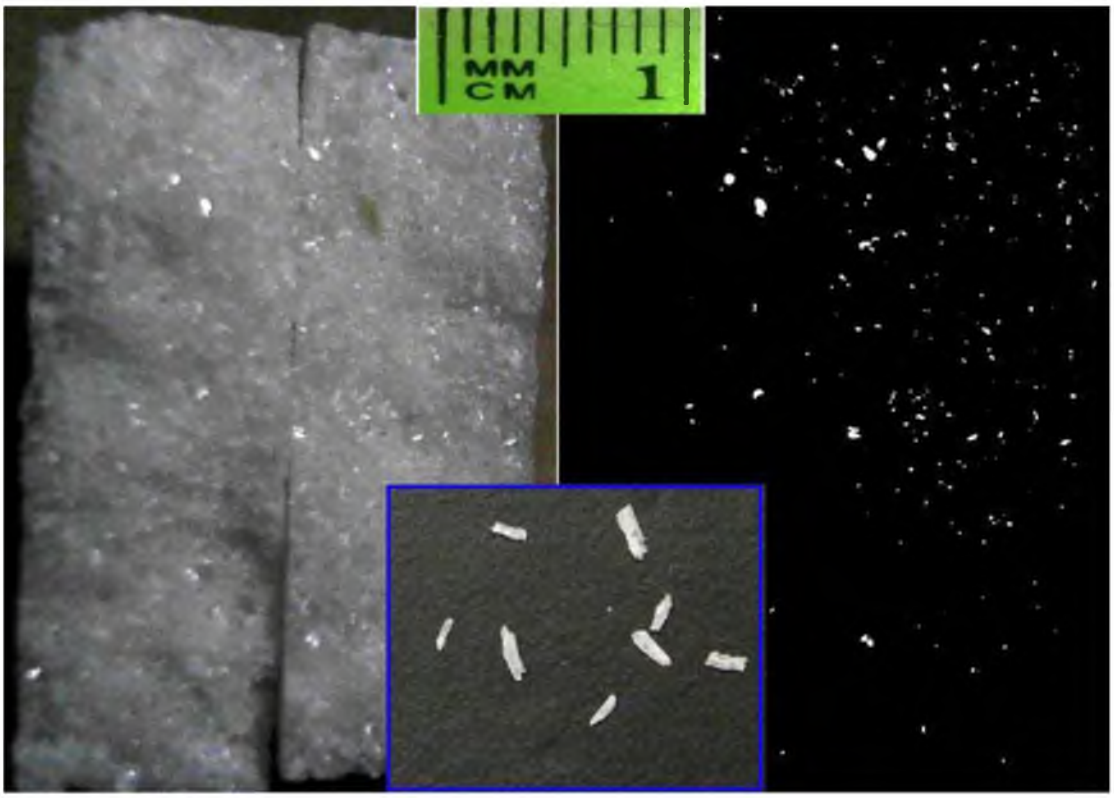

Figure 3.8. Reflection of light from crystal faces or cleavage planes under bright (Left) and dark environment (Right). The bottom inserted figure shows crystals picked from the brighter regions in the left and right figures.

or planes are seen under light exposure, it is almost certain that no acicular particles will be created after crushing the bulk sample. On the contrary, if the whole facture surface is distributed by those shining crystals, it is likely that acicular particles will be obtained, and the bigger the crystals or planes are, the higher the mean aspect ratios will be. By using this method, one can have a quick and preliminary evaluation to the final products without crushing and sieving, making it useful for the synthesis of wollastonite in industrial scale if the Partial Melting and Recrystallization Process is adopted.

As shown in Figure 3.9, both the SW and the SRW products have a second phase dispersed in the main matrix. Energy Dispersive X-ray Spectroscopy (EDX) results indicate that the major phases in both products have a nearly 1:1 molar ratio of Si to Ca, which conforms to the chemical formula of wollastonite, i.e., $CaSiO_3$. The low content of oxygen is due to its light atomic weight. It is also noted that aluminum and sodium concentrate in grain corners and pores. However, lithium and boron are not seen either in the major phase or in the defects, which is probably due to their light atomic weights.

3.3.2 Particle Morphology

The particle shapes of raw materials and the crushed synthetic wollastonite (SRW) particles are compared in Figure 3.10. As shown in Figure 3.10a to g, all raw materials show either spherical or polygonal shapes with aspect ratios nearly 1:1 except Al_2O_3 particles (Figure 3.10b) presenting some trigonal shapes. The crushed wollastonite particles (from Sample 4), however, show mainly acicular shapes with varying aspect ratios (Figure 3.10h). An optical microscope image shows that these acicular particles are semitransparent with the two longest edges along the major axis parallel to each other, as seen in Figure 3.11. Particle 1 in Figure 3.11 shows an aspect ratio of about 30:1.

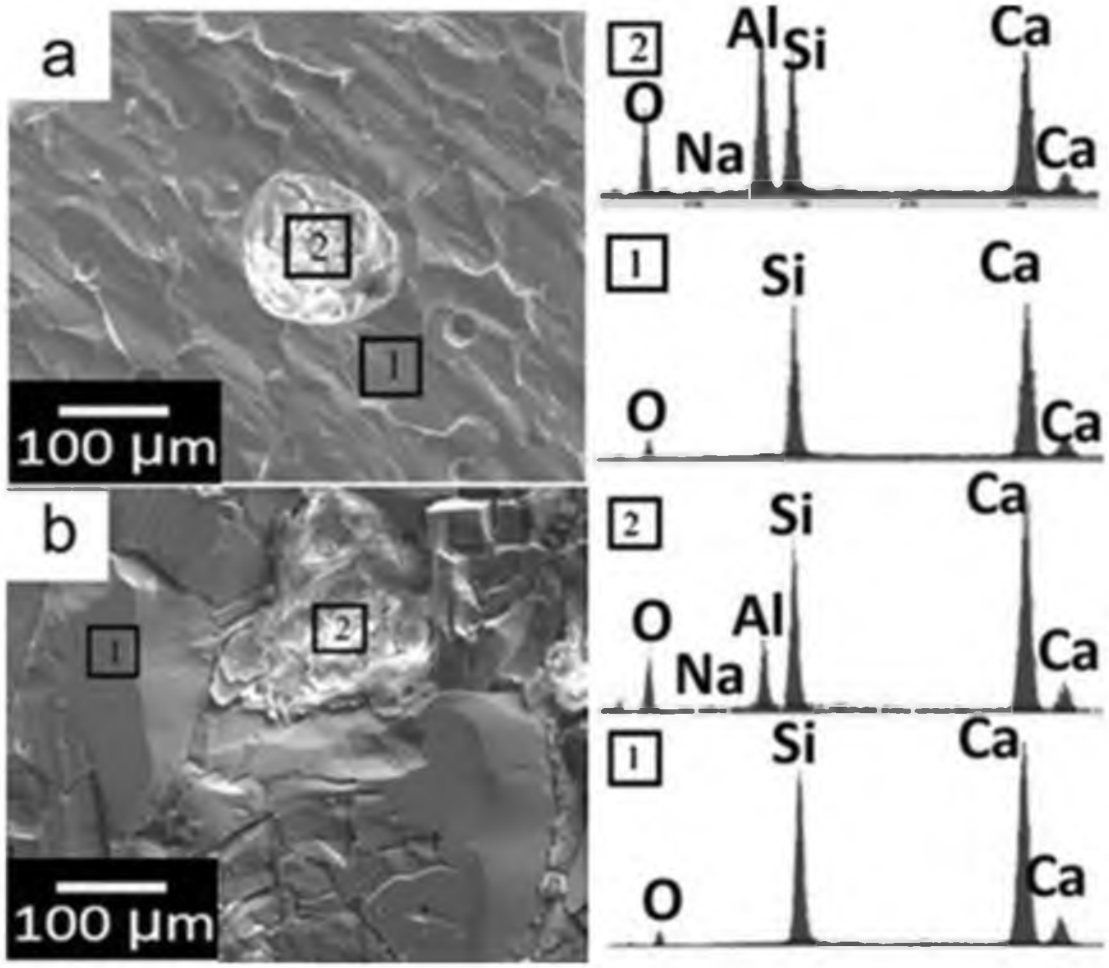

Figure 3.9 SEM images and EDX analysis of samples: (a) with sintering treatment only (SW) - Sample 3 and (b) with both sintering and recrystallization treatments (SRW) - Sample 4. Both samples were etched for 15~20 seconds with 10 vol.% HF solution.

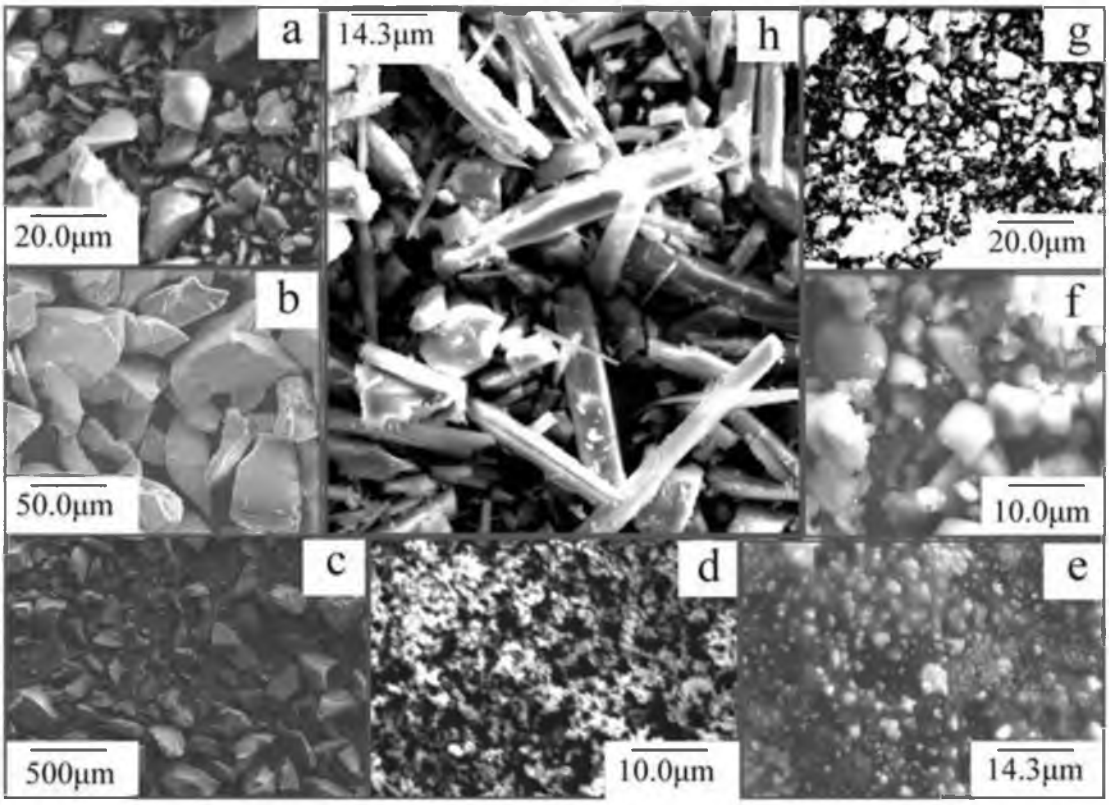

Figure 3.10 Particle shapes of: (a) SiO_2, (b)Al_2O_3, (c) B_2O_3, (d) ZnO, (e)Na_2O (12% Na_2O_2), (f) Li_2O, (g) CaO, (h) Synthetic wollastonite (Sample 4).

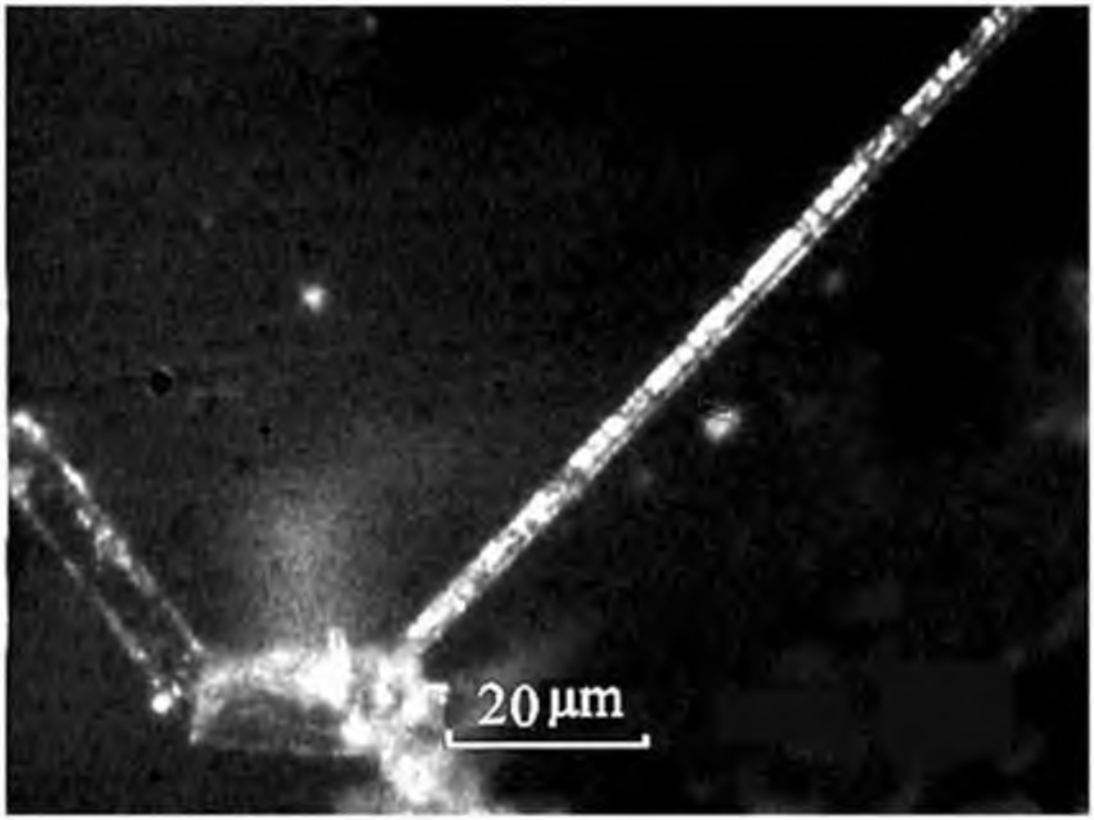

Figure 3.11 Three particles collected from Sample 1 coincidently made up a check mark. Particles 1, 2, and 3 have aspect ratios of 30:1, 5:1, and 2:1, respectively. These particles are semitransparent under an optical microscope.

Compared with Particle 1 and 2, Particle 3 shows not only smaller aspect ratios but also irregular shapes looking like a soft agglomeration. Initially, we thought this particle might be a cluster of small particles. However, these clusters of particles with irregular shapes were also observed by SEM from similar products. With EDX analysis, we found that these particles with irregular shapes were most of the time not wollastonite particles.

Four view fields corresponding to four different particles from Sample 2 were analyzed by SEM and EDX, as shown in Figure 3.12. Two of the four particles have regular shapes, while the other two have irregular shapes. The particles with regular shapes show nearly equal contents of calcium and silicon, and no other metal elements were observed. The particles with irregular shapes show not only calcium and silicon, but also sodium and aluminum at small percentages, which agrees with their small addition during raw materials preparation. The carbon peaks were introduced by the carbon tape used to attach the sample particles. Though these irregular shape particles usually take less than 5% in number, because of their nearly 1:1 aspect ratios, their effects on reducing the mean aspect ratios of the synthetic wollastonite and how to remove them effectively will be investigated in our future study.

As seen from Figure 3.13a through 13d, particles obtained from products with sintering only (SW) have a nearly 1:1 aspect ratio in the range of 38 to 150 μm. Some particles smaller than 38 μm have a 2:1 to 3:1 aspect ratio, as shown in Figure 3.13e and f, but the average aspect ratio is still very low.

The aspect ratios of particles obtained from products with both sintering and recrystallization treatments (SRW) are between 2:1 to 5:1 for the size range of 75 to 150 μm, as shown in Figure 3.14a and 13b. While the aspect ratio of the particles in the

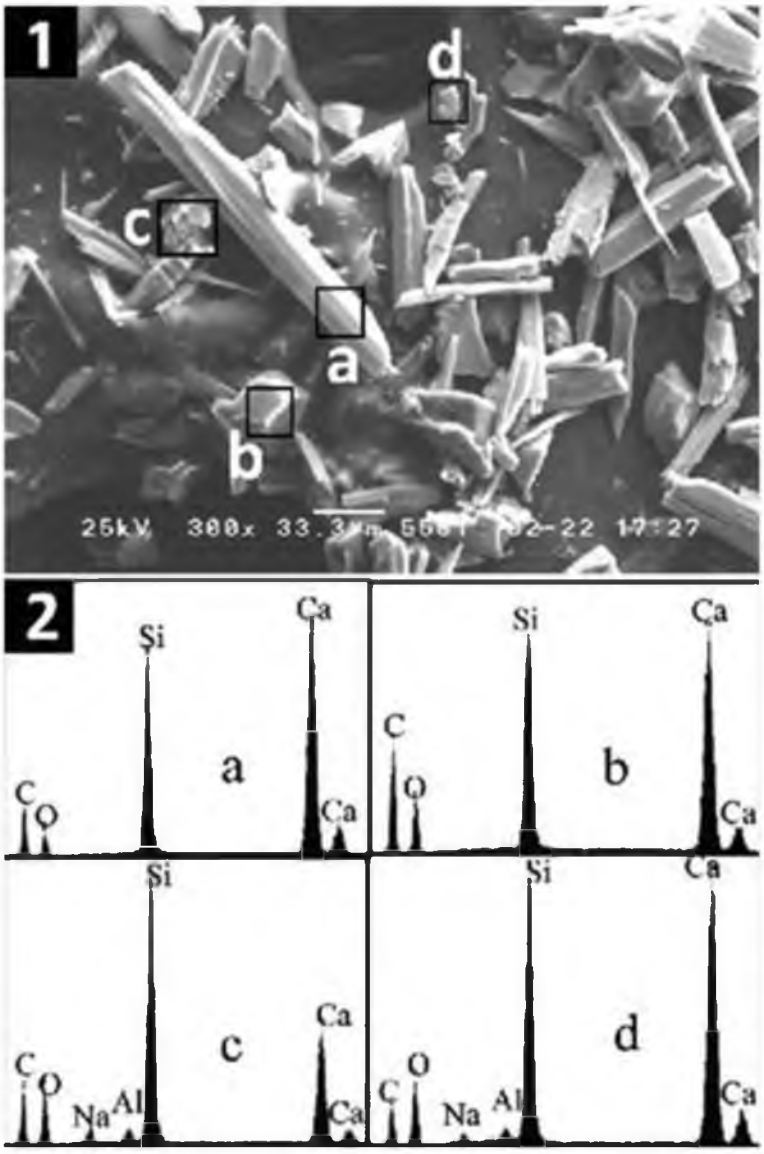

Figure 3.12 SEM images presenting particles obtained from a recrystallized product (Sample 2): (1a and 1b) particles with regular shapes; (1c and 1d) particles with irregular shapes; (2a to 2d) EDX spectrum of particles 1a to 1d. While only calcium and silicon are observed as metal elements in the particles with regular shapes, additional metal elements including sodium and aluminum appear in the particles with irregular shapes.

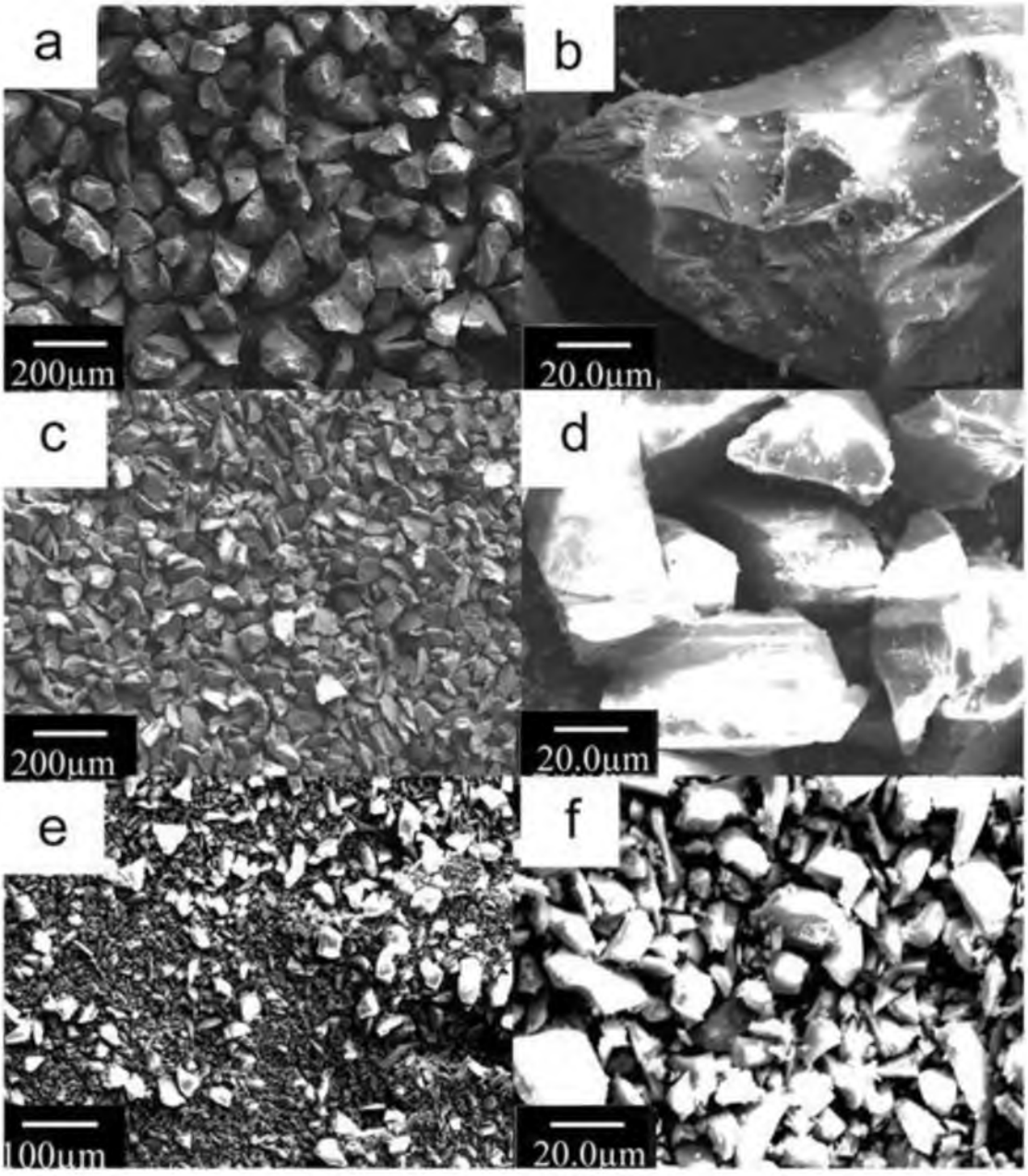

Figure 3.13 SEM images of particles obtained from product with sintering only (SW) -Sample 3: (a and b) size range of 75~150 µm under low and high magnification; (c and d) size range of 38~75 µm under low and high magnification; (e and f) size range of below 38 µm under low and high magnification.

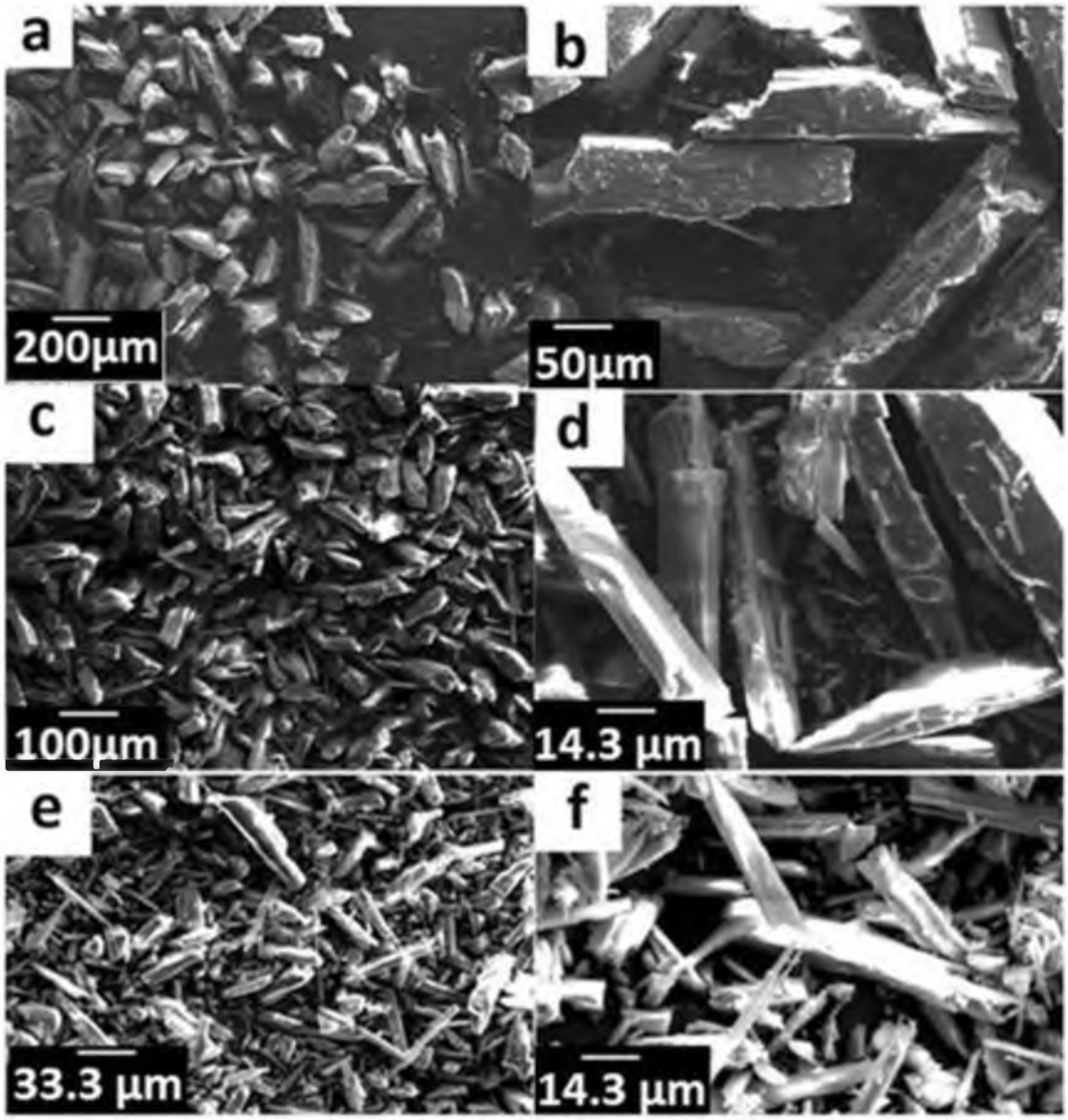

Figure 3.14 SEM images of particles obtained from product with both sintering and recrystallization treatments (SRW) - Sample 4: (a and b) size range of 75~150 µm under low and high magnification; (c and d) size range of 38~75 µm under low and high magnification; (e and f) size range of below 38 µm under low and high magnification.

range of 38 to 75 μm is about 3:1 to 8:1, it increases to 5:1 to 15:1 for the particles smaller than 38 μm.

The difference in the aspect ratio between the SW and the SRW particles can be explained by their microstructures shown in Figure 3.15. The SW particles have a smooth fracture surface with no obvious cracks or faults on the surface. These particles look like tiny hard stones, as seen in Figure 15a and 15b. The SRW particles have straight parallel cracks and stacking faults extending along the major axis, as seen in Figure 15c and 15d. When particles with such cracks or faults are pressed under external forces, they are much easier to break into more acicular particles, making them different from the SW particles.

3.3.3 Formation of Single Crystals

From Chapter 1 and Chapter 2, we know that the precondition of forming acicular wollastonite particles is to form 2M-wollastonite crystals. We produce acicular particles by crushing these crystals to allow themselves to cleave along special planes rather than forming individual acicular crystals directly. This means the crystals grown by this process must be large enough so that they have the capability to be ground into smaller particles. The aspect ratios of wollastonite particles vary from a few micrometers to a few tens of micrometers on average. Therefore, even in a case even when we had formed 2M-wollastonite single crystals, if they were not large enough, for example a few tens or hundreds of nanometers in size, they are useless in current industrial applications, at least before new applications or evidences can be found for such fine acicular particles.

The first evidence of forming single crystals is from the direct observation of fracture surfaces of samples that produce acicular particles after being crushed. As can be

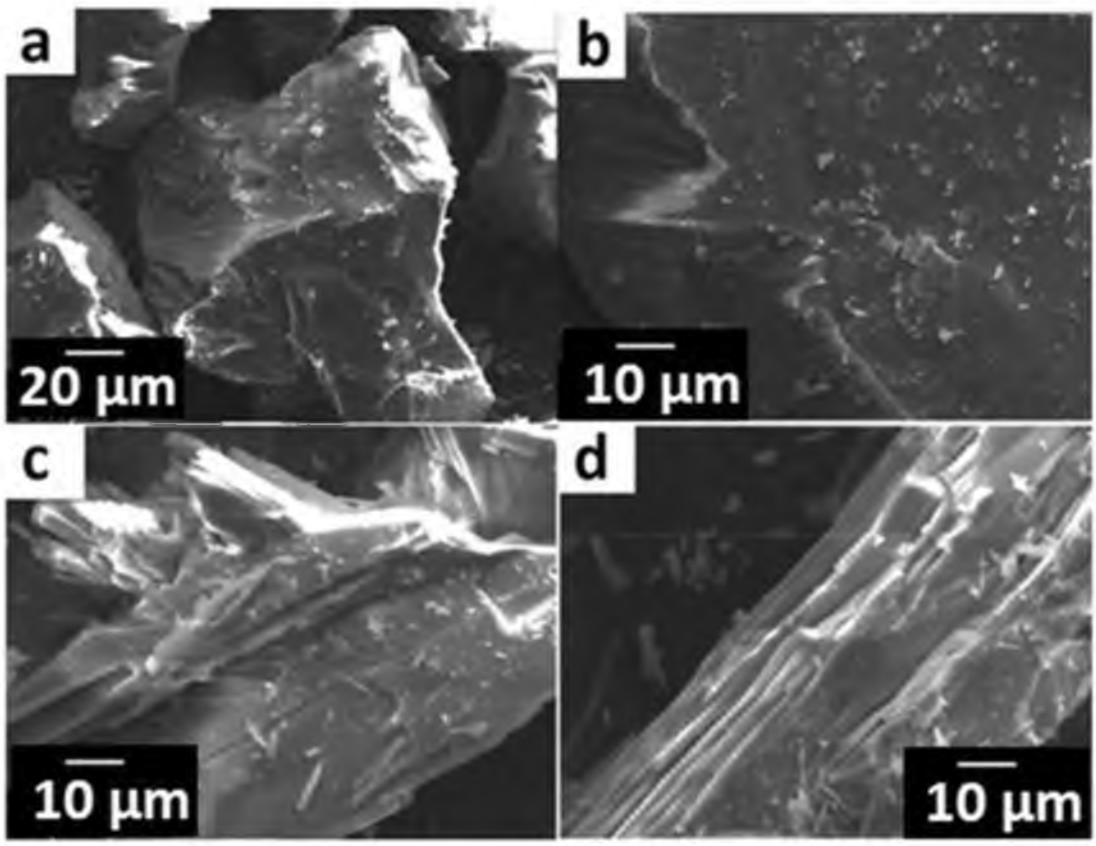

Figure 3.15 SEM images of individual particles in the size range of 75~150 µm: (a and b) two random particles from product with sintering only (SW) - Sample 3, they have a smooth fracture surface with no obvious cracks on the surface; (c and d) two random particles from product with both sintering and recrystallization treatments (SRW) - Sample 4, presenting parallel cracks and stacking faults extending along the major axis.

seen from Figure 3.16, the center two crystals labeled as 2 and 3 are apparently single crystals because of their well-developed crystal faces. Compared with Crystal 2 and 3, the crystals within the circle 4 are much smaller, but they have even more well-developed faces because they formed inside a corner surrounded by bigger crystals, which made the competition less severe. Another example of forming such single crystals within corners is shown in Figure 3.17. The second evidence of forming single crystals comes from the crystal above 2 and 3 in Figure 3.16; it is labeled as Crystal 1. This crystal does not show perfect crystal faces, but it has many cracks parallel to each other. Since we have confirmed that the crystals are 2M-wollastonite crystals that have good cleavage along the b direction, if these cracks were from different crystals, i.e., polycrystals, they are unlikely to be parallel. These cracks are also free of mechanical effects because in other crystals of different crystal orientations, we also see parallel cracks, as shown in Figure 3.18. Lastly, these crystals can be found from either nonetched or etched surfaces of polished samples that yielded acicular particles, as shown in Figures 3.19 and 3.20, respectively.

3.3.4 Effects of Additives on Aspect Ratio

As shown in Figure 3. 21, additives play different roles on the mean aspect ratio of wollastonite particles. It is clearly seen that particles obtained from products containing one of the four additives, namely B_2O_3 (melting point 450°C), Na_2CO_3 (melting point 851°C), Na_2O (melting point 1132°C), and Al_2O_3 (melting point 2072°C), have mean aspect ratios that are nearly 1:1. However, compared with the other three additives whose melting points are lower than the applied sintering temperature (usually

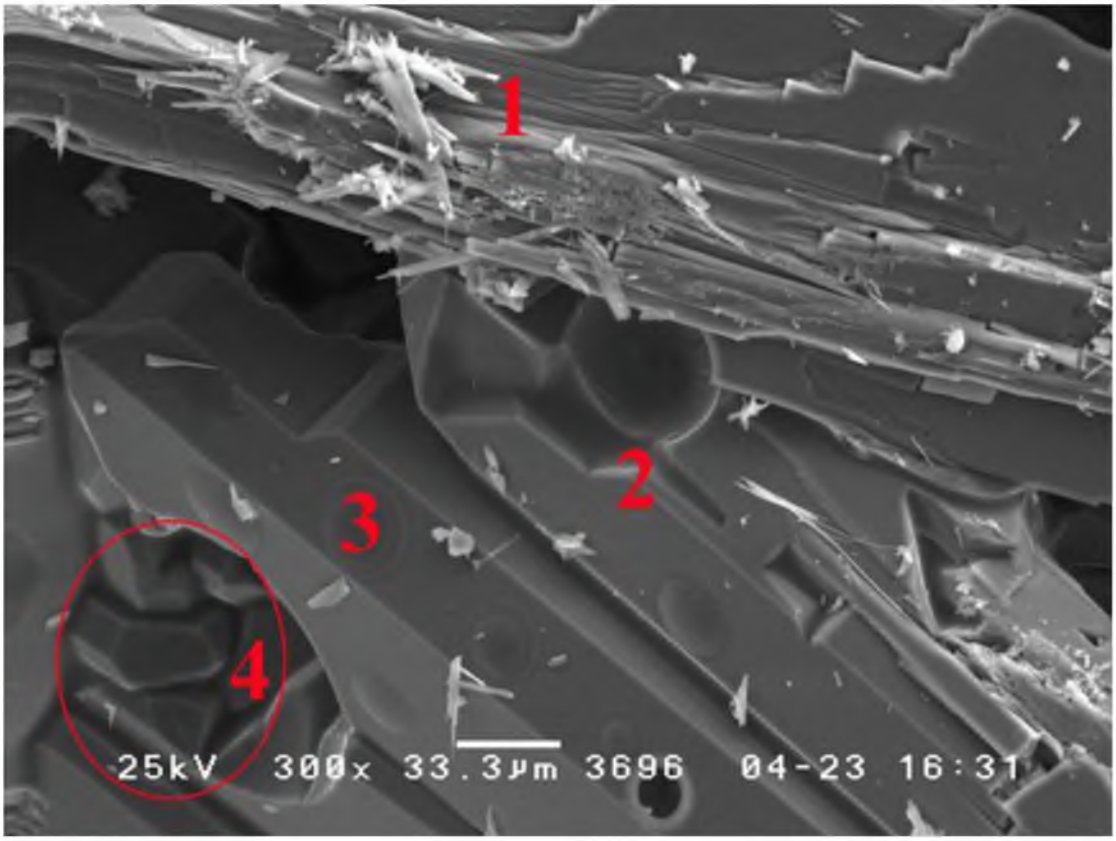

Figure 3.16 Formation of single crystals: (1) parallel cracks from an individual crystal, (2) and (3) are individual crystals that have well-developed crystal faces, (4) shows crystals of smaller size forming around the corners of bigger crystals.

Figure 3.17 A second demonstration on the formation of small crystals around corners of bigger crystals with well-developed crystal faces. These crystals may help to understand the growth behavior of 2M-wollatonite crystals.

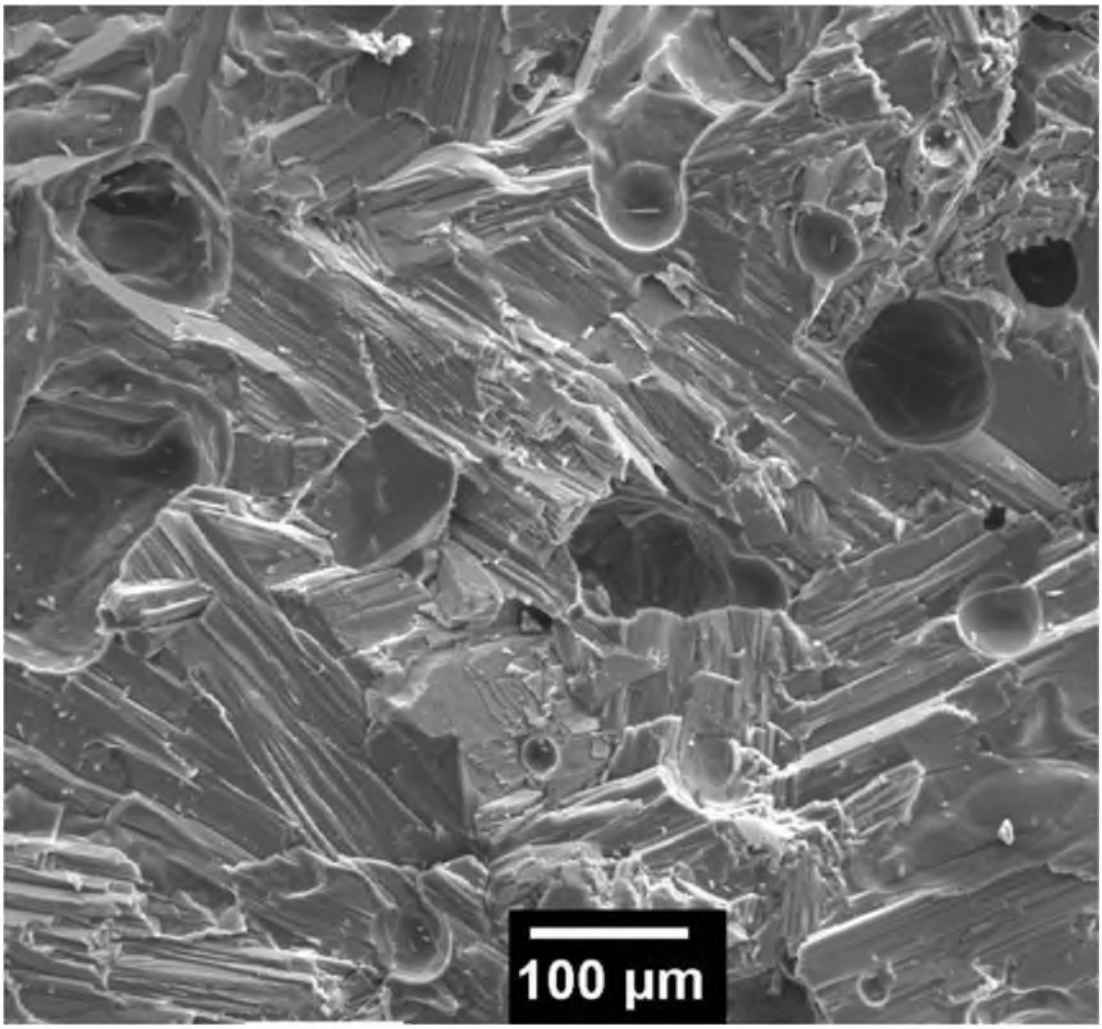

Figure 3.18 Parallel cracks within individual crystals of random growth orientations.

Figure 3.19 A quasi "3D" image made of three single optical images presenting the microstructures of three polished surfaces from a PMR product. The three surfaces are perpendicular to each other but the locations of the three viewing areas are independent of each other. All the surfaces are as polished without etching.

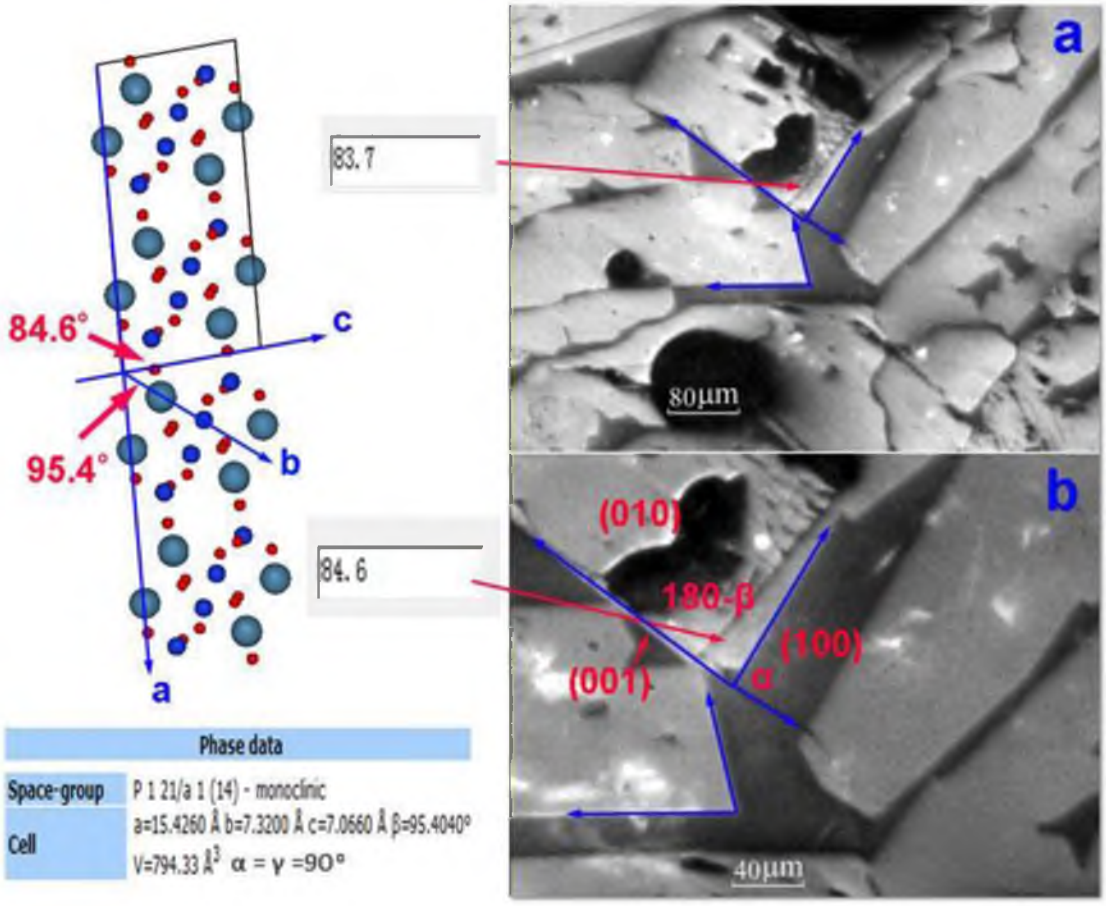

Figure 3.20 Exposure of single crystals from a PMR product (polished and etched by 10% HF).

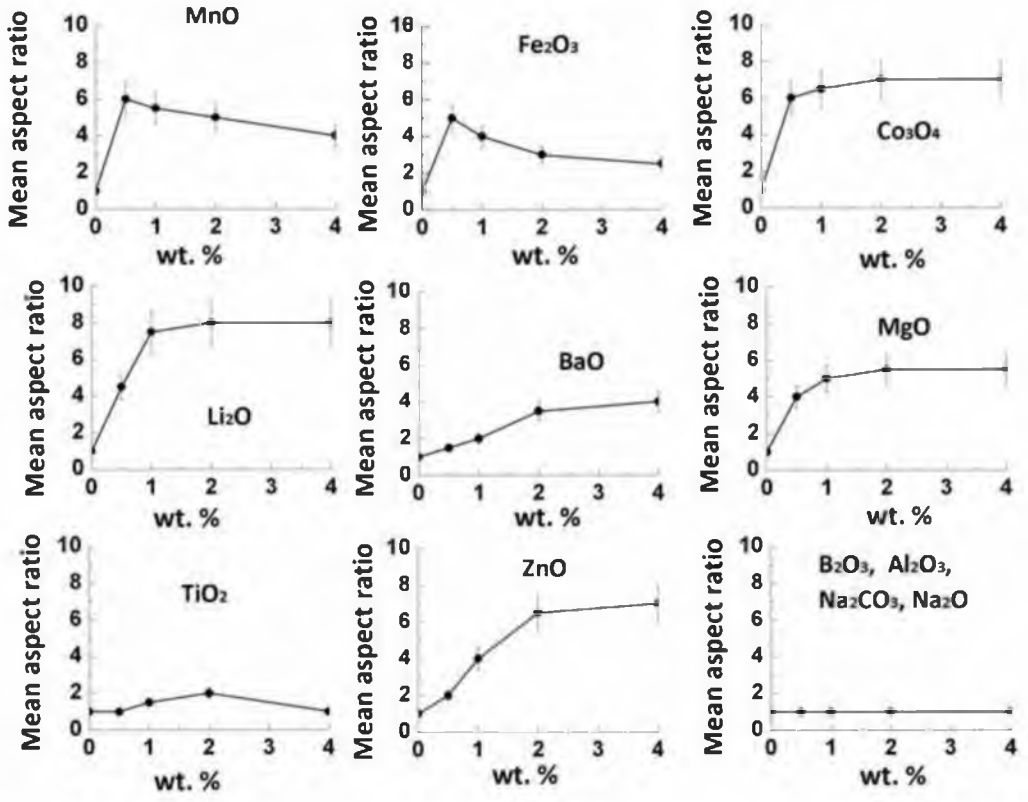

Figure 3.21 Plots of the mean aspect ratios of the products containing different additives as a function of additive contents in the raw materials.

1270°C, Al_2O_3 has a much higher melting point. Therefore, it is unlikely that Al2O3 can help to form partially melted phase. However, when added with one or more of the other three additives together, Al_2O_3-containing discs shrank more in dimensions compared with the discs containing only the three other additives, resulting in an increased densification.

The remaining eight additives, Li_2O, Co_3O_4, MnO, Fe_2O_3, BaO, MgO, TiO_2, and ZnO, all promote the formation of acicular wollastonite particles, but they show different efficiencies on the mean aspect ratios of wollastonite particles. In general, the mean aspect ratios of the particles containing one of the eight additives increase with increasing additive content, and gradually level off at about 2 wt.%, except MnO, TiO_2, and Fe_2O_3 containing particles showing a decrease in mean aspect ratios to some degree after they reach the maximum effect, as shown in Figure 3.21. Taking the experimental error into consideration, the three exceptions follow a similar trend as that of the other five additives, which means the effects of additives on the mean aspect ratio of wollastonite particles will saturate at low levels and will no longer increase the mean aspect ratio if added in excess. Among the eight additives, particles containing Li_2O, ZnO, and Co_3O_4 show the highest maximum mean aspect ratios, followed by particles containing MgO, MnO, and Fe_2O_3 as having medium mean aspect ratios. Particles containing TiO_2 and BaO show the lowest mean aspect ratios among the eight. However, products containing Co_3O_4, MnO, and Fe_2O_3 have blue, pink, and brown appearances, respectively, with only 0.5 wt.% addition, while products containing other additives have white appearances.

Products with colorized appearances may not be accepted if used as commercial wollastonite substitutes, such as in plastic and paint applications.

Based on the description above, these additives are classified into three groups. The first one is melting point depressing additives, which lower the melting point of the starting mixture significantly in a small amount (less than 10 wt.%). These oxides are B_2O_3, Na_2O, and Na_2CO_3. The second group is regulatory additives, which do not lower the melting point of the mixture significantly or help to produce acicular wollastonite particles, but modify the properties of the sintered products, such as reducing the pores in the products, resulting in a higher density. Al_2O_3 is one of these additives. The role of such a regulatory additive is very much like sintering of Al_2O_3 with MgO as additive [35] and sintering of ZnO with Al as additive [36]. Pure Al_2O_3 does not sinter to high density and typically has abnormal grain growth. A small amount of MgO, as low as 300 ppm, cuts down grain growth and enhances density. Several explanations have been offered to explain the role of MgO in the sintering of Al_2O_3. One can find a good review in the article by Bennison and Harmer [35]. In ZnO sintering, the addition of Al significantly inhibited the grain growth of ZnO; it was observed that a small amount of Al dopant (less than 1.2 mol%) was beneficial to achieve dense ZnO ceramics with more than 99% densification. From this point of view, Al_2O_3 might actually be adverse to the formation of acicular particles because it can have the potential of cutting down the initial crystal growth of newly formed 2M-wollastonite crystals, resulting in formation of smaller crystals; this is supported by the nearly 1:1 molar ratio of sample containing only B_2O_3 and Al_2O_3 as additive. However, our experimental results indicated that with this increased densification, the crystals exposed to the facture surface of samples containing

Al_2O_3, Li_2O, and also B_2O_3 as additives were actually larger and more visible, and meanwhile, the sample still kept a higher densification after heat treatment. Therefore, the grain growth theory can explain well the higher densification of the samples containing Al_2O_3 but may not be applied to the formation of 2M-wollastonite crystals when it is added simultaneously with catalytic additives, which will be discussed below.

The third group is catalytic additives, which promote or accelerate the formation of acicular wollastonite. Such additives are Li_2O, ZnO, Co_3O_4, MgO, MnO, Fe_2O_3, BaO, and TiO_2. Considering the maximum mean aspect ratios and appearances, Li_2O was determined as the best catalytic additive because of its high efficiency (smaller amount to reach the same mean aspect ratio) and higher acicularity of samples containing Li_2O as the catalytic additive.

In order to understand the mechanism of these additives, especially the catalytic additives, on the formation of 2M-wollastotnie crystals, we did further experiments as explained in the Experimental Procedure section. The results are shown and analyzed below.

As can be seen from Figure 3.22, the fracture surfaces of the sample containing SiO_2 and CaO only present a porous structure made of spherical to elliptical grains. From later XRD analysis, we know that these grains are mainly α-wollastonite crystals along with some 2M-wollastonite crystals, but apparently both did not have a chance to grow bigger during the recrystallization stage, probably due to the low diffusion rate at solid state. Thus, the formed crystals are small in size and have mainly irregular shapes. When such samples were crushed, the particles failed to produce acicular particles in large quantity, as seen in Figure 3.23. However, in these spherical particles, we could also see acicular particles of very small amounts (typically less than 5%). The reason of having

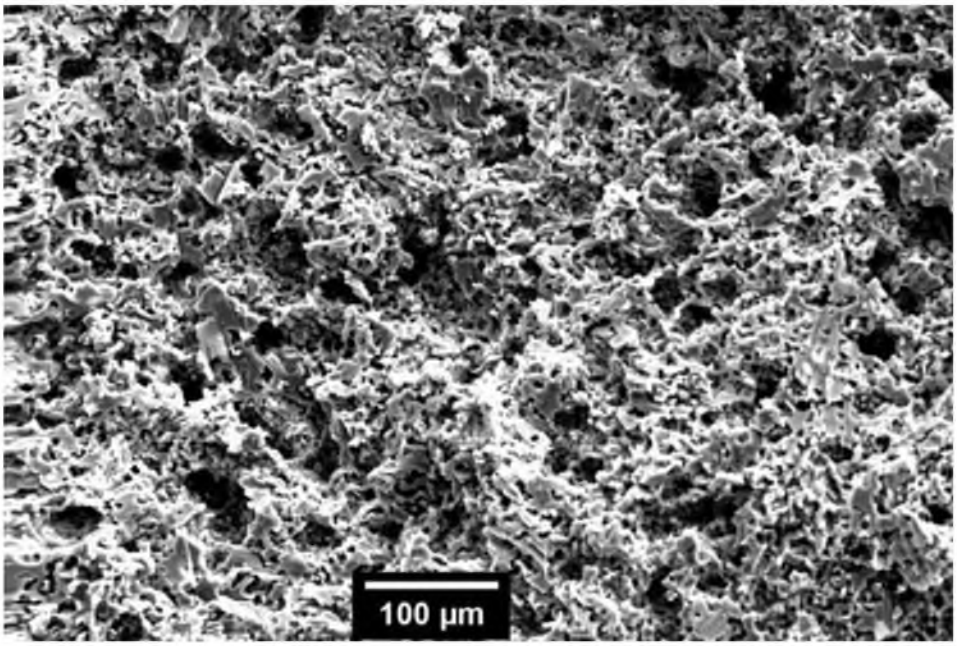

(a)

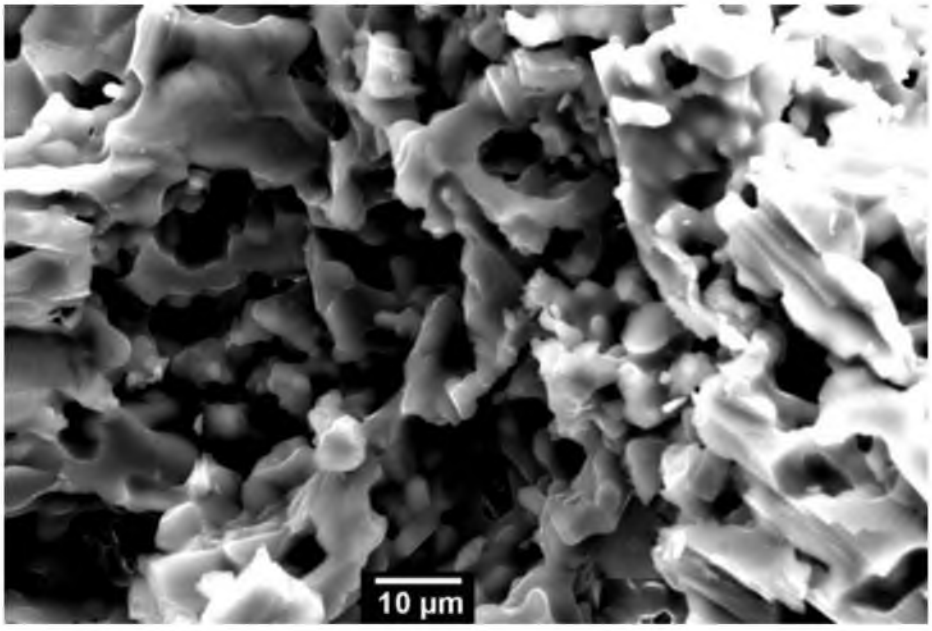

(b)

Figure 3.22 Fracture surfaces of the sample containing SiO_2 and CaO only (S5) presents porous structure made of spherical to elliptical grains under low (a) and high (b) magnifications.

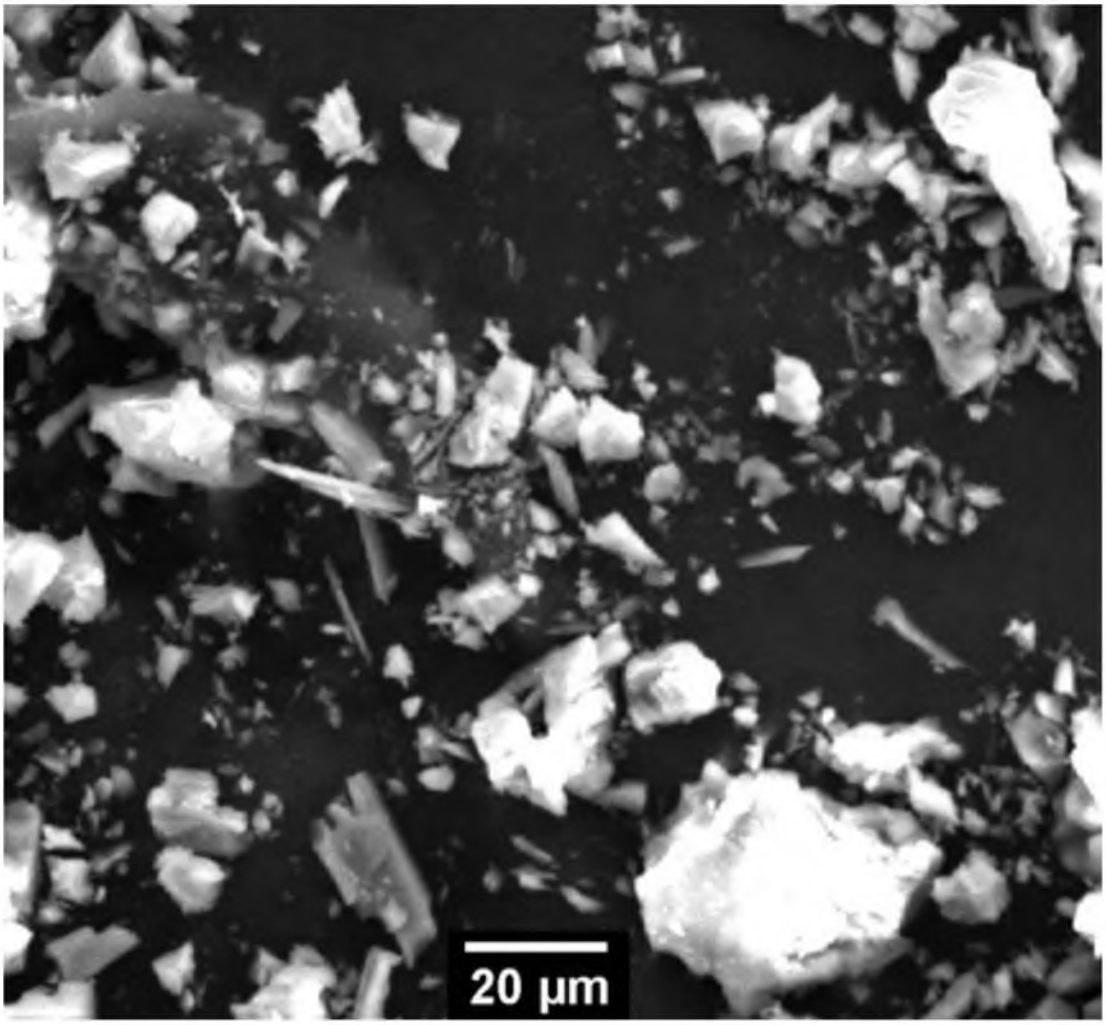

Figure 3.23 Morphology of particles obtained from the sample as shown in Figure 3.22. The overall particles display a low mean aspect ratio.

these acicular particles is because of the relatively larger regular crystals formedoccasionally within the porous structure, as seen in Figure 3.24. These crystals are very likely 2M-wollastonite crystals.

The fracture surface of the sample containing SiO_2, CaO, and B_2O_3 presents also irregular particles, but it seems the particles are coated by a liquefied layer (see Figure 3.25). Under higher magnification, we can see some spherical agglomerates or tumor-like structures, as shown in Figure 3.25b. The absence of regular crystals indicates that the obtained particles will probably have a low aspect ratio, and this is confirmed by Figure 3.26.

The fracture surface of the sample containing SiO_2, CaO, B_2O_3, and Li_2O, however, presents a very different structure. As can be seen in Figure 3.27a, under the same low magnification with Figures 3.22a and 3.25a, the fracture surface containing Li_2O displays regular crystals of much bigger sizes. Meanwhile, some of these crystals have flat surfaces or cracks parallel to each other, as seen in Figures 3.16, 3.18, and 3.27. In wollastonite synthesis, this type of structure is very favorable; it is a direct indication of the ability to form acicular particles, which is verified in Figure 3.28. Note that the particle in the right bottom corner of Figure 3.28 does not have a large apparent aspect ratio, but it has many cracks extending along the same direction; thus, it has the capability to break into more acicular particles during further crushing.

In order to understand the morphology differences caused by additives, samples heated at various temperatures were analyzed by XRD. The observed XRD patterns are shown in Figures 3.29 to 3.31. Before going to the analysis, it is necessary to explain the rules used in these figures. The label corresponding to each pattern follows the rule of "*SX - T_S* °C - *t_S h - T_C°C - T_R°C - t_R h - 25*°C ", where SX stands for samples having

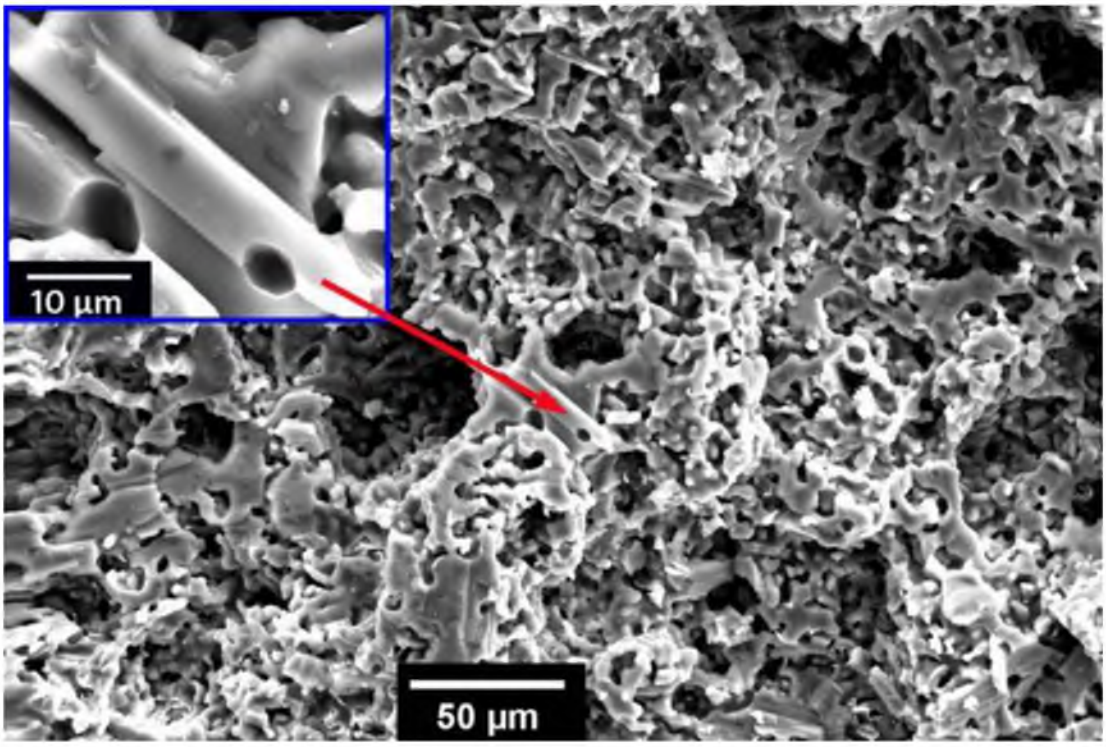

Figure 3.24 Evidence on the formation of regular crystals among irregular grains in Sample S5. The regular crystals are likely 2M-wollastonite crystals. They may have contributed to the presence of small amounts of acicular particles in Figure 3.23.

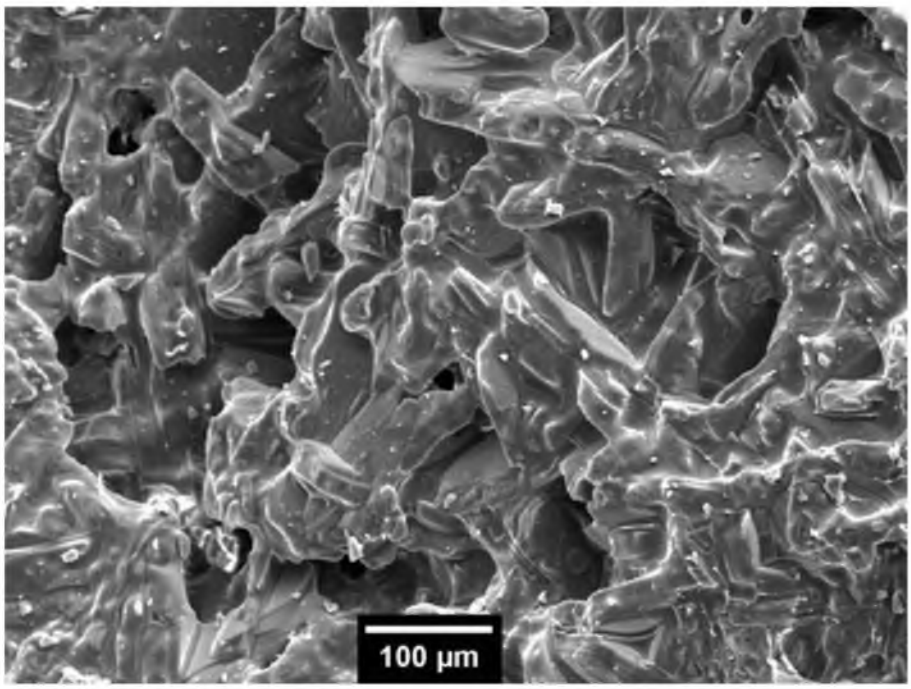

(a)

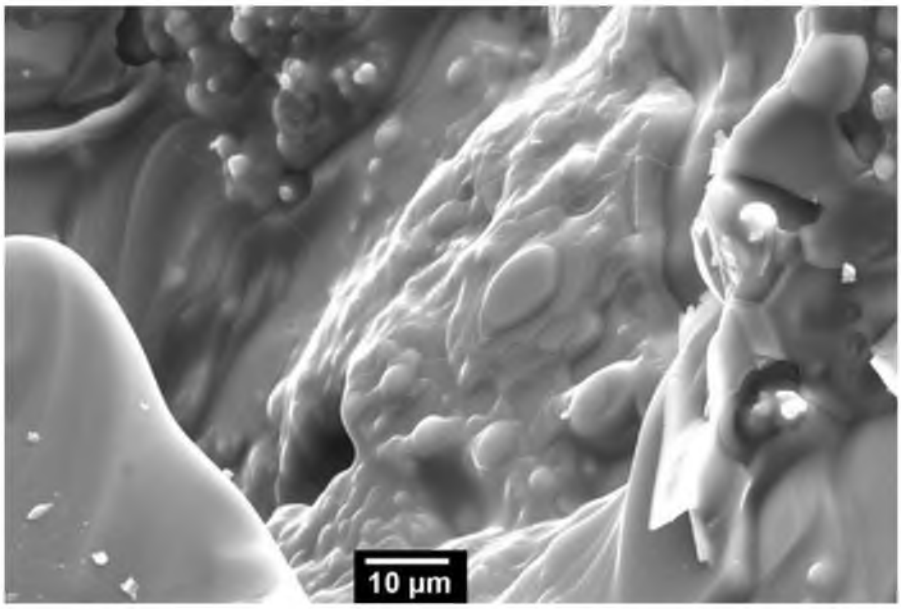

(b)

Figure 3.25 Fracture surfaces of the sample containing SiO_2, CaO, and B_2O_3 (S6) presents irregular grains that seem to be coated by a liquified layer under low (a) and high (b) magnifications.

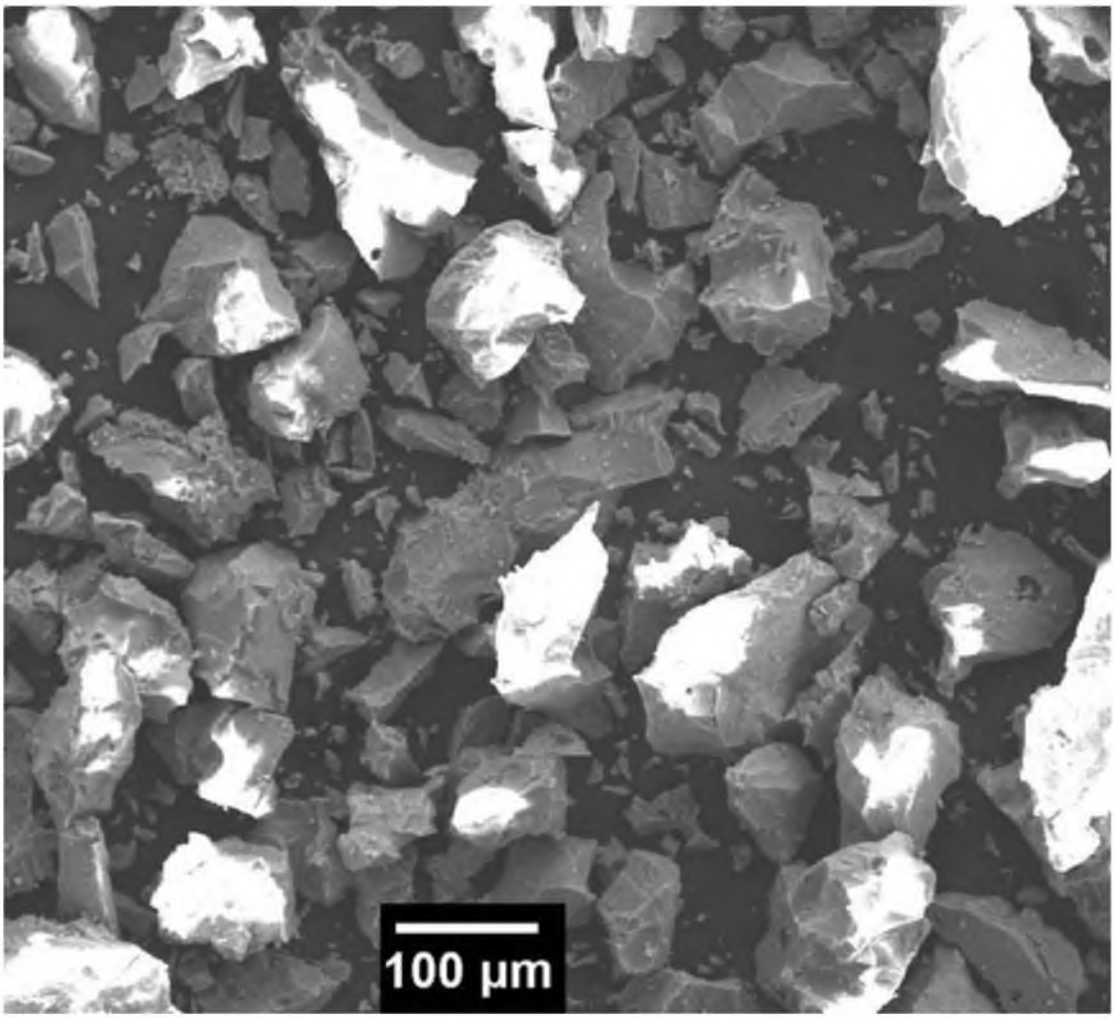

Figure 3.26 Morphology of particles obtained from the sample as shown in Figure 3.25. The overall particles display a low mean aspect ratio of between 1:1 and 2:1.

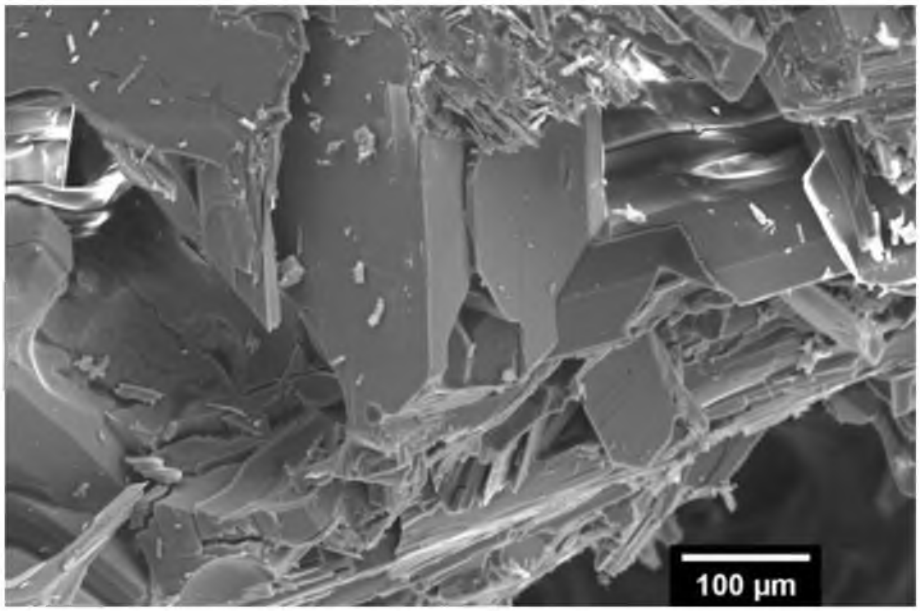

(a)

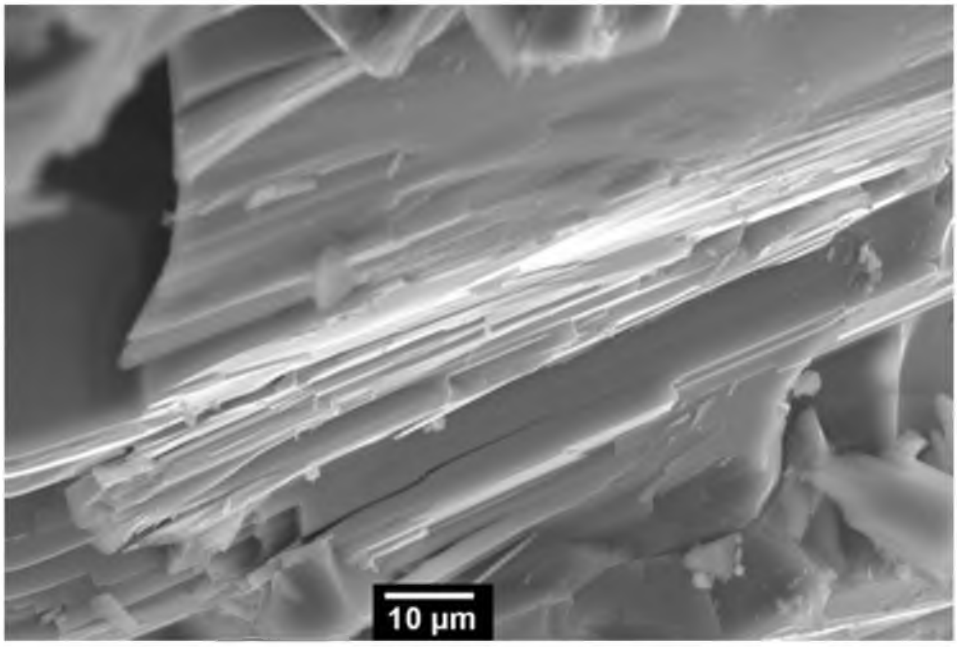

(b)

Figure 3.27 Fracture surfaces of the sample containing SiO_2, CaO, B_2O_3, and Li_2O (S7) presents well-developed crystal faces or parallel cracks, which are very favorable for the formation acicular particles under low (a) and high (b) magnifications.

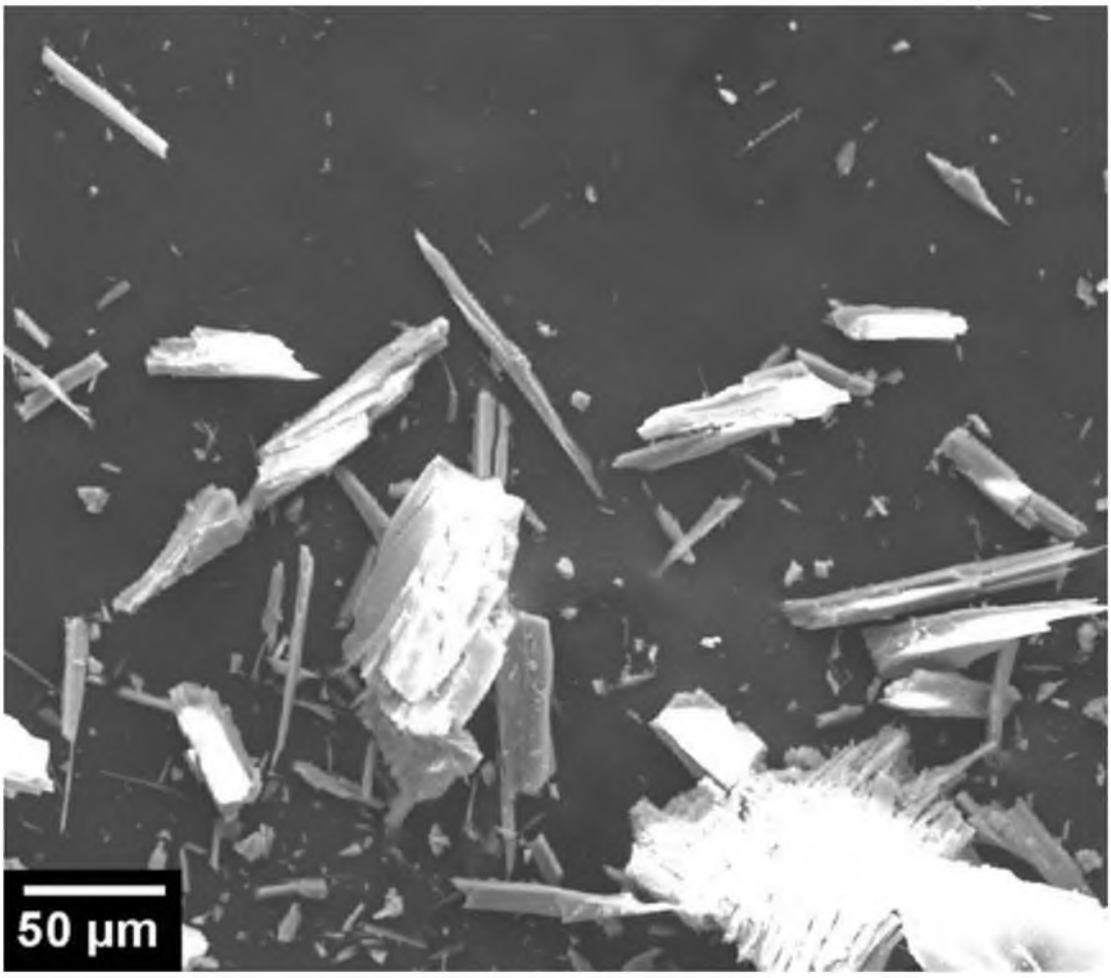

Figure 3.28 Morphology of particles obtained from the sample as shown in Figure 3.27. The particles mainly display acicular shapes. Note that even though the particle in the bottom right corner does not have a large apparent aspect ratio, it has many cracks extending along the same direction, which allows it to break into more acicular particles during further crushing.

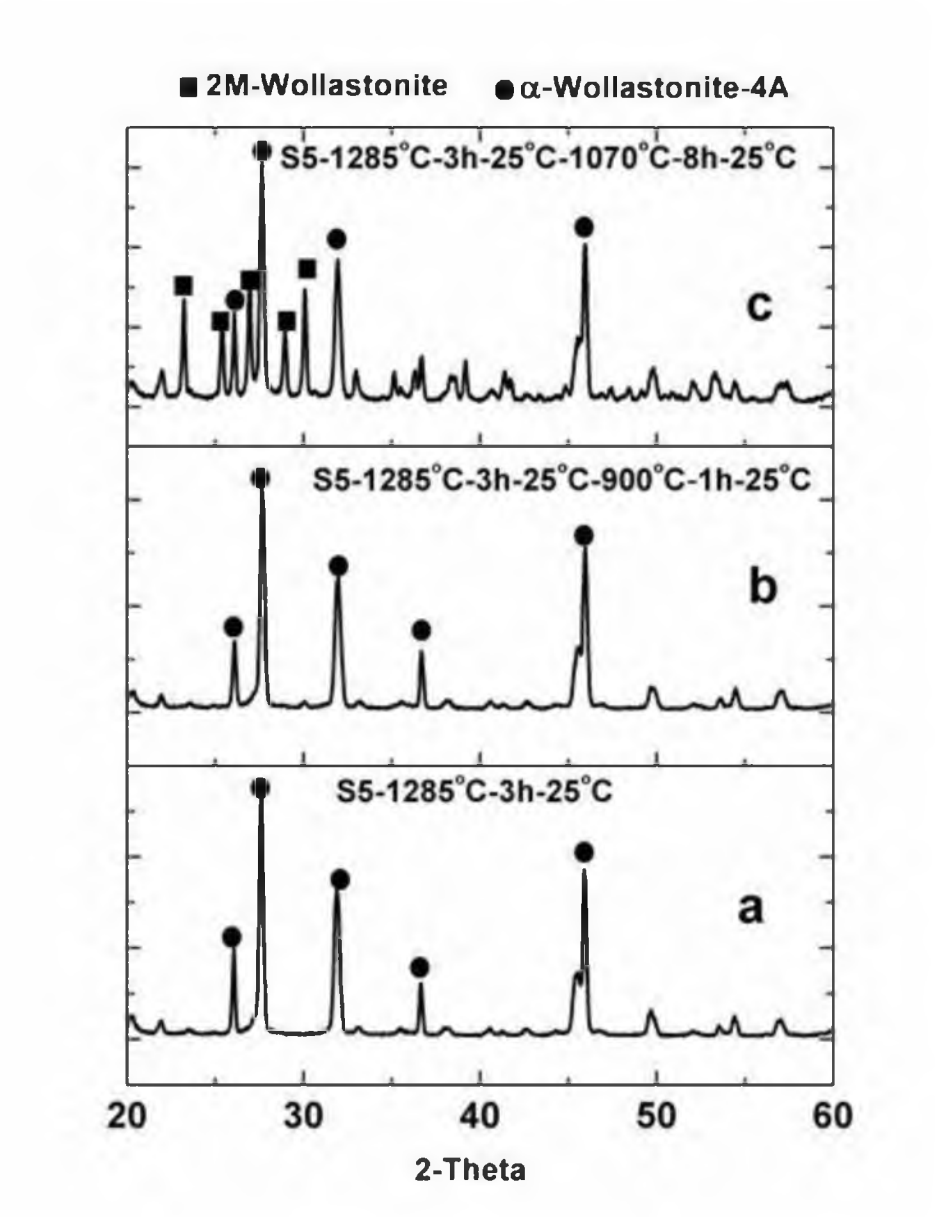

Figure 3.29 XRD patterns of the sample containing only SiO_2 and CaO and under various heat treatments. The label corresponding to each pattern follows the rule of "*SX - T_S*°C - *t_S h - T_C°C - T_R°C - t_R h - 25*°C ", where SX stands for samples having composition of S5, S6, and S7, respectively, as listed in the Experimental Procedure section. T_S^o, t_S, T_C, T_R, *and* t_R have been defined in the Experimental Procedure section. h after t_S and t_R stands for hours.

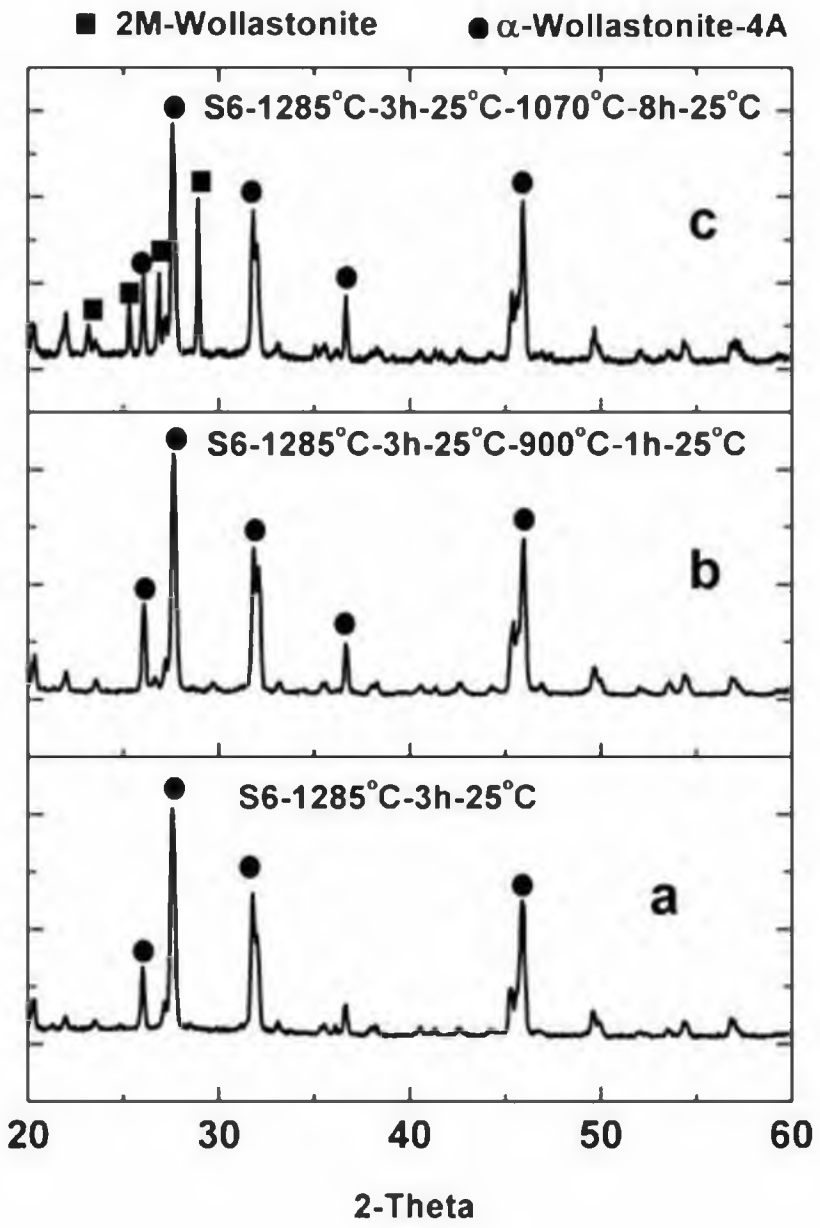

Figure 3.30 XRD patterns of the sample containing SiO_2, CaO, and B_2O_3 and under various heat treatments. Explanation regarding the labeling rules remains the same as defined in Figure 3.29.

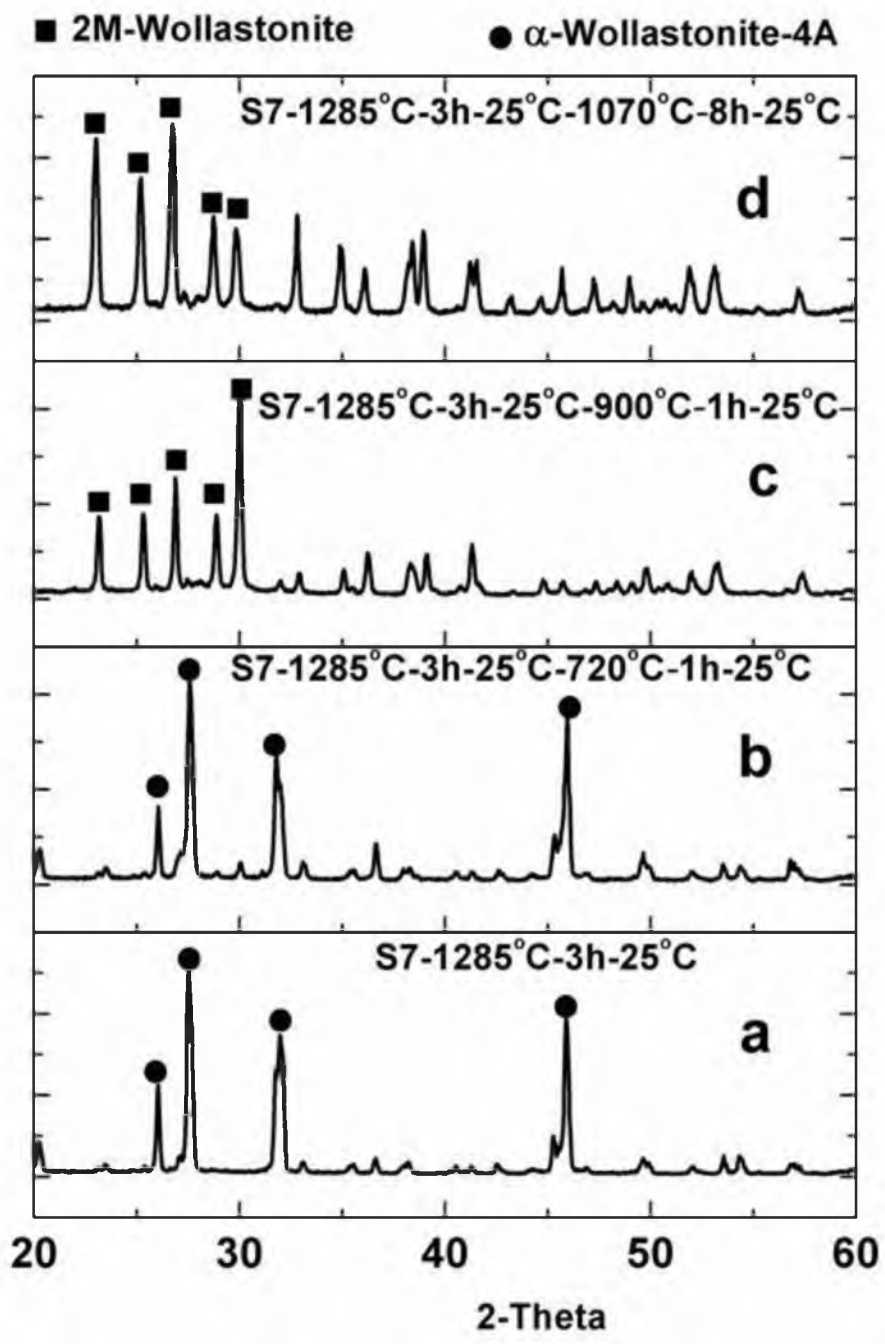

Figure 3.31 XRD patterns of the sample containing SiO_2, CaO, B_2O_3, and Li_2O and under various heat treatments. Explanation regarding the labeling rules remains the same as defined in Figure 3.29.

composition of S5, S6, and S7, respectively, as listed in the Experimental Procedure section. T_S^o, t_S, T_C, T_R, *and* t_R have been defined in the Experimental Procedure section. h after t_S and t_R stands for hours.

In Figure 3.29, we can see that the sample containing SiO_2 and CaO only (S5) is α-wollastonite (we have mentioned that α-wollastonite-4A equals α-wollastonite in Chapter 2 without special notification) after sintering treatment at 1285°C. After recrystallization at 900°C for 1 hour, the sample is still α-wollastonite. However, after recrystallization at 1070°C for 8 hours, the sample transfers to a mixture of α-wollastonite and 2M-wollastonite. The relatively stronger intensities from α-wollastonite indicate that it is the major component. This explains why we see mainly nonacicular particles together with small amounts of acicular particles in Figure 3.23.

The sample containing SiO_2, CaO, and B_2O_3 only (S6) presents almost identically the same patterns with S5 under the same heat treatment, as seen in Figure 3.30. This result agrees with the observed particle morphology shown in Figure 3.26. Meanwhile, it implies that adding B_2O_3 only will not help the formation of 2M-wollastonite.

The sample containing SiO_2, CaO, B_2O_3, and Li_2O (S7) presents α-wollastonite after heat treatment at 1285°C and also with recrystallization temperature at 720°C, as shown in Figure 3.31a and b. After recrystallization at 900°C for 1 hour, it transfers completely to 2M-wollastonite (Figure 3.31c). With recrystallization at 1070°C for 8 hours, the only detected crystalline phase is also 2M-wollastonite, as seen in Figure 3.31d. This result means that Li_2O can not only help to lower the nucleation temperature of 2M-wollastonite phase but also speed up the transformation rate at the same temperature. This explains why Li_2O is classified as a catalytic additive.

To verify the XRD results, we did further differential scanning calorimetry (DSC) analysis; the measured heat flow versus temperature profiles are plotted in Figure 3.32. To compare with the above XRD results, the interested temperatures are marked by dashed lines. As can be seen from Figure 3.32, when the sample contained only SiO_2 and CaO, there were no obvious peaks observed; heat flow was relatively smooth during the whole ramp-up stage. Even though there might be a small amount of α phase transfers to 2M phase at temperatures above 900°C, the small heat release was possibly not detected from the background information; thus, no peaks formed even though we found small amounts of 2M phase in the sample recrystallized at 1070°C. When B_2O_3 was added to the raw materials, we detected a small peak at 950°C, which means there might be an exothermal reaction occurring at this temperature. From Figure 3.30, we have seen the formation of 2M-wollastonite when temperature changes from 900°C to 1070°C. By using XRD analysis software X'Pert High Score Plus, the 2M phase weighs about 25% of the two-phase mixture; these two factors probably have contributed to this small peak. However, the sample containing both B_2O_3 and Li_2O as additives clearly showed a relatively large heat release starting at 790°C, and reached the maximum at 855°C. The exothermal reaction finished up around 900°C. In Figure 3.31, the sample of the same composition was determined as 2M-wollastonite at 900°C, which matches well with this DSC analysis. In Chapter 2, we have melted pure SiO_2 and CaO and allowed the grounded glass powder that was obtained by quenching the melt in cold water to crystallize at different temperatures. We found that the nucleation of 2M-wollastonite would occur at an observable level only when temperature exceeded 860°C. With the addition of Li_2O, this temperature was decreased to 790°C, and the transformation of α

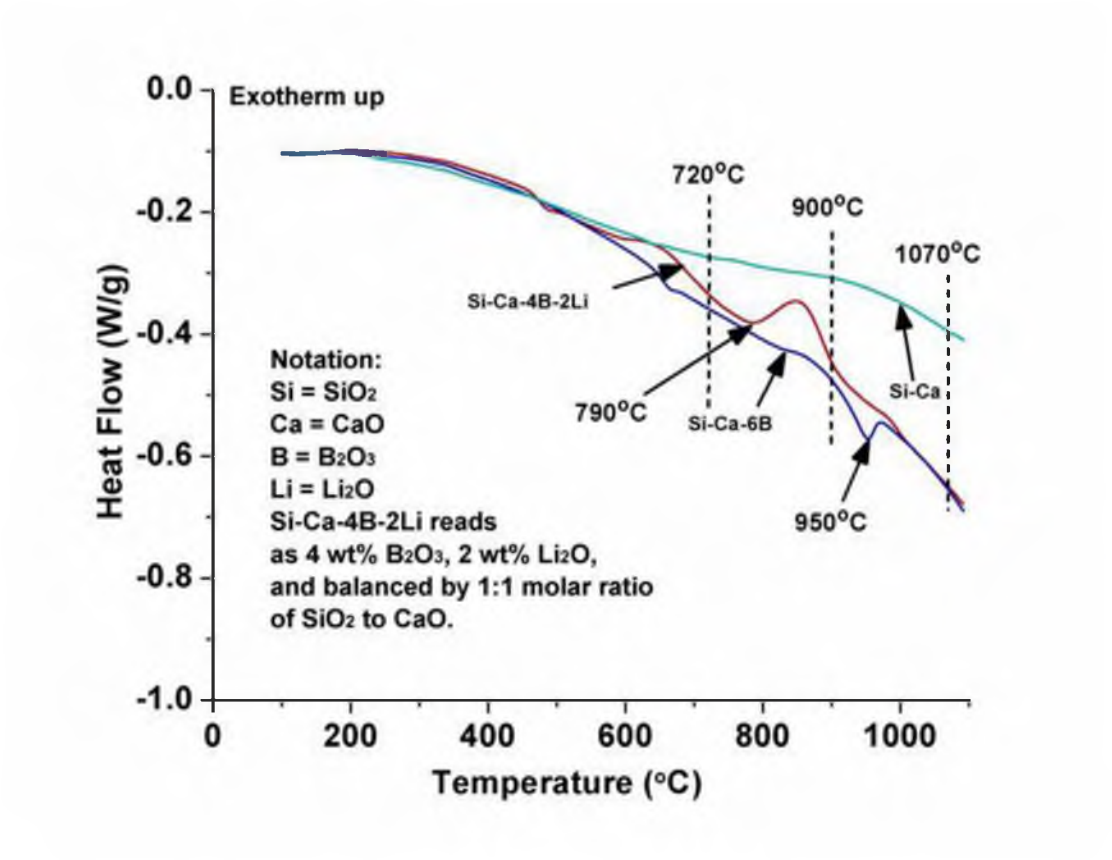

Figure 3.32 Differential scanning calorimetry (DSC) analysis reveals that the addition of Li_2O helped to lower the nucleation temperature of 2M-wollastonite and speeded up the transformation rate at lower temperatures (higher heat release).

phase to 2M phase completed within only 1 hour; it thus directly proves that Li_2O acts a catalytic additive.

3.3.5 Effects of Heat Treatment on Aspect Ratio

Figure 3.33 shows the relationship between the mean aspect ratio of each sample and the recrystallization temperature. As seen from this figure, under the same recrystallization time, the optimum recrystallization temperature is between 1050°C to 1070°C. When temperature is below or above this range, the mean aspect ratio of the products decreases obviously. When temperature is close to 1125°C, which is the approximate transformation temperature of wollastonite from the 2M phase to the alpha phase, the products show nearly no acicular properties. At a lower temperature, the nucleation and growth of 2M-wollastonite from alpha wollastonite is thermodynamically favorable, but from the kinetic point, it is unfavorable compared with a higher recrystallization temperature, resulting in a lower mean aspect ratios under given recrystallization time. At a higher temperature close to the transformation temperature from beta to alpha phase, the kinetic factor is high, but the nucleation of 2M-wollastonite and its growth is thermodynamically restricted; therefore, one will see reduced mean aspect ratios at the higher temperature side in the plot.

As seen from Figure 3.34, initially the mean aspect ratios of the tested samples increases rapidly with increasing recrystallization time, and then it reaches the maximum level after 8 hours of recrystallization treatment. A longer recrystallization time does not increase the mean aspect ratio significantly.

It was noticed when the sintered products were cooled from temperatures above 1200°C with a cooling rate less than 3°C/min and then went through the recrystallization

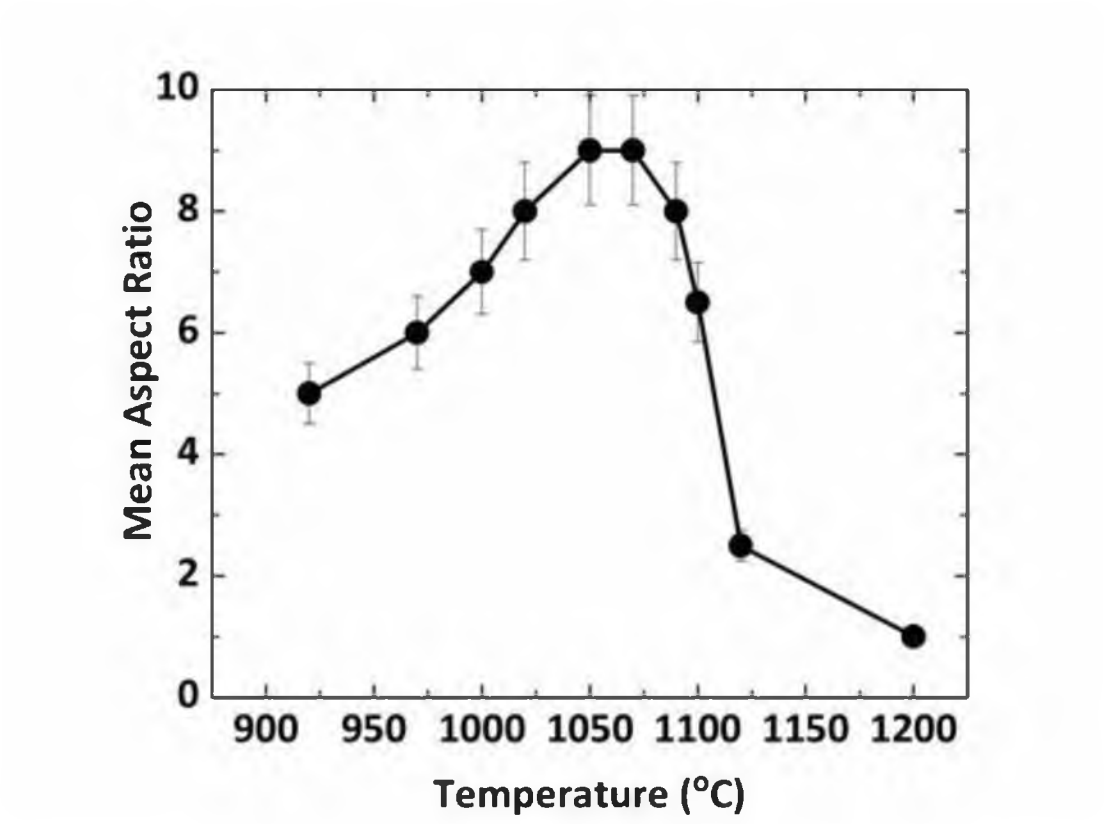

Figure 3.33 The relationship between mean aspect ratio and recrystallization temperature. Ts = 1270°C, Tc =25°C, tS = 3 h, t_R = 8 h.

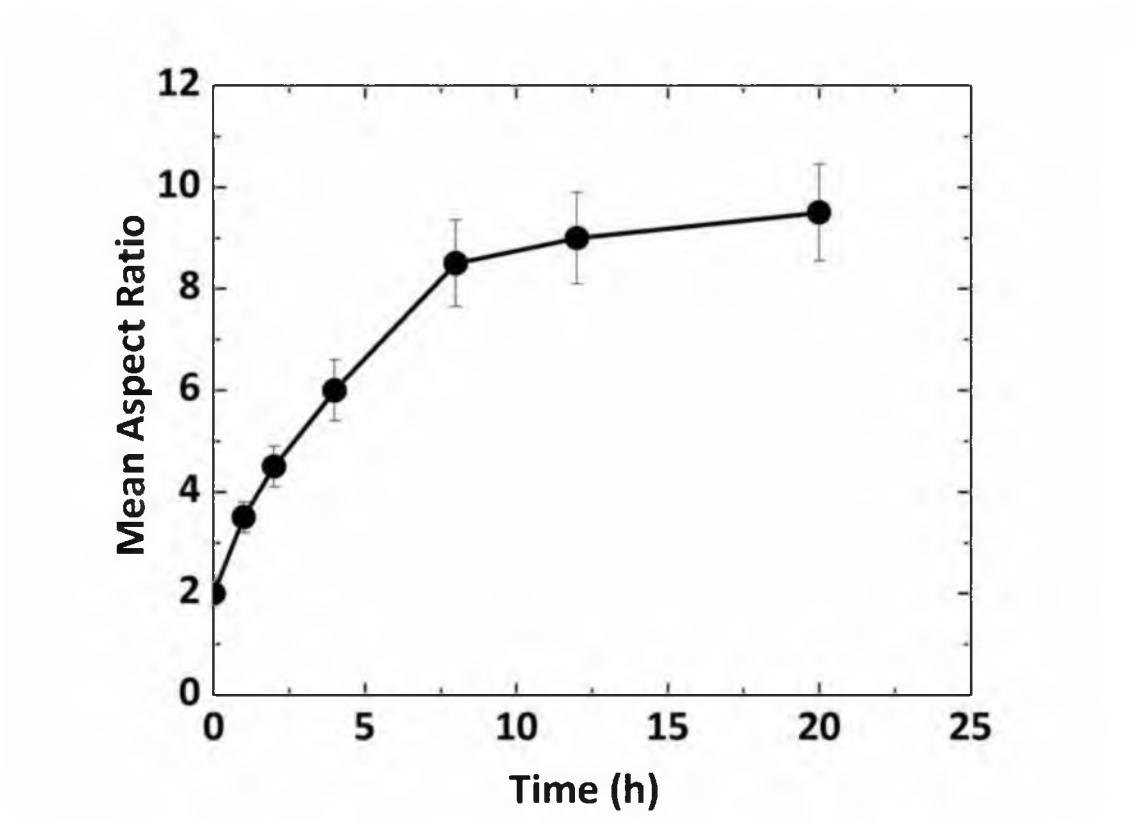

Figure 3.34 The relationship between mean aspect ratio and recrystallization time. Ts = 1270°C, TR = 1070°C, Tc =25°C, t_S = 3 h.

stage directly, the products failed to yield acicular particles after being crushed. However, the same raw materials yielded acicular particles under the same heat treatment except that it was cooled to room temperature before entering the recrystallization stage. In order to verify this observation, we did a series of tests that are described in detail in the Experimental Procedure section.

As seen in Figure 3.35, when the critical cooling temperature is above 970°C, the mean aspect ratio of the particles obtained from the tested samples is nearly 1:1. When the critical cooling temperature is between 550°C and 970°C, the mean aspect ratio of the particles obtained from the tested samples is quite sensitive to temperature change. If the critical cooling temperature is decreased further to below 550°C, the mean aspect ratios of the tested samples remained almost unchanged, meaning the critical cooling temperature has negligible effect on the mean aspect ratio, or in other words, the mean aspect ratio is insensitive to the critical cooling temperature under this condition. Therefore, a critical cooling temperature of lower than 550°C is necessary to form acicular wollastonite particles in an efficient way under the fixed recrystallization temperature and time.

Combining the cooling temperature and recrystallization process, which includes recrystallization temperature and time, one conclusion is drawn that when critical cooling temperature is satisfied, the recrystallization process controls the mean aspect ratio, and on the contrary, if cooling temperature is not sufficient, it will dominate the final product.

The dependence of mean aspect ratio on critical cooling temperature indicates that nucleation of 2M-wollastonite starts at a lower temperature and the newly formed nuclei begin to grow slowly while the temperature starts increasing. The growth of these crystals

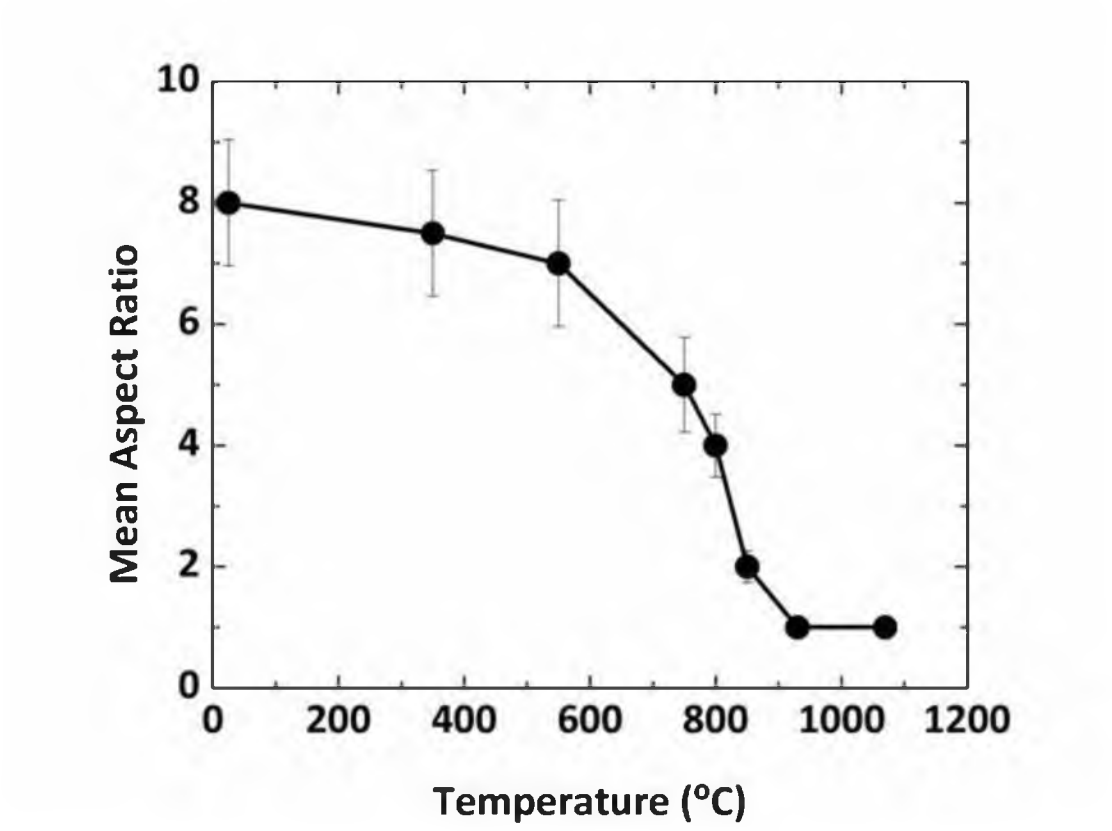

Figure 3.35 The relationship between mean aspect ratio and critical cooling temperature. Ts = 1270°C, TR = 1070°C, t_S = 3 h, t_R = 8 h.

becomes faster when temperature rises closer to the recrystallization temperature (for t_R test, $T_R = 1070^oC$). Upon reaching the recrystallization temperature ($t_R = 0$), the crystals are still small compared with those crystals given enough recrystallization time ($t_R > 8$ h). At this point, 2M-wollastonite crystals occupy a small volume fraction of the whole matrix, resulting in a mean aspect ratio of slightly greater than 1 at $t_R = 0$. Because of this small volume fraction, the space surrounding a 2M-wollastonite crystal is sufficient for further growth. Therefore, they will grow fast, resulting in a rapid increase of volume fraction of 2M-wollastonite, which explains the increase in the mean aspect ratios of the tested samples with increasing recrystallization time in the first few hours ($t_R < 5$ hours) under the fixed recrystallization temperature. After 5 hours, the 2M-wollastonite crystals have dominated the matrix, and they begin to compete with each other for the space. It becomes harder for the crystals to grow larger, and this competition contributes to the slow increase in the mean aspect ratio during this period ($5 < t_R < 8$ hour). The recrystallization from alpha wollastonite to 2M-wollastonite will complete upon the depletion of alpha-wollastonite, resulting in a nearly unchanged mean aspect ratio with increasing time ($t_R > 8$ hours), as shown in Figure 3.34.

3.4. Conclusions

High-aspect-ratio wollastonite powder was successfully prepared by using the Partial Melting and Recrystallization Process. This process was found to be simple but effective to synthesize wollastonite powder without completely melting the raw materials. The results further indicate the following.

The synthetic wollastonite produced without recrystallization treatment is alpha-wollastonite; whereas 2M-wollastonite is formed with both sintering and

recrystallization treatments. While alpha-wollastonite yields low aspect ratio wollastonite particles, 2M-wollastonite yields particles with aspect ratios as high as 15:1.

The as-grown 2M-wollastonite single crystals are much larger than the average size of final particles, which provides the possibility of generating acicular particles after proper crushing treatment of such crystals.

2M-wollastonite particles have straight parallel cracks or stacking faults extending from one end of the particle to the other end. When particles with such cracks or faults are pressed under applied stress, they are much easier to break into more acicular particles, making them different from alpha-wollastonite particles.

Additives play important roles on the preparation of high-aspect-ratio wollastonite particles. B_2O_3 is a good additive to lower the melting point of the raw mixtures. Al_2O_3 can adjust the properties of the raw mixtures if added with other additives together. Li_2O is a good additive that promotes the formation of acicular wollastonite particles.

Heat treatment is critical to the aspect ratios of synthetic wollastonite particles. A heat treatment schedule with a sintering temperature of 1270°C; a recrystallization temperature between 1050°C and 1070°C; a critical cooling temperature of lower than 550°C; with the sintering and recrystallization time no less than 3 and 8 hours, respectively, is determined to yield particles with a high mean aspect ratio.

CHAPTER 4

FLUX GROWTH OF 2M-WOLLASTONITE CRYSTALS FOR THE PREPARATION OF HIGH-ASPECT-RATIO PARTICLES

4.1. Introduction

In this chapter, a process called top-cooled flux growth of 2M-wollastonite crystals will be discussed. For this process, we first preheated and melted a mixture made of oxides above its melting temperature inside an alumina crucible and then quickly transferred the crucible and the melt to a muffle furnace set at a predetermined lower temperature that is favorable for 2M-wolalstonite crystal growth. During the cooling stage, we took advantage of much larger overall heat transfer coefficients at the top melt surface compared with the side and bottom crucible wall, which created a temperature gradient nearly along the vertical direction of the melt without using a specially designed furnace as used for other crystal growth processes [37]. Because of the faster heat transfer at the top melt surface, its temperature decreased faster than the melt below. A layer of 2M-wollastonite nuclei was thus formed at the top surface that acted as seeds for further growth; the final products were made of many individual crystals having a growth orientation perpendicular to the top surface and advanced into the inner melt.

Using this process, 2M-wollastonite was successfully grown from the melt, and acicular particles were prepared from the as-grown crystals. Under appropriate conditions, fine particles with mean aspect ratios of greater than 8, including particles with aspect

ratios of greater than 20, were obtained. These particles were determined to be 2M-wollastonite, which is of the same crystal structure as that of high-aspect-ratio natural wollastonite particles. Meanwhile we applied an in situ, fast, and accurate method based on LA-ICP-MS technique to track the distribution of light trace elements such as Li and B, which are hard to be detected by other techniques.

4.2. Experimental Procedure

4.2.1. Synthesis and Crystal Growth

Raw materials of various compositions were prepared first according to the experimental flow chart as seen in Figure 4.1. B_2O_3 and Li_2O were used as additives based on the experimental results from Chapter 3. While the former was mainly used for lowering the melting point of the mixture, the latter was proved to have catalytic effect for the formation of 2M-wollastonite.

20 grams of the tested mixtures were placed in an alumina crucible (99.6% Al_2O_3). The crucible was then placed into a muffle furnace at a preheating temperature (Tp) for 30 minutes to preheat the crucible and mixtures to avoid cracks in the following step. At the end of the preheat treatment, the crucible was transferred into a vertical furnace at a melting temperature (T_M) and held for a melting time of t_M. The reason for placing the crucibles directly in the furnace at the target temperature was to avoid contamination from alumina crucible as much as possible during the heat-up period. At proper T_M, it usually took about 5 minutes to completely melt the solid mixtures. We added another 10 minutes to allow the melt to become as homogeneous as possible without involving a

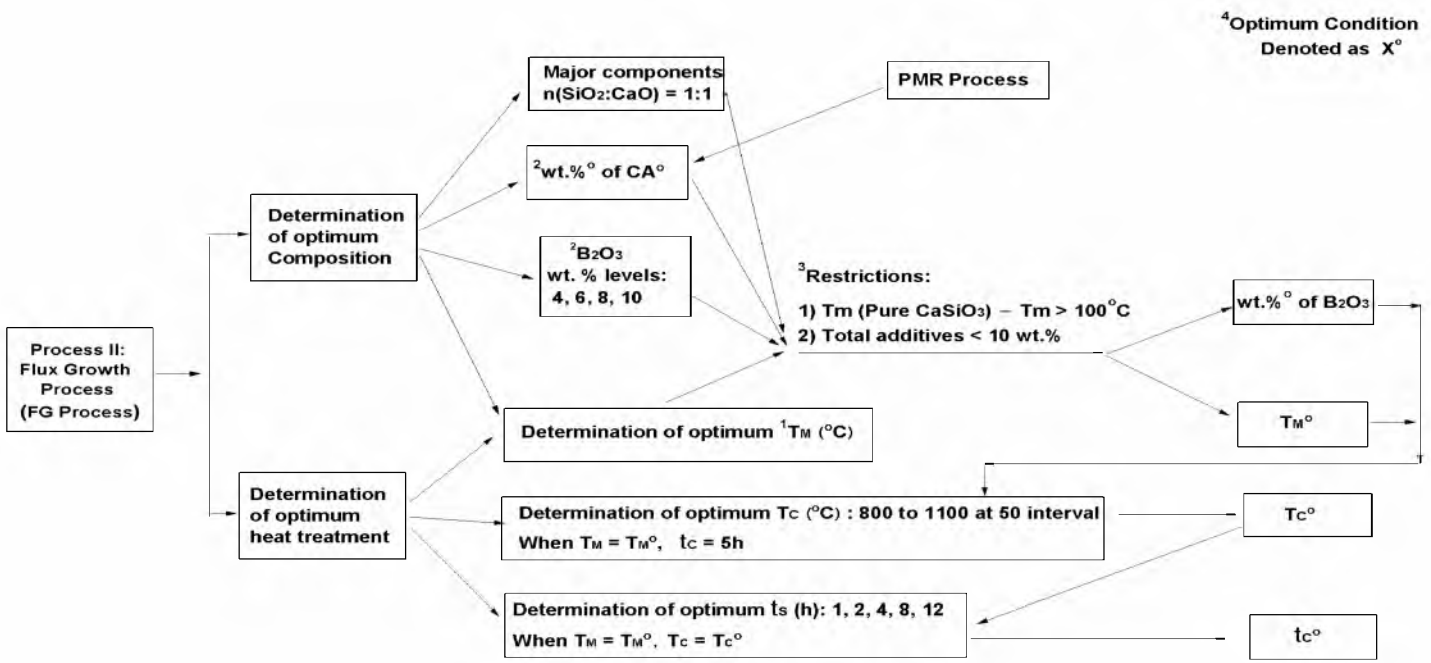

Note:
1: All symbls have been defined in the heating schedule corresponding to this process.
2: Assumption is made here that the optimum Catalytic Additive and its percentage obtained from PMR Process also applys to FG Process. B_2O_3 is used to lower the melting of the melts. RA is not used because density and porosity is no longer a concern in the melts.
3: The restrictions are set empirically. Pure $CaSiO_3$ has a melting point of Tm (Pure $CaSiO_3$) = 1544°C.
4: The mutual effect among the individual optimum conditions is considered as negligbile to simplify the experimental procedures.

Figure 4.1 Experimental flow chart for the Flux Growth (FG) process.

significant reaction between the melt and the crucible wall. Once the homogeneous melt was ready, the crucible was taken out of the vertical furnace and transferred back into the muffle furnace at a crystallization temperature (T_C) and held for a crystallization time (t_C) to allow the crystallization of the melt. At the end of crystallization stage, the muffle furnace was turned off and the product began to cool down slowly. The crystals grown from the melt were analyzed in the following sections.

4.2.2. Characterization Methods

Aspect ratio was the most important factor in this study. It was determined by following the procedure explained in Chapter 3. The crystal structure of the synthesized products was determined by X-ray diffraction (XRD). The morphology, microstructure, and phase composition were analyzed by scanning electron microscopy (SEM), energy-dispersive X-ray spectroscopy (EDS), laser ablation inductively coupled plasma mass spectrometry (LA-ICP-MS), and scanning white light interferometer (SWLI). The LA-ICP-MS analysis is critical in this study for determining the composition of the as-grown crystals, especially for trace light elements such as Li and B.

The concentrations of elements of interest in this study, namely Li, B, Si, and Ca, are determined by the LA-ICP-MS technique based on the following equation [38, 39].

$$\frac{C_{ie}^{S}}{C_{is}^{S}} = \frac{I_{ie}^{S}}{I_{is}^{S}} \times \frac{C_{ie}^{R}}{C_{is}^{R}} \times \frac{I_{is}^{R}}{I_{ie}^{R}} \qquad (4.1)$$

where **C** and ***I*** stand for concentrations and background-corrected signal intensity (cps) of the selected isotope ***i*** of a given element ***e***, respectively. The superscripts ***S*** and ***R*** refer to the sample that is to be analyzed and the reference standard (NIST-610 glass in this

study), respectively. The subscripts ***ie*** and ***is*** denote the isotope ***i*** of a given element ***e*** and the internal standard (^{29}Si in this study), respectively. For example, C_{ie}^{S} is the concentration of ***ie*** in sample ***S***. In actual experiments, ***I*** terms can be measured directly, and C_{ie}^{R} and C_{is}^{R} can be calculated by combining the known composition of the reference standard and the Relative Isotopic Abundance Table. The contents of Li, B, Ca, and Si in the reference standard, i.e., NIST-610 glass, and the relative abundances of their analyzed isotopes, namely, ^{7}Li, ^{9}B, ^{29}Si, and ^{44}Ca, are listed in Table 4.1.

Based on Equation (4.1) and the above description, the concentration of ***ie*** in the sample normalized by the concentration of the internal standard in the sample can be solved. Since the internal standard is the same for all four isotopes, the mass ratio of the four isotopes can be calculated first and then based on their relative abundances, the mass ratio of Li : B : Ca : Si is obtained. Furthermore, based on mass balance and the original oxide form of each element, that is Li_2O, B_2O_3, CaO, and SiO_2, the mass ratio or the contents of these oxides in tested sample can be calculated. An assumption is made here that these oxides diffuse or react with others in their original forms, e.g., CaO reacts with SiO_2 to form $CaSiO_3$ ($CaO{\bullet}SiO_2$).

4.3. Results and Discussion

4.3.1 Effects of Cooling Rate on Solidification of Molten Melt

In this process, depending on the cooling rates, there are three possible modes for the solidification of the molten silicate melt, as illustrated in Figure 4.2.

Table 4.1 Contents of selected elements in NIST-610 glass and the relative abundance of their analyzed isotopes for LA-ICP-MS analysis.

	Element			
	Li	B	Si	Ca
Concentration (ppm)	482	358	326758	84334
Analyzed isotope	^{7}Li	^{11}B	^{29}Si	^{44}Ca
Relative isotopic abundance (%)	92.41	80.1	4.683	2.086

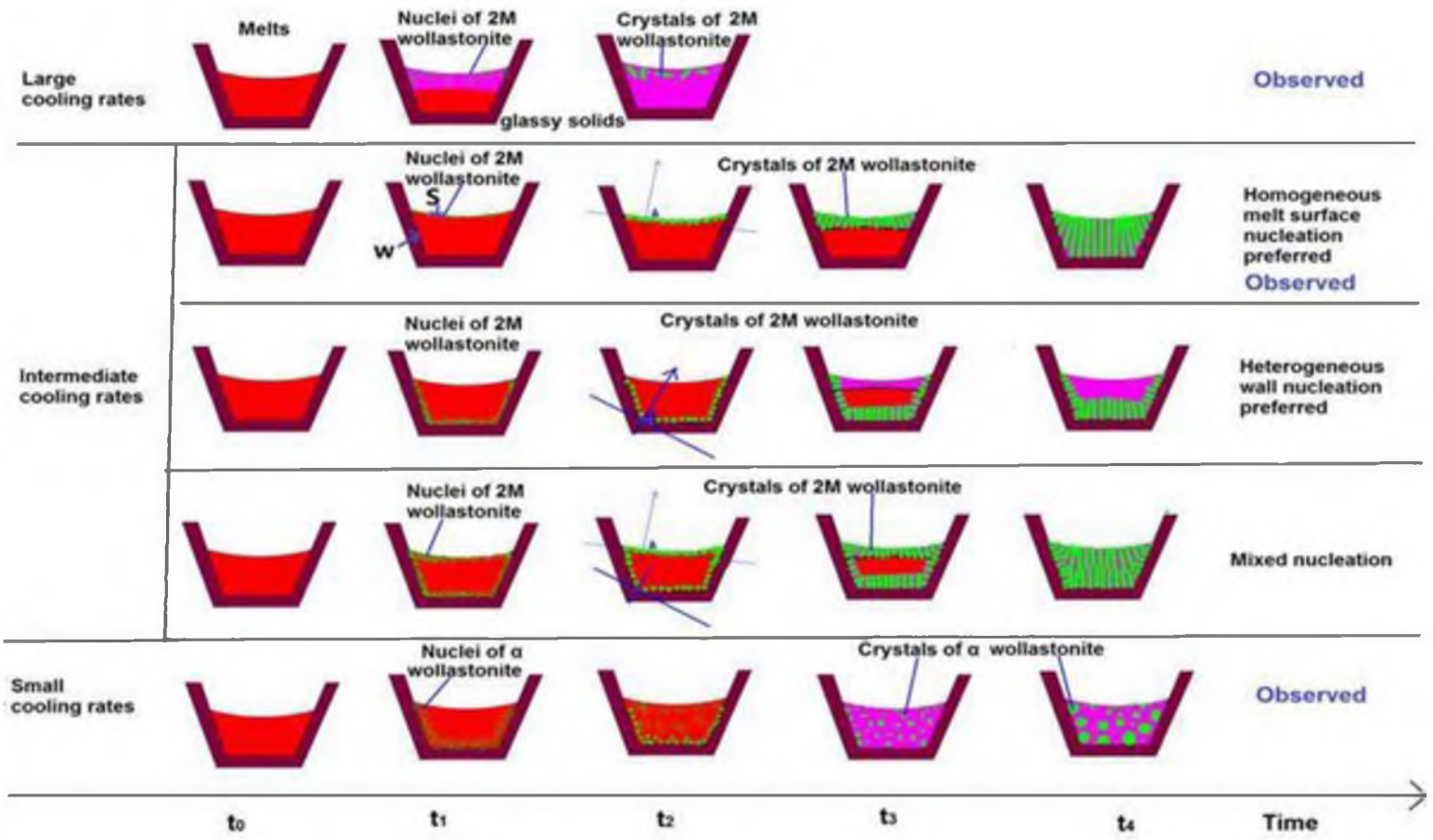

Figure 4.2 Illustration of three possible modes based on three types of cooling rates for the solidification of wollastonite in the FG process.

4.3.1.1 Mode 1: Fast Cooling with No Holding Time

In this mode, since the cooling rate is very fast, taking air quench for example, the melt will not have time to crystallize and thus should form transparent glass. However, at the top surface of the melt (hereafter called top surface), temperature drops even faster compared with the center melt because of its direct contact with cold air. This temperature drop can give sufficient driving force for the nucleation of α or 2M-wollastonite; meanwhile, because of the typical low thermal conductivity of glass materials, the melt right below the top surface may still stay in molten phase providing a favorable environment for the diffusion of calcium and silicon atoms or clusters to the newly grown crystals. However, this benefit will be terminated soon after the melt below the top surface solidified. Because of the low thermal conductivity within the melt, the temperature drop caused by heat conduction within the melt will be much lower than that of the top surface caused by heat convection. Therefore, even though the kinetic factor for the formation of 2M-wollastonite is satisfied, the thermal driving force is low so that the nucleation of 2M-wollastonite is unfavorable at other positions within the melt. Consequently, the final product will actually be made of nearly pure glass phase with small amounts of α and 2M-wollastonite at the top surface. Since 2M phase is stable at lower temperature, and the temperature of the top surface may have quickly dropped to the transformation temperature between the two phases at the beginning because of the large temperature difference between the top surface and the cold air (meanwhile the favorable temperature range for the nucleation and growth of α wollastonite is between 1200 and 1400^{o}C according to the experiments in Chapter 2) the chance for the nucleation of 2M phase is therefore much higher, resulting in a larger percentage in the crystallites. This mode is well proved by a sample cooled in air, as shown in Figure 4.3.

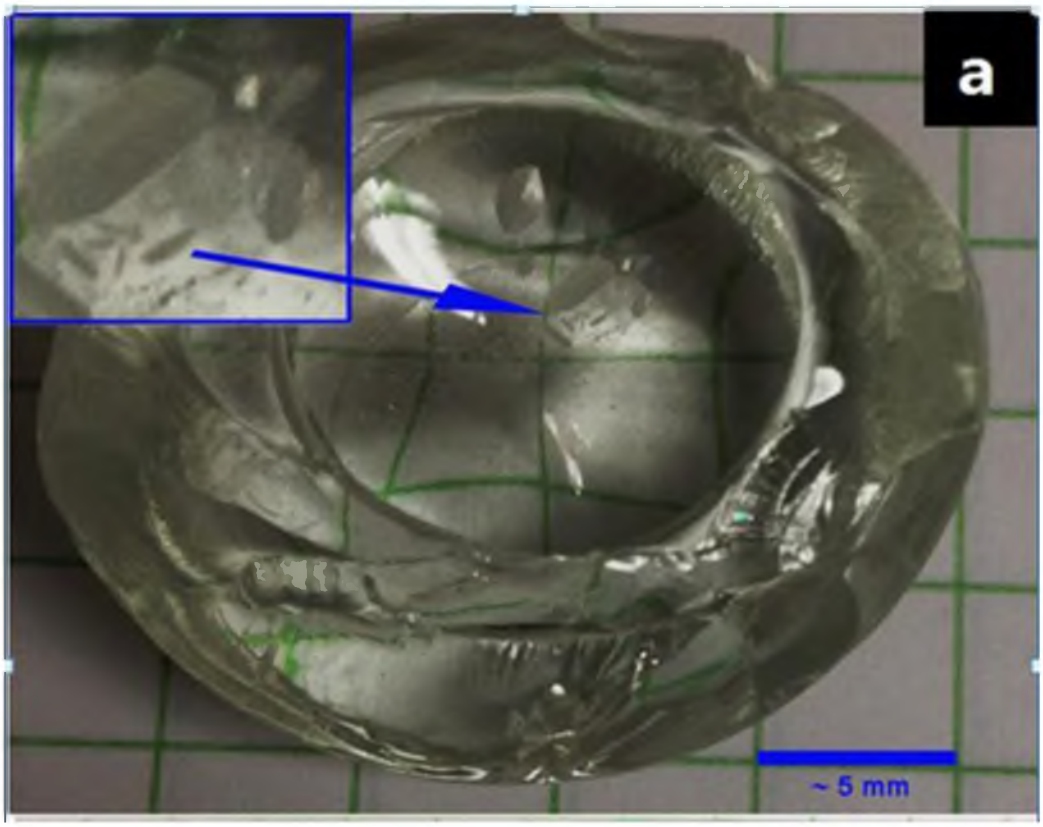

Figure 4.3 A sample quenched in air. A few elongated crystals are seen at the top layer.

4.3.1.2 Mode 2: Intermediate Cooling Rates with Sufficient Holding Time

In this mode, the melt will be cooled to a lower temperature below the transformation temperature of α to 2M phase under intermediate cooling rates and the sample will be held at that temperature for a sufficient time to allow the complete crystallization of 2M phase. Apparently, both thermodynamic and kinetic factors are satisfied. However, depending on the nucleation mechanisms, i.e., homogenous versus heterogeneous nucleation, this mode can have three possible nucleation and growth scenarios. The scenarios were derived based on the following reasoning.

Unlike the PMR process where the temperature is uniform within the sample, in this model, the sample will undergo a fast cooling stage to avoid the nucleation of α phase, because of the lower thermal conductivity of molten glass material, and higher conductivity of the crucible wall, the temperature of the melt at different positions remains unknown without experimental determination or theoretical calculations. Suppose at time $t = t_1$ in Scenario 1 of mode 2 in Figure 4.2, the temperature for point S and W is T_S and T_W, and the melting temperature is T_M, then $T_M - T_S$ will provide a driving force for the homogeneous nucleation with a minimum activation energy barrier of ΔG^*_{hom} at the top surface. $T_M - T_W$ will provide a driving force for the heterogeneous nucleation with minimum activation energy barrier of ΔG^*_{het} at the wall side. Though the ΔT term at W is lower than at S, the energy required for heterogeneous nucleation is only one third of the homogeneous nucleation; therefore, it can have three possibilities to give the following three scenarios.

If $\Delta G^*hom \leq \Delta G^*het$, nucleation is preferred to occur from the top surface and growth of 2M phase will advance into the inner and bottom melt with increasing time, resulting in a

crystallization sequences as seen in scenario 1. If $\Delta G^{*}hom \geq \Delta G^{*}het$, nucleation is preferred to occur from the wall sides and advance into the inner and top melt with increasing time, resulting in Scenario 2. If $\Delta G^{*}hom \approx \Delta G^{*}het$, nucleation will occur simultaneously from both of the top surface and wall sides, and growth of 2M phase will advance into the center melt with increasing time, resulting in a crystallization sequences as seen in Scenario 3. By comparing the growth direction of a sample prepared by the FG process with the three scenarios, the experimental results are more close to Scenario 1, as shown in Figure 4.4.

4.3.1.3 Mode 3: Slow Cooling Rates with No Holding Time

In this mode, the melt will be cooled directly in the same furnace with slow cooling rates all the way to room temperature. When temperature is reaching the nucleation temperature of α wollastonite, it will begin to nucleate and grow from the wall side first because the thermal driving force to overcome the activation barrier is lower at this position as being a heterogeneous nucleation. With decreasing temperature, the thermal driving force will then meet the minimum energy requirement for homogeneous nucleation. Since the cooling rates are slow, the temperature within the melt can be considered as uniform, the homogeneous nucleation of α phase thus will start simultaneously from both the top surface and the inner melt.

However, because the diffusion rate of atoms in silicates is usually low, even under slow cooling rates, if no sufficient time is provided for the crystal growth, the melt will not have time to have a complete crystallization of α phase before the temperature reaches the phase transformation temperature of 2M-wollastonite. Now the nucleation of 2M phase becomes possible, but because the temperature keeps decreasing, even though nucleation of 2M phase can occur, the diffusion rate of atoms in the silicates becomes even lower, so the growth of 2M phase

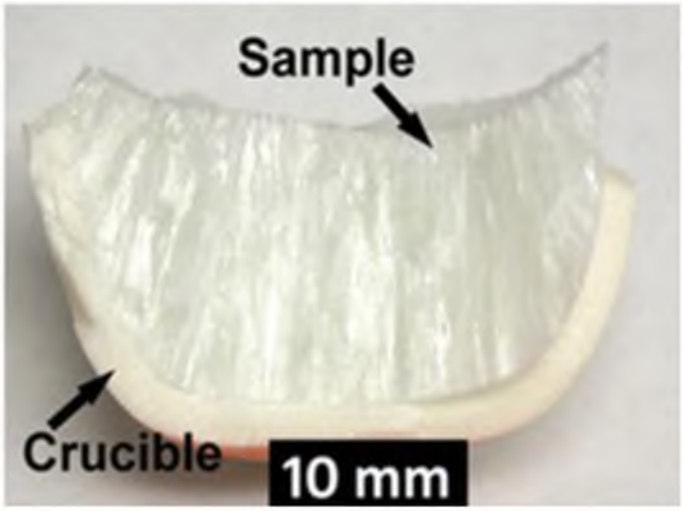

(a)

(b)

Figure 4.4 Fracture surfaces of samples solidified inside a crucible of (a) truncated-cone shape and (b) cylindrical shape. Both samples were cut along its centerline. Parallel faults indicate the preferred growth orientation of the sample. Note that the growth direction is more or less perpendicular to the top surface rather than the crucible wall.

also becomes unfavorable. Combining the nucleating sequence, and growth rates of α and 2M phases, the final product should have certain amounts of crystals throughout the whole melt with a large amount of uncrystallized materials existing in glass phase. This model was also directly observed, as shown in Figure 4.5.

Since both Model 1 and 3 are undesired, they will not be studied in detail. The Scenario 1 in Model is observed directly during the initial experimental test; therefore, it will be used as the standard procedure for this process and all the following discussions are based on this procedure without special notification.

4.3.2. Growth Orientation and Fracture Surface

Once Mode 2 was selected as the preferred cooling profile for growing wollastonite crystals, further experiments were carried out following this mode. In the remaining sections to be discussed, without special notification, all the samples used in these sections have a composition of 46.8% SiO_2 (99.5%), 43.7% CaO (99%), 8.0% B_2O_3 (97.5%), and 1.5% Li_2O (99.5%) on weight basis.

After the solidification of the melt, the sample was cut into two approximately equal parts, as seen in Figure 4.4a. An immediate observation was that the growth of the crystals had preferred orientation along the fracture surface. Parallel faults extend from the top surface of the melt to the edge of the alumina crucible wall. As indicated in Figure 4.4a, the direction of these faults is more or less perpendicular to the top surface, rather than the crucible wall. This type of growth orientation is directly related to the heat transfer mechanism, as will be studied in detail in later chapters.

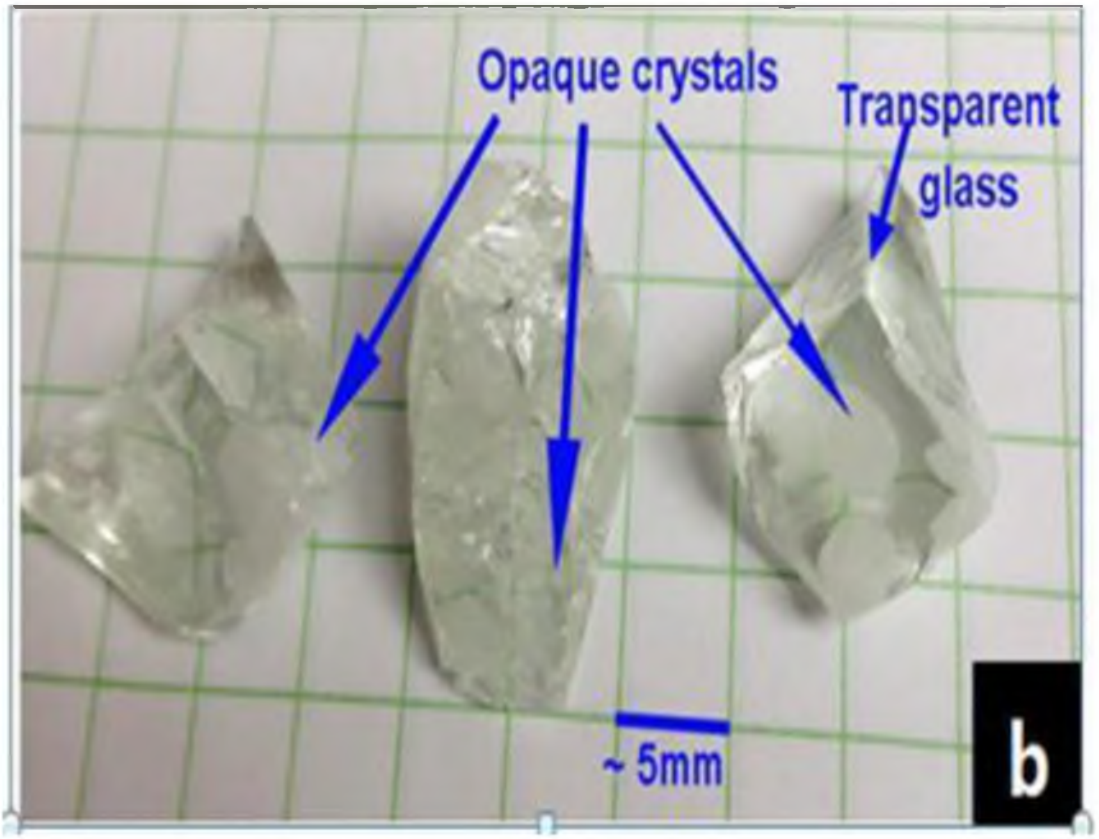

Figure 4.5 A sample slowly cooled (1°C/min) in the vertical furnace mentioned in the experimental procedure. After being cooled to room temperature, the sample contains certain amounts of crystals throughout the whole melt with a large amount of uncrystallized melt existing as glass phase.

4.3.3 Microstructure

The sample was further cut along the directions indicated by the dashed horizontal and vertical lines in Figure 4.6. The smaller part was marked as the S part, and the remainder is designated as the R part. The S part has three of its surfaces exposed, i.e., the front longitudinal surface (parallel to the paper), the side longitudinal surface (perpendicular to the paper), and the transverse surface.

Figures 4.6b to 6e show images corresponding to small regions 1 to 4 located on the front longitudinal surface (S part) along the solidified melt-crucible wall boundary, respectively. As can be seen from the four images, each consists of an alumina crucible wall; a thin layer which is later analyzed as the Al_2O_3-rich layer; and crystallized melt. It is clear that all four regions have cellular structures, the orientation of which is almost the same in each region. This orientation property agrees well with that seen in Figure 4.4. It is also noticed that the thicknesses of the Al_2O_3-rich layers along the boundary are almost the same.

Figure 4.7a and 7c show structures from the center areas of the two longitudinal surfaces. They all show regular and uniform cellular structures of the same orientation. Figure 4.7b is from the transverse surface, and it shows irregular elliptical cross sections of rod-like structure. The cross-sectional areas of these structures are approximately the same as those of the cellular layers. Combining the three images, it is evident that the melt solidified into rod-shaped single crystals of similar growth orientation. The overall structure is shown in Fig. 4.7d, which is assembled by properly adjusting Fig. 4.7a to 4.7c.

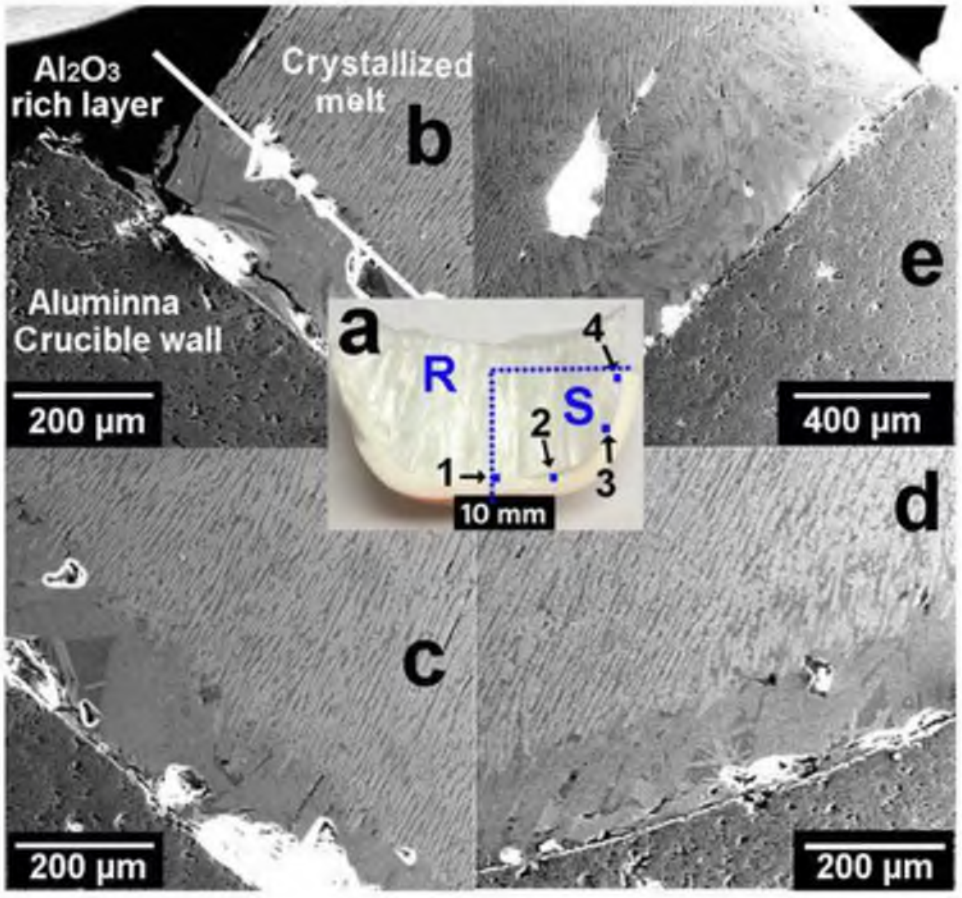

Figure 4.6 The center image (a) shows that the sample in Fig. 4.4a is cut along the dashed vertical and horizontal lines. *S* denotes the smaller part and *R* refers to the remaining part. The four small regions marked 1 to 4 and located on the front longitudinal surface (*S* part) along the solidified melt-crucible wall boundary are selected for the SEM analysis corresponding to b to e, respectively.

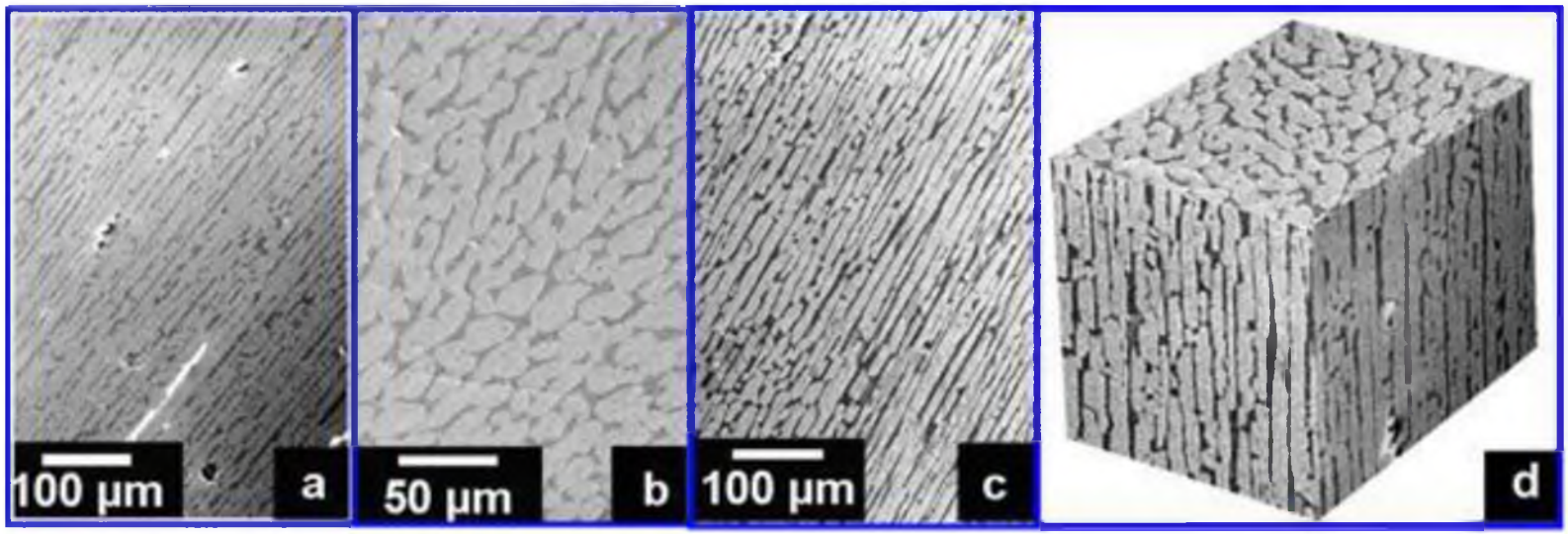

Figure 4.7 SEM images showing structures of the *S* part in Fig. 2a from the center areas of: (a and c) the two longitudinal surfaces presenting regular and uniform cellular structures of the same orientation, and (b) the transvers surface displaying an irregular elliptical interconnecting structure. (d) A quasi "3D" image assembled by properly adjusting images a to c to show the same structure.

4.3.4 Phase Composition

Figure 4.8 shows the regions of a representative brighter phase and a darker phase along the transverse surface. While the brighter phase has a composition very close to the theoretical values of pure wollastonite, the darker phase shows a much higher content of oxygen. However, neither Li nor B that was added in the form of Li_2O or B_2O_3 as a flux is seen in either phase. Their absence under EDS analysis is understandable and expected considering their light atomic weights. However, from the point view of mass and charge balance, a higher content of oxygen with lower contents of Si and Ca in the darker regions indicates that they should have higher contents of B and Li to compensate the differences.

From Figure 4.6b to e, we see that there is a thin layer in between the cellular structure and the alumina wall. The thickness of this thin layer is about 150 μm in all four regions. The phase composition of this layer was analyzed by EDS. The results in Figure 4.9 show that the composition of a region within the layer and close to the alumina wall is almost the same as that of a region close to the matrix side, meaning the composition of this layer is almost uniform. Both regions have a high Al content, which is expected because of their direct contact to the alumina wall. However, the concentration of Al in the region just next to the thin layer decreases dramatically to a very low level. These results indicate that once the molten phase began to form, it reacted with the alumina wall to form an Al_2O_3-rich thin layer. This layer appears to have prevented further dissolution of Al_2O_3 in the main melt. Without the protection of this thin layer, more Al_2O_3 would diffuse into the whole matrix, making the formation of wollastonite unfavorable or even impossible. Meanwhile, from later chapters, we will see that this layer is also rich in

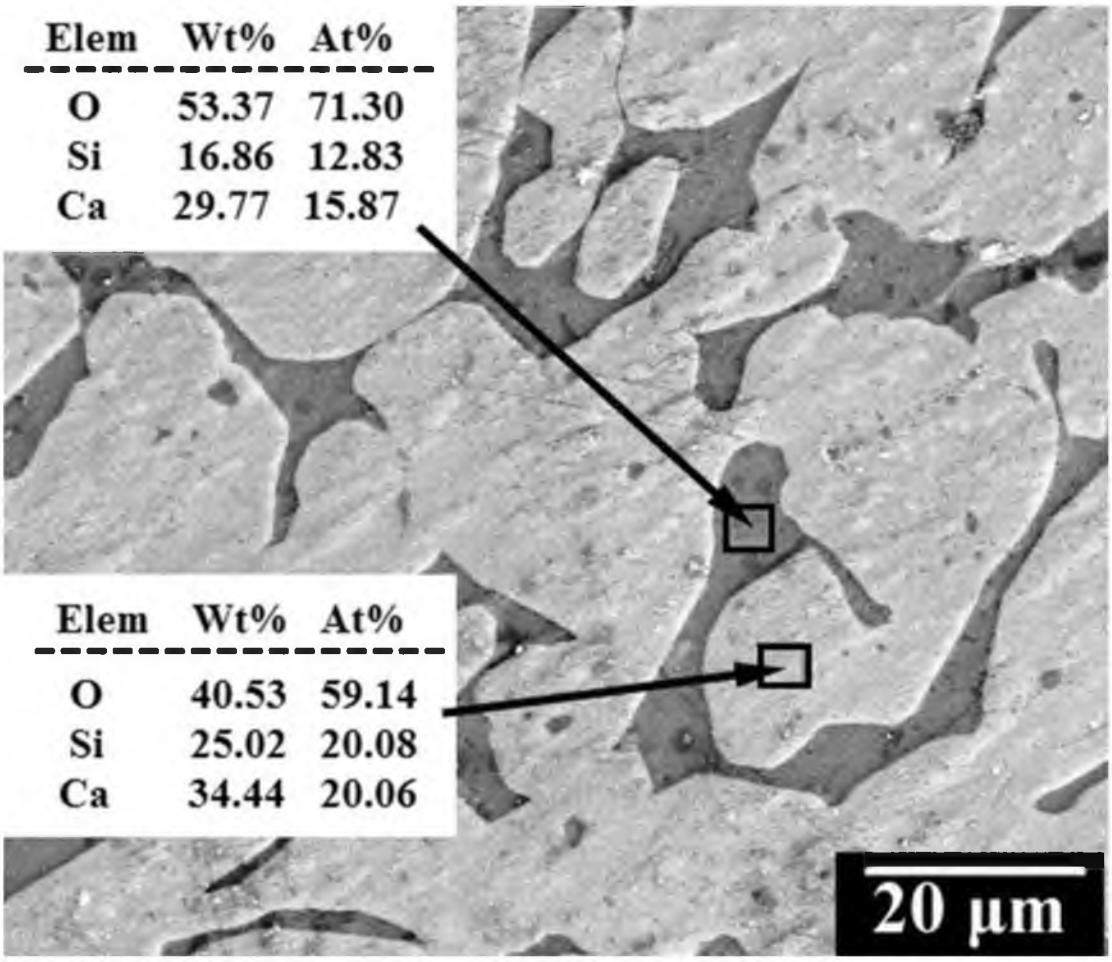

Figure 4.8 EDS analysis of two representative areas from the brighter phase and the darker phase located at the transverse surface of the *S* part in Figure 2a. While the brighter phase has a composition very close to the theoretical values of pure wollastonite ($CaSiO_3$), the darker phase shows higher oxygen content.

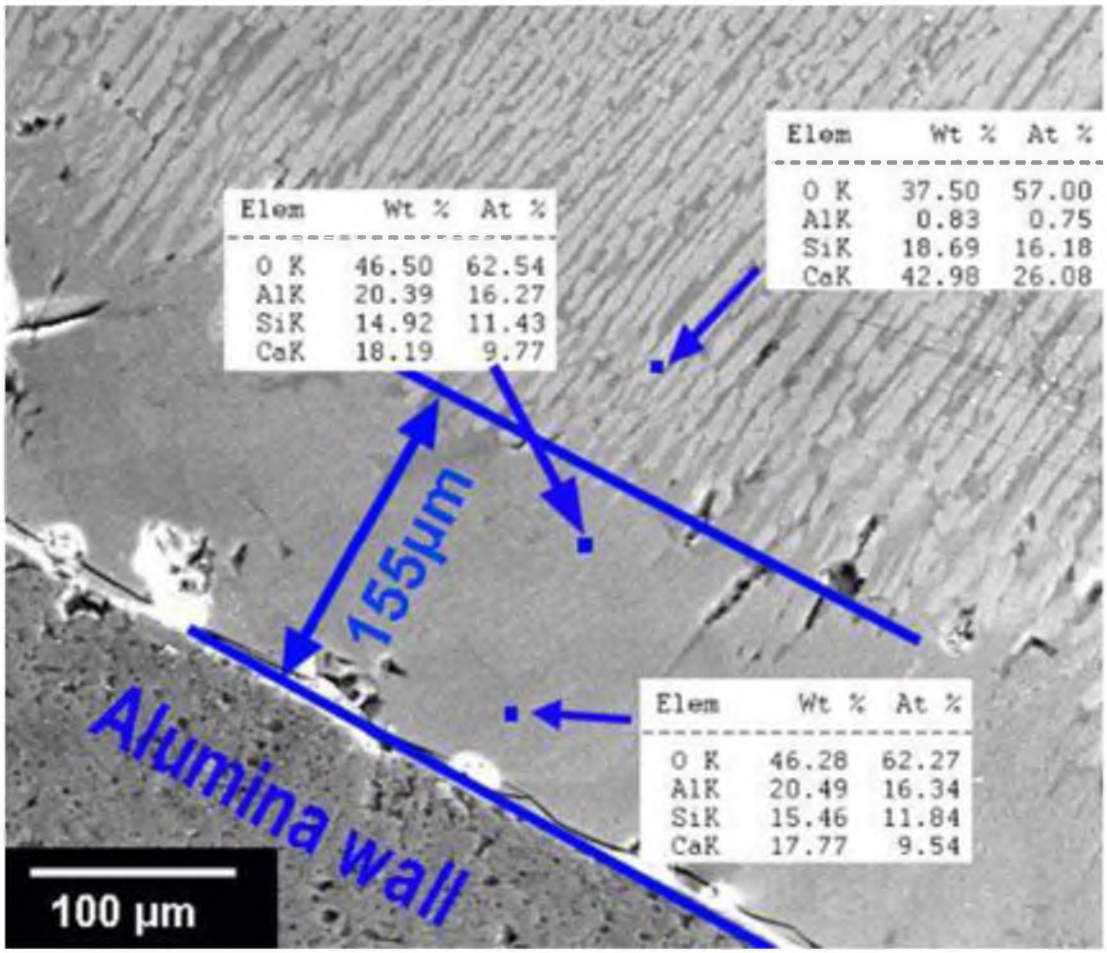

Figure 4.9 An SEM image shows a thin layer existing in between the alumina wall and the crystallized sample. EDS analysis revealed that the composition of this layer is almost uniform and it has a high Al_2O_3 content. The concentration of Al_2O_3 in the region just next to the thin layer decreases dramatically to a very low level.

B_2O_3, thus it stays as glass phase after being cooled to room temperature.

In order to track the distribution of Li and B, we performed a LA-ICP-MS analysis. Since those individual darker regions are smaller than that of the minimum laser spot size that could be focused, a relatively large error in the analysis of this region can be introduced because of the undesired ablation from neighboring brighter regions. This problem was solved by a continuous ablation where a laser beam advanced across a few distinguishable brighter regions and corresponding darker regions in between. Figure 4.10a shows a trench ablated by the focused laser beam with a diameter of 9.7 μm. As can be seen from this figure, the ablation totally covers six brighter regions and five darker regions along the ablation direction. Because of the fact that the brighter regions are larger than the laser beam size while the darker regions are smaller, the beam either ablated a pure brighter region or a darker region with parts of a brighter region. As a consequent, the intensity of each isotope changed periodically with increasing ablation time (longer ablation length), as seen in Figure 4.10b. All the maxima for ^{44}Ca and ^{29}Si appear at the center of the brighter regions and the minima occur at the center of the darker regions, meaning a higher concentration of these two elements in the brighter phase, which agrees with EDS analysis of pure wollastonite. On the contrary, both ^{7}Li and ^{11}B have their maxima occur at the center of the darker regions and minima at the brighter regions, indicating these two elements concentrated in the darker phase, which is also consistent with the observation based on EDS analysis.

Table 4.2 provides the experimental data collected from the LA-ICP-MS analysis. In this table, the average intensities of the brighter phase consist of the average of minima of ^{7}Li and ^{11}B and the maxima of ^{29}Si and ^{44}Ca. Using Eq. 1 as explained in the

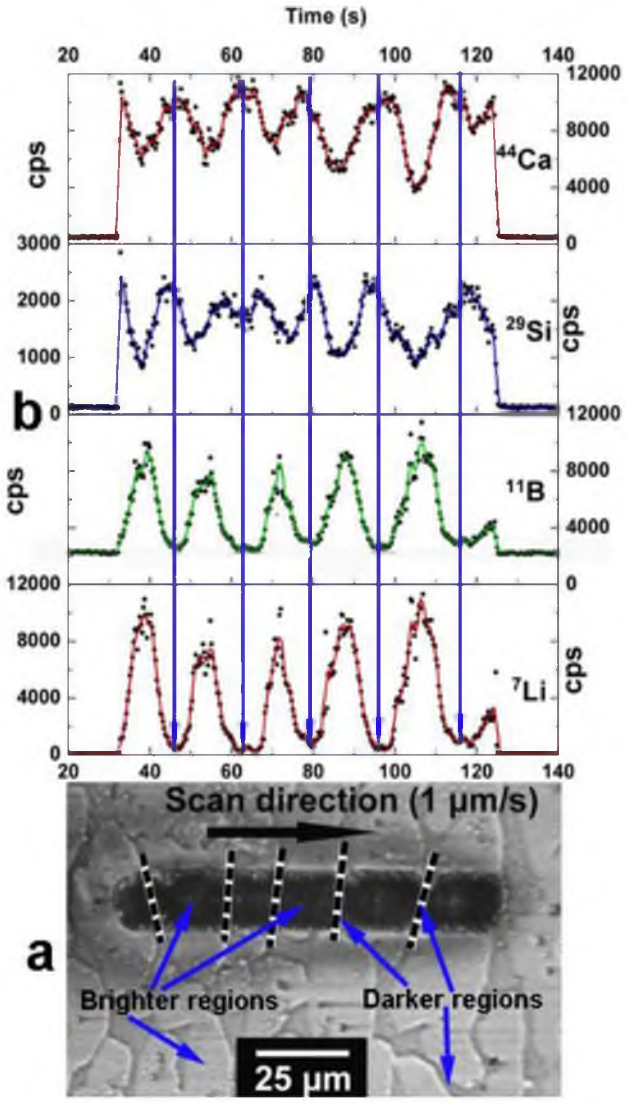

Figure 4.10 Determination of phase composition by LA-ICP-MS analysis: (a) a trench after laser ablation. Scan parameters: scan speed =1 µm/s; laser spot size = 9.7 µm, circle; laser frequency = 10 Hz. Arrows indicate the original and ablated major and minor phases (dashed lines). (b) Intensities of selected isotopes. Raw data were smoothed based on the adjacent-average method that calculates the average of 3 adjacent points and plots the average values into a continuous curve.

Table 4.2 Background-corrected average intensity (cps) of reference standard (NIST-610 glass) and ablated sample.

Isotopes	Reference standard	Ablated sample	
		Brighter phase	Darker phase
^{7}Li	374	532	9864
^{11}B	144	569	7836
^{29}Si	1827	2152	1011
^{44}Ca	1478	9604	4573

Note: (1) The brighter or darker phase refers to the brighter or darker regions in Figgures 4.4 to 4.6; (2) The darker phase includes signals collected from darker regions as well as parts of brighter regions; see the text in Section 3.2 for more detailed information.

Experimental Procedure section, the average composition of the brighter phase is calculated first and listed in Table 4.3. We can see that the brighter phase has a composition almost the same as that of pure wollastonite. Only trace amounts of Li_2O and B_2O_3 exist in this phase. This result agrees with the previous EDS analysis (atomic ratio of Ca : Si : O ≈ 1 : 1 : 3, Figure 4.8) and subsequent XRD analysis, meaning the measured composition of the brighter phase is reliable. The average intensities of the darker phase include both the darker phase and parts of the brighter phase, and thus its composition if calculated based on those maxima and minima will not truly represent the content of each element. However, since we can trust the composition of the brighter phase, the composition of the darker phase could still be determined based on mass balance by neglecting the density difference between the brighter and darker phases and considering 90 vol.% for the brighter phase, as discussed previously. Its final composition thus calculated is also listed in Table 4.3. The LA-ICP-MS analysis thus has provided strong evidence for the formation of wollastonite and successfully tracked the distribution of Li and B, which is difficult by other techniques.

The last issue that may affect the accuracy of the LA-ICP-MS analysis is the depth of the ablated trench. If the depth was smaller than required, the signal collected during a unit time might not well represent the local composition. On the contrary, if the depth was larger than required, the laser might have penetrated into the second layer, which might be a different phase, thus affecting the final results. Therefore, the depth of the ablated trench was measured by SWLI analysis, as shown in Figure 4.11. The average depth calculated from five measurements at positions along the length direction is 11 μm, which is much shorter than the average length of the brighter or darker phase (>100 μm,

Table 4.3 Phase composition analyzed by LA-ICP-MS analysis compared with that of pure wollastonite.

	Composition (wt.%) in terms of oxides			
	Li_2O	B_2O_3	SiO_2	CaO
Brighter phase (major phase)	0.09	0.29	51.59	48.03
Darker phase (minor phase)	14.19	77.39	3.69	4.73
Pure wollastonite ($CaSiO_3$)	–	–	51.73	48.27

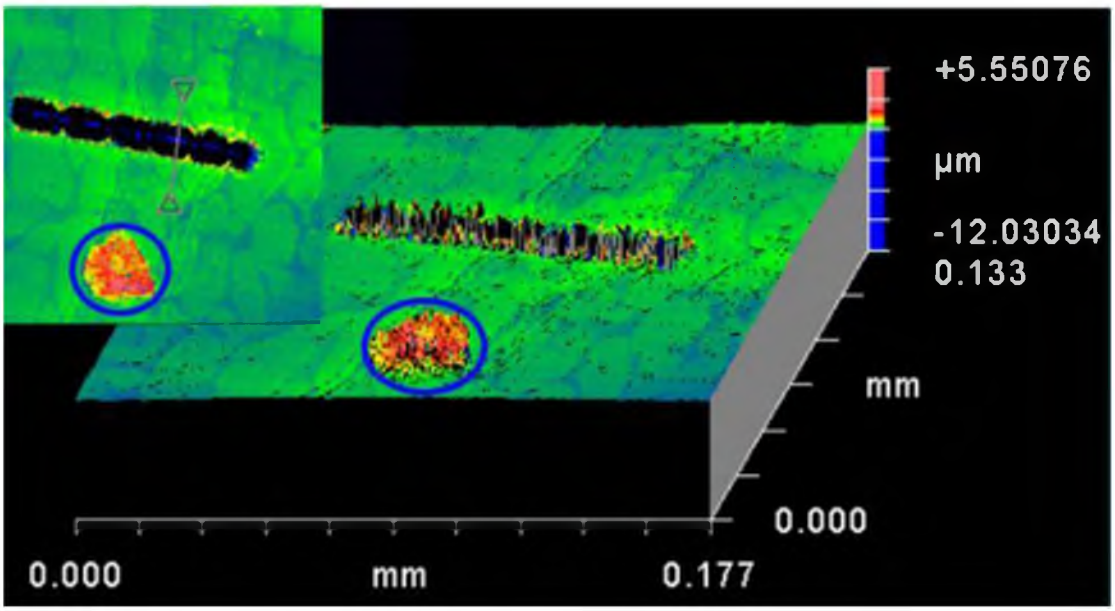

Figure 4.11 Measurement of depth of the ablated trench shown in Figure 4.10a by scanning white light interferometer (SWLI). The line with two triangles in the inserted figure shows an example of depth measurement. The circled spot is a defect area.

viewed along the longitudinal direction as shown in Figures 4.6 and 4.7). Therefore, it is reasonable to neglect the error caused by over-penetration during laser ablation.

4.3.5 Particle Morphology and XRD Analysis

The particle shapes of raw materials and the crushed synthetic wollastonite particles are compared in Figure 4.12. As clearly shown in Figure 4.12a to d, all of the raw materials show either spherical or polygonal shapes with aspect ratios of nearly 1:1. The crushed wollastonite particles, however, show mainly acicular or needle-like shapes with varying aspect ratios (Figure 4.12e). It is worth mentioning that straight parallel cracks and stacking faults extend along the major axis of those acicular particles, shown in Figure 4.12e, while the particles of raw materials have a smooth fracture surface with no obvious cracks or faults, as seen in Figures 4.12a to d. When particles with such cracks or faults are pressed under external forces, they are much easier to break into more acicular particles, making them different from other particles.

Figure 4.13 presents the XRD pattern of the particles shown in Figure 9e. 2M-wollastonite (JCPDS 43-1430) is observed as the only crystalline phase, and all of the collected peaks completely match the standard pattern. However, as seen in Figures 4.2 to 4.4, the solidified sample has two phases. The minor phase occupies approximately 10 vol.% of the total sample. It has high contents of B_2O_3 and Li_2O, and can easily be a glass phase, which is not detected by XRD.

4.3.6 Benefits of Having Aligned Growth

From previous chapters, we have shown that 2M-wollastonite tends to cleave along certain directions. Because of this property, even spherical to cubic bulk

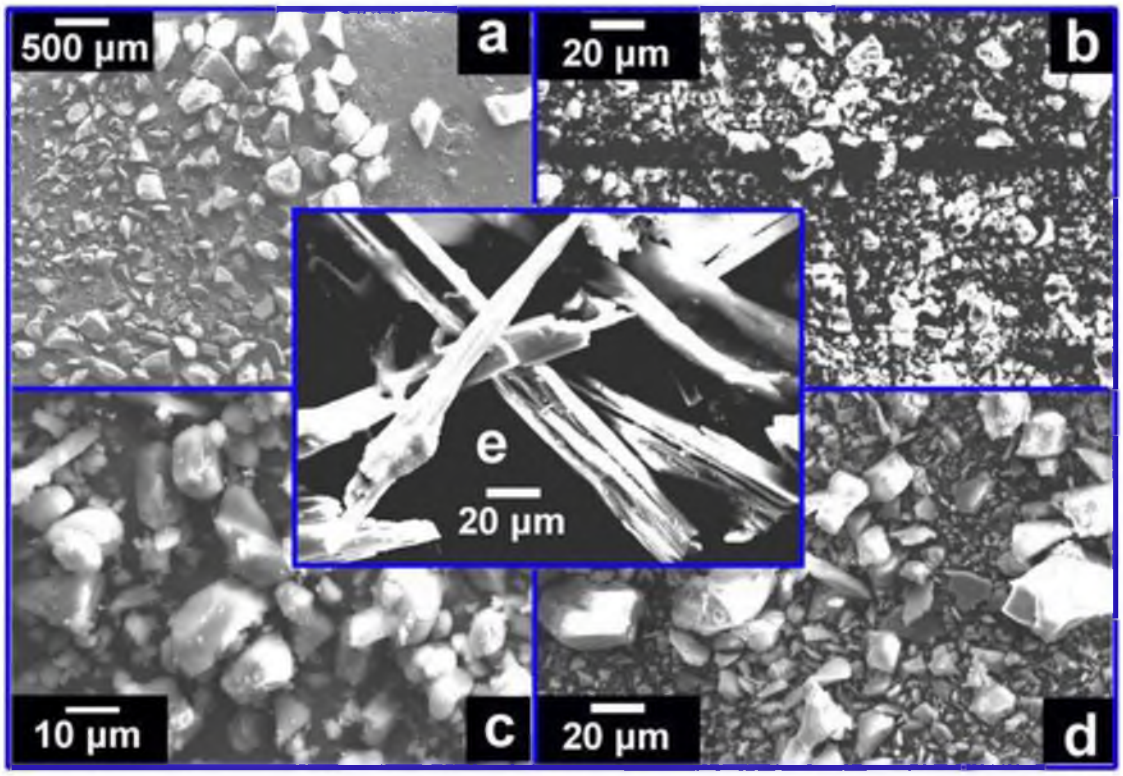

Figure 4.12 Morphology of particles: (a) B_2O_3, (b) Li_2O, (c) CaO, (d) SiO_2, and (e) Synthetic wollastonite crushed from the *R* part in Figure 4.6a.

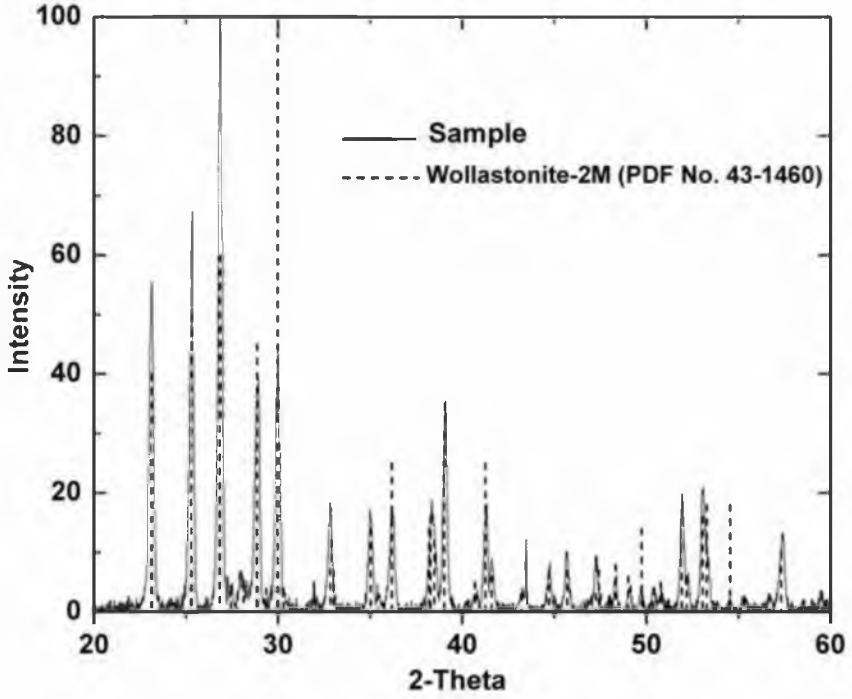

Figure 4.13 XRD pattern of the powder corresponding to Figure 4.12e.

2M-wollastonite single or poly crystals can yield acicular particles after being crushed tosmaller particles. With the controlled growth of wollastonite not only of 2M polytpe but also kept to one-dimensional growth, we gain additional benefits. Figure 4.14 shows the aligned growth of 2M-wollasotnite crystals (or grains) from a sample containing 16 wt.% B_2O_3, 1.5% Li_2O, and balanced by a 1:1 molar ratio of SiO_2 and CaO. In this figure, the length to width ratio of these crystals is extremely large, typically from 150:1 to 300:1 (here these two ratios are compared with the general definition of high-aspect-ratio (HAR), which equals 5:1, and the maximum aspect ratios (20:1 to 30:1) from natural wollastonite particles under ideal pulverization processes). Therefore, the first possible benefit is to selectively etch one phase, glass in this case, out of the target phase, i.e., wollastonite in this case. To achieve this goal, the critical and limiting step is to find a suitable etchant that only dissolves the glass phase without affecting the wollastonite phase. Unfortunately, both of the two phases are made from oxides and contain largely SiO_2, the common solvents that can dissolve SiO_2 such as HF acid, and concentrated NaOH solution will simultaneously remove the two phases. Thus, we have not found a proper etchant so far. However, if the same structure were grown from metal or organic alloys, it might be easier to find suitable solvents; thus, this structure provides a possibility to produce fibrous metal wires from binary metal alloys or organic fibers from binary organic alloys. By removing hydrogen and elements other than carbon from the organic fibers, there is a chance to produce carbon micro to nano fibers. Since these alloys can be treated at much lower temperature, the aligned growth should be much easier to control than this ceramic alloy.

Even though we lose the first benefit on selectively etching, there is still another

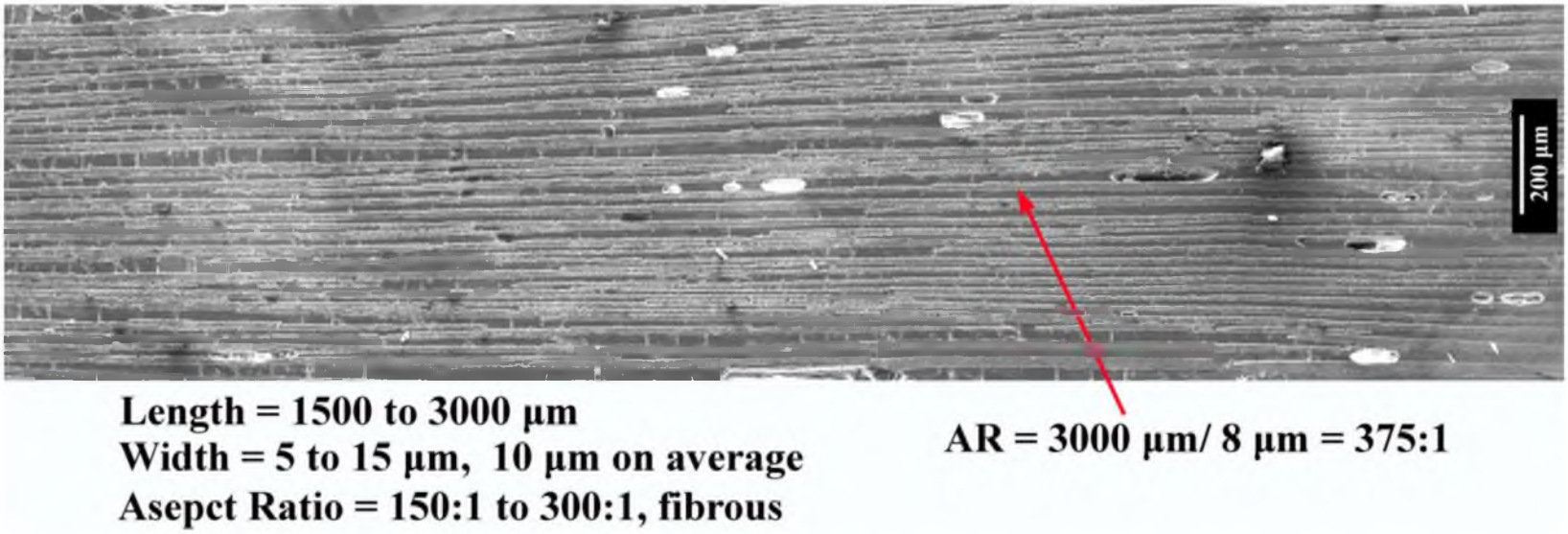

Figure 4.14 One-dimensional growth of 2M-wollastonite crystals. the length to width ratio of these crystals is extremely large, typically from 150:1 to 300:1 (here these two ratios are compared with the general definition of high-aspect-ratio (HAR) which equals 5:1, and the maximum aspect ratios (20:1 to 30:1) from natural wollastonite particles under ideal pulverization processes). If we can find a way to selectively etch the glass phase out of the target wollastonite phase, we will be able to produce not only acicular but also fibrous 2M-wollastonite single crystals. The sample contains 16 wt.% B2O3, 1.5% Li2O, and is balanced by a 1:1 molar ratio of SiO_2 and CaO.

benefit we can use, as shown in Figure 4.15. The sample shown in this figure consists of 20 wt.% B_2O_3, 1.5wt% Li_2O, and a balanced 1:1 molar ratio of SiO_2 and CaO. As can be seen from this figure, the wollastonite crystals generally do not have cracks while glass phase has many random cracks due to larger thermal expansion or mechanical friction during the sample preparation stage. However, if these long wollastonite crystals ever have cracks, the cracks will extend along the growth direction, which is the desired cleavage direction for producing one-dimensional particles. This type of structure serves as the best evidence for the second possible benefit that is the directional cleavage.

In Figure 4.16, we were rolling a steel tube set over a wollastonite sample that had the growth orientation parallel to the arrow direction. After rolling 5 times, the sample broke into smaller particles, and it is clearly seen that these particles cleaved along the growth direction. After rolling 10 times, the particles became much smaller so that we could not distinguish their orientations to the naked eye, but under optical microscope, we began to see more acicular particles. After rolling more than 20 times, the particles became even smaller but more acicular.

Similarly, we repeated the same experiments on natural quartz and marble of similar size. These two did not show any preferred growth orientation. As you can see from Figure 4.17, after rolling any number of times, the particles from these two samples neither showed directional cleavage nor acicular shapes.

4. 4 Conclusions

In conclusion, the top-cooled flux growth of 2M-wollastonite has been proved to be suitable for preparing acicular or needle-like particles. The FG process has the following characteristics.

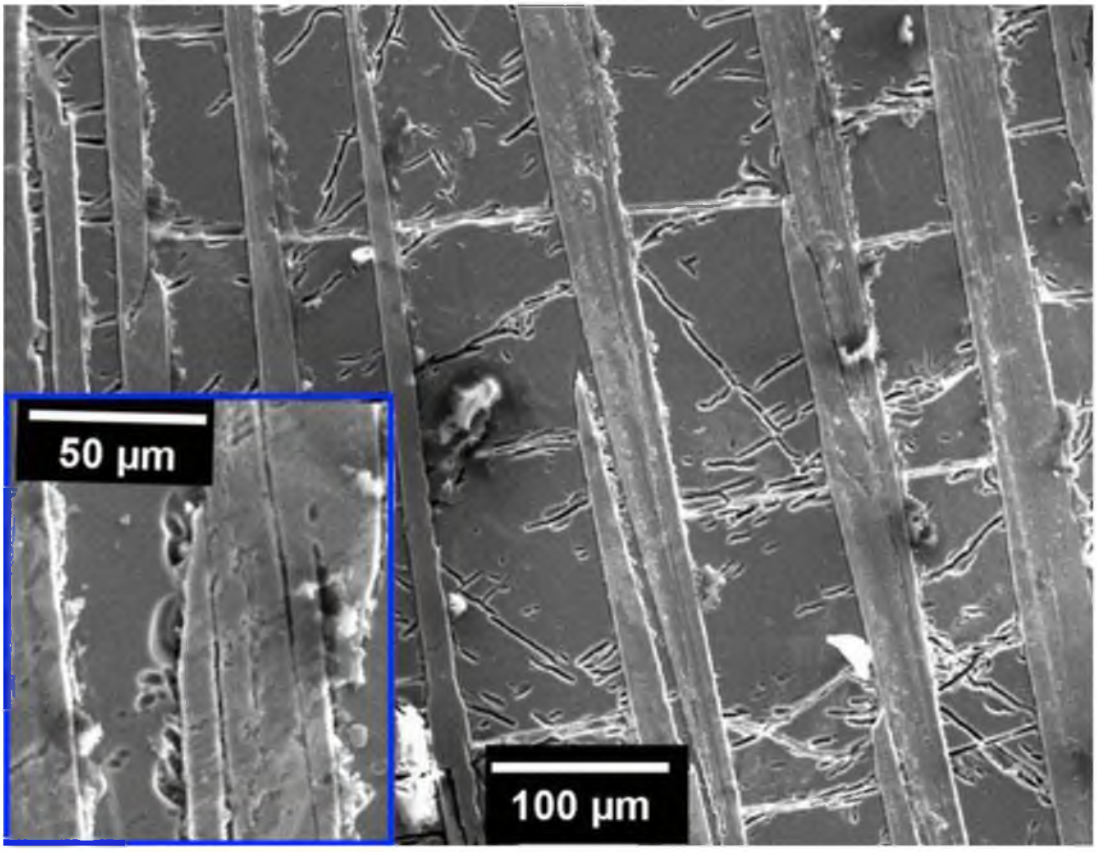

Figure 4.15 Demonstration of directional cleavage of wollastonite crystals (the lighter phase with fewer cracks). Wollastonite crystals generally do not have cracks while the glass phase has many random cracks due to larger thermal expansion or mechanical friction during the sample preparation stage. However, if these long wollastonite crystals ever have cracks, the cracks will extend along the growth direction (the inserted figure), which is the desired cleavage direction for producing one-dimensional particles. The sample consists of 20 wt.% B_2O_3, 1.5wt% Li_2O, and a balanced 1:1 molar ratio of SiO_2 and CaO.

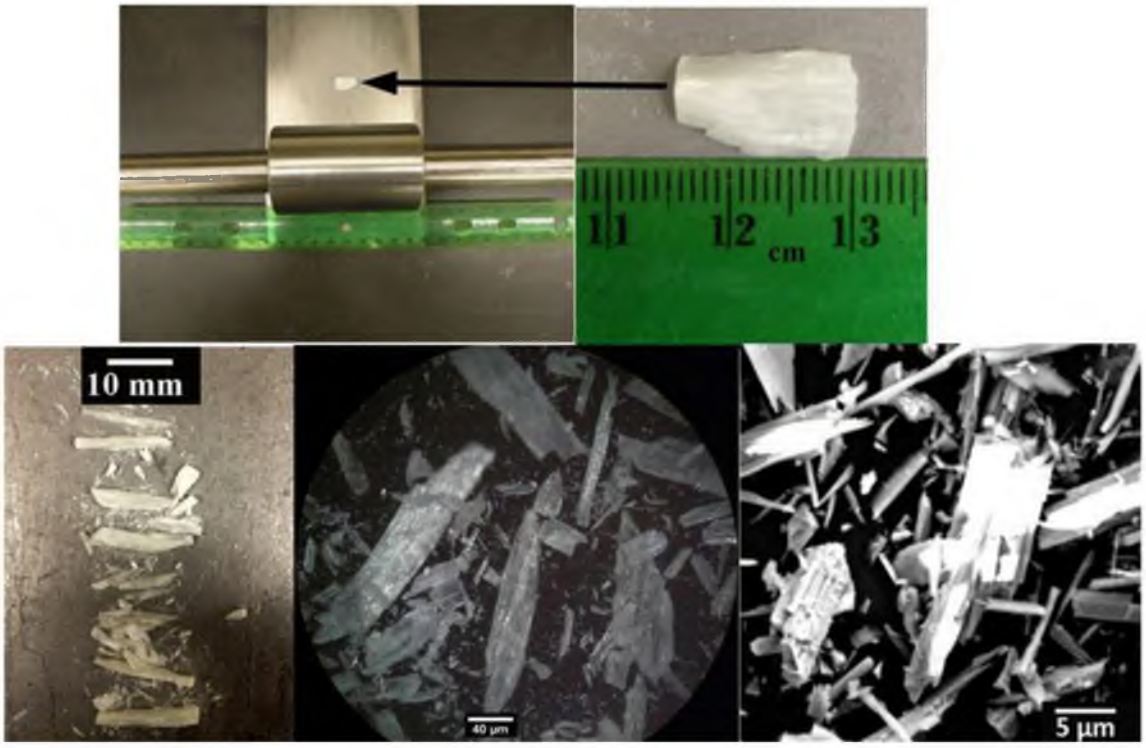

Figure 4.16 Cleavage response from a sample solidified by the FG process and has the directional growth pattern.

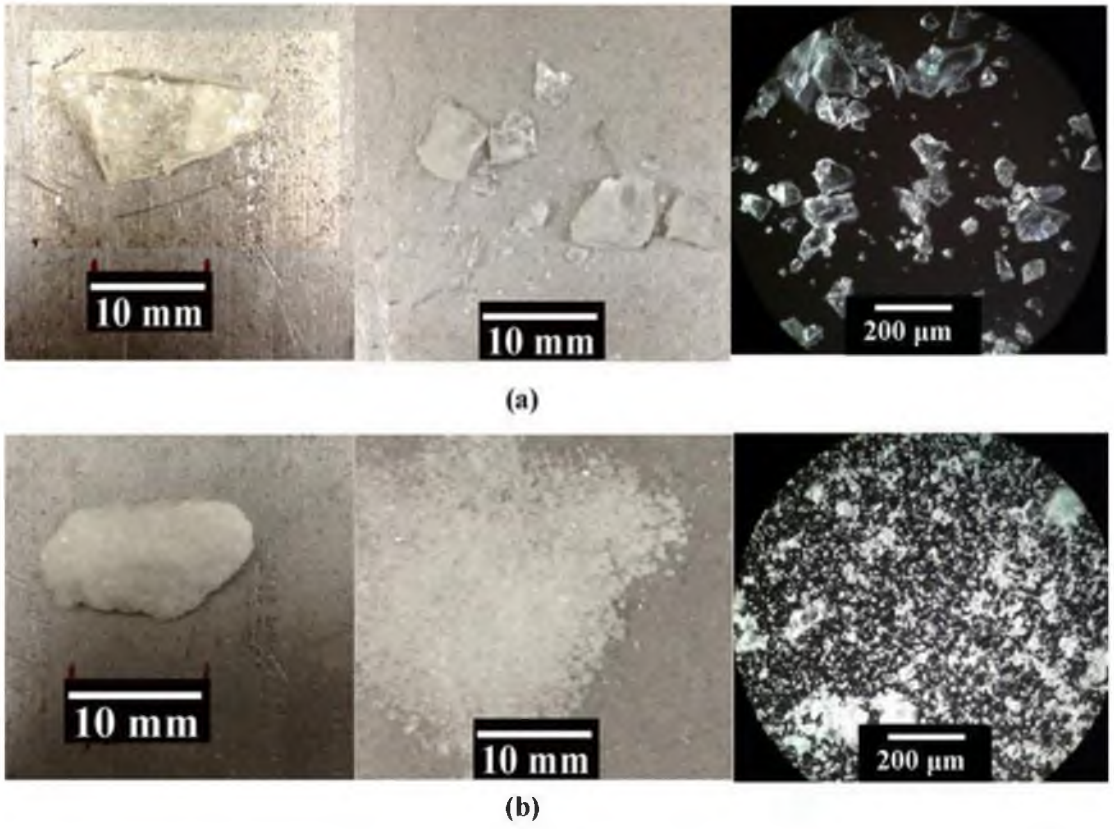

Figure 4.17 Cleavage responses from: (a) Milky quartz (purchased from Ward's Science with item # 6035101), and (b) Valley Gold Vein marble from Arizona Tile in West Valley City, Utah. The samples were crushed in the same way as used in Figure 4.17.

It takes advantages of the heat transfer properties of the melt-crucible-furnace wall (MCF) system; a vertical temperature gradient is achieved to provide sites for the nucleation of 2M-wollastonite crystals.

The solidified products contain nearly pure 2M-wollastonite crystals as the major component and amorphous glass phase as the minor part.

Under intermediate cooling rates, a solidified sample consists of approximately one-dimensional growth of rod crystals that display uniform cellular structure under 2D microstructure observation.

The aligned growth of 2M-wollastonite crystals provides additional benefits to its acicular cleavage property.

The determination of phase composition demonstrates that LA-ICP-MS analysis is a useful and reliable tool for analyzing the composition of multiphase microstructures containing large to trace amounts of Li and B.

CHAPTER 5

CELLULAR AND DENDRITIC GROWTH UNDER UNSTEADY-STATE SOLIDIFICATION: PART I. EXPERIMENTAL STUDIES ON WOLLASTONITE GROWTH

5.1 Introduction

Cellular and dendritic growth mechanisms have been extensively studied in the past by many researchers [40-45]. They exist very commonly during casting and welding of metals and can affect the mechanical properties of metals significantly. Their characteristic patterns include primary arms, secondary arms, and tertiary arms under certain conditions [46]. When only primary arms are well developed, the corresponding structure is cellular structure. When both primary and secondary arms are developed simultaneously, they become dendritic structure. Tertiary arms either exist in small volume fraction or growth into primary arms [46, 47]; thus, they did not attract too much attention in these studies. Two important parameters corresponding to the primary arms and secondary arms are the primary arm spacing (λ_1) and secondary arm spacing (λ_2). Other parameters include dendrite tip radius (ρ) and mush zone depth (d). These parameters are directly related to growth parameters: the temperature gradient (G) ahead of the growth front and growth rate (v) [43, 48].

Experiments on cellular and dendritic growth have been carried out in various systems. They can be classified into two general systems. The first system contains metal

alloys; examples are Pb-Sn [49], Sn-Zn [50], and Al-Cu [51] binary alloys. The second system covers organic alloys such as succinonitrile-acetone [41], succinonitrile-salol [52], and pivalic acid-ethanol [43]. A more detailed list of such organic compounds or combinations of them can be found in Jackson and Hunt's work [40], where they believed that these organic compounds have a small α factor that is defined by Jackson [53] as $\alpha = L\xi / RT_E$ where L is the difference between the internal energy of the two phases, R is the gas constant, T_E is the equilibrium temperature between the two phases, and ξ is a factor that depends on the crystallography of the interface. A small α factor is likely to form dendritic structure during solidification while a larger α factor tends to lead to the formation of faceted crystals. Most metal alloys and the aforementioned organic compounds have small α factors and thus, they are relatively easy to grow into dendritic morphologies. Compared with metal alloys, those organic alloys have two important advantages. Firstly, they have a low melting point, for example the melting point of succinonitrile is only 54.5°C [40], thus they can be handled more easily. Secondly, they more often form transparent crystals that make in-situ measurements or real-time monitoring possible. Because of these unique properties, such organic alloys were frequently used for modeling cellular and dendritic growth [40, 41, 43]. However, to the best of my knowledge, little study has been made in the dendritic growth of ceramic alloys, for example the $CaO\text{-}SiO_2\text{-}B_2O_3\text{-}Li_2O$ system in this study, where the highest operating temperature was around 1500°C. During a high-temperature solidification process, many properties may have changed, so the models developed from organic alloys or even metals of low melting point such as Sn metal may not apply directly due to a solubility difference caused by different bonding mechanisms. And at these high

temperatures, either in-situ measurement or real-time monitoring becomes unrealistic and extremely difficult. The lack of information on the ceramic alloys suggests that a detailed study on the cellular and dendritic growth in ceramic alloys is necessary.

In the studies on cellular and dendritic growths mentioned above, most were carried out under steady-state heat flow, meaning a constant temperature gradient. However, in solidification processes where unsteady-state heat flow is dominant, the growth behavior may differ from those steady-state dendritic growths. Even in the few studies discussing unsteady-state heat transfer, they focused only on metal alloys [54, 55].

Because of the issues mentioned above, we designed a series of experiments to investigate the cellular and dendritic growth of a ceramic alloy under high-temperature unsteady-state heat transfer. Meanwhile, we provided a simple approach to achieve unidirectional temperature gradient, which usually requires either delicate apparatus or specially designed furnaces. In our approach, we simply utilize the heat transfer theories to a Melt-Crucible-Furnace wall (MCF) system to enforce the nucleation and growth along the unidirectional temperature gradient direction.

5.2. Experimental Procedure

5.2.1 Raw Material Preparation

The experimental procedure used in this work is very similar to the procedure discussed in a previous chapter except that a wider and specially designed range of values for some critical parameters were studied to understand the behavior of cellular and dendritic growth. The experiments started with making mixtures having a composition as provided in Table 5.1 by using laboratory mortar and pestle.

Table 5.1 Raw material composition and heat treatments of samples discussed in Chapter 5.

Sample number	Content (wt.%)				Heat treatment (temperature in K, and time in minutes)					
	SiO_2	CaO	B_2O_3	Li_2O	T_P	t_P	T_M	t_M	T_C	t_C
S1	46.8	43.7	8.0	1.5	1253	30	1693	20	1253	**0**
S2	46.8	43.7	8.0	1.5	1253	30	1693	20	1253	**3**
S3	46.8	43.7	8.0	1.5	1253	30	1693	20	1253	**5**
S4	46.8	43.7	8.0	1.5	1253	30	1693	20	1253	**11**
S5	46.8	43.7	8.0	1.5	1253	30	1693	20	1253	**15**
S6	46.8	43.7	8.0	1.5	1253	30	1693	20	1253	**20**
S7	46.8	43.7	8.0	1.5	1253	30	1693	20	1253	**300**
S8	46.8	43.7	8.0	1.5	1253	30	1693	20	**1153**	300
S9	46.8	43.7	8.0	1.5	1113	30	1693	20	**1113**	300
S10	46.8	43.7	8.0	1.5	1023	30	1693	20	**1023**	300
S11	44.7	41.8	**12.0**	1.5	1253	30	1653	20	1253	300
S12	42.7	39.9	**16.0**	1.5	1253	30	1613	20	1253	300
S13	40.6	37.9	**20.0**	1.5	1253	30	1573	20	1253	300
S14	34.4	30.7	**35.0**	1.5	1253	30	1423	20	1253	300
S15	26.6	23.4	**50.0**	1.5	1253	30	-	-	-	-

Note: 1. The symbols T and t represent temperature and time, respectively. The corresponding subscripts, P, M, and C, stand for Preheating, Melting, and Crystallization, respectively.
2. Major change in each sample compared with others is indicated by a bold number.

5.2.2 Equipment Setup for Self-Controlled Directional Solidification

As shown in Figure 5.1, the aforementioned mixtures along with the corresponding crucible were first preheated in a muffle furnace at a preheating temperature of T_P for a preheating time of t_P. Then, it was transferred to the vertical furnace, which was heated to a melting temperature of T_M and held for a melting time of t_M. The T_M applied here had been predetermined before the actual experiment so that it melted the mixture completely within a time of t_M. At the end of t_M, the crucible along with the melt was transferred back to the muffle furnace at a crystallization temperature of T_C for a crystallization time of t_C to solidify the melt. The complete experimental conditions for the samples used in this chapter are also provided in Table 5.1.

As shown in Figure 5.2, once the crucible was transferred from the vertical furnace to the muffle furnace, heat losses from the side and bottom crucible walls were much slower compared with that from the top melt. This type of heat transfer offered a temperature gradient that was approximately perpendicular to the melt-air interface with top melt being the cooler part.

5.2.3 Measurement of Growth Rate

To measure the growth rate, samples S1-6 were prepared and allowed to crystallize for a time, as indicated in Table 5.1. At the end of the crystallization time, each sample was taken out of the muffle furnace and quenched in air. After being cooled to room temperature, each was crushed into two parts. One part was mounted and polished. Since the crystallized melt was opaque while the noncrystallized melt remained a transparent glass, the thickness of the crystallized layer was then measured directly. The

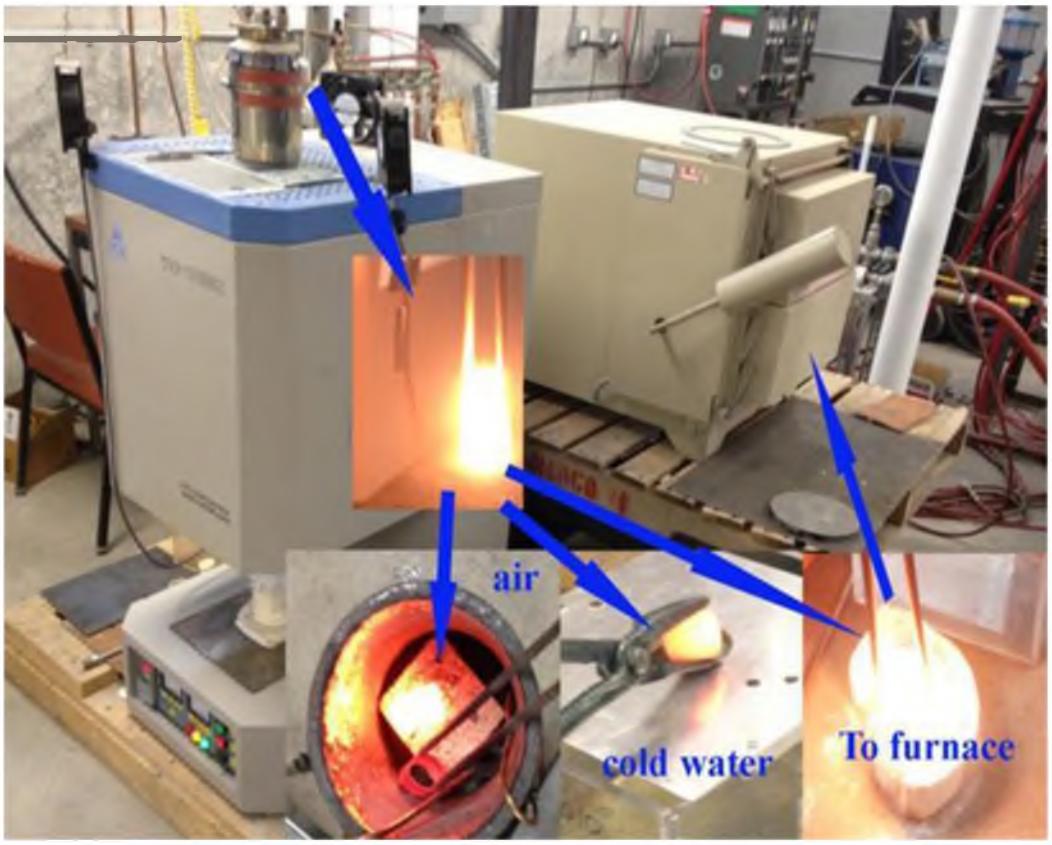

Figure 5.1 Equipment setup for self-controlled directional solidification: the vertical furnace (left) and the muffle furnace (right). Three types of cooling methods used were: water quenching, air quenching, and furnace cooling.

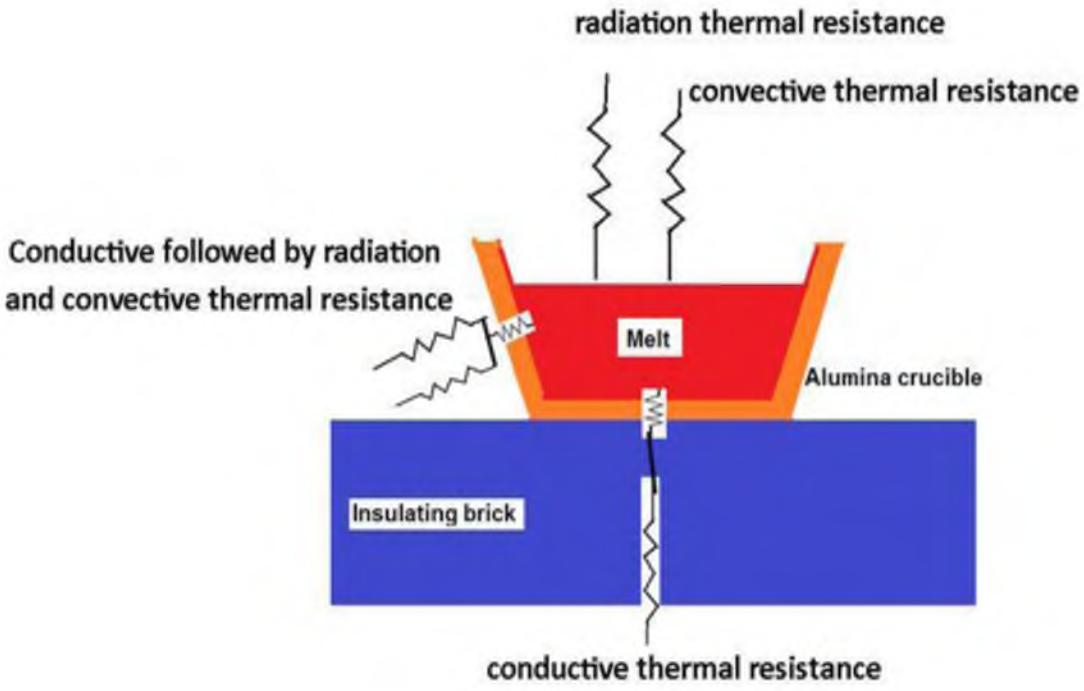

Figure 5.2 Illustration of heat transfer mechanism of the Melt-Crucible-Furnace system used for the Flux Growth Process.

ratio of the increased thickness of crystallized layer to the time interval is the average growth rate.

5.2.4. Measurement of Primary Spacing

Even though dendrites can have primary arms and secondary arms, in this system, only the primary arm spacing (hereafter referred to as primary spacing) is our major interest because it does not coarsen with time while secondary arm spacing may vary during the quenching of alloys [43]. Therefore, we shall use λ_1 to compare the growth behaviors of each sample. It is worth mentioning that for any cellular or dendritic structure, the primary spacing is very rarely a fixed value. It usually falls into a certain range between λ_{1min} (minimum primary spacing) and λ_{1max} (maximum primary spacing) [41]. Therefore, without a special notation, the primary spacing in this study refers to the average primary spacing.

5.3 Results and Discussion

5.3.1 Characteristic Morphologies of Cellular and Dendritic Structure

Depending on temperature gradient, cellular and dendritic structure can grow into cells when only primary arms are well developed or into dendrites when both the primary and secondary arms are well developed simultaneously. In our case, both cellular structure and dendrites with primary and secondary arms were observed, as seen in Figures 5.3 and 5.4, respectively.

5.3.2 Average Growth Rate under Unsteady-state Heat Transfer

Figures 5.5 and 5.6 show the appearance of six samples which have the same composition but were quenched in air at the end of different solidification times in the

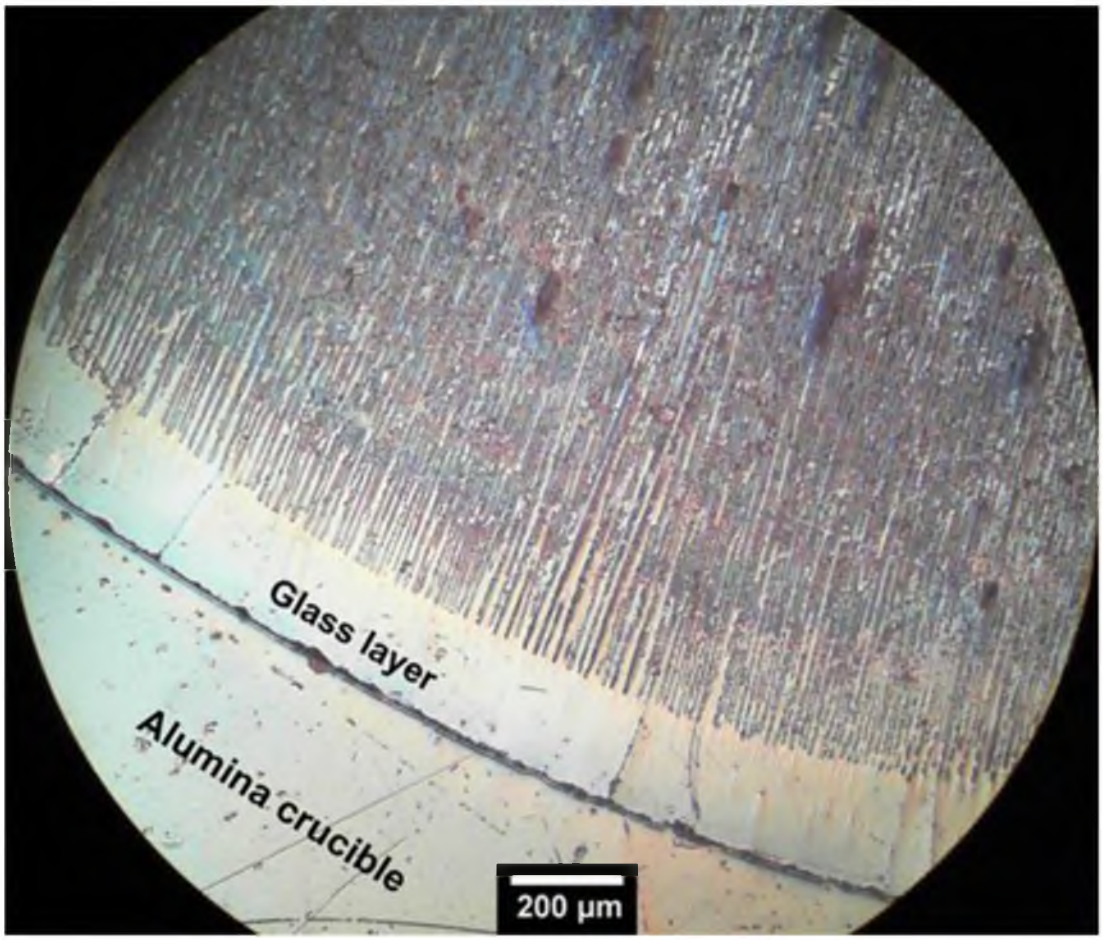

Figure 5.3 Demonstration of cellular growth from the sample S11 under unidirectional growth.

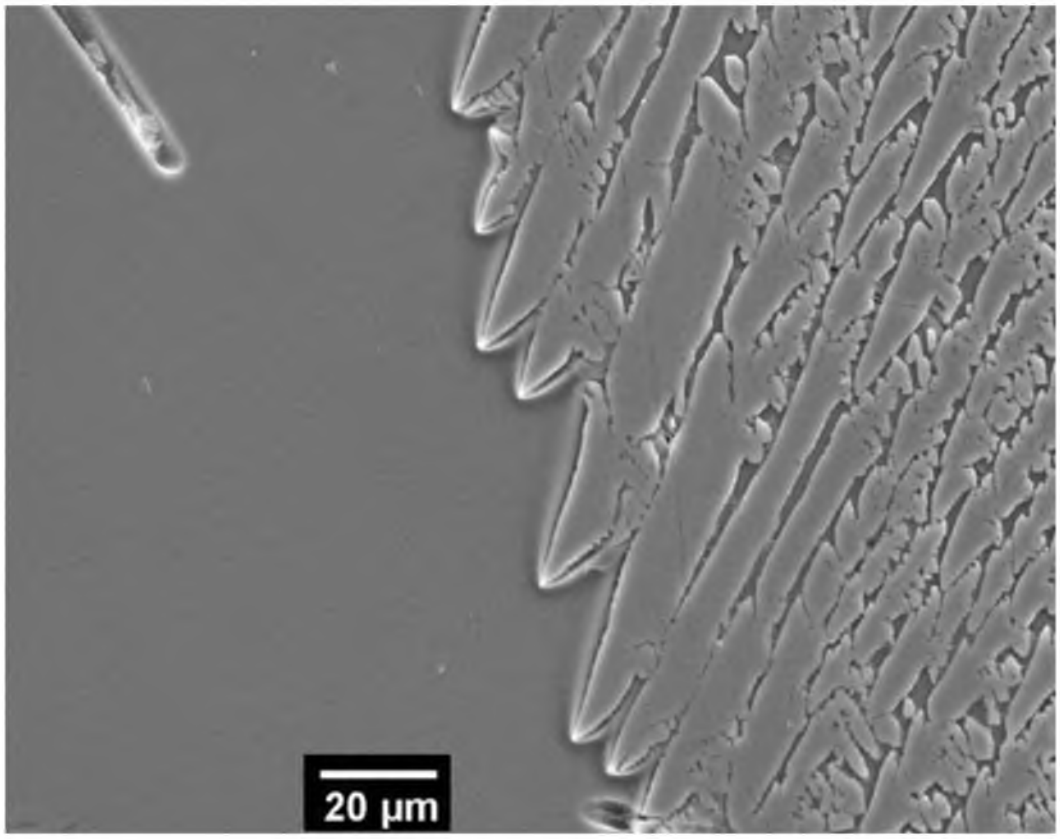

Figure 5.4 Demonstration of dendritic growth from the sample S2 under unidirectional growth.

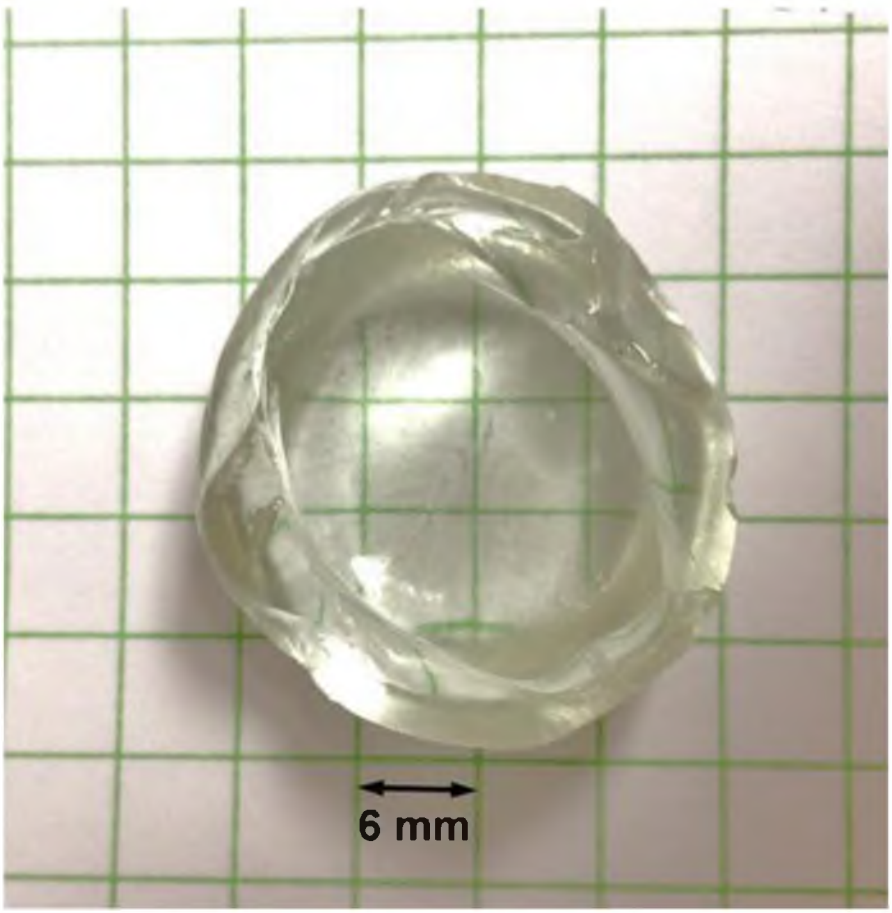

Figure 5.5 With no crystallization time, sample S1 remained as transparent glass after being cooled to room temperature by air quenching.

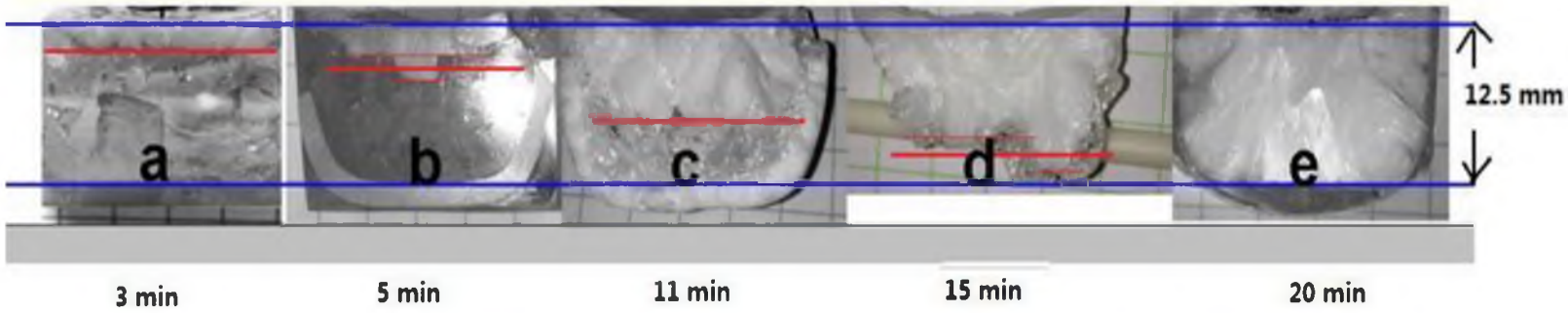

Figure 5.6 Digital images showing the thicknesses of solidified layers of samples S2-6 under various crystallization times (a) to (e). Red lines indicate the growth front/fronts of each sample.

muffle furnace. In Figure 5.5, the sample was quenched immediately without being transferred to the muffle furnace. The quenched sample was transparent glass. With a finite cooling rate, the cooled samples began to have an opaque layer, as shown Figure 5.6a-e, and the thickness of this layer increased with increasing crystallization time. As seen in Figure 5.6e, the melt solidified completely after 20 minutes. In Fig 5.6b and d, there are two growth fronts with a smaller and narrower front slightly ahead of the major front. The average of the two fronts was considered as the average thickness of the growth.

The average growth rate during each time interval, i.e., 0 to 3 min, 3 to 5 min, etc., was then measured based on the thicknesses of solidified layers in Figure 5.6. The result is plotted in Figure 5.7, which indicates the growth rate decreased with increasing crystallization time. The decreasing growth rate was likely caused by a lower temperature as well as a lower temperature gradient ahead of the growth front near the end of crystallization process.

5.3.3 Crystal Growth Orientation

Figure 5.8 shows a polished cross-section parallel to the growth direction of the sample S4. Both of them display crystals of high-aspect-ratio because of their strongly preferred growth orientation. To confirm this preferred orientation, XRD analysis was performed for a powder specimen and a bulk specimen from the same sample. The bulk specimen was cut in a way shown in Figure 5.9b. The surface along the transverse direction is almost parallel to the top melt surface and polished before analysis. As shown in Figure 5.9a, the powder specimen has all of the characteristic peaks corresponding to the standard 2M-wollastonite XRD pattern detected, while the bulk specimen only shows

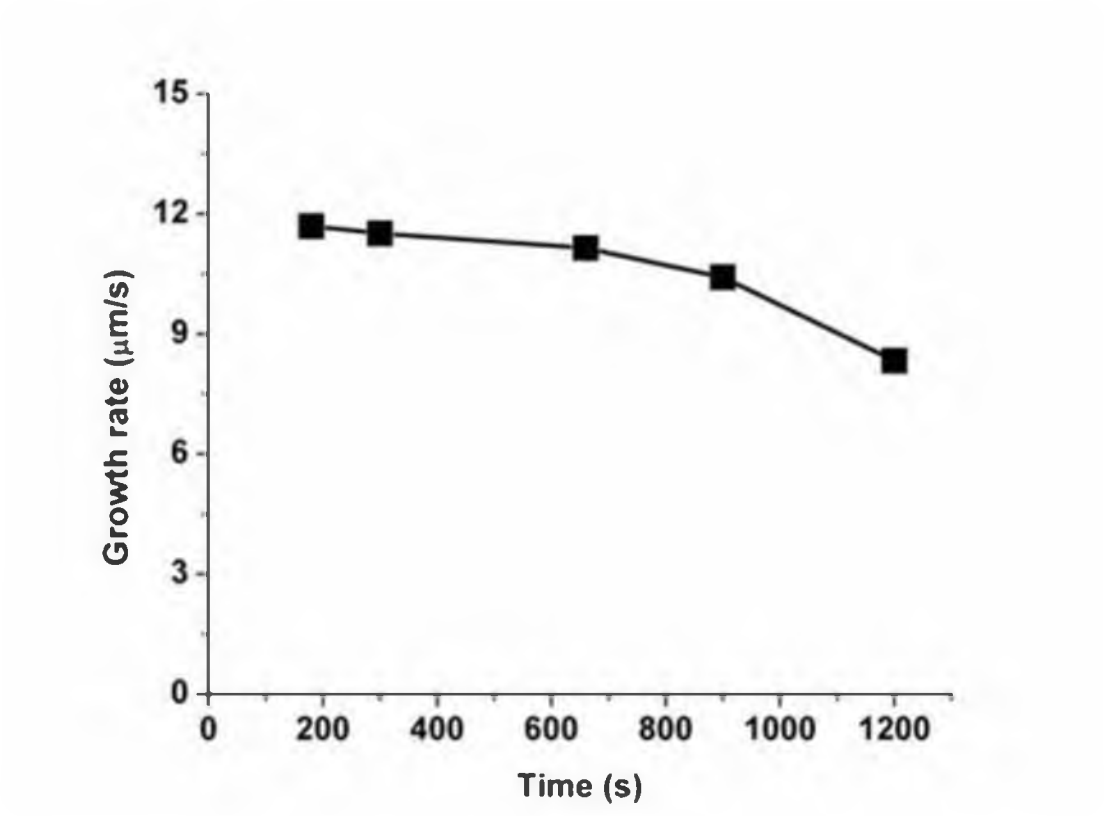

Figure 5.7 Relationship between average growth rate and crystallization time.

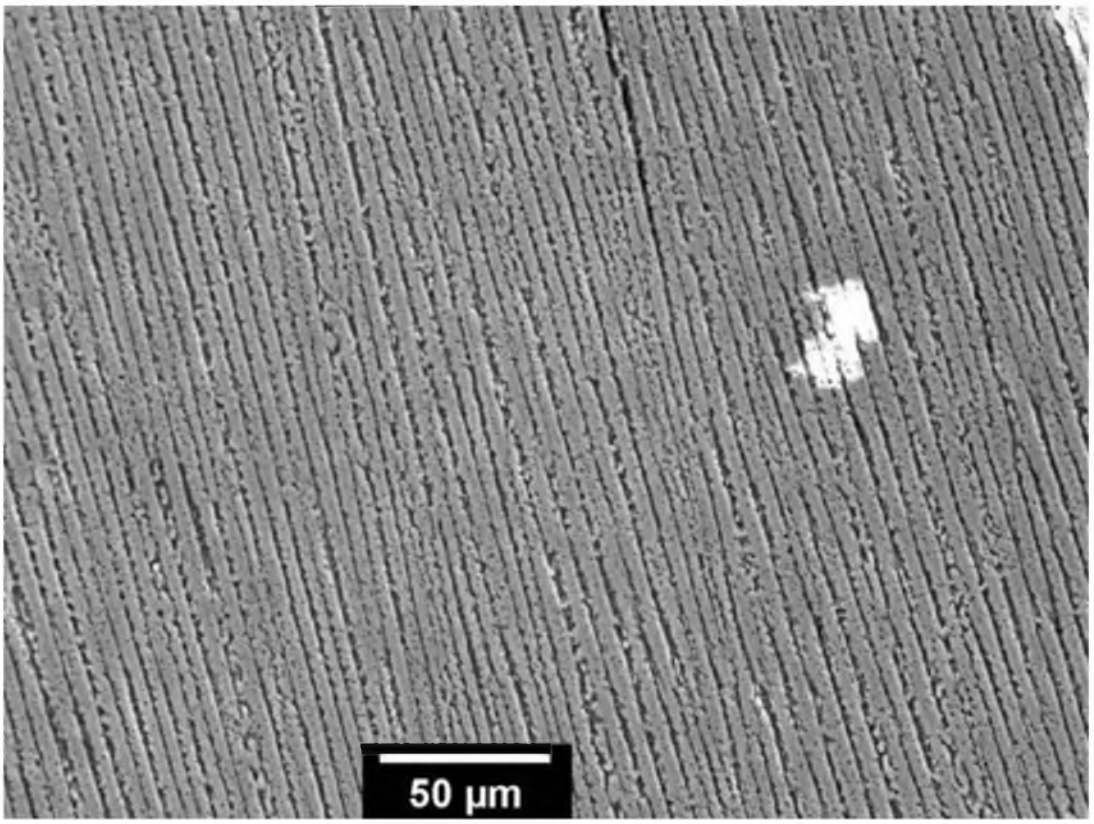

Figure 5.8 SEM image presenting directional growth from the sample S4.

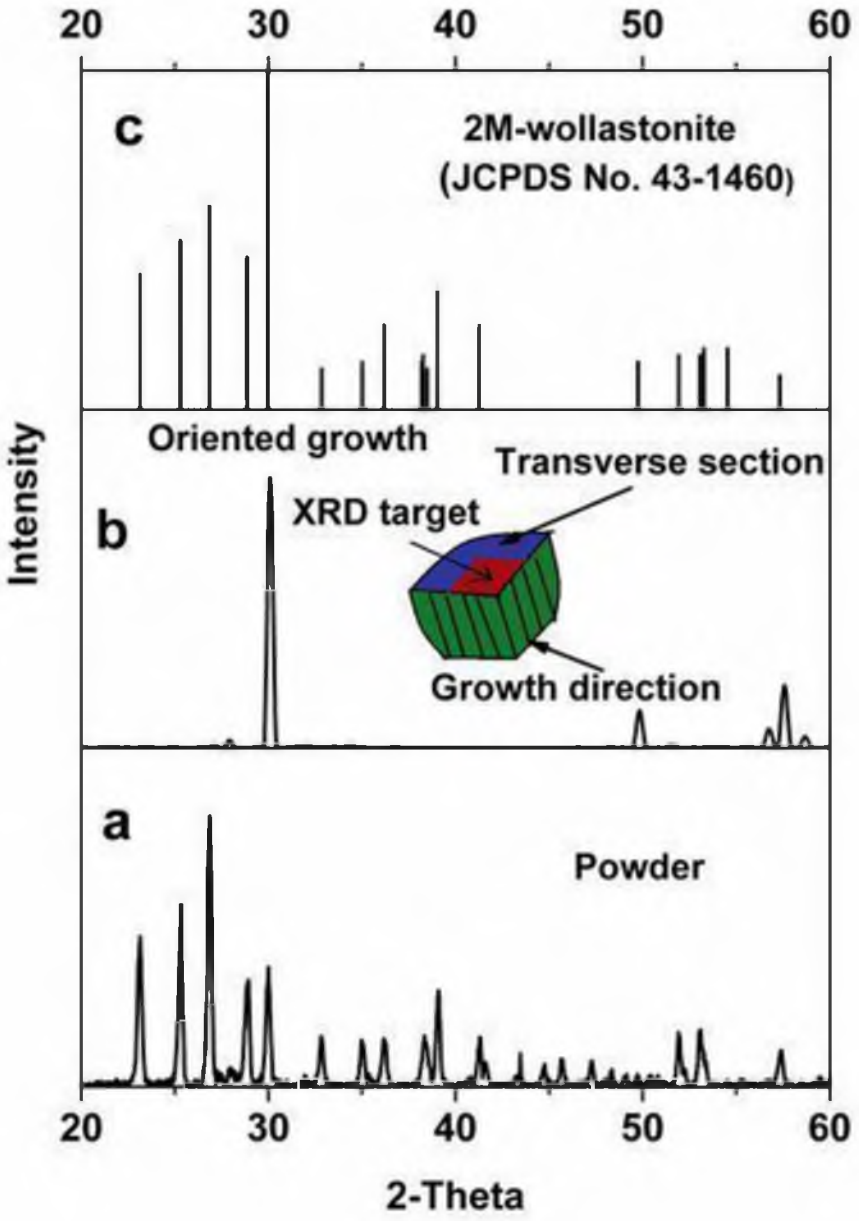

Figure 5.9 XRD patterns of: a powder specimen from the sample S7 (a), a bulk specimen from the same sample cut as indicated by the inserted figure (b), and 2M-wollastonite (c).

a few peaks. The reason more than one peak was detected if all crystals have perfect orientation as shown in Figure 5.8 is because of the scale associated with the two figures. In Figure 5.8, the maximum view filed is about 0.2 mm^2 while the area for XRD analysis of the bulk specimen was about 25 mm^2. With an area difference of about 125 times, the chance of having a different orientation for some regions is very high; it is likely to consist of regions that have different orientations, as shown in Figure 5.10.

5.3.4 Effects of Crystallization Time on Primary Spacing

In order to study the effect of crystallization time on the primary spacing λ_1, samples S1-6 were used again. The commonly accepted way to obtain λ_1 is to measure the distance between the two nearest dendrite tips, as shown in Figure 5.11. To increase the accuracy, this parameter is usually measured based on an array of continuous tips. However, during the initial measurements of these samples, it was noticed that the structure of a crystallized sample varied slightly across the temperature gradient direction, as illustrated in Figure 5.12.

As can be seen in Figure 5.12, the overall structure of a crystallized sample presents an inverse configuration of corn plants. The first region is the Root-Zone where the nucleation and growth start. In the actual experiments, the melt were just transferred from a vertical furnace at a higher temperature to a muffle furnace at a lower temperature, so both radiation and convection heat transfer were at the strongest stage; thus, the top melt began to cool very fast, and heat flow within this layer is also more complicate than the melt underneath. As a consequence, the structure of this zone is much less ordered than the other two zones, as will be discussed below. After a while, the top melt solidified into crystals, and they were nearly opaque; meanwhile, they also separated the

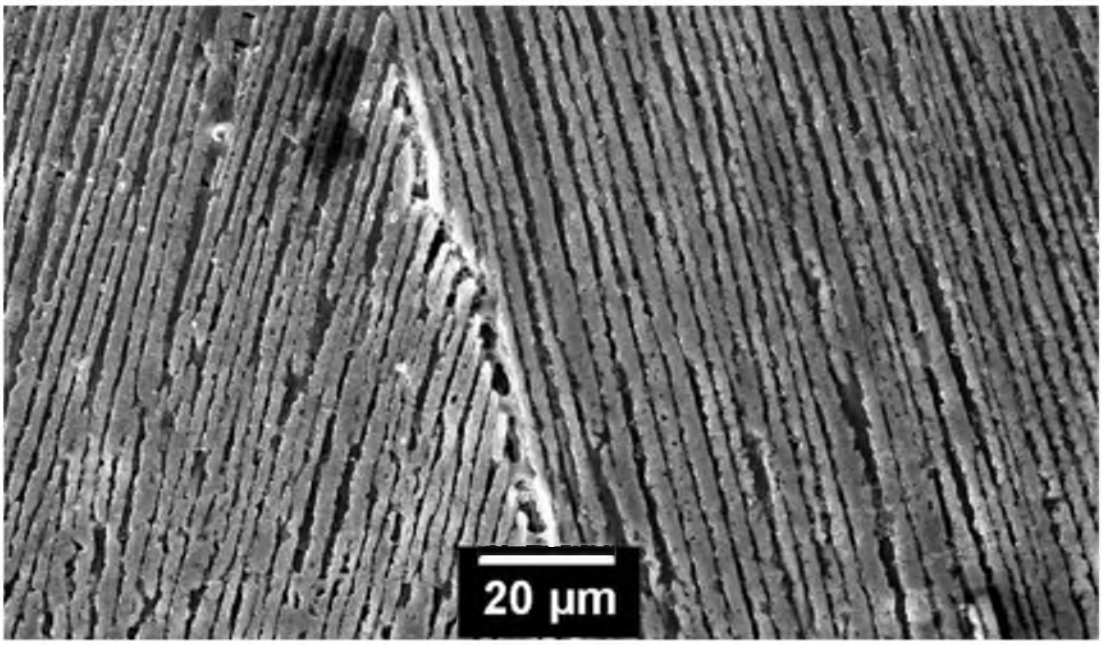

Figure 5.10 Sample (S6) showing regions of different growth orientations.

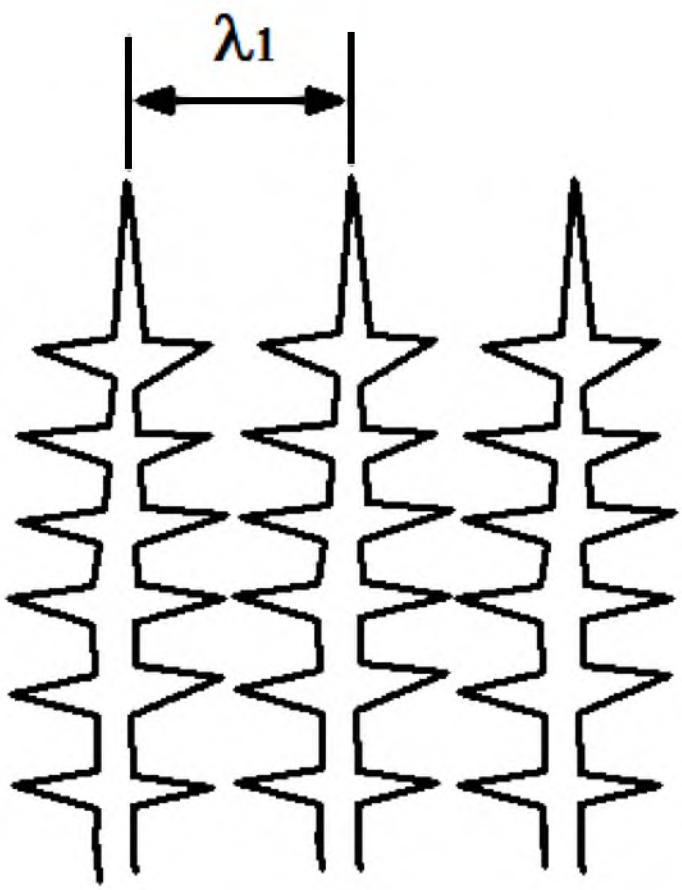

Figure 5.11 Illustration on measuring λ_1 in a cellular/dendritic structure.

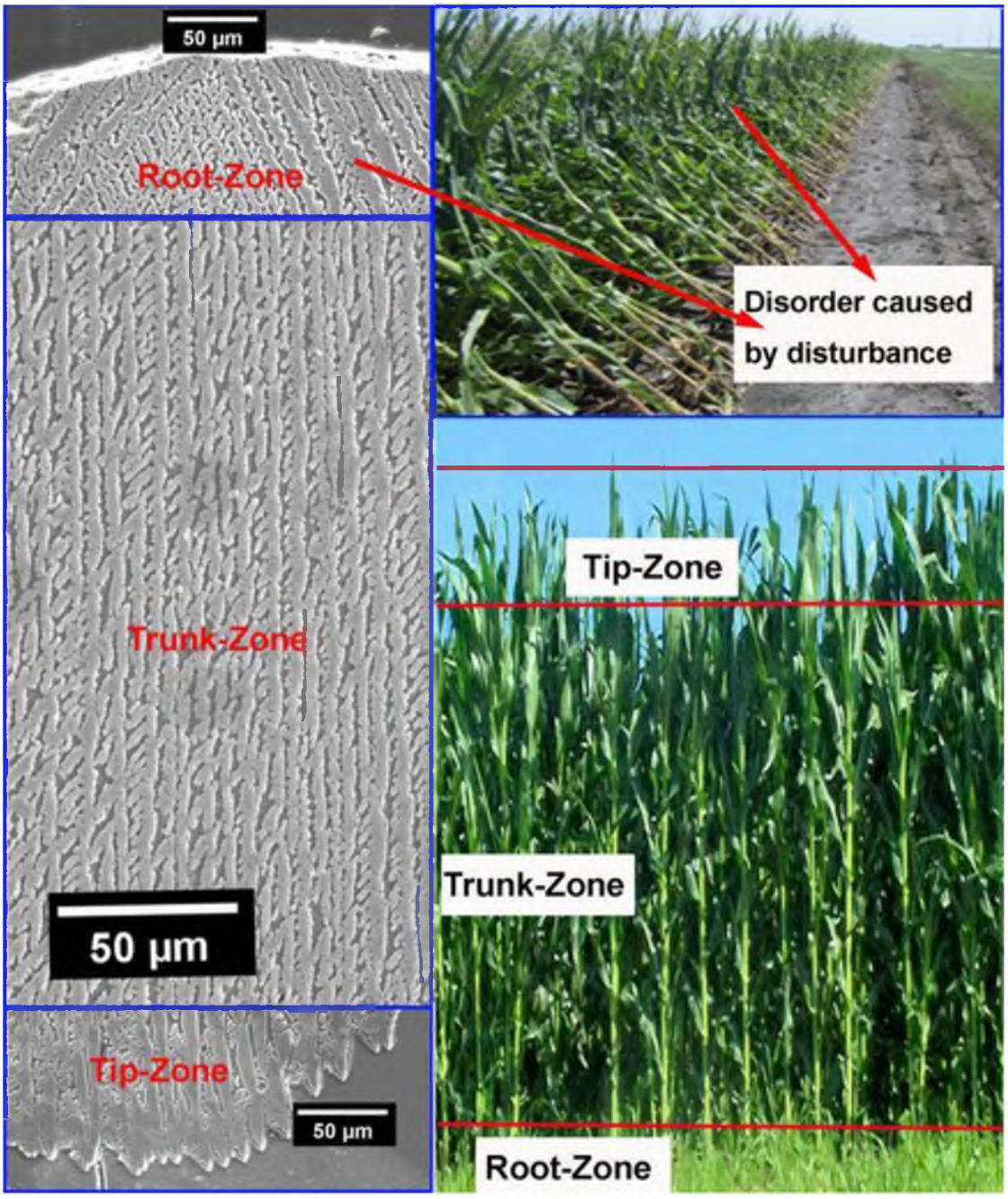

Figure 5.12 The overall structure of a crystallized sample presents an inverse configuration of corn plants.

underneath melt from contacting with air directly; thus, both convection and radiation heat transfer were reduced, leading to a more uniform structure in the second layer, discussed below. The second layer is defined as the Trunk-Zone because of its relatively uniform morphology properties and growth orientation. This property has been shown clearly in Figure 5.8. However, very often we will lose the local uniform orientation at a larger scale but still keep uniform spacing. Figure 5.13 presents another orientation mismatch in a sample that is different from Figure 5.10 and was taken at a lower magnification. Since a local misorientation conflicted with the overall orientation that followed the temperature gradient, and the latter generally does not vary too much, thus such local "wrong" orientations would vanished soon and only occupied a small volume. As can be seen in Figure 5.13, R1 and R2 represent the main growth orientation with R2 slightly shifting away from R1. R3 is almost perpendicular to both R1 and R2. However, even when the growth orientation has changed, the spacing between the crystals from the three regions do not vary significantly; instead, they are very uniform. Because of these properties, the Trunk-Zone is actually more important than the other two zones in this study.

Now comes the third layer, where the heat flow is a little more complicated again because of the existence of the liquid/solid interface. This layer was defined as the Tip-Zone simply because of the dendrite tips, as seen in Figures 5.4 and 5.12c.

A further observation was that in all the samples, the Trunk-Zone dominated the whole sample. For a crystallization time of 3 minutes, the Trunk-Zone had a volume fraction of about 60%, this percentage increased rapidly with increasing time, and it reached more than 95% in the sample S6, which was completely solidified.

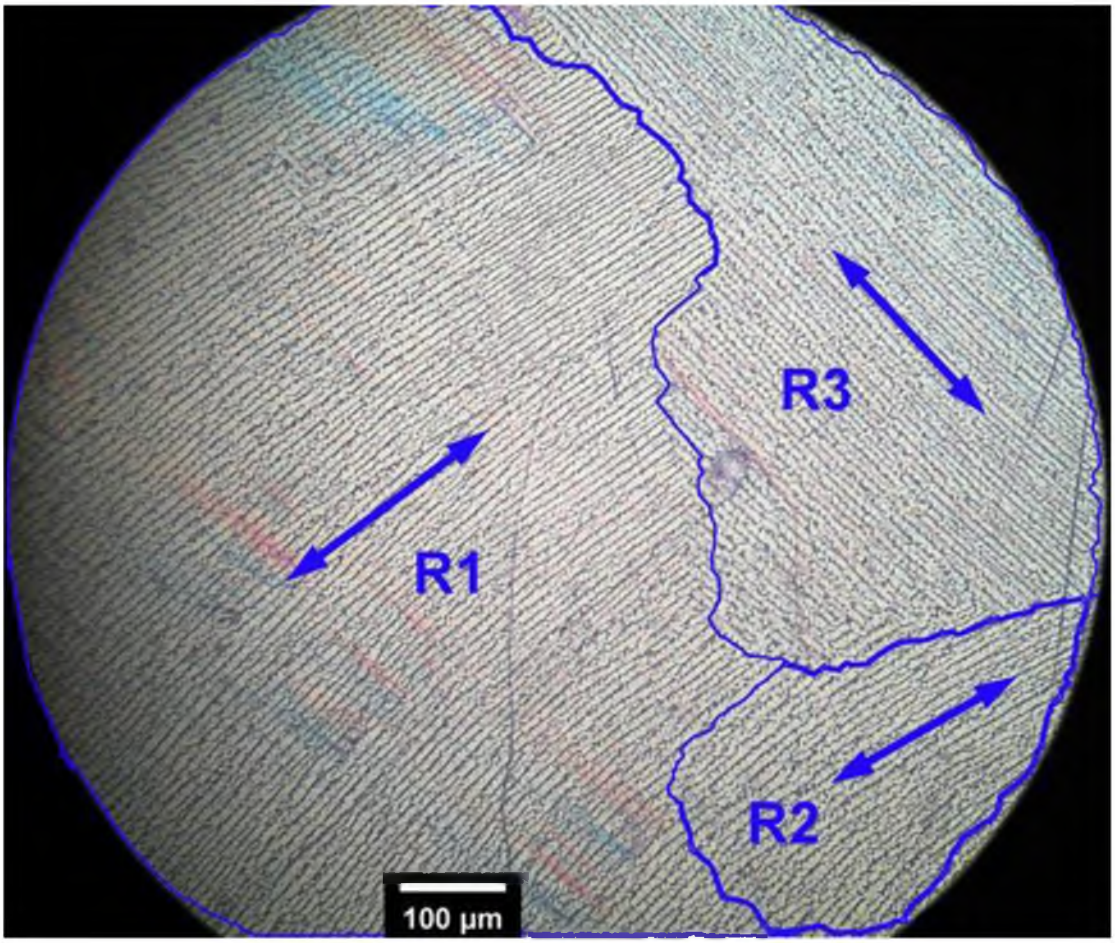

Figure 5.13 A crystal orientation map from the sample S5 showing nonuniform cellular growth orientation but uniform spacing.

With the above explanation, the primary spacing at the Tip-Zone of each sample, hereafter defined as λ_{1tip}, was measured first. To improve the accuracy of measurement, dendrite or cell tips from about 4 to 5 SEM images of the corresponding sample were used as representative samples. Figure 5.14 shows typical tip morphology of the sample S1 and how its average primary spacing was measured. In a similar way, λ_{1tip} of other samples was also measured.

λ_{1tip} only represents a small portion of the overall length of a solidified sample; it is more representative to use the primary spacing within the Trunk-Zone, hereafter defined as λ_{1trunk}. Figure 5.15 shows the microstructures of the Trunk-Zone of samples S2-6. The average spacing λ_{1tip} and λ_{1trunk} with increasing crystallization time are then plotted in Figure 5.16.

From the two plots in Figure 5.16, we can see that both λ_{1tip} and λ_{1trunk} decrease slightly with increasing crystallization time. More specifically, λ_{1tip} drops approximately from 9 to 7.5 μm while λ_{1trunk} drops from 8 to 7 μm. To explain the difference between λ_{1tip} and λ_{1trunk}, it is necessary to introduce some defects that commonly exist in cellular/dendritic growth. These defects are elimination, tip splitting, and growth of tertiary arms [41].

Figure 5.17 illustrates these defects in the tested samples. As can be deduced from Figure 5.17, when dendrites have a large portion of such defects, it results in a difference between λ_{1tip} and λ_{1trunk}. One mechanism to understand these defects is that at the tips, i.e., the growth front, the dendrites are newly forming, the structures are not that stable, and they are not in an equilibrium state with the liquid ahead of them. The higher the temperature gradient in the solid/liquid interface is, the larger the difference will be.

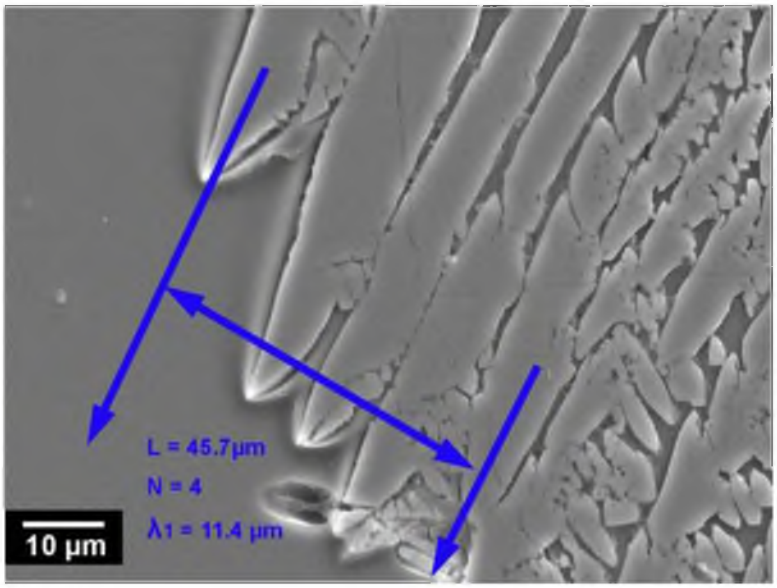

(a)

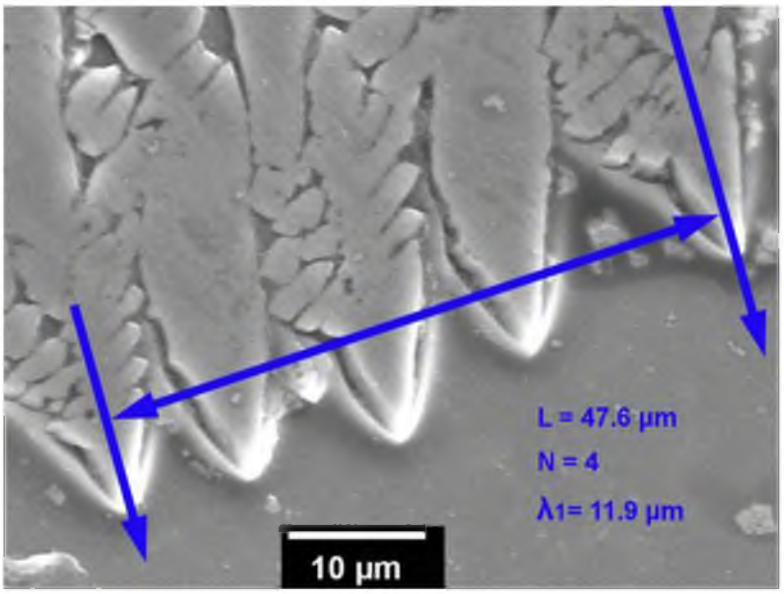

(b)

Figure 5.14 A brief illustration of the measurement of average primary spacing of the sample S1 (t_C = 3 minutes) from growth tips at regions (a), (b), (c), and (d). The average primary spacing was calculated based on the average of the four regions.

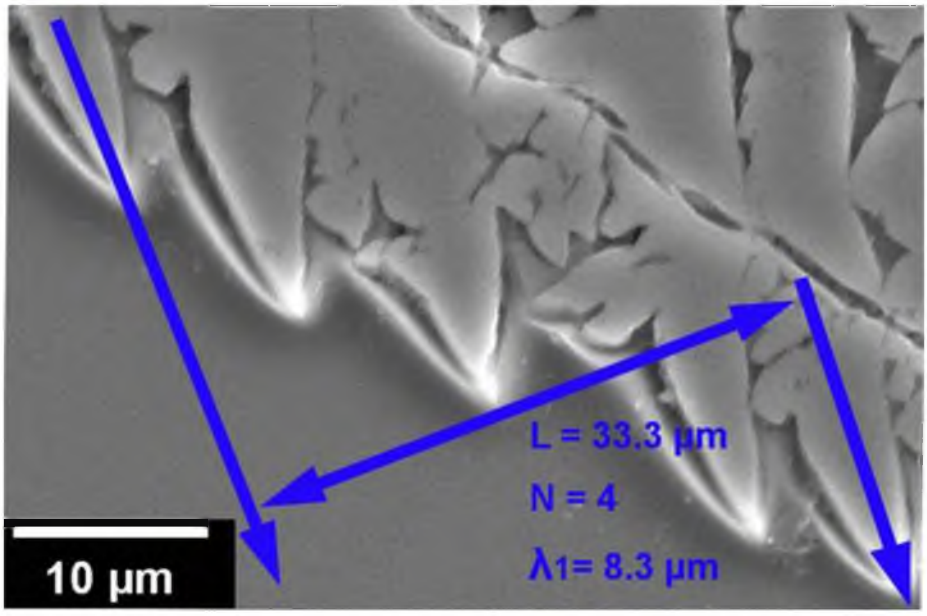

(c)

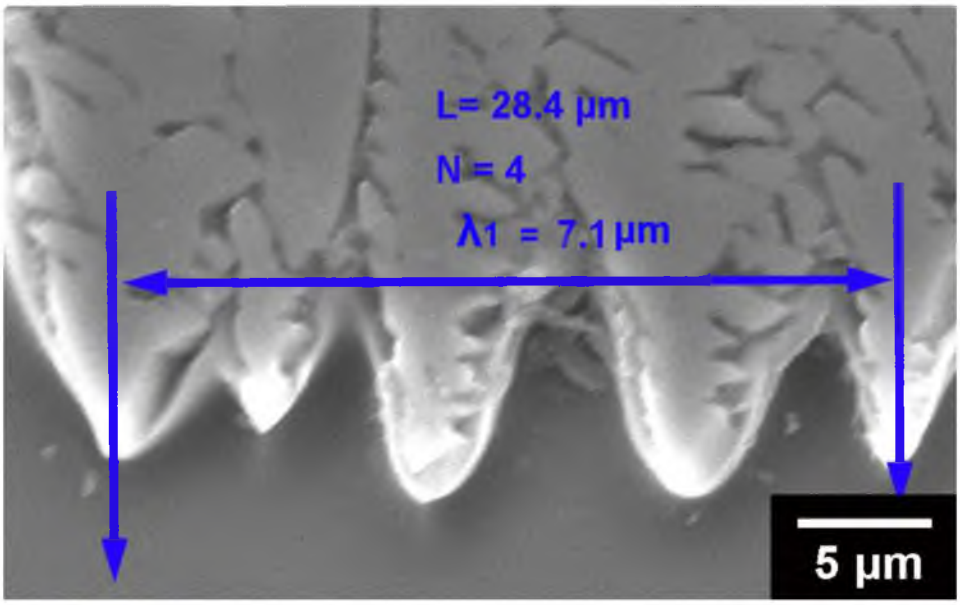

(d)

Figure 5.14 (continued).

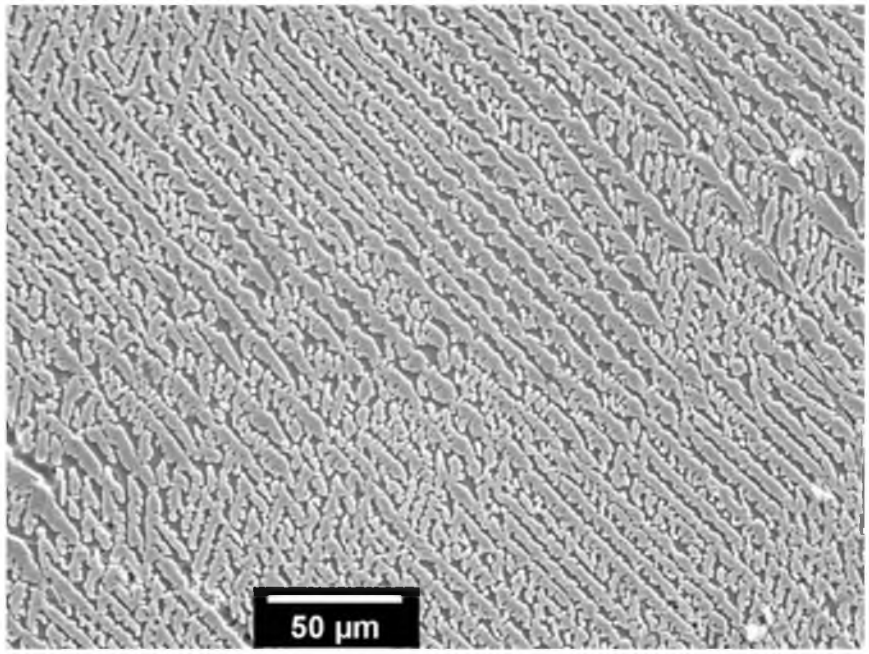

(a)

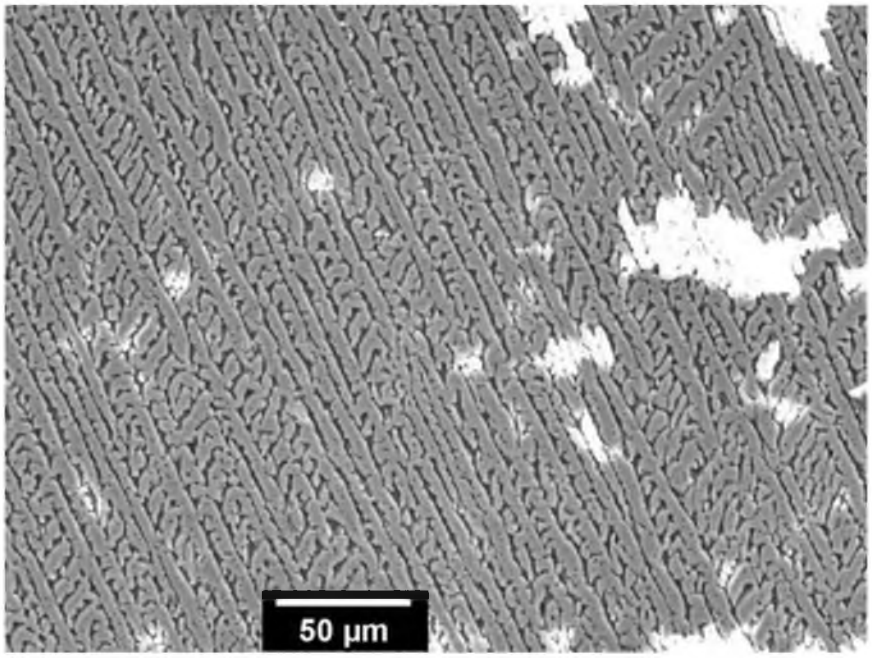

(b)

Figure 5.15 Representative microstructures of samples with a crystallization time of: 3 minutes (a), 5 minutes (b), 11 minutes (c), 15 minutes (d), and 20 minutes (e).

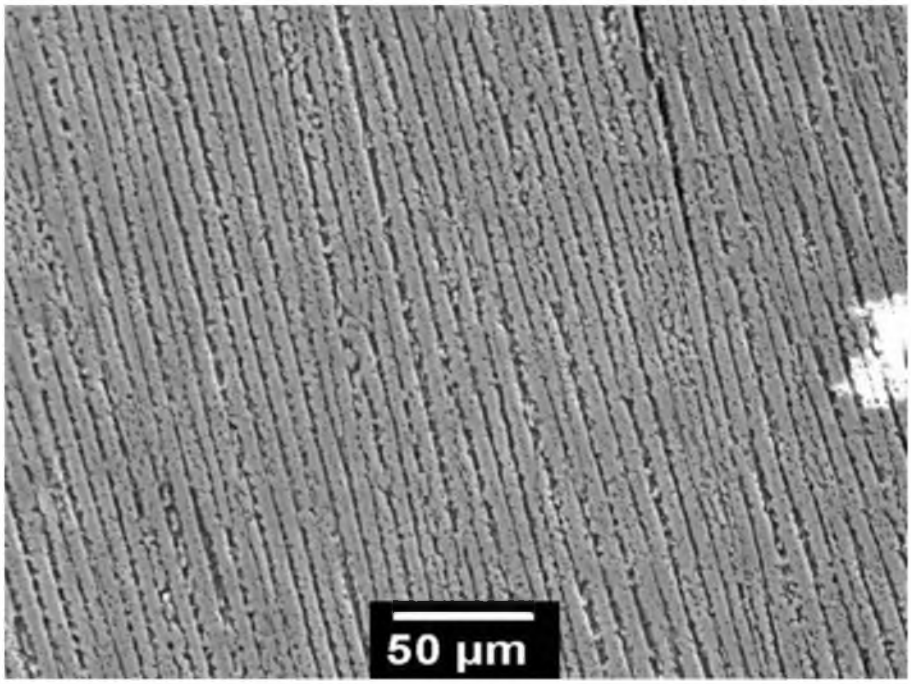

(c)

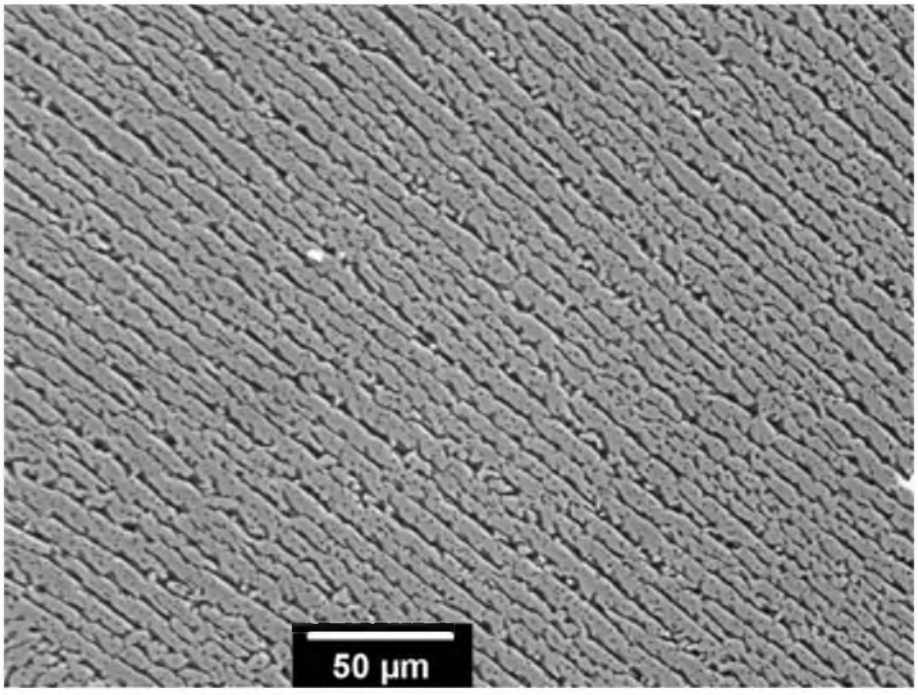

(d)

Figure 5.15 (Continued)

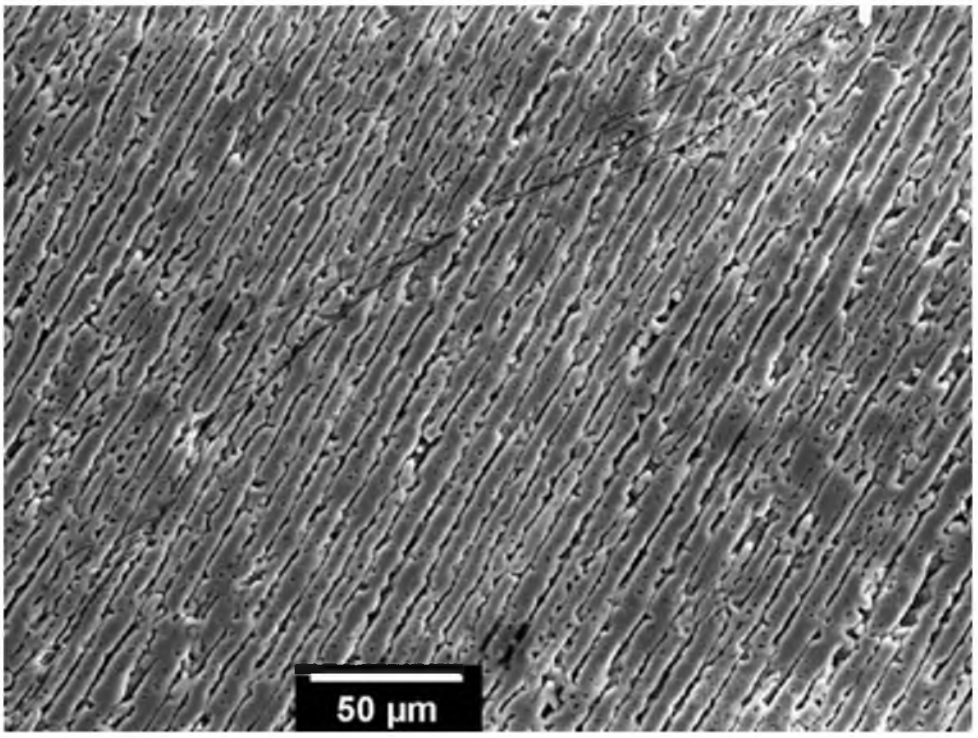

(e)

Figure 5.15 (Continued)

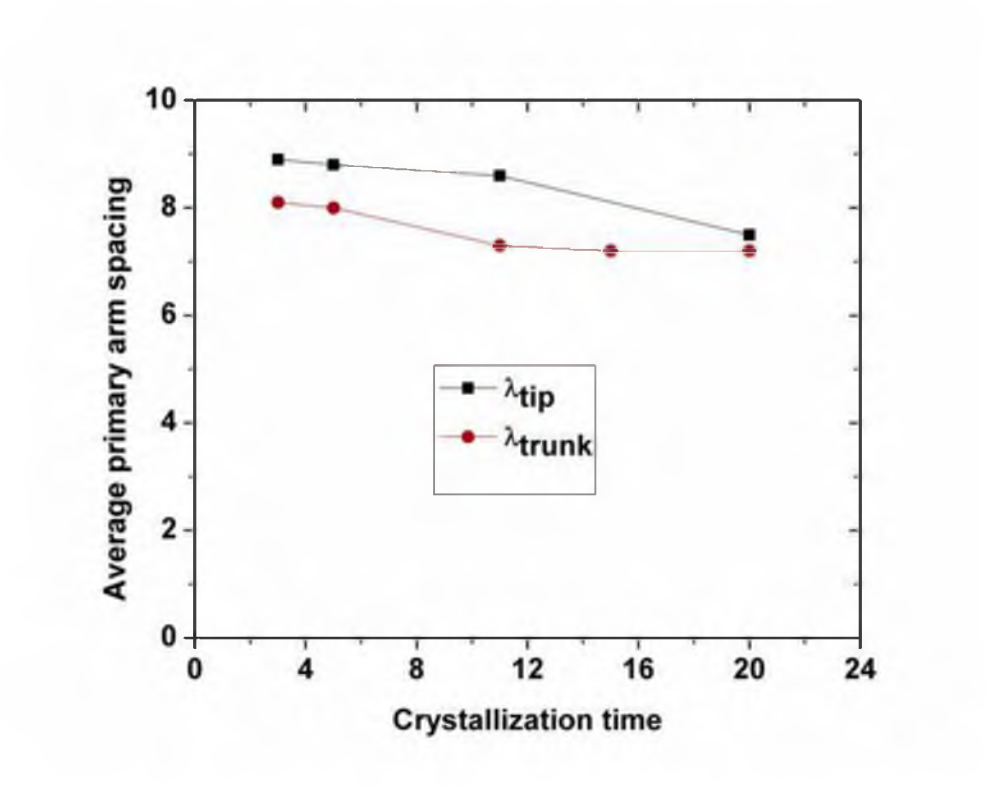

Figure 5.16 Plots of the average primary spacing measured from the Tip-Zone and Trunk-Zone of the samples S2-6 as a function of crystallization time.

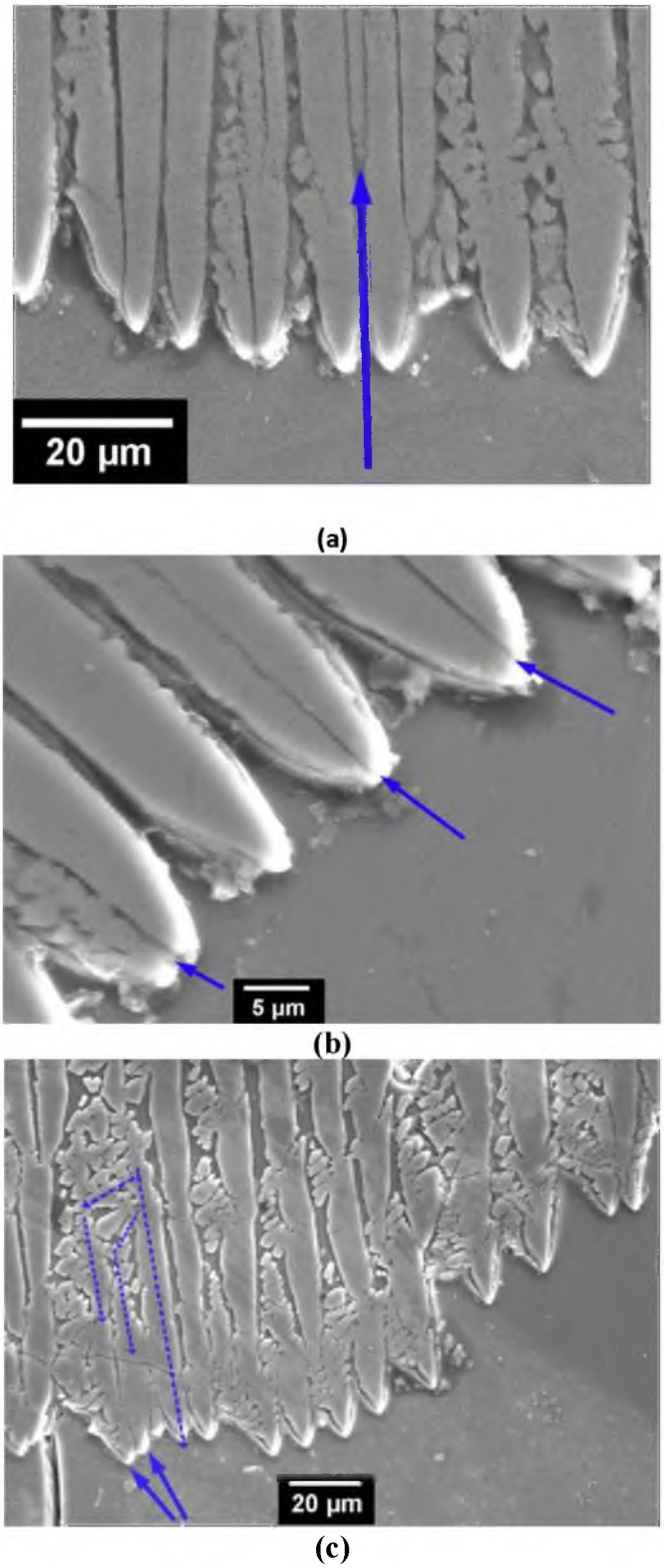

Figure 5.17 Illustration of cellular/dendritic structure defects: elimination (a), tip splitting (b), and growth of tertiary arms (c).

During the remaining crystallization stage, the dendrites adjust themselves to minimizethe difference and eventually reach a more stable state compared with the moment when they just form. Following this reasoning, it is therefore easy to understand why λ_{1trunk} is more close to a constant than λ_{1tip} with increasing crystallization time when the samples have the same initial composition.

Based on the above observation and explanation, it becomes reasonable that the structure of the Trunk-Zone is more suitable to be analyzed than the Tip-Zone as well as the Root-Zone, especially when the Trunk-Zone is the dominant structure in a sample to be measured. In later sections, the default primary spacing will be the average primary spacing of the Trunk-Zone.

5.3.5 Effects of Crystallization Temperature on Primary Spacing

In order to study the effects of crystallization temperature on primary spacing, samples S8-10 were prepared. Figure 5.18 schematically illustrate the appearances of the samples after 5 hours solidification. As can be seen in Figure 5.18a, when crystallization temperature was 750°C, the melt remained a glass phase after the given crystallization time. When the crystallization temperature was 840°C, the sample contained a layer of glass at the bottom that was about one eighth of the total sample volume, as shown in Figure 5.18b. When crystallization temperature was at 880°C, all melt crystallized, as seen in Figure 5.18c. From the previous measurement on growth rate at 980°C, the required time for complete crystallization of the melt and the surrounding temperature should be larger, which means a faster heat loss; therefore, the required crystallization time should be less than 20 minutes at 840°C. However, we still see glass phase even terminated after after 5 hours of crystallization time; this shows that the crystallization

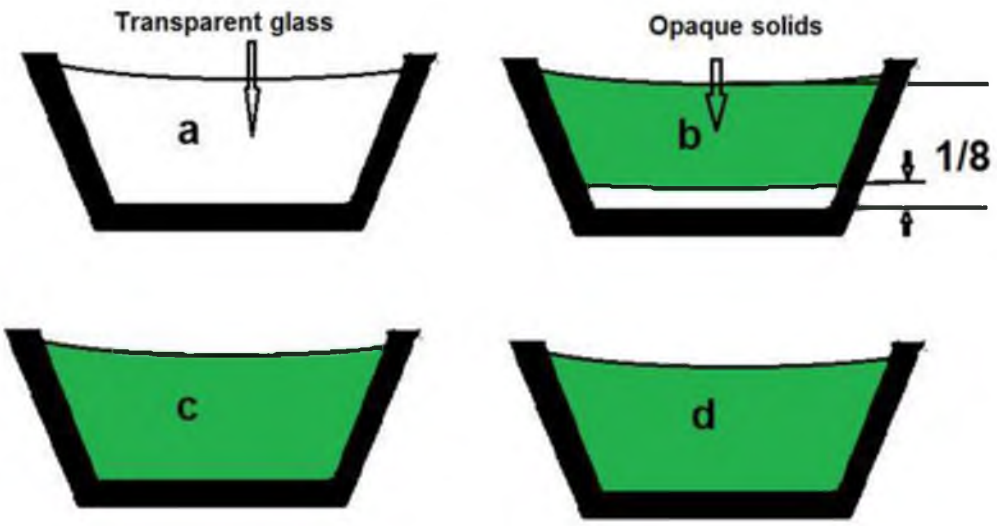

Figure 5.18 Schematic drawings showing the appearances of samples after 5 hours crystallization under a temperature of: 750°C (a), 840°C (b), 880°C (c), and 980°C (d).

had been terminated after some time, and the minimum of a sample that has the same composition is about 20 minutes (Figure 5.18d). By taking the average of 880°C and 840°C, the minimum crystallization temperature is 860°C, which agrees with the XRD results as discussed in Chapter 2.

Then in the next step, the opaque solids at the top part of samples S8-9 were analyzed similar to the previous sections. As expected, these samples also presented cellular/dendritic structures, as shown in Figure 5.19. The primary spacings of these two samples as well as the sample S7, which crystallized at 980°C, are plotted in Figure 5.20.

As shown in Figure 5.20, the primary spacing decreases with decreasing crystallization temperature, which equals an increasing cooling rate. This observation agrees with the conclusion made by Fredriksson in his book [47], where he claims that the higher the cooling rate is, the smaller will be the dendrite spacing.

5.3.6 Effects of B_2O_3 Contents on Primary Spacing

The primary spacings of samples S11-15 which contain different contents of B_2O_3 were measured. Figure 5.21 shows typical structures of these samples.

As seen in Figure 5.21a-c, dendrites are absent from samples S11-13 in which the content of B_2O_3 was no greater than 20 wt.%, leaving pure cellular structure. From 8 to 20 wt.% B_2O_3, the primary spacing increased with the measured values plotted in Figure 5.22.

However, at 35 wt.% of B_2O_3, all cellular structures disappeared, the corresponding structures consisting of a two-layer structure with a semitransparent white layer on top and a transparent glass layer phase at bottom, as shown in Figure 5.23a. Under SEM and optical microscope, it was found that the white layer consisted of a

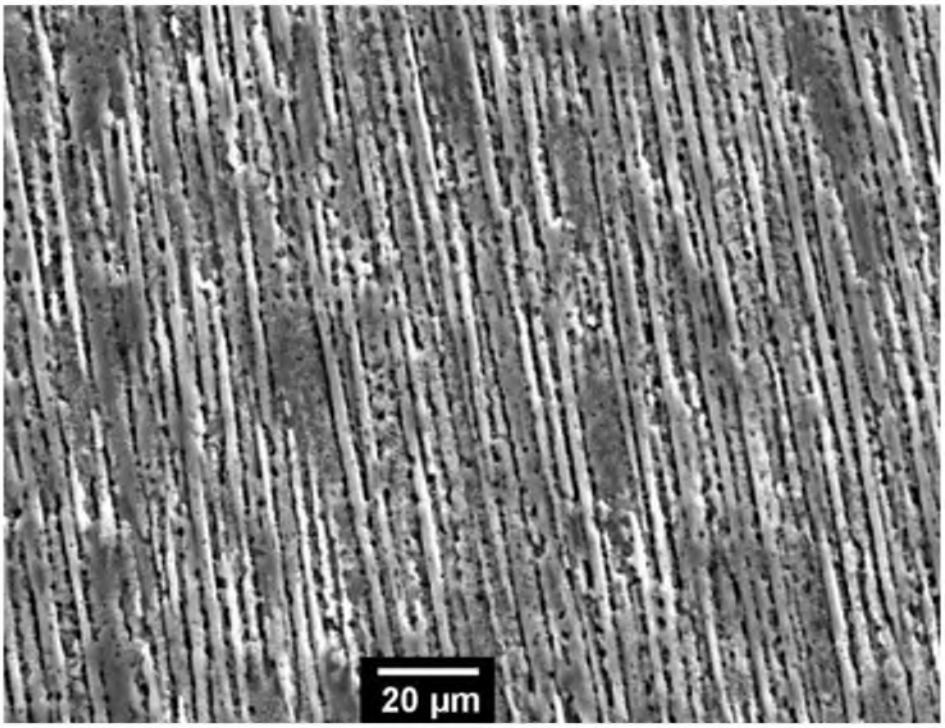

(a)

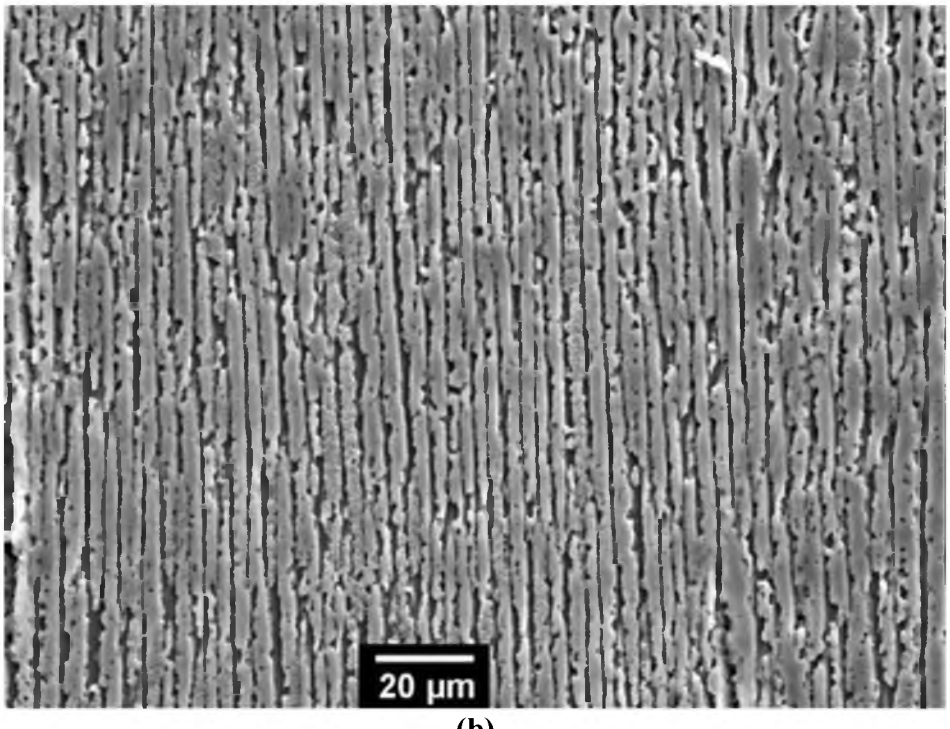

(b)

Figure 5.19 Representative microstructures of samples with a crystallization temperature of: 840 °C(a) and 880°C (b).

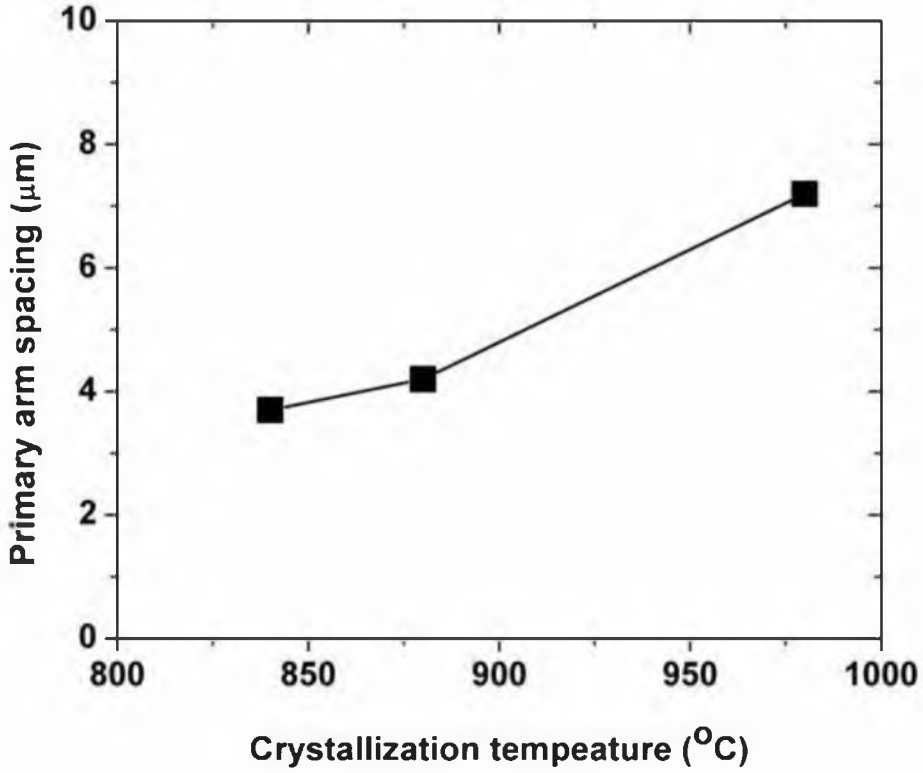

Figure 5.20 Plot of primary arm spacing as a function of crystallization temperature.

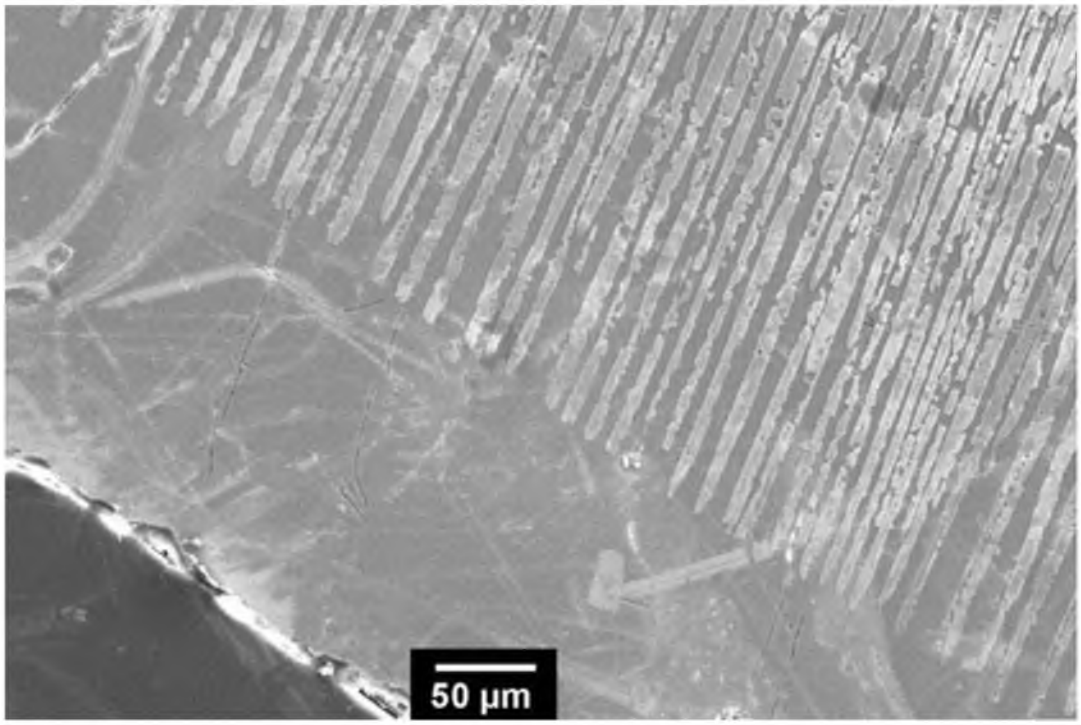

(a)

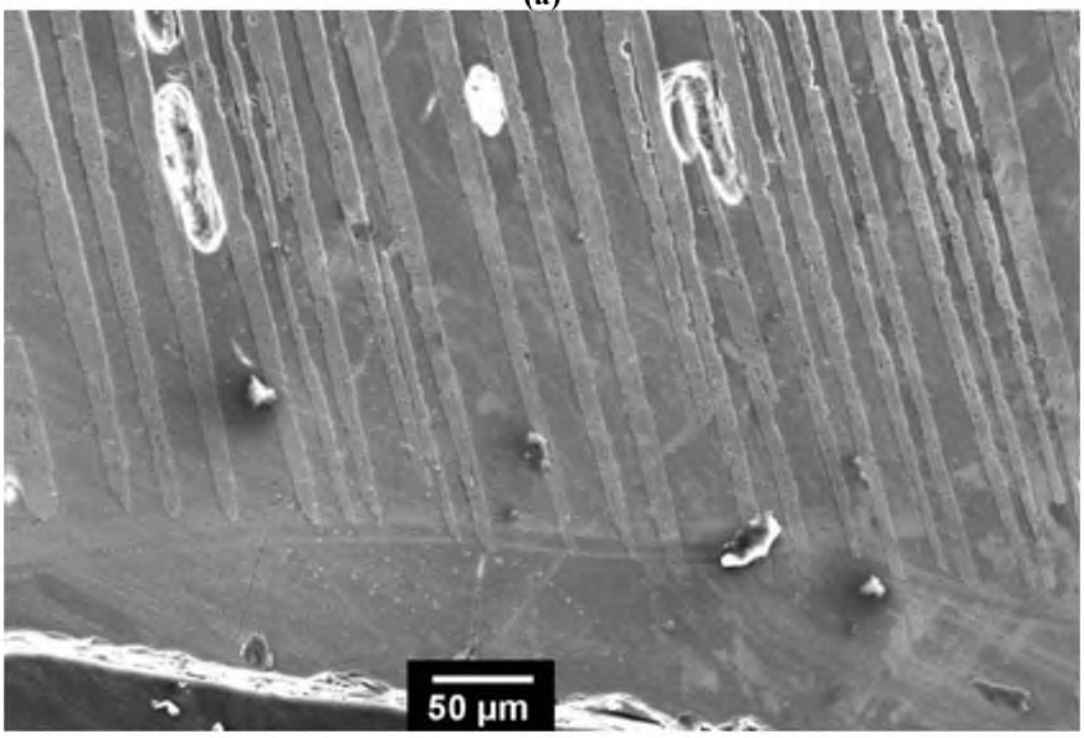

(b)

Figure 5.21Representative microstructures of samples containing: 12 wt.% B_2O_3, (sample S11) (a), 16 wt.% B_2O_3 (sample S12) (b), and 20 wt.% B_2O_3 (sample S13) (c).

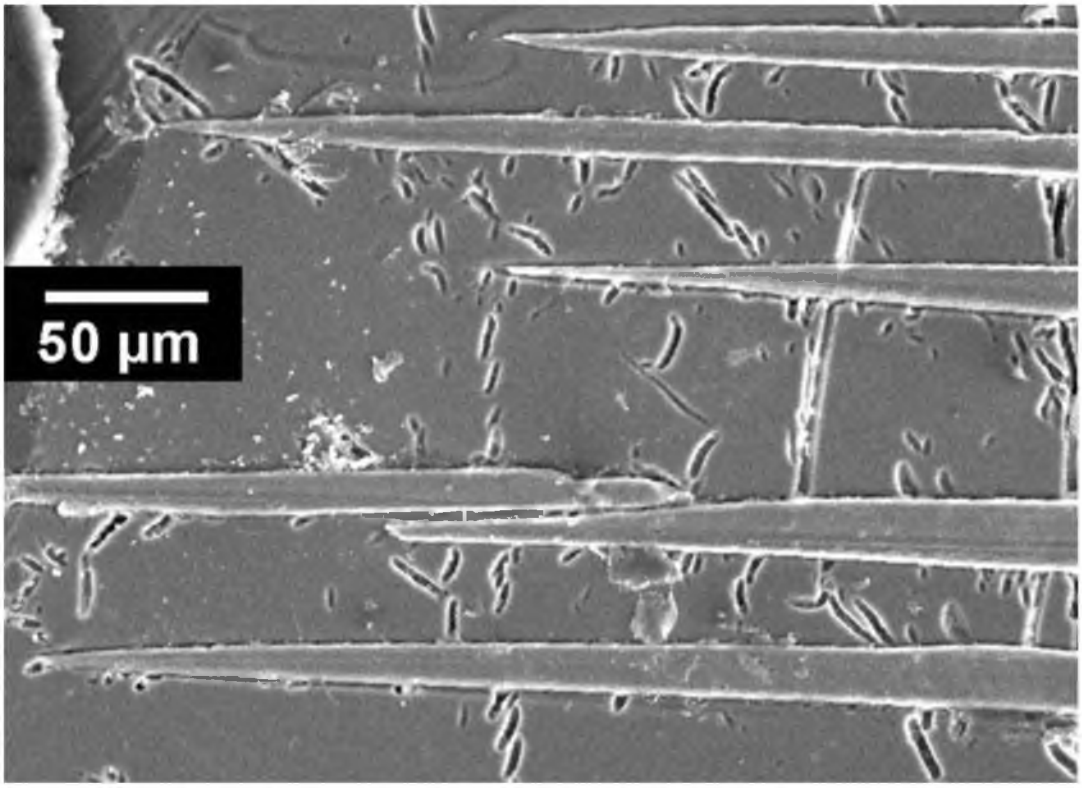

(c)

Figure 5.21(Continued)

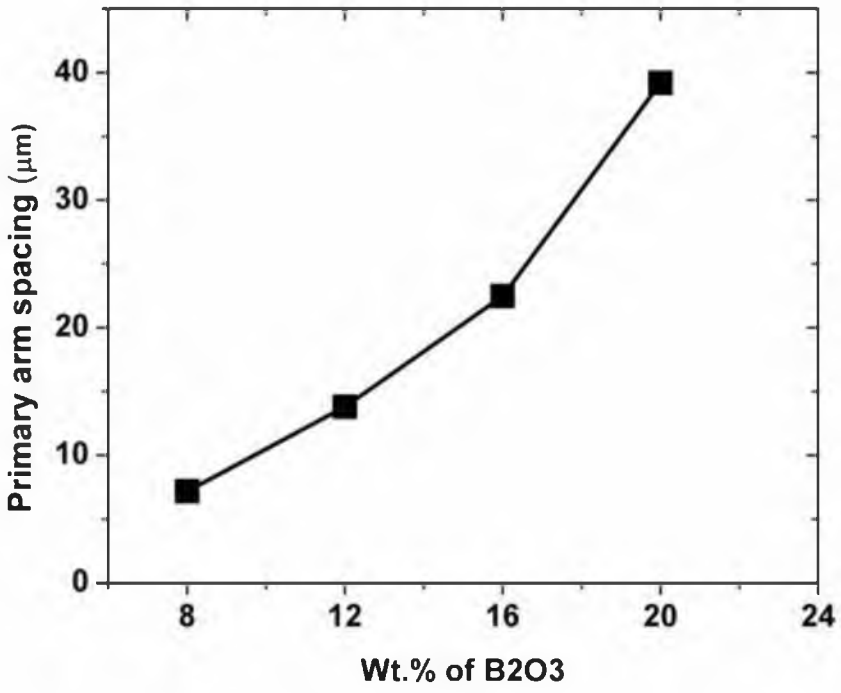

Figure 5.22 Plot of primary spacing as a function of B_2O_3 content.

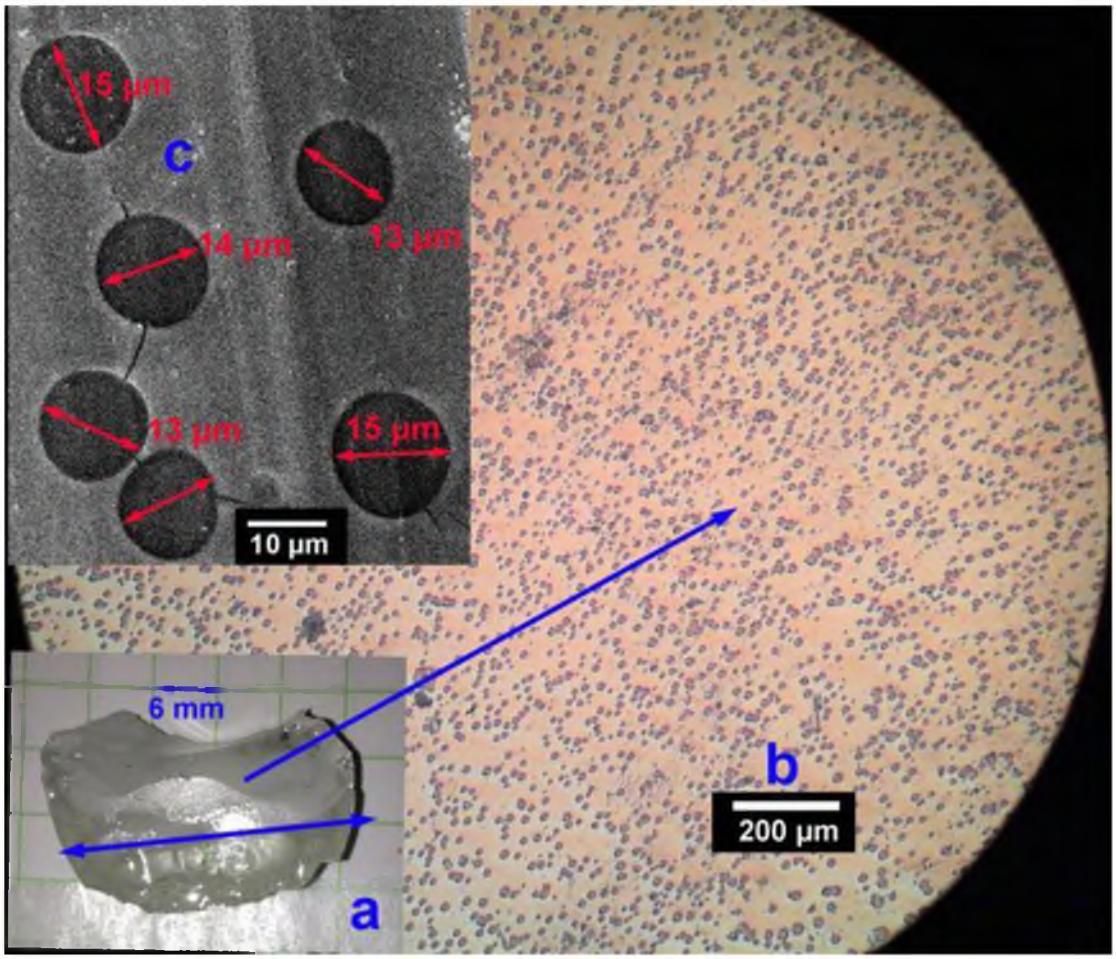

Figure 5.23 Sample (S14) containing 35 wt.% of B_2O_3 shows a two-layer structure after solidification: The top layer is semitransparent while the bottom layer is transparent (a); The top layer has a high density of bubbles with an average diameter of about 14µm (b and c).

major phase that had no distinguishable pattern with a high density of bubbles with an average diameter of about 14 μm, as shown in Figure 5.23b and c. The formation of these bubbles was likely due to a high vapor pressure of B_2O_3 at this high content and high temperature. This type of microstructure indicates that this white layer should be different from previous opaque layers that have cellular and dendritic pattern, and these bubbles imply that this layer more likely consisted of a liquid phase in equilibrium with the bubbles during the solidification process. When such a layer was cooled to room temperature, it should stay in amorphous phase. To confirm this assumption, part of this layer was crushed to fine powder and analyzed by XRD. Figure 5.24 shows the XRD pattern of this layer, indicating that this layer is amorphous.

When the content of B_2O_3 is further increased to 50 wt.%, the mixture formed porous ceramic at 980°C, as shown in Figure 5.25. Apparently, neither of these samples produced acicular particles, as confirmed by aspect ratio analysis. However, this porous ceramic was very light and might find applications where porous structure with light density is preferred.

5.3.7 Dendritic/Cellular Transition

To summarize, two conditions can effectively provide a transition from dendrites to cellular structure. The first is to lower the temperature gradient or cooling rate. This effect is supported through Figures 5.14 and 5.15. The second condition is to increase the content of additives, which can effectively lower the melting point of the liquid but do not co-precipitate with the major phase to a significant extent, and it is B_2O_3 in this study. These effects are compared in Figures 5.15 and 5.21.

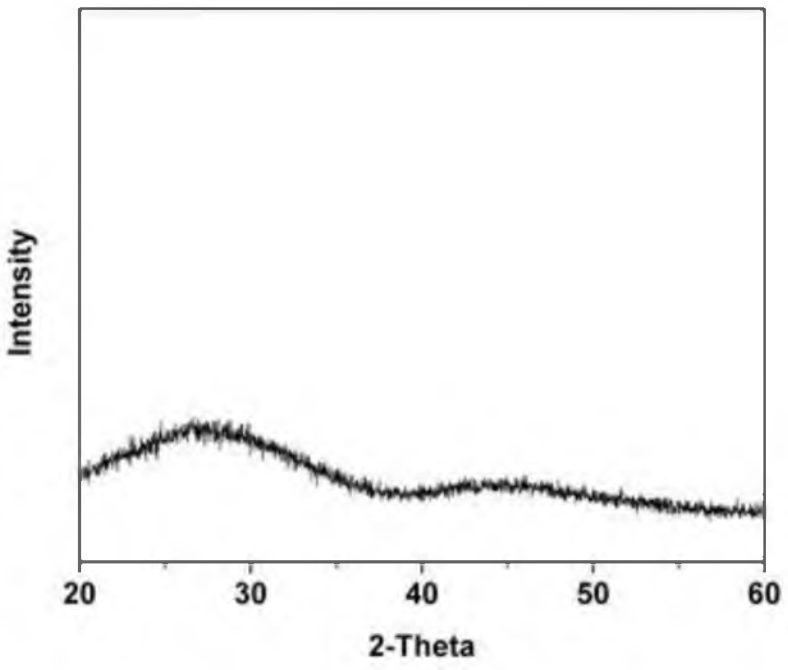

Figure 5.24 XRD pattern of the powder obtained from the top layer as shown in Figure 5.23.

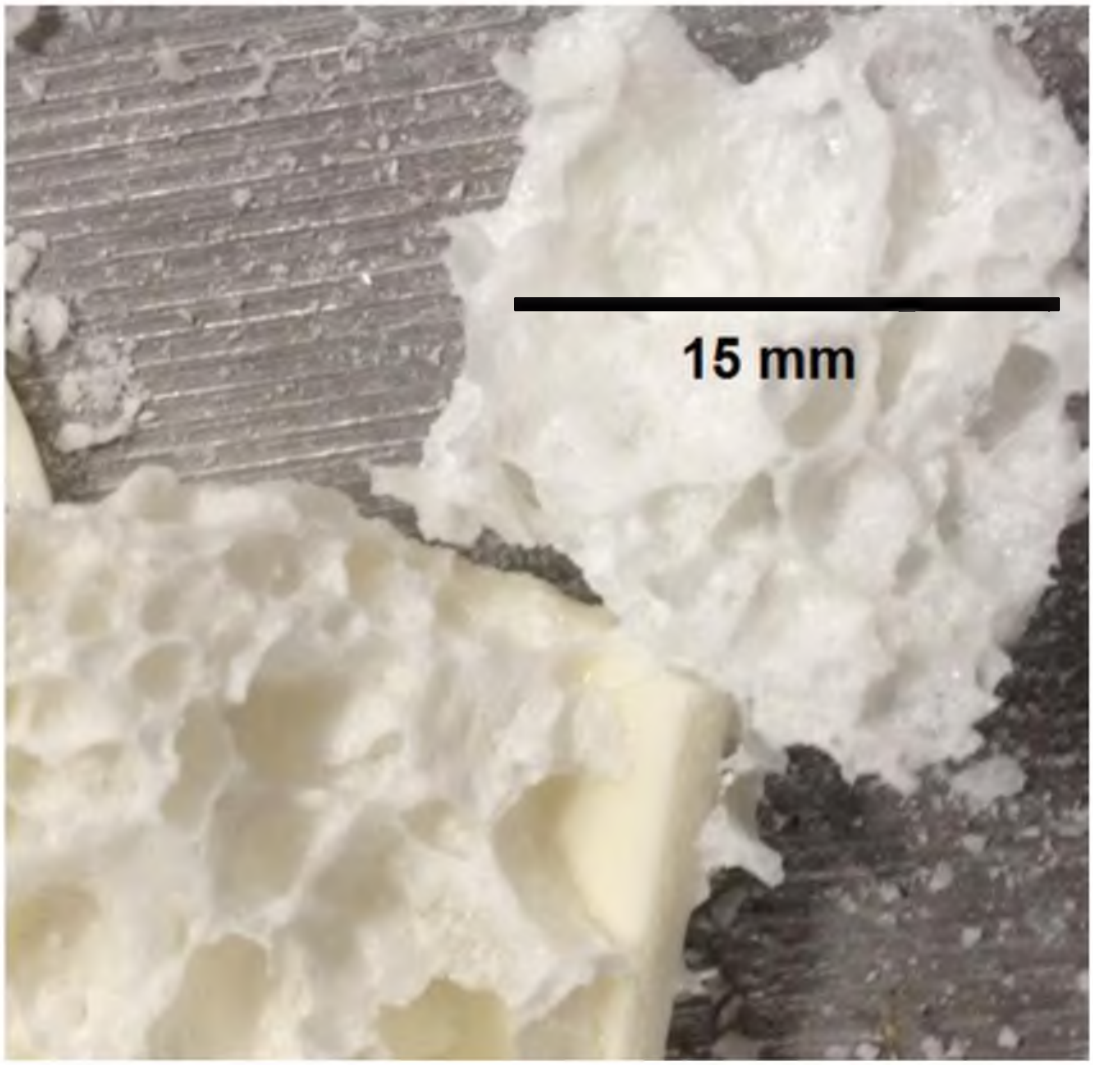

Figure 5.25 A sample (S15) containing 50 wt.% of B_2O_3 shows porous structure after being melted at 980°C. It has a much lower density compared with samples that have a lower B_2O_3 content and were completely solidified.

5.3.8 Effects of Primary Spacing on Aspect Ratios of 2M-Wollastonite Particles

The final goal of studying the cellular/dendritic growth of 2M-wollastonite is to better predict the aspect ratio of wollastonite particles prepared from crystals grown by the Flux Growth process. To achieve this goal, one of the most important parameters is the primary spacing when other conditions are kept the same. Figure 5.26 shows a relationship between mean aspect ratio and primary spacing from different samples.

As can be seen in Figure 5.26, the mean aspect ratio decreases with increasing primary spacing. From Figure 5.22, we have seen that the average primary spacing increases with increasing B_2O_3 content, so it clearly proves that there is strong dependence of mean aspect ratio on primary spacing or B_2O_3 content; which directly implies the importance of modeling the relationship between mean aspect ratio and primary spacing in the following chapter. Note that the mean aspect ratio when primary spacing equals zero is the estimated mean aspect ratio for pure wollastonite particles under an ideal cleavage condition as a reference.

5.4 Conclusions

With the above observation and explanation, the following conclusions are reached.

Cellular and dendritic growths have been clearly observed for the solidification process of a ceramic alloy, the SiO_2-CaO-B_2O_3-Li_2O system, under unsteady-state heat transfer. The cellular/dendritic transition can be affected by crystallization rate and additive contents (B_2O_3 and Li_2O for this study)

The average cellular/dendritic growth rate decreases with decreasing temperature

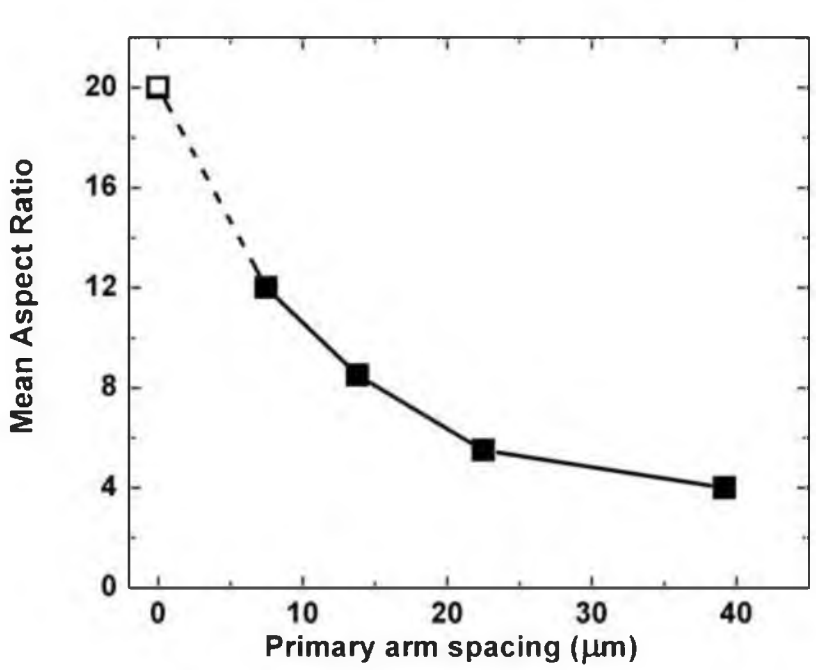

Figure 5.26 Plot of mean aspect ratio as a function of primary spacing. Mean aspect ratio corresponding to primary arm spacing of zero is from natural wollastonite (open rectangle and dashed line).

gradient ahead of the growth front.

The solidified samples present a Root-Trunk-Tip microstructure distribution, where the Root-Zone and Tip-Zone refer to the initial and end stages of the growth process while the Trunk-Zone is located between the other two zones. The Trunk-Zone has the most uniform microstructure and orientation.

The primary spacing measured from the Tip-Zone and Trunk-Zone decreases slightly with decreasing crystallization rate and reach a stable level as a result of the dynamic evolution of a changing concentration of cellular/dendritic growth defects, which are the elimination, tip splitting, and growth of tertiary arms. For approximate calculations and modeling work, the primary spacing can be treated as a constant with changing crystallization rate.

The primary spacing decreases with decreasing crystallization temperature, which represents an increasing cooling rate.

B_2O_3 content can have a significant effect on the primary spacing of this system. It reduces the aspect ratio of the produced wollastonite particles.

CHAPTER 6

CELLULAR AND DENDRITIC GROWTH UNDER UNSTEADY-STATE SOLIDIFICATION: PART II. MODELING OF CELLULAR AND DENDRITIC GROWTH

6.1 Introduction

Modeling of cellular and dendritic growth has been extensively studied for more than forty years [40-45, 52, 54, 56-59]. Various models have been proposed to predict characteristic parameters, including primary arm spacing (λ_1) [40, 56-58], secondary arm spacing (λ_2) [41, 58, 59], dendrite tip radius (ρ) [56-58], and mush zone depth (d) [60, 61] as functions of temperature gradient (G) and growth rate (v). Most of these models found good agreements in metal alloys [49-51, 54] and organic alloys [41, 43, 52].

In this work, we prepared high-aspect-ratio wollastonite particles through flux growth of 2M-wollatonite crystals. This process provides unidirectional solidification of cellular and dendritic forms. Detailed information for the growth conditions and microstructure properties has been discussed in Chapters 4 and 5. When attempting to explain the dendritic growth behavior of 2M-wollastonite, we found a relatively large disagreement with those models mentioned above, as will be discussed subsequently.

Most of the existing models were developed based on steady-state heat flow [56-58]. One of the most important growth parameters is temperature gradient G,

which equals $\frac{dT}{dx}$ for one-dimensional steady-state heat transfer and $\frac{\partial T}{\partial x}$ for multidimensional heat transfer. As will be discussed later, these models generally have the form of $\lambda_1^4 G^2 v = Const.$ However, in 2M-wollastonite growth, we have unsteady-state heat flow, which means not only $\frac{dT}{dx}$ or $\frac{\partial T}{\partial x}$ but also $\frac{\partial T}{\partial t}$ should simultaneously affect the overall cellular and dendritic growth. Meanwhile, there have been a few studies on the prediction of unsteady-state cellular and dendritic growth as well. Among these studies, the one proposed by Bouchard and Kirkaldy [59] is best known, and has been agreed with by Rocha et al. [54]. In these studies, a new parameter, cooling rate, is introduced and defined as Gv [59] or $\dot{T}$ [54]. Even though time factor plays a role in these models, they do not include the true cooling rate, $\frac{\partial T}{\partial t}$, and thus they have limitations to predict 2M-wollastonite growth.

These models are compared in detail in the following section. We will collect the most important parameters that have been considered by these models, and will add factors that are important but are missing in these models. Based on this, we will propose a new model that successfully predicts the cellular and dendritic growth of 2M-wollastonite. The new model covers both steady-state and unsteady-state heat flow, with a particular focus on unsteady-state heat transfer of ceramic alloys under high-temperature conditions. It does not conflict with the other models; on the contrary, it strengthens and extends the applications of the other models to a wider range of systems. The new model reduces to other models under special conditions.

6.2 Existing Models of Primary Arm Spacing

The best known model to characterize primary cellular/dendrite spacing λ_1 is the Hunt model [56].

$$\lambda_1 = 2.83(kD\Delta T_0\Gamma)^{1/4}\nu^{-1/4}G^{-1/2} \qquad \text{(Hunt Model)} \qquad (6.1)$$

where k is the equilibrium solute partition coefficient, D is the liquid solute diffusivity, Γ is the Gibbs Thompson parameter, ΔT_0 is the temperature difference between the solidus and liquidus lines at C_0, which is the composition of starting alloy, ν is the growth rate, and G is the temperature gradient.

Kurz and Fisher [57] have also proposed a similar model as follows.

$$\lambda_1 = 4.3(\frac{D\Delta T_0\Gamma}{k})^{1/4}\nu^{-1/4}G^{-1/2} \qquad \text{(KF model)} \qquad (6.2)$$

The Hunt model has been further modified by Trivedi [58], as shown below

$$\lambda_1 = 2.83(kD\Delta T_0\Gamma L)^{1/4}\nu^{-1/4}G^{-1/2} \qquad \text{(Trivedi Model)} \qquad (6.3)$$

where L is a constant depending on the harmonic of perturbation.

Another important model that covers both unsteady- and steady-state heat flow conditions is suggested by Bouchard and Kirkaldy [59] as follows:

$$\lambda_1 = a_1(\frac{16C_0^{1/2}(G_0\varepsilon)\Gamma D}{k\Delta T_0})^{1/2}(Gv)^{-1/2} \qquad \text{(BK model)} \qquad (6.4)$$

where $G_0\varepsilon$ is a characteristic parameter ($\approx 600\times 6$ K cm^{-1}) and a_1 is the primary dendrite calibrating factor. Gv is defined as the time-dependent cooling rate. This model

has been agreed with by Rocha et al. [54] where Gv is replaced by a new symbol $\dot{T}$.

As can be seen from the above models, they differ from each other slightly by some constants and power exponents. To better expose this property, we can rewrite them in the following way.

$$\lambda_1^4 G^2 v = Const. \qquad \text{(Hunt-KF-Trivedi Model)} \qquad (6.5)$$

Since Equation (6.5) is obeyed by the Hunt model, KF model, and Trivedi model, it can therefore be combined into a single model and is defined as the Hunt-KF-Trivedi model here. This model works for steady-state heat flow condition.

For unsteady-state heat flow, we have

$$\lambda_1^2 Gv = Const. \qquad \text{(BK model)} \qquad (6.6)$$

Equations (6.5) and (6.6) can be further generalized into the following format.

$$\lambda_1^{n'} G^{q'} v^{m'} = Const. \qquad (6.7)$$

where m', n', and q' are some integers no greater than 4.

The above equation covers the existing theories on cellular and dendritic growth under both steady- and unsteady-state heat flow conditions.

However, these models failed to predict the cellular and dendritic growth of 2M-wollastonite crystal from a molten silicate, as will be demonstrated in later sections. After carefully examining the experimental conditions of these models, it is noticed that these models may not be applied to this ceramic alloy under unsteady-state heat transfer for a few observations.

The first observation is the type of phase diagram used for the solidification process. One of the most famous models on describing cellular and dendritic growth is proposed by Hunt, as seen in Equation (6.1), where he studied the Al-Cu binary alloy system. Let us first look at the phase diagram of this alloy system, as provided in Figure 6.1.

As can be seen from Figure 6.1, at low Cu concentration (Cu less than 53 wt.%), Al and Cu form a typical partially miscible binary eutectic phase diagram (hereafter simplified as PM eutectic system). Assume the starting alloy has a composition of C_0, and initially is above the liquidus line. Upon cooling of this alloy, there are two possibilities. Firstly, the alloy solidifies at the fixed given temperature of T_1; thus, the growing cellular or dendritic tips also have a fixed temperature. With the moving of the solidified layer, the growing tips advance to the unsolidified melt, but the tip temperature is assumed the same as T_1; this is the case where Hunt and Fisher developed their models. In these models, a common assumption was made that the dendritic growth that occurred under the usual criterion of maximum velocity or minimum undercooling, which is a constant. However, practically speaking or from the simulated results as provided in later sections, it is unlikely that this temperature remains a constant, as heat will be continuously extracted from the inner melt no matter whether it is solidified or not. Thus, a fixed growing tip temperature conflicts with a changing temperature of the melt ahead of the tip. And meanwhile, in the case of wollastonite solidification, the initial composition of B_2O_3 was 8 wt%; if we neglect the small amount of Li_2O, and considering SiO_2 and CaO in the form of $CaSiO_3$, then B_2O_3 will form a PM eutectic system with $CaSiO_3$; with this initial concentration and this type of phase diagram, the expected solid solution should

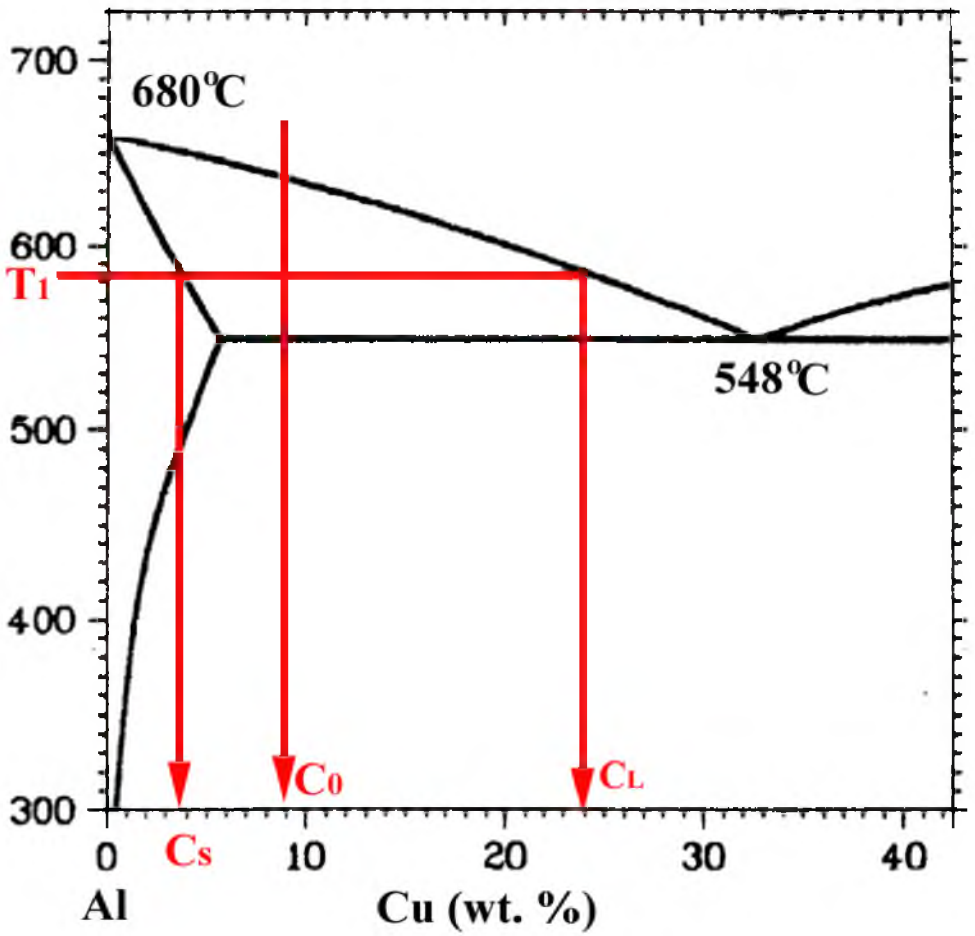

Figure 6.1 Illustrative solidification procedure for a partially miscible binary eutectic system using Al-Cu binary alloy as an example. Modified from reference [62].

contain a considerable amount of B_2O_3, for example 2 wt.%. However, in Table 4.3, we have determined the B_2O_3 content in the wollastonite phase is only 0.29 wt.%, which is far from 8 wt.%. Another way to understand the low concentration of B_2O_3 in $CaSiO_3$ is from the valences of the cations in the two species. B cation is typically in the form of B^{3+}, while Ca and Si in $CaSiO_3$ are commonly Ca^{2+} and Si^{4+}, respectively; therefore, it is unlikely that B can replace Ca and Si in large quantity in the crystal of wollastonite.

Using the same phase diagram, if we consider that the growing tips have a changing temperature following the liquidus line all the way to the eutectic point, obviously from this figure, the boron content in the later solidified wollastonite will be even higher, which also conflicts with the observed low boron contents. Therefore, no matter how the tips grow, this phase diagram seems unsuitable for the case of the wollastonite solidification in the presence of B_2O_3.

However, this problem may be removed by choosing a simple binary eutectic phase diagram. The reason is that since $CaSiO_3$ is a salt, it has ionic bonding. However, B_2O_3 is mainly covalent bonding; therefore, such a liquid mixture when cooled is more likely to be rejected by each other, which is similar to a salt-salt simple binary phase solidification, for example the LiCl-KCl eutectic system, as shown in Figure 6.2.

As you can see from this type of binary phase diagram, at each side of the eutectic point and when temperature is above the eutectic temperature, only one type of pure crystal forms along with a liquid phase. Assume the CaSiO3-B_2O_3 system also follows this type of phase diagram. For an initial B_2O_3 composition as indicated by the arrow in Figure 6.2, when temperature reaches the liquidus line, pure wollastonite will begin to appear in the form of cellular or dendritic structure. With decreasing temperature, the

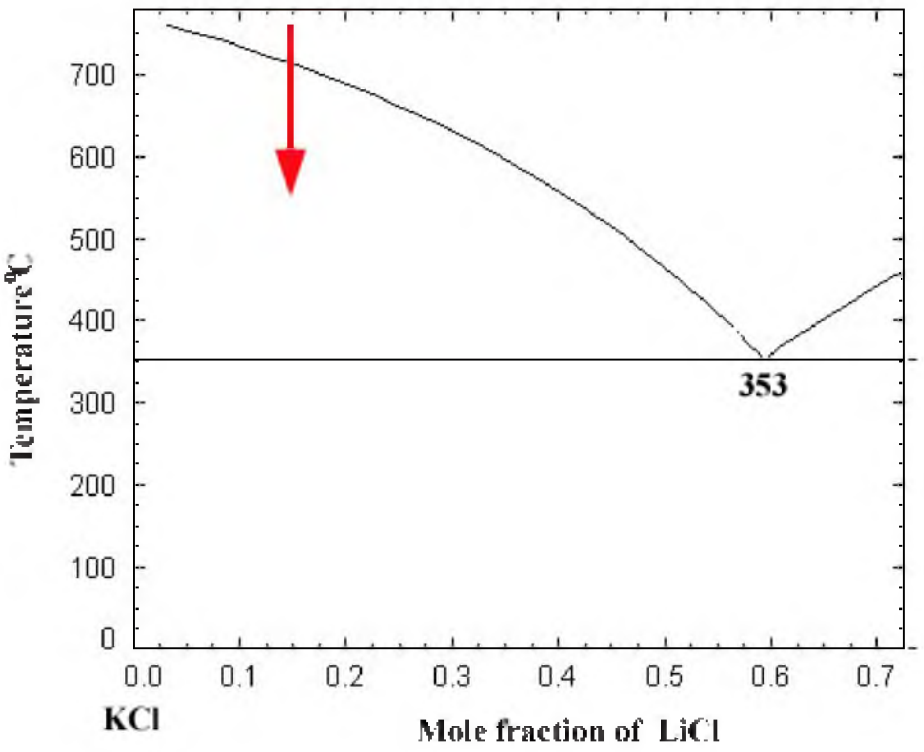

Figure 6.2 Illustrative solidification procedure for a simple binary eutectic system using LiCl-KCl binary system as an example. Modified from reference [63].

cellular or dendritic growth will not stop; instead, it continues to grow following the liquidus line until it reaches the eutectic temperature. If this is responsible for wollastonite solidification, it can lead to two results. Firstly, the major phase, i.e., wollastonite phase, should have very low concentration of B_2O_3; this has been supported by the LA-ICP-MS analysis directly. Secondly, from the B_2O_3 side, with decreasing temperature, the content of B_2O_3 in the liquid mixture that remains as glass phase in the $CaSiO_3$-B_2O_3 system should increase. Thus, at a point when temperature becomes lower but still above the eutectic temperature, even theoretically, $CaSiO_3$ can still be separated from the B_2O_3 or vice versa, so the high content of B_2O_3 can easily change the liquid into a glass, resulting in a low diffusion rate, and the growth of wollastonite crystals will essentially be prohibited from the point of view of kinetic factor; therefore, the expected cellular or dendritic growth may be terminated before its theoretical ending point, which means the remaining melt toward the end of solidification will likely stay in glass phase. Figure 6.3 shows a sample after being solidified for 1 hour at the same temperature with the samples used in Figure 5.6. From that figure, we have seen that all melt solidified within 20 minutes without considering the thickness of a thin glass layer (about one to two hundred micro meters) which is similar to Figure 6.3.

From Figure 6.3, we can clearly see that all the melt has solidified into opaque crystals, except that there is still a thin layer in the form of transparent glass, as shown by G1 to G3. From Figure 5.6, the average growth rate was measured as about 10 μm/s. Assuming the glass was about 200 μm which is close to the value measured by SEM in Figure 4.9, then it should take only 20 seconds to be solidified into a cellular structure. However, it still remained as glass phase even after 40 more minutes. The only reason

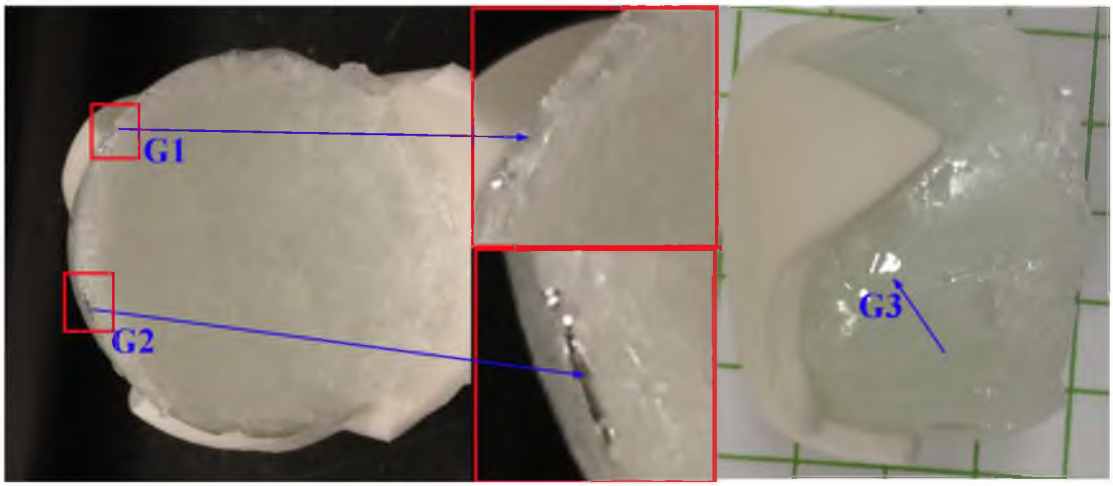

Figure 6.3 A thin glass layer existing in between the solidified melt and the alumina crucible wall after 1 hour solidification implies that the melt at the very end of the solidification stage has much higher B_2O_3 concentration than that of the initial melt. G1 to G3 are the spots where the reflection of light from the thin glass layer is the strongest.

that can explain this observation is that the melt at this point had much higher B_2O_3 concentration than that of the initial melt rejected by wollastonite crystal; such a high B_2O_3 concentration will greatly slow down the crystallization process of the remaining melt even with longer holding time. In our experiments, it was found that a minimum of 5 hours holding time was required to completely transfer this thin glass layer into an opaque crystallized layer. The consequence was that it was much harder to separate the melt from the alumina crucible with 5 hours or longer crystallization time than with less than 1 hour crystallization time. Both this thin glass layer and this particular separation phenomenon have been observed many times during our experiments.

Thus, apparently, our experimental results support the simple binary eutectic phase diagram. Besides, the minor phase has been determined as glass phase, and we all know that glass can have various compositions; this explains why we can form nearly pure wollastonite crystals even though we have relatively high B_2O_3 concentration because of the capability of the glass phase on taking whatever is rejected by the wollastonite crystals to the liquid phases according to Figure 6.2.

If Figure 6.2 is to be used for the phase diagram of the $CaSiO_3$-B_2O_3 system, then both the measured low B_2O_3 concentration and a changing temperature of the growing tips are reasonable and understandable. Meanwhile, a changing tip temperature simultaneously indicates that a varying temperature gradient is preferred rather than a fixed temperature gradient as used for most of the older models (here we assume the tip radius remains the same). With this precondition, we shall now continue to introduce two parameters that we believe are missing from the existing models.

The first missing parameter is the true cooling rate T', where $T' = \frac{\partial T}{\partial t}$. Note

that this cooling rate differs from the cooling rate Gv defined by Bouchard and Kirkaldy, or $\dot{T} = Gv$ by Rocha et al. As briefly compared in Figure 6.4, in the steady-state experiments where the Hunt-KF-Trivedi Model, i.e., Equation (6.5) applies, the growth front that is the location of cellular or dendrite tips is controlled nearly as a constant by specially designed experimental setup; therefore, $\frac{\partial T}{\partial z}$ is independent of time; this explains why this model does not include time factor $\frac{\partial T}{\partial t}$; meanwhile it also implies that this model cannot be applied to unsteady-state systems without appropriate modification. However, in the case of wollastonite growth, $\frac{\partial T}{\partial z}$ is strongly time-dependent, meaning $\frac{\partial T}{\partial t}$ has to be taken into consideration.

The second missing parameter is the reference undercooling temperature ΔT_r. It is defined as

$$\Delta T_r = (T_r - T^*) \tag{6.8}$$

where T^* is the dendrite tip temperature, T_r is the reference temperature. Here we consider two types of references temperature. The first one is T_M, which is the melting point of a pure solvent; in this study, it is the melting point of pure 2M-wollastonite, which has a theoretical T_M of 1544°C; the corresponding reference undercooling is defined as ΔT_r^M. The second type is the liquidus temperature T_L at a given composition; the corresponding reference undercooling is defined as ΔT_r^L In the general models, the

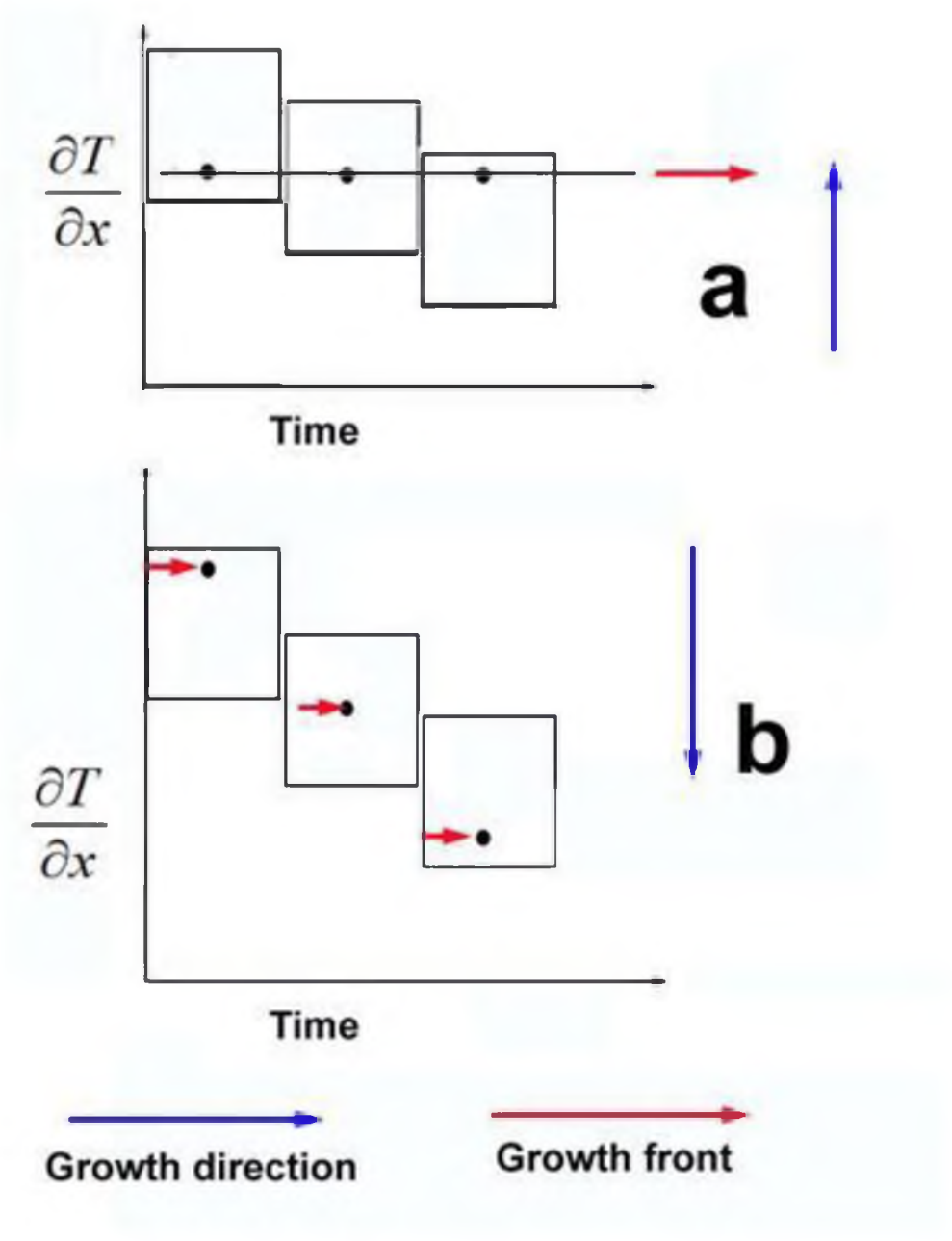

Figure 6.4 An illustration of the growth condition difference between a unidirectional solidification under (a) steady- and (b) unsteady-state heat flow. Dots and horizontal arrows indicate the position of the growing tips. Vertical arrows indicate the growing direction.

undercooling temperature refers to ΔT_0. We shall use Figure 6.2 to better explain the difference among these temperatures and undercooling temperatures.

In Figure 6.5, ΔT_0 and $\Delta T'$ have been defined by Hunt [56] and Fisher [57]. The reference undercooling temperature ΔT_r has not been used in the above existing models and is introduced in this study; it plays a critical role for the modeling of this work. The reasoning goes as follows: in the Hunt-KF-Trivedi Model, the systems are under steady-state heat transfer, the temperature gradient is maintained constant; thus, the cellular/dendrite tip temperature T^* is also a constant. Since T_S and T_L, the solidus and liquidus temperature at the given starting composition, respectively, are also constants, not only ΔT_0 but also $\Delta T'$ and ΔT_r are constants. In our study, we found that T^* is not a constant; instead it changes with time; therefore, all the four undercooling temperatures except ΔT_0 are time-dependent, meaning they cannot be excluded from a suitable model. Since T_{M} or T_L in this study is much easier to obtain than T_S, we prefer to use either ΔT_r^M or ΔT_r^L rather than $\Delta T'$ to express the new model. In the new model, we shall consider the two parameters missing or neglected in the existing models. Based on the above explanations, we propose a new model as shown below.

$$\lambda_1 = c\left(\frac{kD\Delta T_0 \Gamma L}{\Delta T_r}\right)^{n/4} \nu^{-p/4} \left(|G|/|T'|\right)^{-q/4} \tag{6.9}$$

or

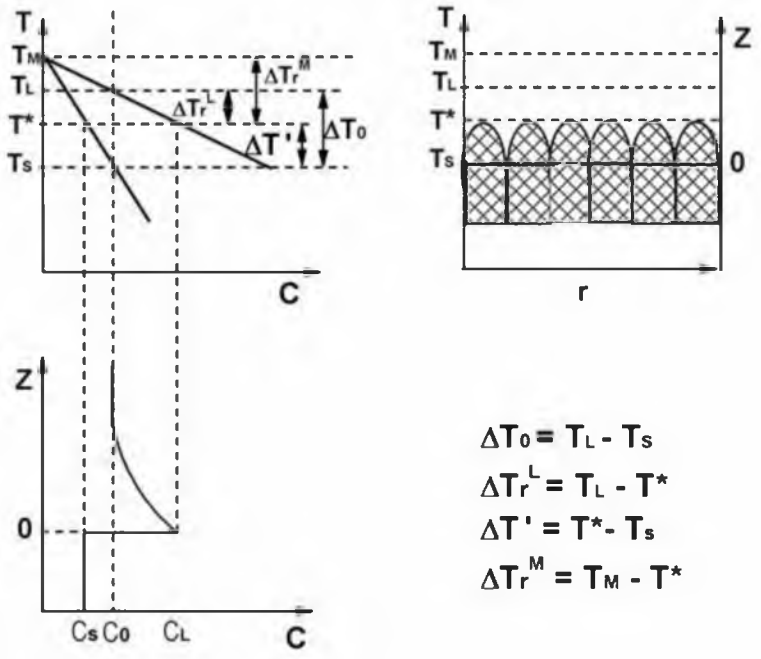

Figure 6.5 Definitions of various temperatures and undercooling temperatures of a melt having unidirectional cellular and dendritic growth. Modified from reference [57].

$$\lambda_1 = c(\frac{kD\Delta T_0 \Gamma L}{\Delta T_r})^{n/4} v^{-p/4} (\frac{|\partial T / \partial z|}{|\partial T / \partial t|})^{-q/4} \quad (6.10)$$

where c is the calibrating constant, k is the equilibrium solute partition coefficient, D is the liquid solute diffusivity, Γ is the Gibbs Thompson parameter, and ΔT_0 is the temperature difference between the solidus and liquidus lines at the starting composition. ΔT_r is the reference undercooling temperature, which has been defined in Equation (6.8). For steady-state heat flow where the stability criterion proposed by Langer and Müller-Krumbhaar [64] applies, that is that the dendrite growth occurs at the maximum velocity or minimum undercooling, which simply means tip temperature T^* equals the liquidus temperature T_L, ΔT_r is thus a constant, as shown in Figure 6.5. For unsteady-state heat flow, the growth condition is changing; it is unlikely that the dendrite growth can always grow at the maximum velocity; ΔT_r is more likely to change with temperature gradient and cooling rate; therefore, we suggest to include this term in the model to be proposed. v is the growth rate, G is the temperature gradient $\frac{\partial T}{\partial z}$. T' is the true cooling rate $\frac{\partial T}{\partial t}$. Because G can have positive or negative values based on the selected coordinates set up. T' is always negative for a cooling process; thus, we take the absolute values of these two parameters for convenience. The ratio of $\frac{|\partial T / \partial z|}{|\partial T / \partial t|}$ can be understood as how temperature gradient can be affected by cooling rate for an unsteady-state heat flow system. For steady-state heat flow, temperature has no time-dependence; thus, $\frac{\partial T}{\partial t}$ is removed from Equations (6.9) or (6.10). n, q, and p are some

integers with the following suggested values:

$$n, p, q = 0, 1, 2, 3, 4. \tag{6.11}$$

Rearranging Equation (6.9) by moving the constants to one side, we have

$$\lambda_1 v^{p/4} (G / T')^{q/4} \Delta T_r^{n/4} = Const. \tag{6.12}$$

Now we examine some special combinations of p, q, and n.

Case 1: Under steady-state heat transfer, ΔT_r is a constant; thus, it goes to the *Const.* part. Since under this condition G has no time dependence, T' is removed; when $p = 1$, $q = 2$, we have

$$\lambda_1^4 G^2 v = Const. \tag{6.13}$$

This new model reduces to the Hunt-KF-Trivedi model, as seen in Equation (6.5).

Case 2: Under steady- or unsteady-state heat transfer where ΔT_r being a constant still applies and no cooling rate in the form of $\frac{\partial T}{\partial t}$ is considered, when $p = 2$, $q = 2$, we have

$$\lambda_1^2 G v = Const. \tag{6.14}$$

The new model reduces to the BK model, as seen in Equation (6.6).

Now we examine the validity of the new model to a ceramic alloy that has a growth behavior that could not been explained by the order models. Based on the

experimental data we obtained, we proved that a combination of $p=1$, $q=3$, and $n=1$ yields a good agreement with the cellular and dendritic growth of 2M-wollastonite. In the following few sections, we will demonstrate how these values, especially temperature gradient and true cooling rate, are determined.

6.3 Simulation of Unsteady-state Heat Transfer

6.3.1 Geometry Parameters

Figure 6.6 shows the geometry of the heat transfer system. Two types of crucibles of different shapes and dimensions were used in this experiment: cylindrical crucibles (Figure 6.6a) and high form crucibles (truncated-cone shape, Figure 6.6b). The latter has a volume capacity of about 3 times larger than the former. Right below the crucible in each system is an insulating brick that is placed on top of the bottom furnace wall. Since the angle between the side wall of the truncated-cone shape crucible and the vertical direction is very small and close to a cylindrical shape, a cylindrical coordinate is selected for both geometries. By choosing the center of interface between the top melt surface and air as the origin, the dimensions of crucibles, melt, and insulating brick are listed in Tables 6.1 and 6.2. Since the size of the muffle furnace is much larger than the crucible-melt system, its wall temperature does not change significantly with time and thus, it can be treated as a constant during the cooling stage.

6.3.2 Mathematical Calculations

Since cylindrical coordinate is selected above to represent the system geometry, the general heat transfer formula for the melt-crucible-furnace wall (hereafter defined as

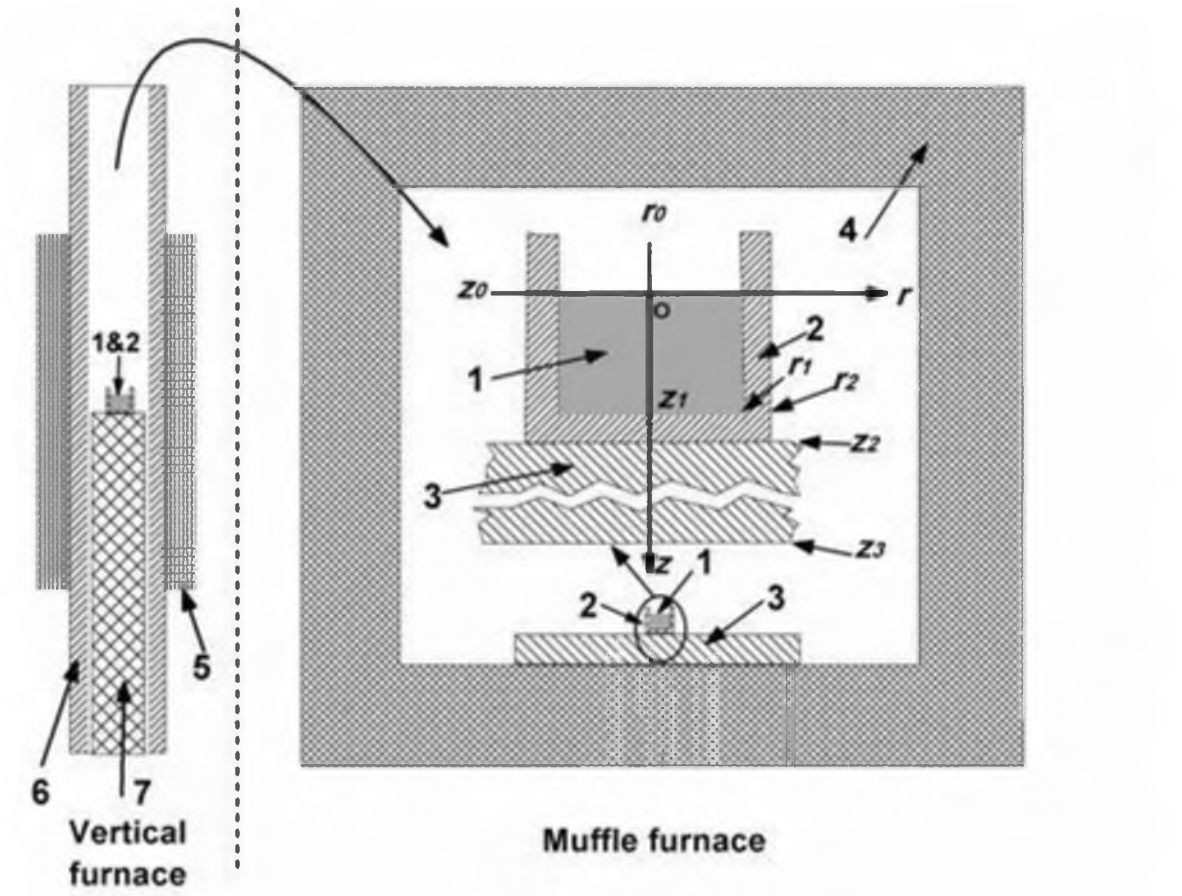

(a)

Figure 6.6 Geometry of the melt-crucible-furnace wall system (MCF system) used in this study: (a) a cylindrical crucible is used and (b) a truncated-cone shape crucible is used. Marked numbers stand for: (1) melt, (2) alumina crucible wall, (3) insulating brick, (4) furnace wall, (5) vertical furnace body, (6) alumina tube, (7) ceramic support.

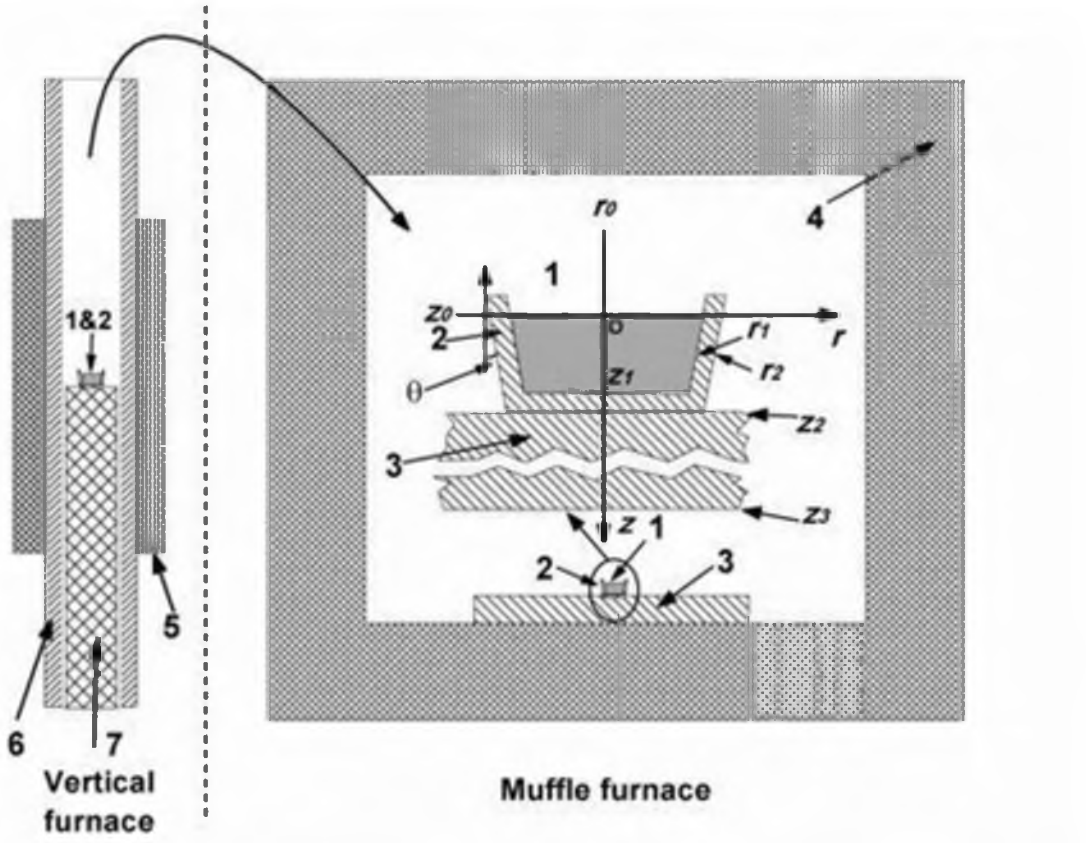

(b)

Figure 6.6 (Continued

Table 6.1 Parameters for temperature simulation of melt in the cylindrical crucible.

Parameter	Definition	Value	Unit	Comments
z_0	Melt-air interface (also called top-melt surface)	0	mm	M
z_1	Melt-bottom crucible wall interface	9	mm	M
z_2	Bottom crucible wall-insulating brick interface	12	mm	M
z_3	Insulating brick-muffle furnace wall interface	52	mm	M
r_1	Melt-side crucible wall interface	9.5	mm	M
r_2	Side crucible wall-air interface	12.5	mm	M
$Th_{crucible}$	Thickness of crucible wall	3	mm	M
Th_{ib}	Thickness of insulating brick	40	mm	M
Ts_0	Initial melt temperature, at which the oxides mixture were melted	1693	K	M
Ts_0'	Adjusted initial melt temperature which considers the temperature drop during transfer process	1682	K	C
T_b	Bulk temperature of the muffle furnace	1253	K	M
T_f	Film temperature or mean temperature at which the properties of air and radiation are evaluated.	1468	K	C
h_{c1}	Convective heat transfer coefficients at z_0	1.29×10^{-5}	W/mm.K	C
h_{c2}	Convective heat transfer coefficients at r_2	1.78×10^{-5}	W/mm.K	C
h_{r1}	Radiation heat transfer coefficients at z_0	1.53×10^{-4}	W/mm.K	C
hr_2	Radiation heat transfer coefficients at r_2	7.26×10^{-4}	W/mm.K	C
h_{1all}	Overall heat transfer coefficients at z_0	8.31×10^{-5}	W/mm.K	C
h_{2all}	Overall heat transfer coefficients at r_2	4.28×10^{-5}	W/mm.K	C
h_{3all}	Overall heat transfer coefficients at z_1	4.38×10^{-6}	W/mm.K	C
Symbols for Comments: M = Measured, C = Calculated, E = Estimated.				

Table 6.1 (Continued)

Parameter	Definition	Value	Unit	Comments
σ	Boltzmann's constant	5.73×10^{-14}	J/mm^2.sec.K	Known
ε_{melt}	Emissivity of melt at z_0	0.8	None	E
ε_{sw}	Emissivity of alumina crucible at r_2	0.5	None	E
η_{melt}	Efficiency of radiation heat transfer at z_0, it considers geometry relationship between the melt-air interface and the surrounding environment	0.33	None	E
η_{sw}	Efficiency of radiation heat transfer at r_2, it considers geometry relationship between the side crucible wall-air interface and the surrounding environment	0.25	None	E
ρ_{melt}	Density of melt	2.7×10^{-3}	g/mm^3	M
k_{melt}	Thermal conductivity of melt	1.2×10^{-3}	W/mm.K	E
Cp_{melt}	Heat capacity of melt	1.27	J/g.K	C
$\rho_{crucible}$	Density of alumina crucible	3.8×10^{-3}	g/mm^3	E
$k_{crucible}$	Thermal conductivity of alumina crucible	5×10^{-3}	W/mm.K	C
$Cp_{crucible}$	Heat capacity of alumina crucible	1.29	J/g.K	C
ρ_{ib}	Density of insulating brick	6.04×10^{-3}	g/mm^3	M
k_{ib}	Thermal conductivity of insulating brick	3.5×10^{-4}	W/mm.K	E
Cp_{ib}	Heat capacity of insulating brick	1.07	J/g.K	E
Errorf	Calibrating factor to minimize the difference between simulated and measured temperature resulted by the overall error of other parameters, it has a range of -1 to 1.	0.5	None	M
Symbols for Comments: M = Measured, C = Calculated, E = Estimated.				

Table 6.2 Parameters for temperature simulation of melt in the truncated-cone-shape crucible

Parameter	Definition	Value	Unit	Comments
z_0	Melt-air interface (also called top-melt surface)	0	mm	M
z_1	Melt-bottom crucible wall interface	12.5	mm	M
z_2	Bottom crucible wall-insulating brick interface	15.5	mm	M
z_3	Insulating brick-muffle furnace wall interface	55.5	mm	M
r_1	Melt-side crucible wall interface at half melt thickness	11.3	mm	M
r_2	Side crucible wall-air interface at half melt thickness	14.5	mm	M
θ	Angle between side crucible wall and z direction.	19.8	degree	M
$Th_{crucible}$	Thickness of crucible wall	3	mm	M
Th_{ib}	Thickness of insulating brick	40	mm	M
Ts_0	Initial melt temperature, at which the oxides mixture were melted	1693	K	M
Ts_0'	Adjusted initial melt temperature which considers the temperature drop during transfer process	1682	K	C
T_b	Bulk temperature of the muffle furnace	1253	K	M
T_f	Film temperature or mean temperature at which the properties of air and radiation are evaluated.	1468	K	C
h_{c1}	Convective heat transfer coefficients at z_0	1.19×10^{-5}	W/mm.K	C
h_{c2}	Convective heat transfer coefficients at r_2	7.30×10^{-5}	W/mm.K	C
h_{r1}	Radiation heat transfer coefficients at z_0	1.53×10^{-4}	W/mm.K	C
hr_2	Radiation heat transfer coefficients at r_2	7.26×10^{-4}	W/mm.K	C
h_{1all}	Overall heat transfer coefficients at z_0	8.31×10^{-5}	W/mm.K	C
h_{2all}	Overall heat transfer coefficients at r_2	4.25×10^{-5}	W/mm.K	C
h_{3all}	Overall heat transfer coefficients at z_1	4.35×10^{-6}	W/mm.K	C
Symbols for Comments: M = Measured, C = Calculated, E = Estimated.				

Table 6.2 (Continued)

Parameter	Definition	Value	Unit	Comments
σ	Boltzmann's constant	5.73×10^{-14}	J/mm^2.sec.K	Known
ε_{melt}	Emissivity of melt at z_0	0.8	None	E
ε_{sw}	Emissivity of alumina crucible at r_2	0.5	None	E
η_{melt}	Efficiency of radiation heat transfer at z_0, it considers geometry relationship between the melt-air interface and the surrounding environment	0.33	None	E
η_{sw}	Efficiency of radiation heat transfer at r_2, it considers geometry relationship between the side crucible wall-air interface and the surrounding environment	0.25	None	E
ρ_{melt}	Density of melt	2.7×10^{-3}	g/mm^3	M
k_{melt}	Thermal conductivity of melt	1.2×10^{-3}	W/mm.K	E
Cp_{melt}	Heat capacity of melt	1.27	J/g.K	C
$\rho_{crucible}$	Density of alumina crucible	3.8×10^{-3}	g/mm^3	E
$k_{crucible}$	Thermal conductivity of alumina crucible	5×10^{-3}	W/mm.K	C
$Cp_{crucible}$	Heat capacity of alumina crucible	1.29	J/g.K	C
ρ_{ib}	Density of insulating brick	6.04×10^{-3}	g/mm^3	M
k_{ib}	Thermal conductivity of insulating brick	3.5×10^{-4}	W/mm.K	E
Cp_{ib}	Heat capacity of insulating brick	1.07	J/g.K	E
Errorf	Calibrating factor to minimize the difference between simulated and measured temperature resulted by the overall error of other parameters, it has a range of -1 to 1.	0.5	None	M
Symbols for Comments: M = Measured, C = Calculated, E = Estimated.				

MCF) system can be written as

$$\rho C_p\left(\frac{\partial T}{\partial t}+f(v)\right)=\frac{1}{r}\frac{\partial}{\partial r}\left(kr\frac{\partial T}{\partial r}\right)+\frac{1}{r^2}\frac{\partial}{\partial \phi}\left(k\frac{\partial T}{\partial \phi}\right)+\frac{\partial}{\partial z}\left(k\frac{\partial T}{\partial z}\right)+f(\mu)+\dot{Q}_v \tag{6.15}$$

where

$$f(\mu)=2\mu\left\{\left(\frac{\partial v_r}{\partial r}\right)^2+\left[\frac{1}{r}\left(\frac{\partial v_\phi}{\partial \phi}+v_r\right)\right]^2+\left(\frac{\partial v_z}{\partial z}\right)^2\right\} \tag{6.16}$$
$$+\mu\left\{\left(\frac{\partial v_\theta}{\partial z}+\frac{1}{r}\frac{\partial v_z}{\partial \phi}\right)^2+\left(\frac{\partial v_z}{\partial r}+\frac{\partial v_r}{\partial z}\right)^2+\left[\frac{1}{r}\frac{\partial v_r}{\partial \phi}+r\frac{\partial}{\partial r}\left(\frac{v_\phi}{r}\right)\right]^2\right\}$$

It considers the effect of viscosity on temperature distribution. This term is usually negligible except in systems where the velocity gradient is very large. In this case, it is zero.

$$f(v)=v_r\frac{\partial T}{\partial r}+\frac{v_\theta}{r}\frac{\partial T}{\partial \phi}+v_z\frac{\partial T}{\partial z} \tag{6.17}$$

It is the effect of velocity on temperature distribution. Since the system is not moving, it becomes zero.

$\dot{Q}_v$ is the volumetric heat source. In this system, no heat is generated within the melt; therefore, it is also zero.

6.3.3. Governing Equations for a Melt-Crucible-Furnace Wall (MCF) System

Before writing complete equations, a few assumptions are claimed here.

1) Since both the melt and crucible are symmetrical and they are placed right at

the center of the muffle furnace, heat conduction along ϕ is negligible; the temperature profile is then reduced to $T \equiv T(t,z,r)$.

2) For the side crucible wall when a nonrectangular crucible is used, if the angle between the wall and the z direction is relatively small and the wall is much thinner compared with the width of the melt, it is reasonable to assume that heat is nearly lost to the environment through the side wall along the r direction only, and neglect heat transfer in the z direction. However, the angle mentioned here will be counted toward the calculation of convective heat transfer coefficients in later sections.

3) For the bottom crucible wall, since its thickness is much smaller than its width, assume heat transfers only along z direction

Based on the above explanation and assumptions, temperature profile $T(t,z,r)$ can be calculated in the following way.

T in the melt (T_m):

$$\rho C_p \frac{\partial T_m}{\partial t} = \frac{1}{r}\frac{\partial}{\partial r}\left(k_m r \frac{\partial T_m}{\partial r}\right) + \frac{\partial}{\partial z}\left(k_m \frac{\partial T_m}{\partial z}\right) \tag{6.18}$$

where k_m is the thermal conductivity of the melt. Apply separation of variables, T in the bottom crucible wall (T_{bw}):

$$\rho C_p \frac{\partial T_{\mathrm{bw}}}{\partial t} = \frac{\partial}{\partial z}\left(k_{crucible} \frac{\partial T_{bw}}{\partial z}\right) \tag{6.19}$$

where $k_{crucible}$ is the thermal conductivity of the crucible.

T in the side crucible wall (T_{sw}):

$$\rho C_p \frac{\partial T_{sw}}{\partial t} = \frac{\partial}{\partial z}\left(k_{crucible} \frac{\partial T_{sw}}{\partial z} \right) \tag{6.20}$$

T in the bottom insulating brick (T_{ib}):

$$\rho C_p \frac{\partial T_{ib}}{\partial t} = \frac{\partial}{\partial z}\left(k_{ib} \frac{\partial T_{ib}}{\partial z} \right) \tag{6.21}$$

where k_{ib} is the thermal conductivity of the insulating brick.

To solve the above equations, the required number of independent boundary conditions are 5, 3, 3, and 3 for Equations (6.18) to (6.21), respectively.

Note that the crucible and the melt are at high temperature; therefore, radiation has to be considered for better accuracy. The rate at which a solid body emits radiation is given by the Stefan-Boltzmann law:

$$q_R = \varepsilon \sigma T_s^4 \tag{6.22}$$

where q_R is the radiant flux emitted by the surface, ε is the emissivity of the surface, σ is the Boltzman constant, and T_S is the surface temperature in absolute units. For the case of a small pellet located in a large cavity with an isothermal surface-temperature, which is also true for this melt-crucible-furnace wall system, a simple expression can be applied [65]

$$q_R^{'} = \varepsilon \sigma \left(T_E^4 - T_S^4 \right) \tag{6.23}$$

where T_E is the temperature of the walls of the cavity, q_R' is the net radiative flux at the solid surface. Rewrite Equation (6.23) in a manner similar to the heat convection formula,

and we have

$$q_R^{'} = h_r\left(T_E - T_S\right) \tag{6.24}$$

where $h_r = \varepsilon\sigma(T_E^2 + T_S^2)(T_E + T_S)$.

6.3.4 Boundary Conditions for the MCF System

Based on known temperature, flux, or temperature continuity, a complete list of boundary conditions is written as follows.

B. C. s for the melt:

B. C. 1, at t = 0

$$T_m = T_0 \tag{6.25}$$

T_0 is the temperature at t = 0; that is when the melt just leaves the vertical furnace and it is the highest temperature for the cooling system.

B. C. 2, at z = h

$$-k_m \frac{\partial T_m}{\partial z} = h_{c1}(T_m - T_b) + h_{r1}(T_m - T_E) \tag{6.26}$$

h_{c1} and h_{r1} are the convective and radiative heat transfer coefficients at the top surface, respectively. T_b is the bulk fluid temperature.

B. C. 3, at z = 0

$$T_m = T_{bw} \tag{6.27}$$

B. C. 4, at r = 0,

$$--k_m \frac{\partial T_m}{\partial r} = 0 \tag{6.28}$$

B. C. 5, at $r = r_1$,

$$T_m = T_{sw} \tag{6.29}$$

B. C.s for the side wall:

B. C. 6, at $t = 0$,

$$T_{sw} = T_0 \tag{6.30}$$

B. C.7, at $r = r_2$,

$$-k_{crucible} \frac{\partial T_{sw}}{\partial r} = h_{c2}(T_{sw} - T_b) + h_{c2}(T_{sw} - T_E) \tag{6.31}$$

h_{c2} and h_{r2} are the convective and radiative heat transfer coefficients at the outer surface of the side crucible wall, respectively.

B. C. 8, at $r = r_1$

$$-k_{crucible} \frac{\partial T_{sw}}{\partial r} = -k_m \frac{\partial T_m}{\partial r} \tag{6.32}$$

B.C.s for the bottom crucible wall:

B. C. 9, at t = 0

$$T_{bw} = T_0 \tag{6.33}$$

B. C. 10, at z = 0

$$-k_{crucible}\frac{\partial T_{bw}}{\partial z} = -k_m \frac{\partial T_m}{\partial z} \tag{6.34}$$

k_{bw} is the thermal conductivity of the bottom crucible wall.

B. C. 11, at $z = z_1$

$$T_{bw} = T_{ib} \tag{6.35}$$

B.C.s for the bottom insulating brick:

B. C. 12, at t = 0

$$T_{ib} = T_E \tag{6.36}$$

B. C. 13, at $z = z_1$

$$-k_{crucible}\frac{\partial T_{bw}}{\partial z} = -k_{ib}\frac{\partial T_{ib}}{\partial z} \tag{6.37}$$

k_{ib} is the thermal conductivity of the insulating brick.

B. C. 14, at $z = z_2$

$$T_{bw} = T_E \tag{6.38}$$

6.3.5 Calculation of Natural Convection Heat Transfer Coefficients

In the above boundary conditions, h_{c1} and h_{c2} represent the convective heat transfer coefficients at the top melt surface and the outer surface of the side crucible wall, respectively. From heat transfer theories, mean convective heat flux is given by [66]

$$\bar{q} = \bar{h}(\overline{T_s} - T_F) = \bar{h}(\overline{T_s} - T_b) \tag{6.39}$$

where $\bar{h}$ is the mean convection heat transfer coefficient. $\overline{T_s}$ is the mean surface temperature. T_F is the reference temperature. T_b is the bulk fluid temperature. $\bar{h}$ is expressed in terms of mean Nusselt number $\overline{Nu}_L$ by the following formula.

$$\bar{h} = \frac{L}{k\overline{Nu}_L} \tag{6.40}$$

where L is the characteristic length. k is the thermal conductivity of air at interested temperature.

Depending on the geometry of a surface, different equations are used to calculate $\overline{Nu}_L$.

Case 1: Vertical and inclined surface. For a vertical surface, if the air movement near the surface is laminar flow ($Ra_L < 10^9$),

$$\overline{Nu}_L = 0.68 + \frac{0.670 Ra_L^{1/4}}{\left[1 + \left(0.492/\mathrm{Pr}\right)^{9/16}\right]^{4/9}} \tag{6.41}$$

If the air movement near the surface is Turbulent flow ($Ra_L \geq 10^9$),

$$\overline{Nu}_L = \left\{0.825 + \frac{0.387 Ra_L^{1/6}}{\left[1 + (0.492/\mathrm{Pr})^{9/16}\right]^{8/27}}\right\}^2 \tag{6.42}$$

where Ra_L is the Rayleigh number and is defined according to

$$Ra_L = \frac{g\beta(T_s - T_\infty)L^3}{\nu\alpha} \tag{6.43}$$

g is gravity constant. β is the thermal expansion coefficient of air.

For an inclined wall with an angel of θ to the vertical direction, the same equations as shown above still apply, except that we need to replace g by $g\cos(\theta)$.

Case 2: Horizontal surface with the hotter surface facing up

If $Ra_L < 10^7$,

$$\overline{Nu}_L = 0.54 Ra_L^{1/4} \tag{6.44}$$

If $Ra_L \geq 10^7$,

$$\overline{Nu}_L = 0.15 Ra_L^{1/3} \tag{6.45}$$

Pr is defined as Prandtl number; it is given by

$$\Pr = \frac{\mu C_p}{k} \tag{6.46}$$

where μ is the dynamic viscosity, c_p is the heat capacity at constant pressure, and k is the thermal conductivity.

In the above equations, the property constants of air are to be evaluated at T_f. These constants vary with temperature, and their value can be easily found in most heat transfer books in forms of appendices [66, 67].

6.3.6 Determination of Temperature Simulation Parameters

Four important parameters involved significantly in the heat transfer calculation are heat capacity, density, thermal conductivity, and emissivity of the melt, crucible, and insulating brick. In the following, we shall discuss how these parameters were selected.

6.3.6.1 Properties of Melt

The melt is the most important component of the Melt-Crucible-Furnace system. Its physical properties were either found from other oxide systems that have similar compositions to our mixture and fall into our interested temperature ranges, or they were calculated based on theoretical or empirical equations.

Heat capacity Cp**:** Heat capacity of silicate liquid at the temperature range of 800-1500°C is predicted by the additive equation [68]

$$C_p = \sum X_i C_{p,i} \tag{6.47}$$

where X_i and $C_{p,i}$ are the weight fraction and effective heat capacity of the corresponding component, respectively. A complete list of $C_{p,i}$ is provided by Gudovich and Primenko [69] and the interested components are listed in Table 6.3.

When compared with the composition of the mixtures used in this study as shown in Table 5.1, all of the components fall into the listed concentration range except that CaO in this study is about 10% over the maximum range; this error is neglected for our calculation. As discussed in Chapter 4, dissolution of alumina only affected a very thin layer between the melt and crucible wall side, and all of the crucibles remained intact in

Table 6.3 Fit parameters for silicate liquid heat capacities (800-1500°C)

Component	Concentration range (wt.%)	$C_{p,i}$ J/(g.K)
SiO_2	20-85	1.286
CaO	0-30	1.05
B_2O_3	0-60	1.876
Li_2O	0-16	4.197
Al_2O_3	0-30	1.297

terms of thickness compared with the original thickness. Thus, Al_2O_3 is not considered in the calculation of the heat capacity of the melt.

Density**:** Density of the melt was measured by a complete melting of the oxides in a cylindrical crucible followed by being cooled to room temperature. The density is thus calculated by measuring the volume and weight of the melt; the actual value is taken from the average of a few repeating experiments. Here we neglect the small volume shrinkage at different temperatures.

Thermal conductivity**:** Determination of thermal conductivity of the melt is somehow difficult and tricky. This is because in silicate glass, we can have two modes for thermal conduction. When temperature is below 500°C, the dominant mode is phonon thermal conductivity. When temperature is above 1000°C, photon conduction dominates the heat transfer. When temperature is in between of these two values, we have mixed conduction.

For phonon dominant conduction, an empirical fit has been successful by assuming that the conductivity is a linear function of glass composition as follows [68]:

$$k_{phonon} = \sum A_i C_i \tag{6.48}$$

where A_i and C_i are the phonon thermal conductivity coefficient and concentration of component *i* in the glass. In the literature on phonon thermal conductivity of silicates, the concentrations are generally expressed in weight percent. These coefficients have been published for a number of glass systems of varying composition [70-73]. Fit values for coefficient A of selected components are provided in Table 6.4 [68].

Table 6.4 Coefficients for calculation of phonon thermal conductivity from oxide weight percent (W/mK)

Component	A
SiO_2	0.0133
CaO	0.0123
B_2O_3	0.0082
Li_2O	-0.0088

Photon thermal conduction in the optically thick case is given as follows [68].

$$k_r = \frac{8\pi C_0^3 h^2}{3kT^2}\int_0^{\infty}\frac{1}{\kappa_\lambda}\frac{n^2}{\lambda^6}\frac{e^{hc_0/\lambda kT}}{(e^{hc_0/\lambda kT}-1)^2}d\lambda \qquad (6.49)$$

In the above equation, k is Boltzmann's constant, T is temperature in K, h is the Planck's constant, and C_0 is the speed of light. κ_λ is glass absorption coefficient, n is glass refractive index. λ is the wavelength in vacuum. In these parameters, k, h, and C_0 are known. λ, T, and n can be experimentally measured. κ_λ as a function of temperature and glass composition has been discussed in detail in reference [68].

The corresponding values for this study were taken approximately from literature where the systems have similar composition and temperature ranges [74], the suggested value is given in Tables 6.1 and 6.2.

Emissivity**:** Emissivity of the surface of the object can be measured directly by a few methods such as surface treatment and materials heating. For this study, an approximate value is taken by comparing our system to the provided emissivity values for some known silicate glass, as shown in Figure 6.4 [75].

As can be seen from Figure 6.7, the emissivity of the mentioned glasses does not vary significantly with temperature, and they are typically in the range of 0.7 to 0.9. Although the maximum temperature range in this table is at 500°C, because of the relatively low temperature dependence, we shall be able to extend these lines based on their overall trend to a higher temperature for example to 1000°C. The average value of these lines gives the approximate emissivity of the melt, as provided in Tables 6.1 and 6.2.

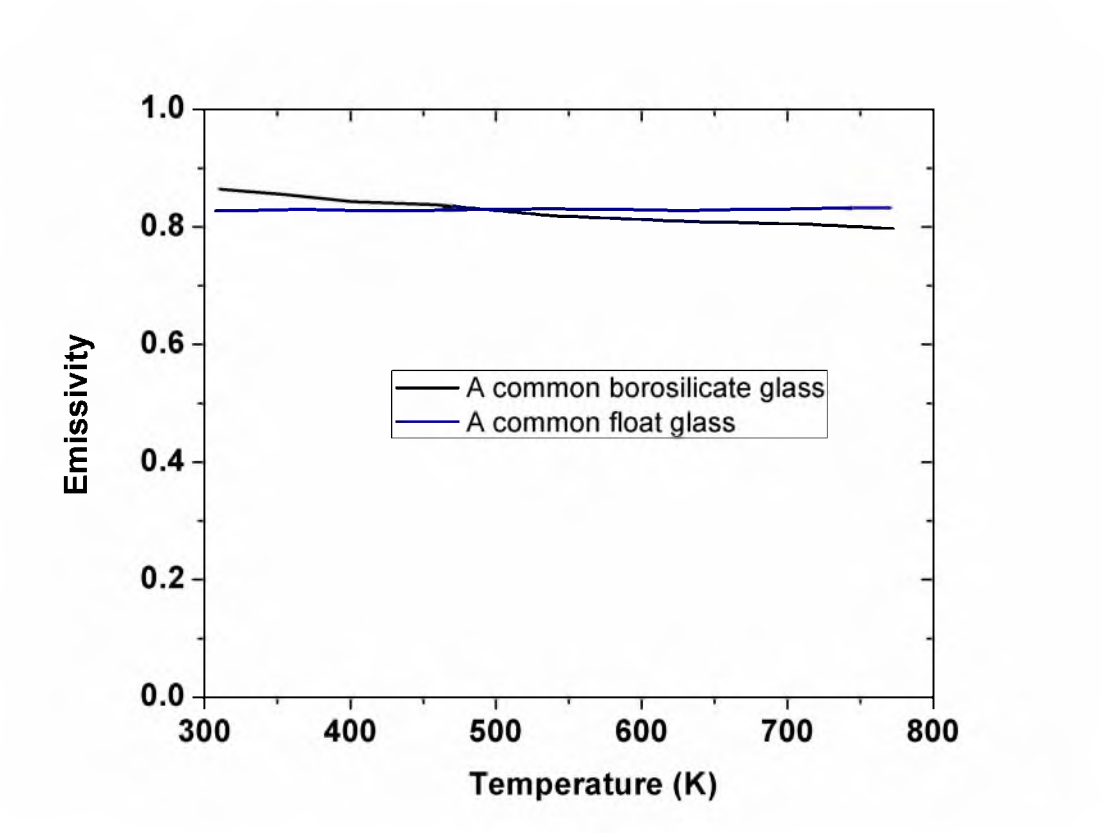

Figure 6.7 Emissivity of some common glass as a function of temperature. Data collected from reference [75].

6.3.6.2 Properties of Crucible

The crucibles used for this study were made of alumina with a purity of 99.6%. For alumina of such high purity, most of its thermal properties are easily available either by empirical calculations or by experimental measurements.

Density: The density of the alumina crucibles were given by the provider.

Heat capacity: Heat capacity of alumina with a purity of greater than 99.5% as a function of temperature can be calculated by the following empirical equation

$$Cp = 1.0446 + 1.742 \times 10^{-4} T - 2.796 \times 10^{4} T^{-2} \qquad (6.50)$$

where C_p has the unit of J/g.K. This equation is valid up to 1500°C [75].

Thermal conductivity: Thermal conductivity of the alumina crucibles at room temperature is provided as 35 W/m.K by the supplier. It matches the value as shown in Figure 6.8 where the thermal conductivity of alumina as a function of temperature is plotted [76]. A polynomial curve fitting was applied to the data points; the fitted equation is shown below.

$$k_{Al_2O_3} = -3 \times 10^{-8} T^3 + 8 \times 10^{-5} T^2 - 0.0779T + 32.38 \qquad (6.51)$$

Emissivity: Emissivity of high grade alumina as a function of temperature hasbeen studied by Morrell [76] and Teodorescu [77]. The emissivity of the crucible outer surface at our interested temperature range is estimated and listed in Tables 6.1 and 6.2.

6.3.6.3 Properties of Insulating Brick

Density and heat capacity: Density of the insulating brick was measured directly based on its mass to volume ratio. Its heat capacity has been measured by reference [78].

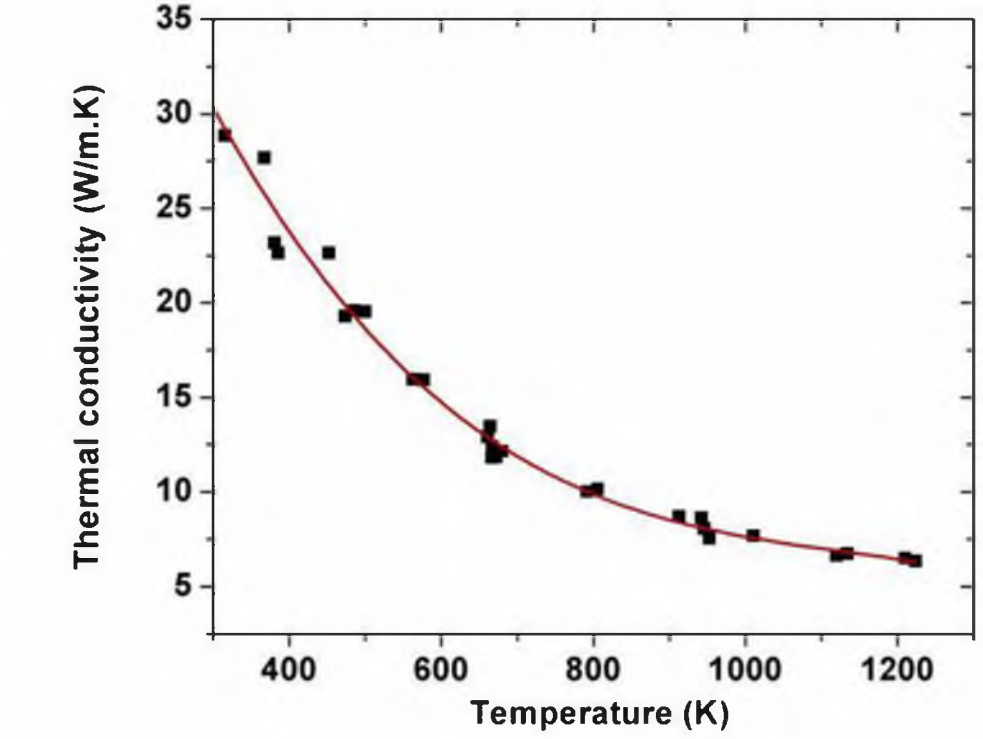

Figure 6.8 Alumina thermal conductivity as a function of temperature. Data collected from reference [76].

Thermal conductivity: The measured thermal conductivity of the same type of insulating brick has a linear relationship with temperature [79], as shown in Figure 6.9. The fitted linear equation becomes

$$k_{ib} = 1.722 \times 10^{-4} T + 0.102 \tag{6.52}$$

where k_{ib} has the unit of W/m.K.

With the above explanations, a complete list of the parameters and constants that will be used for the simulation of temperature profile of the Melt-Crucible-Furnace system is provided in Tables 6.1 and 6.2.

6.3.7 Separation of Melt from the MCF System

Now we have the governing equations, corresponding solutions, and boundary conditions. Once we obtain the required parameters, theoretically, a temperature profile of the MCF system should be available. Practically, however, because we have four governing equations and each of them has a general solution consisting of four elementary solutions, and meanwhile, we still have 14 boundary conditions even after operating dimension reduction for some special case, it is still not easy to completely solve them. Therefore, we shall suggest a simplified method so that we can further reduce the number of governing equations and boundary conditions.

In this simplified method, we take advantage of the composite wall model where we consider that the alumina crucible and the insulating brick act only as adding additional thermal resistance along with the natural convection and radiation heat transfer to the heat loss of the melt; then, we define a new overall heat transfer coefficient at the melt-crucible or melt-air interfaces; in this way, we are able to separate the melt from its

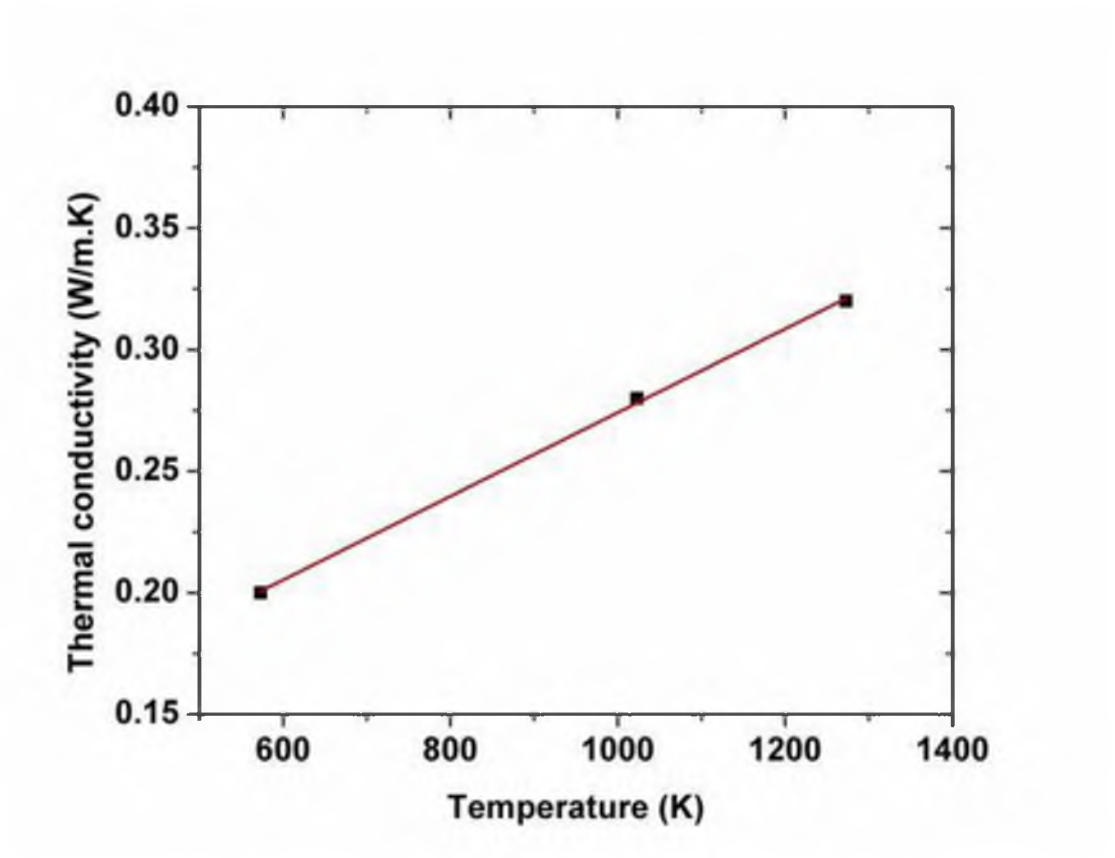

Figure 6.9 Insulating brick thermal conductivity as a function of temperature. Data collected from reference [79].

surrounding heat transfer layers without having significant accuracy loss. This method only requires one governing equation and five boundary conditions; thus, it greatly facilitates the calculation and simulation work and it turns out that this method is actually very reliable and provides good agreement with measured values, as you will see in later discussion.

The overall heat transfer coefficient of a composite wall can be calculated as

$$\frac{1}{h_{all}} = \frac{1}{h_i} + \sum_{j=}^{n} \frac{L_j}{k_j} + \frac{1}{h_o} \tag{6.53}$$

where h_i and h_o are the convective heat transfer coefficients of the inner and outer fluids, respectively, k_j and L_j are the thermal conductivity and thickness of the j^{th} wall in between the inner and outer fluids, respectively.

Once an overall heat transfer coefficient is used, the temperature profile of the melt can be obtained by solving Equation (6.18) only where the melt was assumed as contacting with the surrounding air or furnace wall directly though multiconvection layers. Within the interested temperature range (1000-1450°C) and composition (47 wt.% SiO2 + 44 wt.% CaO + additives), it was found the heat capacity of such a molten silicate is approximately a constant in this temperature range and can be calculated by Equation (6.47) [68]. The density change of a similar silicate system (50 wt.% SiO_2 + 45 wt.% CaO+ additives) in this temperature range is 3% [68]. The thermal conductivity of a similar silicate system (49 wt.% SiO_2 + 42 wt.% CaO + additives) in this temperature range is 5% [80]. Because of these small changes, the heat capacity, density, and thermal conductivity were treated as constants for temperature simulation.

With the above clarification, the new boundary conditions then become

B.C.1, at t = 0,

$$T_m = T_{initial} \tag{6.54}$$

B.C.2, at z = h,

$$-k_m \frac{\partial T_m}{\partial z}\Big|_{z=h} = h_{1all}(T_m - T_0) \tag{6.55}$$

B.C.3, at z = 0,

$$-k_m \frac{\partial T_m}{\partial z}\Big|_{z=0} = h_{2all}(T_m - T_0) \tag{6.56}$$

B.C.4, at r = 0,

$$-k_m \frac{\partial T_m}{\partial r} = 0 \tag{6.57}$$

B.C.5, at r = r_1 ,

$$-k_m \frac{\partial T_m}{\partial r}\Big|_{r=r_1} = h_{3all}(T_m - T_0) \tag{6.58}$$

where h_{1all}, h_{2all}, and h_{3all} are the overall heat transfer coefficients at z = z_0, r = r_2, and z = z_1, respectively, as defined in Figure 6.3 and Table 6.1 and 6.2.

6.4 Temperature Simulation Results

6.4.1 Temperature Distribution

Figure 6.10 shows temperature distribution along z and r directions of the z axis plane of a melt that has a cylindrical shape at different cooling time. As can be seen from Figure 6.10a to d, at each given time, the temperature distribution within the whole melt can be divided into different layers that have the same temperature with the top layers being the cooler part and bottom layers being the hotter part; this temperature distribution proves that heat loss through the bottom crucible wall is small because of the additional insulating brick right underneath the crucible, which provides the expected heat transfer mechanism.

Figure 6.11 shows temperature distribution as a function of time along z and r directions of the axis plane of a melt that has a truncated-cone shape at different cooling time. It has a very similar temperature distribution to the cylindrical, which is one of the reasons why for approximate calculation, we can treat this truncated-cone shape with low inclining angle as a cylindrical shape.

6.4.2 Temperature Gradient

Figure 6.12 shows the temperature gradient in the cylindrical shape melt. It clearly shows that for each given time, the temperature gradient is the largest at the top melt surface, while the bottom melt has the smallest temperature gradient. With increasing time, the temperature gradient at the same position also drops; this observation directly proves that the temperature gradient is time-dependent. In the previous section, we have mentioned the failure of existing models on the prediction of our observed data; one of the major reasons is related to the time dependence of temperature gradient.

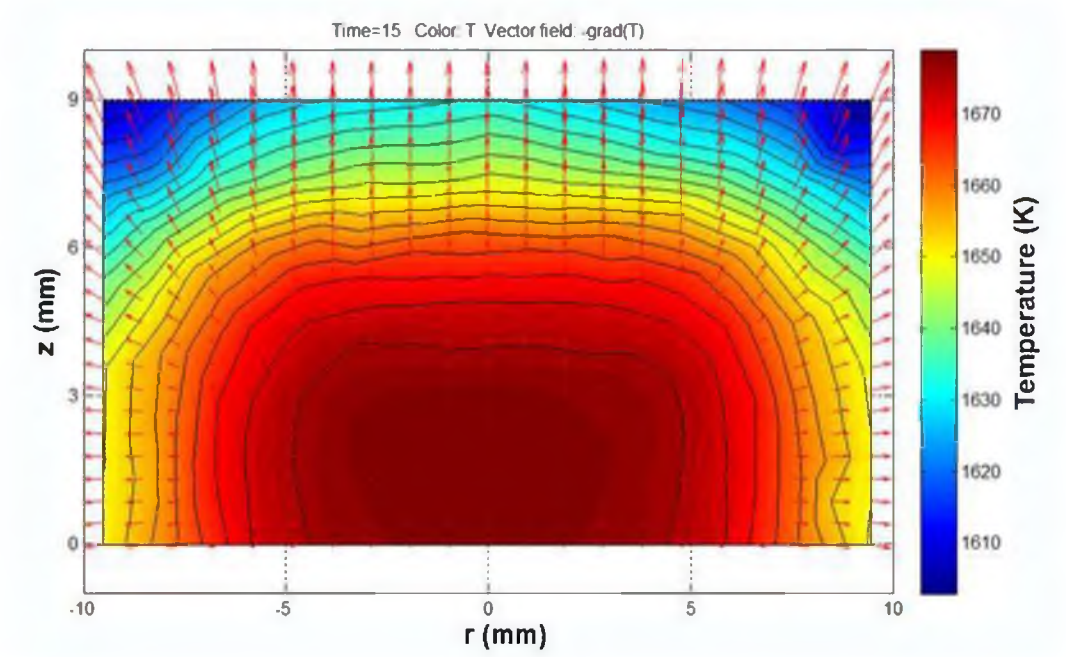

(a)

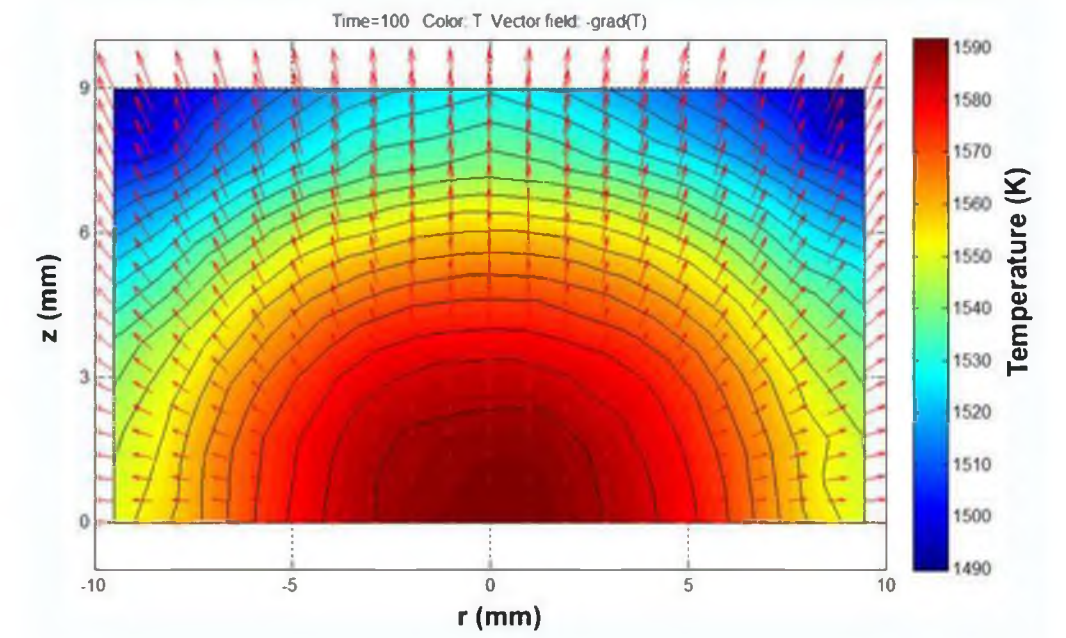

(b)

Figure 6.10 Temperature distribution along z and r direction of the z axis plane of a cooling melt that has a cylindrical shape at a cooling time of: (a) t = 15 s, (b) t = 100 s, (c) t = 400 s, and (d) t = 1200 s.

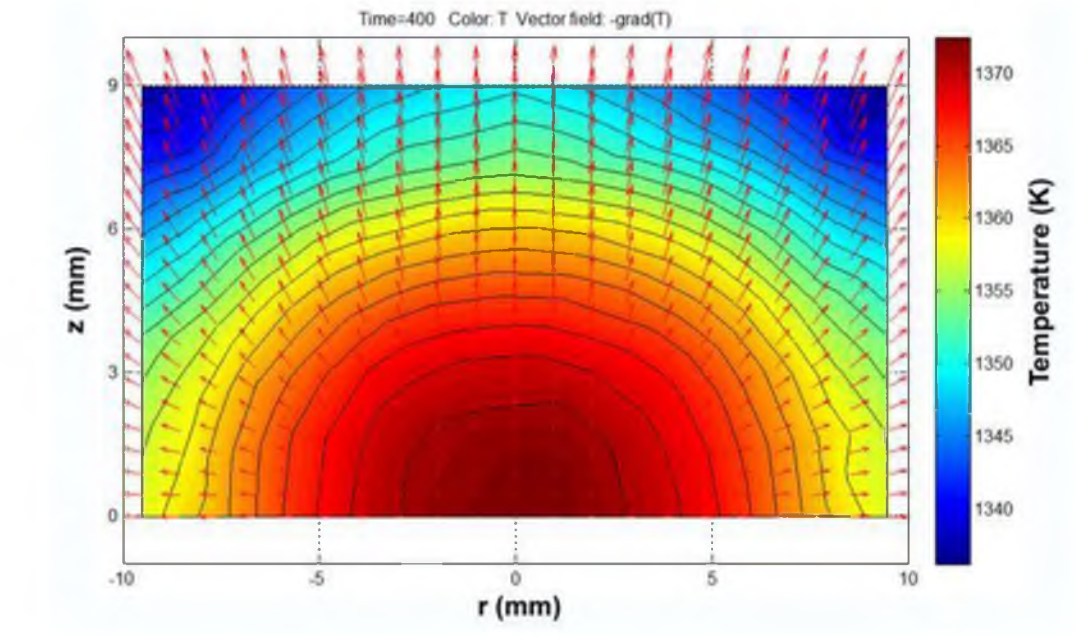

(c)

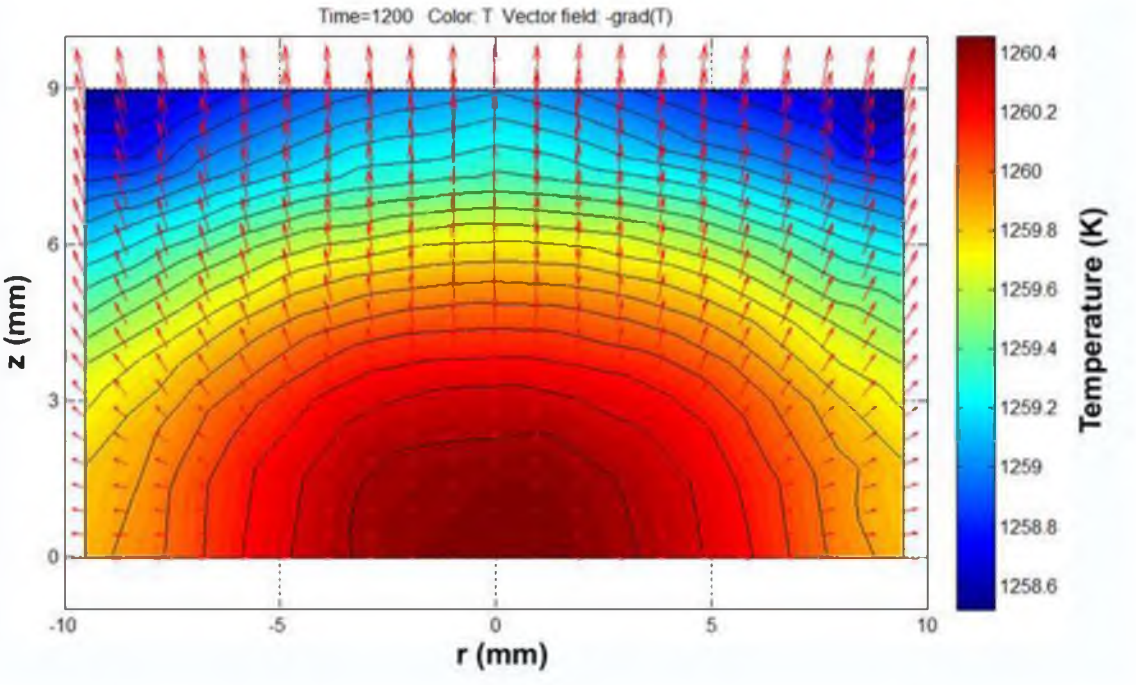

(d)

Figure 6.10 (Continued)

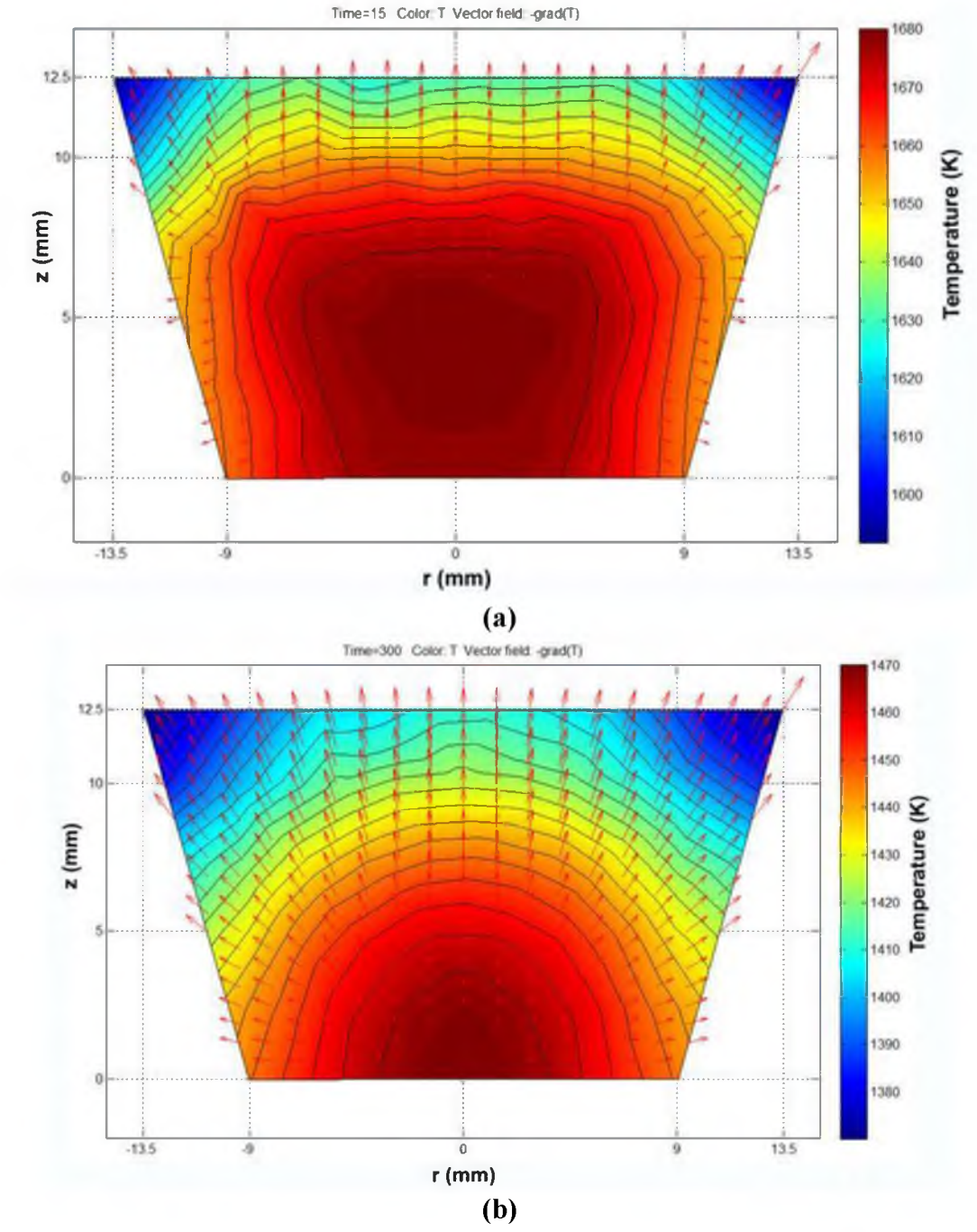

Figure 6.11 Temperature distribution along z and r direction of the z axis plane of a cooling melt that has a truncated-cone shape at a cooling time of: (a) t = 15ss, (b) t = 300 s, (c) t = 660 s, and (d) t = 1200 s.

(c)

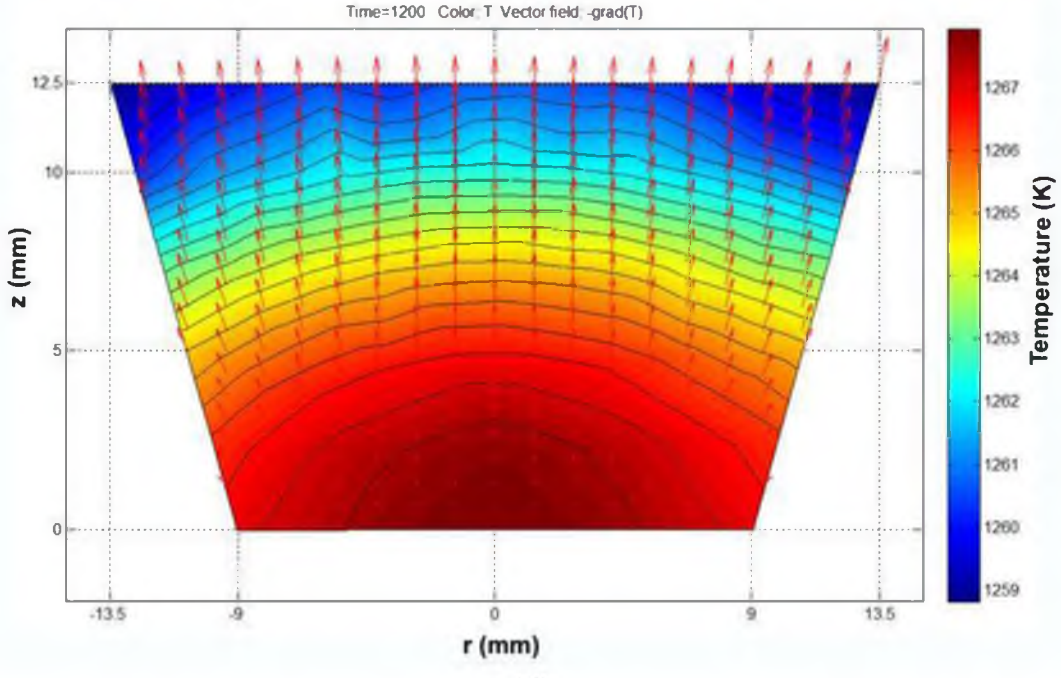

(d)

Figure 6.11 (Continued)

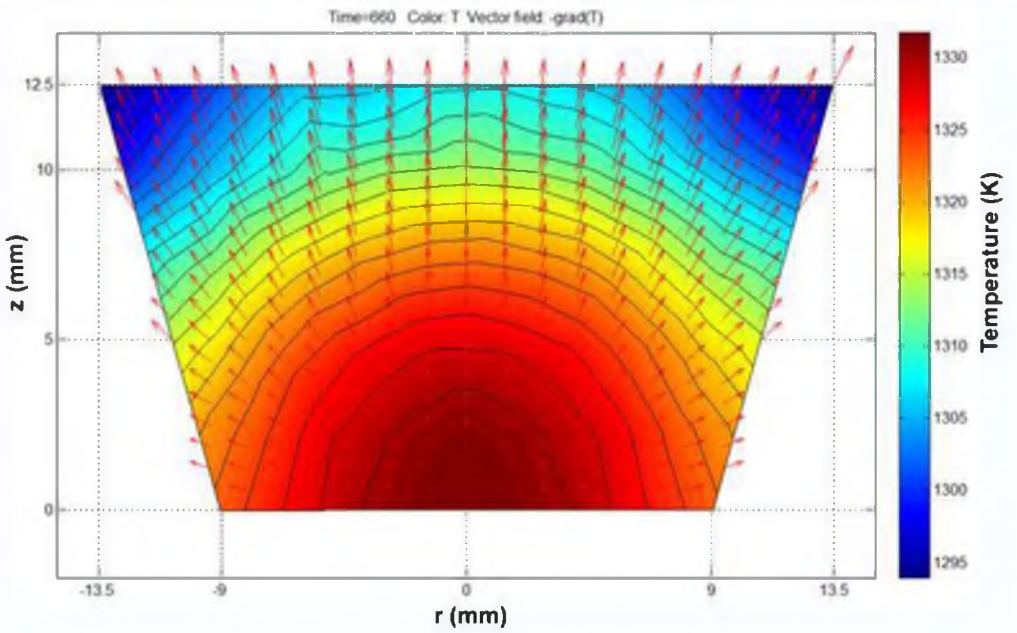
Time=660 Color: T Vector field: -grad(T)
12.5
10
5
0
z (mm)
-13.5
-9
0
9
13.5
r (mm)
1330
1325
1320
1315
1310
1305
1300
1295
Temperature (K)

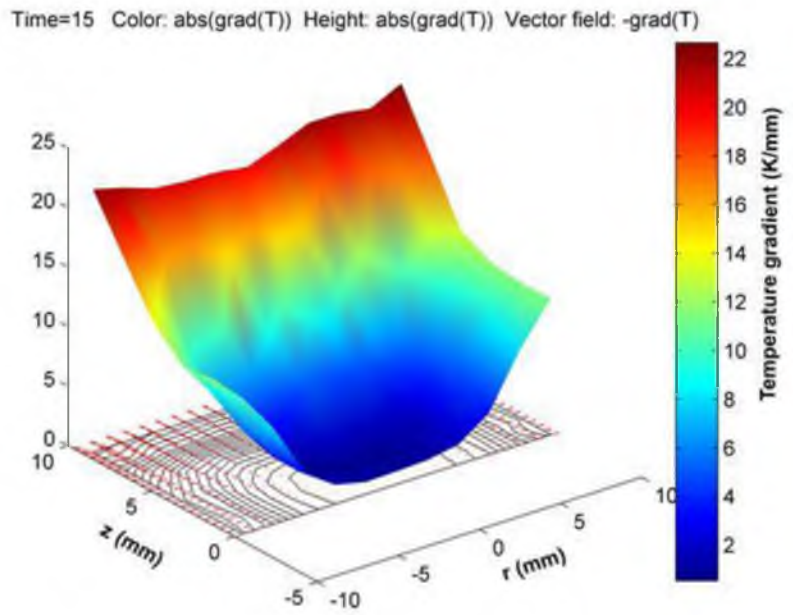

(a)

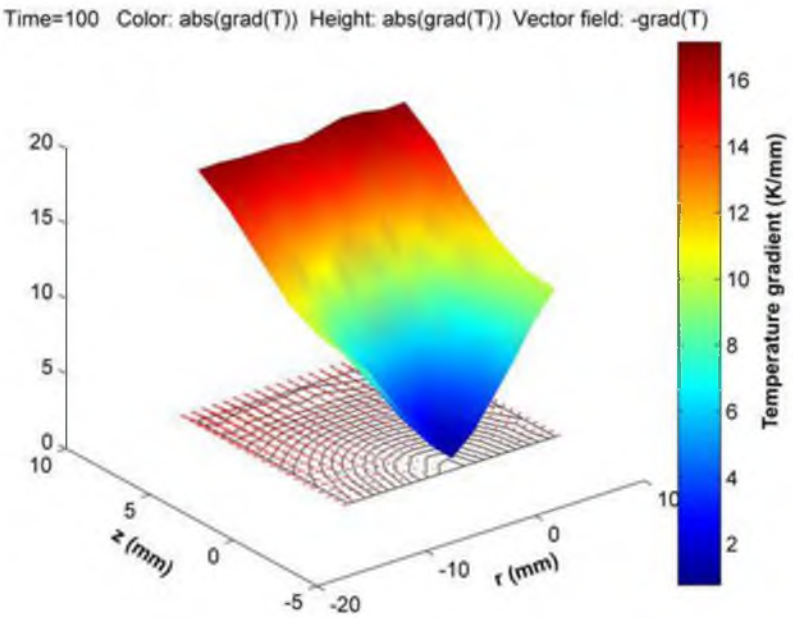

(b)

Figure 6.12 Temperature gradient along z and r direction of the z axis plane of a cooling melt that has a cylindrical shape at a cooling time of: (a) t = 15 s, (b) t = 100 s, (a) t = 400 s, (b) t = 1200 s.

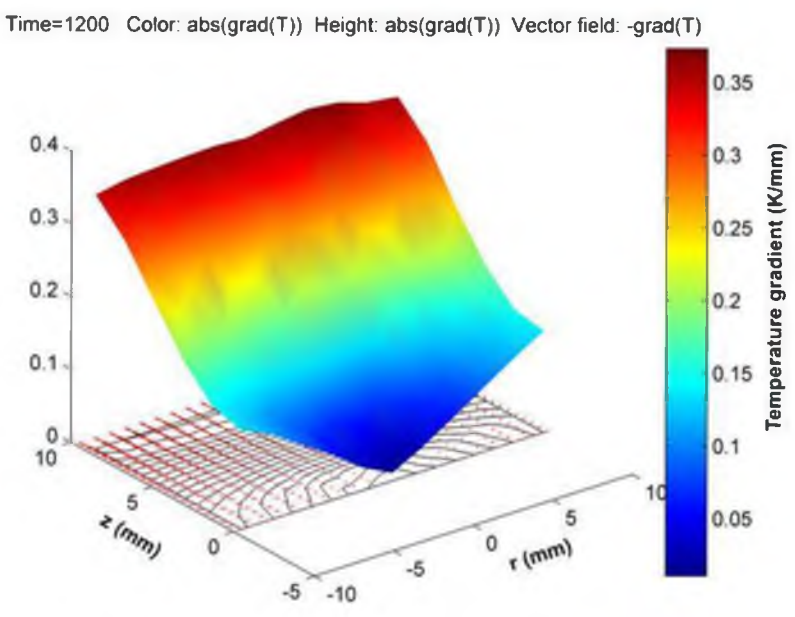

(d)

Figure 6.12 (Continued)

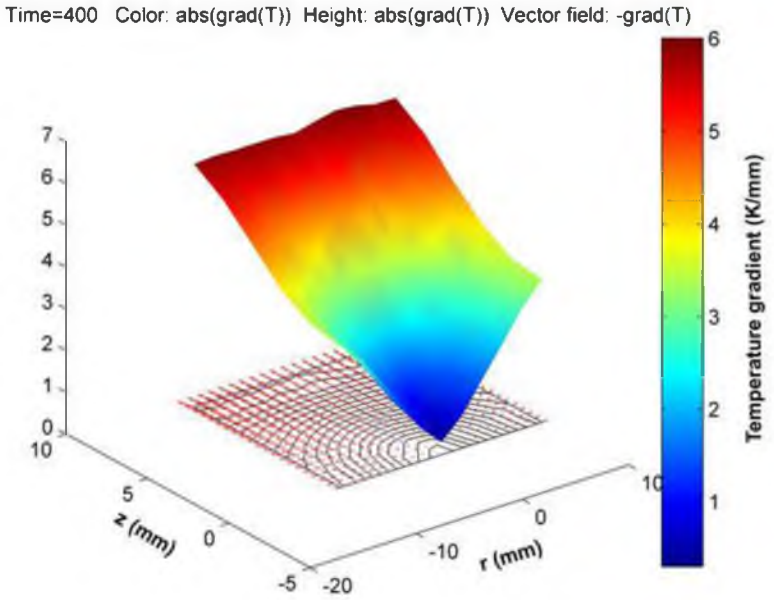
Time=400 Color: abs(grad(T)) Height: abs(grad(T)) Vector field: -grad(T)
7
6
5
4
3
2
1
0
10
5
0
z (mm)
-5
-20
-10
0
r (mm)
10
6
5
4
3
2
1
Temperature gradient (K/mm)

(c)

Figure 6.13 shows the temperature gradient of a truncated-cone shape melt at different cooling time; it has similar temperature gradient distribution to the cylindrical shape melt, but meanwhile, Figure 6.10 compares the temperature gradient and the temperature simultaneously in a 3D format.

6.4.3 Calibration of Simulated Temperature Distribution

In the calculation of convective heat transfer coefficients, the thermal properties of air are evaluated at film temperature, which is the average between the crucible wall and bulk fluid, or melt surface and furnace wall. Because the temperature of the crucible wall or melt changes with time, this average will also changes. The average temperature is valid only if the temperature drop has a linear relationship with time. Meanwhile, because of the difficulty of obtaining accurate physical properties of the melt, crucible, and insulating brick as a function of temperature, estimation has to be made to certain parameters, as discussed in previous sections. In order to minimize this error, a parameter called error factor abbreviated as Errorf is introduced here. It summarizes the overall effects from these errors with a range from -1 to 1. The exact value is determined by assigning a random initial value first, and then by comparing the simulated temperature at a certain position with the measured temperature, we can further adjust the initial value until we found a reasonable value that gives the best fit compared to measured values. This iteration method seems tedious if we do it manually; however, if we do this using a computer, it is not hard. In this way, we might lose some accuracy, but compared with measuring those parameters very accurately, this method can significantly reduce the experimental work and consume much less time. Such a position can be at any point in the system, and the more the better. However, practically, we prefer to choose those

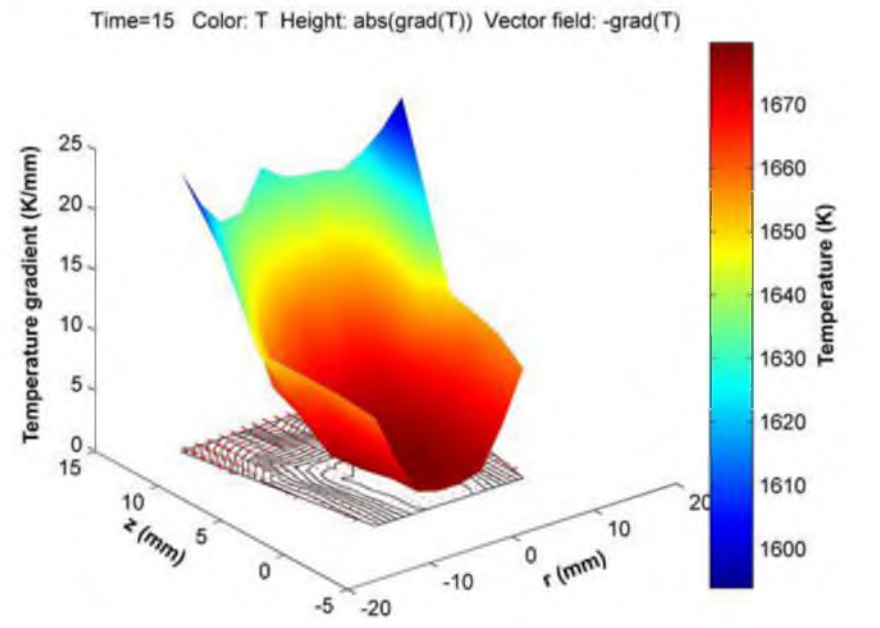

(a)

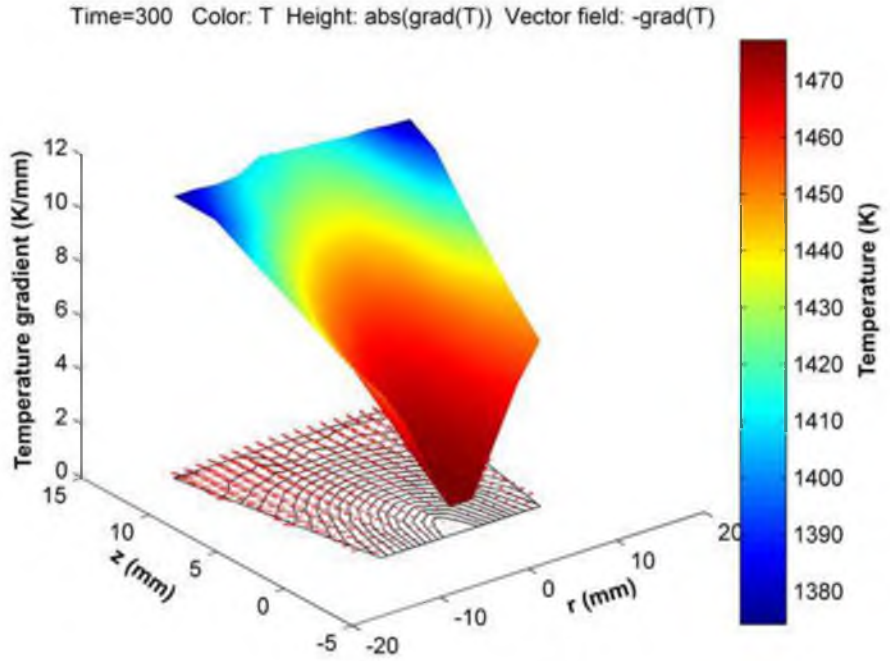

(b)

Figure 6.13 Temperature and temperature gradient along z and r direction of the z axis plane of a cooling melt that has a truncated-cone shape at a cooling time of: (a) t = 15 s, (b) t = 300 s, (c) t = 660 s, and (d) t = 1200 s.

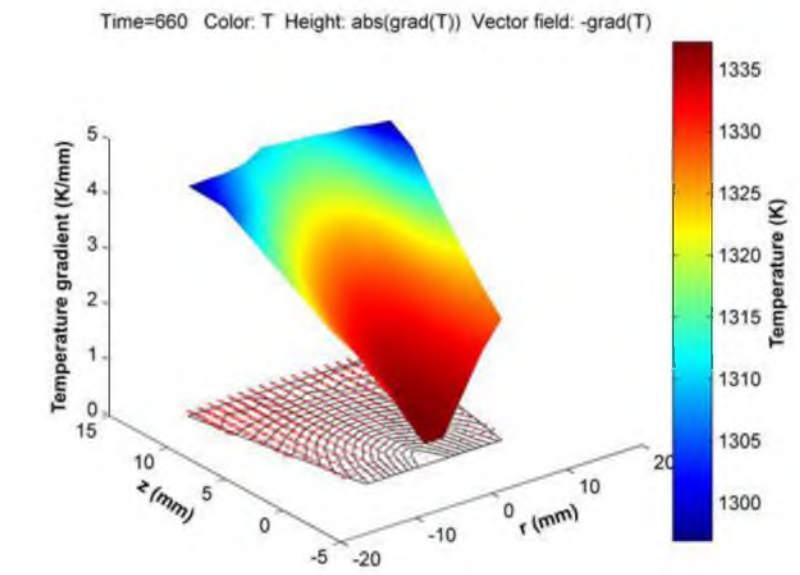

(c)

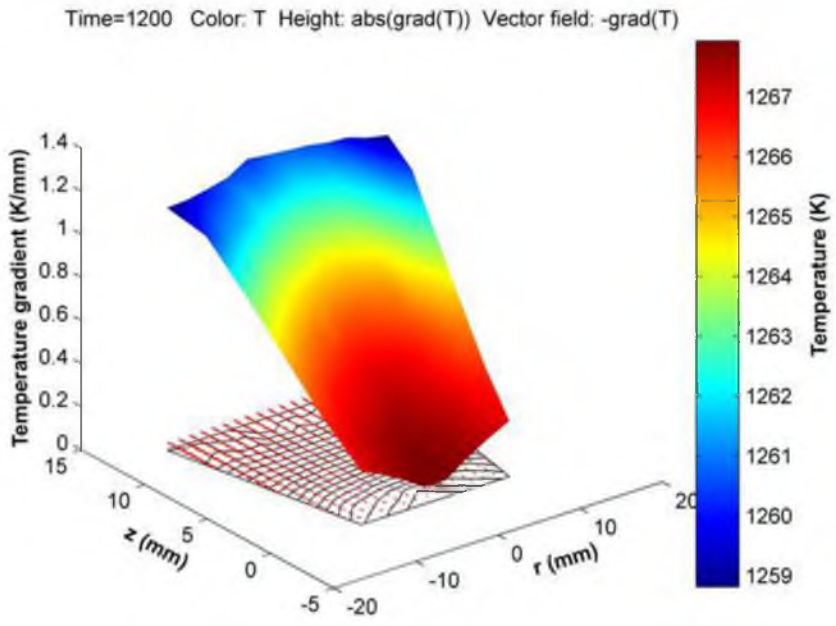

(d)

Figure 6.13 (Continued)

positions that are either the symmetrical center of the system or can be measured relatively easily. In this study, we choose the center of the bottom crucible wall, which is the easiest point to be measured, as shown in Figure 6.14.

Another error that has not been included in the above error factor is the initial temperature of the melt. Since we need to transfer the melt from a furnace at a higher temperature to a furnace at a lower temperature, even though we reduced the transfer time to only about 15 seconds and we avoided touching the crucible that holds the melt directly by putting it inside another bigger crucible, there is still a chance we might have relatively large temperature drops without the evidence of it from either direct measurement or calculation. To verify this error, we first simulate the temperature distribution at 15 seconds using the initial temperature T_0; then, we calculate the average temperature drop at the end of this period by the summation of difference between the temperature of each layer and the initial temperature, as shown in Figure 6.7a; the initial temperature minus the average temperature drop gives the adjusted temperature, which is defined as T_0'. Using the above melt system, we found an average temperature drop of about 10 K, which directly proves that the heat loss during transfer stage is negligible; to improve the accuracy, we will use the adjusted initial temperature as the initial condition for the simulation; thus, t = 0 in the following simulation refers to the time when the melt is newly transferred to the muffle furnace rather than the moment when it just leaves the vertical furnace.

6.4.4 Comparison between Measured and Simulated Temperature

Figure 6.15 compares the measured and simulated temperature at the melt-bottom-crucible wall side, i.e., z = z1 as defined in Figure 6.3. As can be seen from this

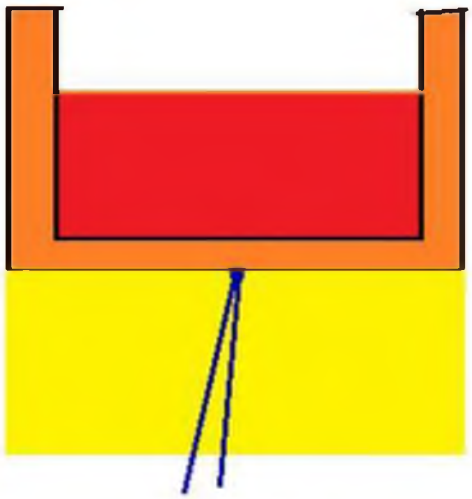

(a)

(b)

Figure 6.14 Illustration (a) on the experimental measurement (b) of the temperature profile as a function of time at the center of the interface between the bottom alumina crucible wall and insulating brick.

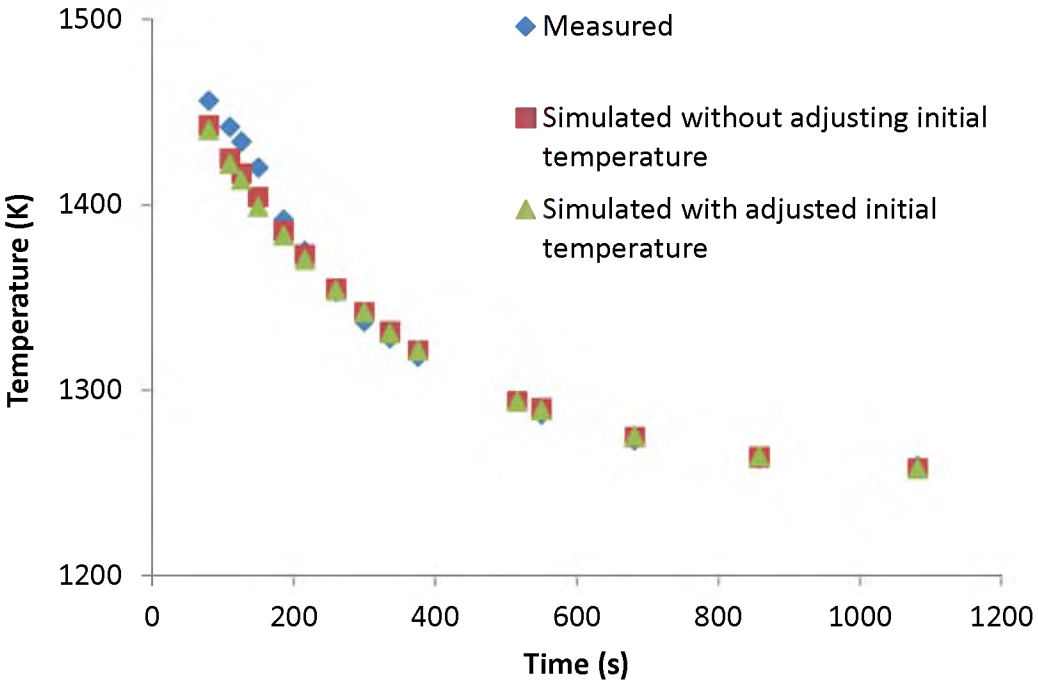

Figure 6.15 A comparision of simulated and measured tempeature at the point as indicated in Figure 6.11.

figure, with the discussed measures to minimize the errors, the simulated temperature and the measured temperature match very well, which provides good reliability for later modeling work. Since it is hard to measure the temperature at a position inside the melt because of the required transfer process, we are unable to compare the simulated temperature with a measured temperature inside the melt. If we can find a method to easily measure the temperature of a few points inside the melt, we will be able to provide an even more reliable temperature profile.

6.4.5 Temperature and Temperature Gradient at the Average Growth Front

In Figure 5.6, we have seen the growth front of samples cooled for various times. The corresponding average growth rate and primary arm spacing, λ_1, for different time intervals were measured and presented in Figures 5.7 and 5.16, respectively. Since the average growth rate and primary arm spacing are used, we shall also use average growth time, meaning we will choose the center of each growth layer as the average growth distance; the corresponding time is the average growth time. By doing this, we automatically assume that for a short time interval, the thickness of the growth layer approximately has a linear relationship with the growth time. Thus, the interested growth time points are the average of each time interval in Figure 5.16, i.e., 90, 240, 480, 780, and 1050 seconds.

To study the temperature profile of the above-mentioned time-distance points, a temperature profile as a function of time and z, which is the distance of a point inside the melt to the top melt surface, is plotted as shown in Figure 6.16.

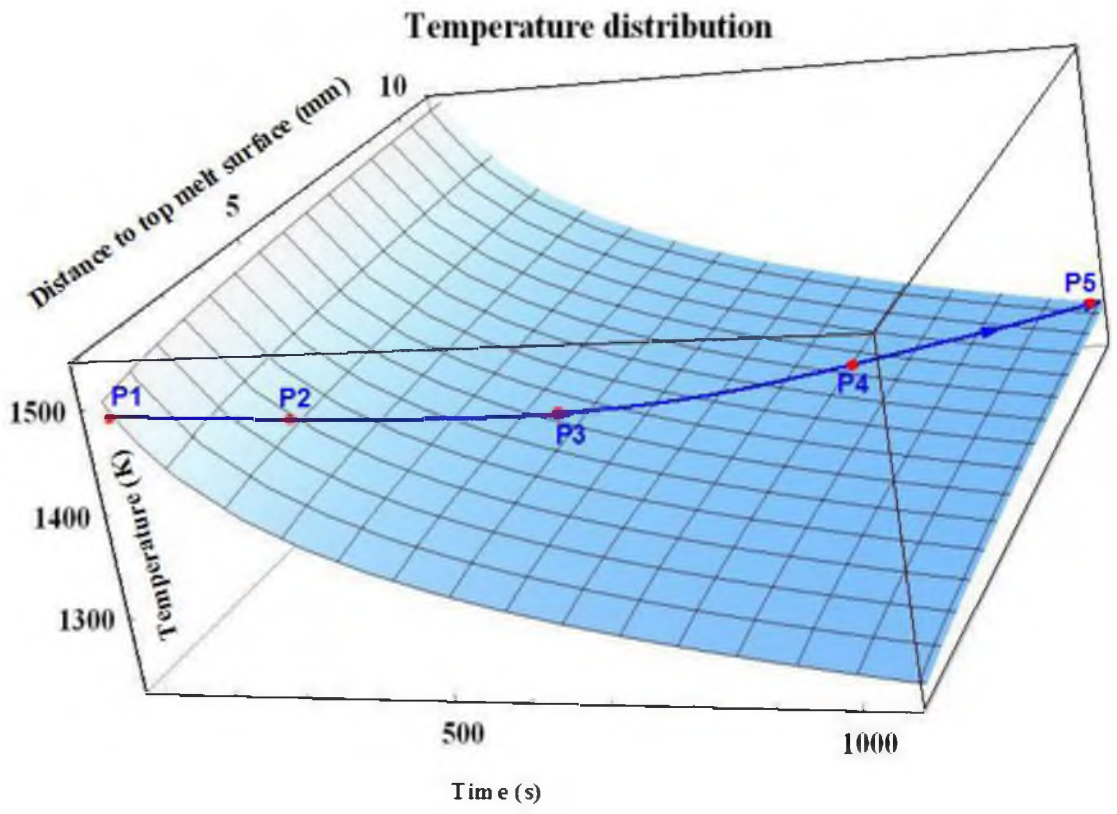

Figure 6.16 Temperature profile as a function of time and z, which is the distance of a point inside the melt to the top melt surface. P1 to P5 represent the locations corresponding to the average growth time of 90, 240, 480, 780, and 1050 seconds, respectively, for the solidified layers as shown in Figure 5.6.

The red dots, P1 to P5 in Figure 6.16, represent the locations corresponding to the times of 90, 240, 480, 780, and 1050 seconds, respectively.

The temperature profile corresponding to Figure 6.16 is given as follows

$$T = 2113t^{-0.076}z^{9.8\times10^{-3}} \tag{6.59}$$

Differentiating Equation (6.59) with respect to z yields the temperature gradient

$$G = \frac{\partial T}{\partial z} = 20.71t^{-0.076}z^{-0.99} \tag{6.60}$$

Differentiating Equation (6.59) with respect to t yields the true cooling rate

$$T' = \frac{\partial T}{\partial t} = -160.59t^{-1.076}z^{9.8\times10^{-3}} \tag{6.61}$$

6.5 Modeling of Cellular and Dendritic Growth

6.5.1 The New Model

In the following sections, we shall present how we developed the model as deduced in Equations (6.9) and (6.12). In order to achieve this, we need first examine some of the results and conclusions we reached in Chapter 5.

- The average cellular/dendritic growth rate decreases with decreasing temperature gradient ahead of the growth front. This conclusion is supported by Figure 5.7 and is replotted in Figure 6.17 as 3D format for a direct comparison.
- The solidified samples present Root-Trunk-Tip microstructure distribution, where the Root-Zone and Tip-Zone refer to the initial and end stages of the

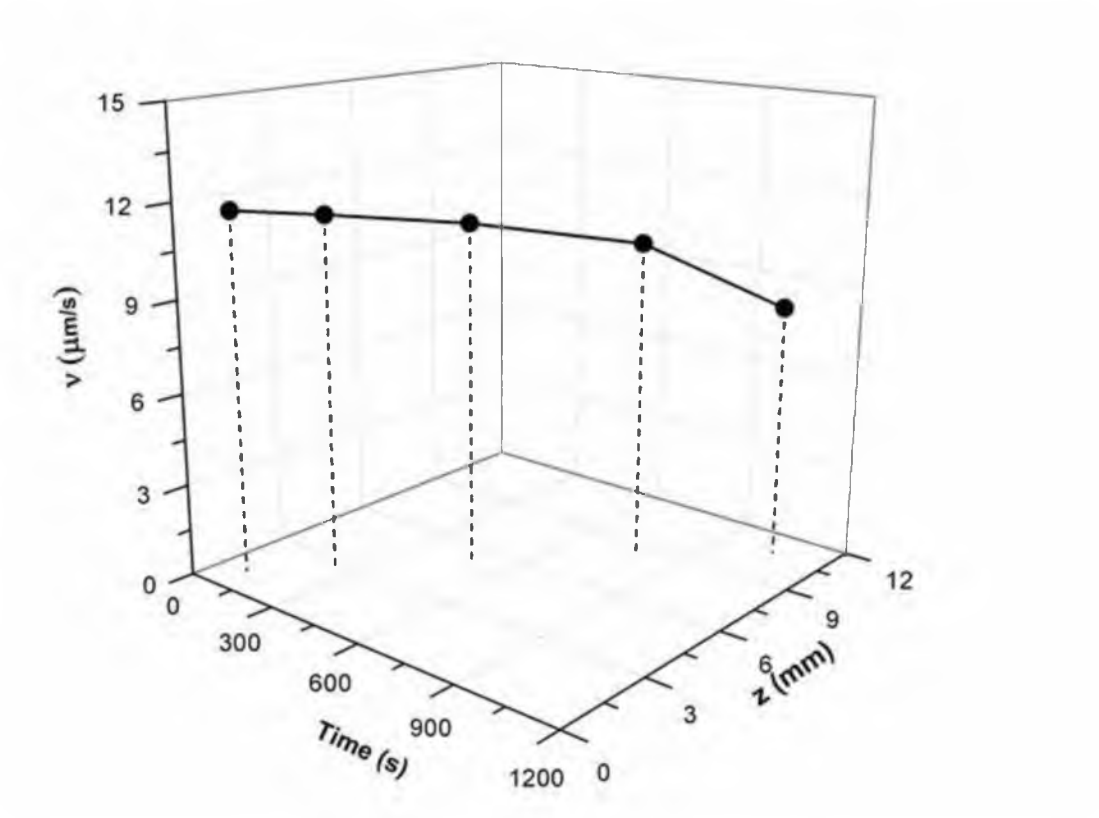

Figure 6.17 The measured average cellular/dendritic growth rate as a function of growth time and distance to the top melt surface.

growth process while the Trunk-Zone is locating in between of the other two zones. The Trunk-Zone has the most uniform microstructure and orientation properties. This feature is seen in Figure 5.12.

- Both the primary spacings measured from the Tip-Zone and Trunk-Zone decrease slightly with decreasing temperature gradient and finally reach a stable level as a result of the dynamic evolution of a changing concentration of cellular/dendritic growth defects, which are the elimination, tip splitting, and growth of tertiary arms. This conclusion is supported by Figure 5.16, and replotted in Figure 6.18.

Using Equations (6.8), (6.60), and (6.61), we then calculated the reference undercooling temperature with respect to T_L or T_M, the temperature gradient G, and the true cooling rate T' for points P1 to P5, and the results are plotted in Figures 6.19 to 6.22.

To fit the data shown in the above figures, we shall reproduce Equation (6.12) here for convenience.

$$\lambda_1 = c\left(\frac{kD\Delta T_0 \Gamma L}{\Delta T_r}\right)^{n/4} \nu^{-p/4} \left(\left|G / T'\right|\right)^{-q/4} \tag{6.62}$$

or

$$\lambda_1 = c\left(\frac{kD\Delta T_0 \Gamma L}{\Delta T_r}\right)^{n/4} \nu^{-p/4} \left(\left|\frac{\partial T}{\partial x} / \frac{\partial T}{\partial t}\right|\right)^{-q/4} \tag{6.63}$$

where all the parameters have been defined in corresponding sections. n, q, and p are

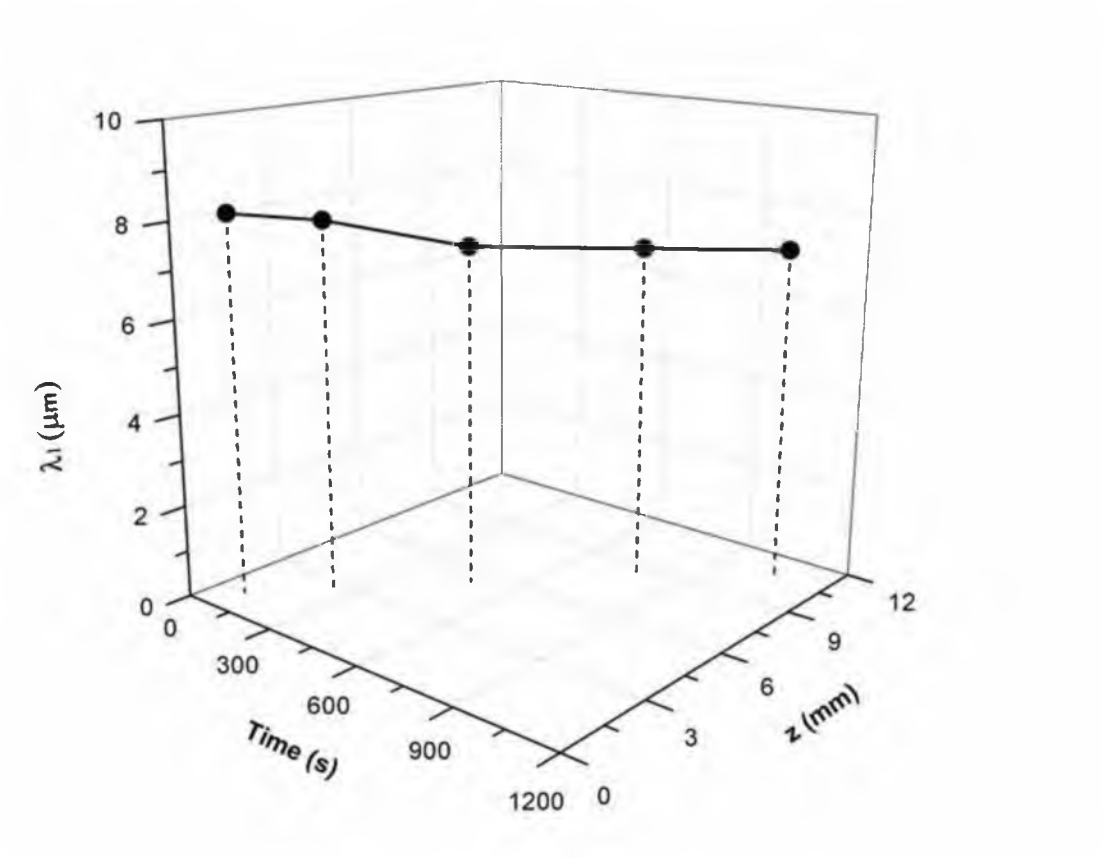

Figure 6.18 The measured average cellular/dendritic primary arm spacing λ_1 as a function of growth time and distance to the top melt surface.

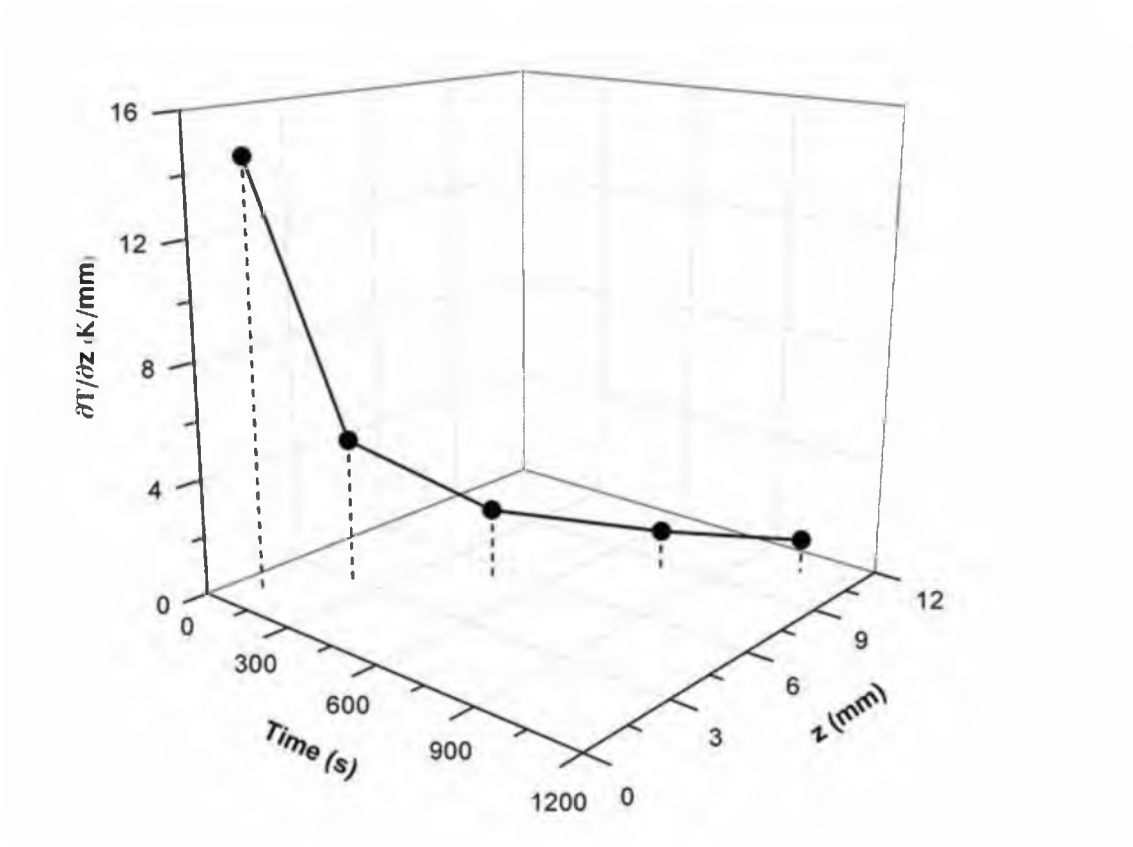

Figure 6.19 The simulated temperature gradient as a function of growth time and distance to the top melt surface.

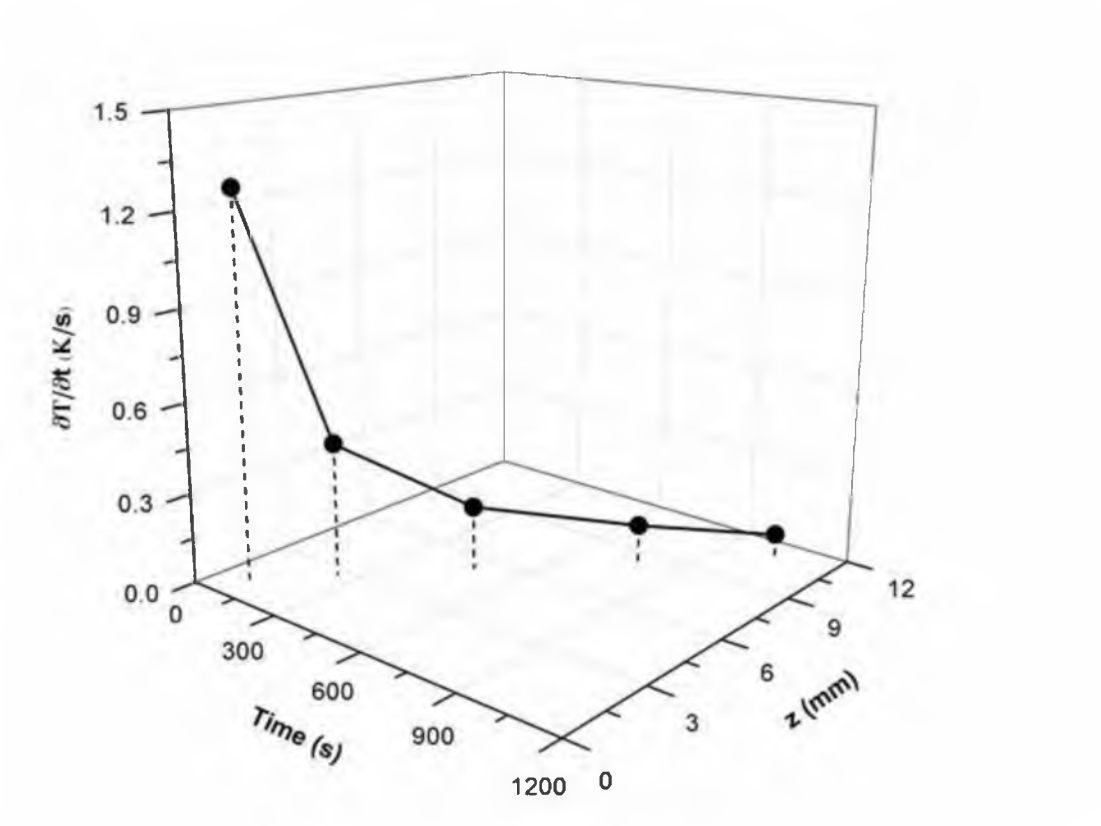

Figure 6.20 The simulated true cooling rate as a function of growth time and distance to the top melt surface.

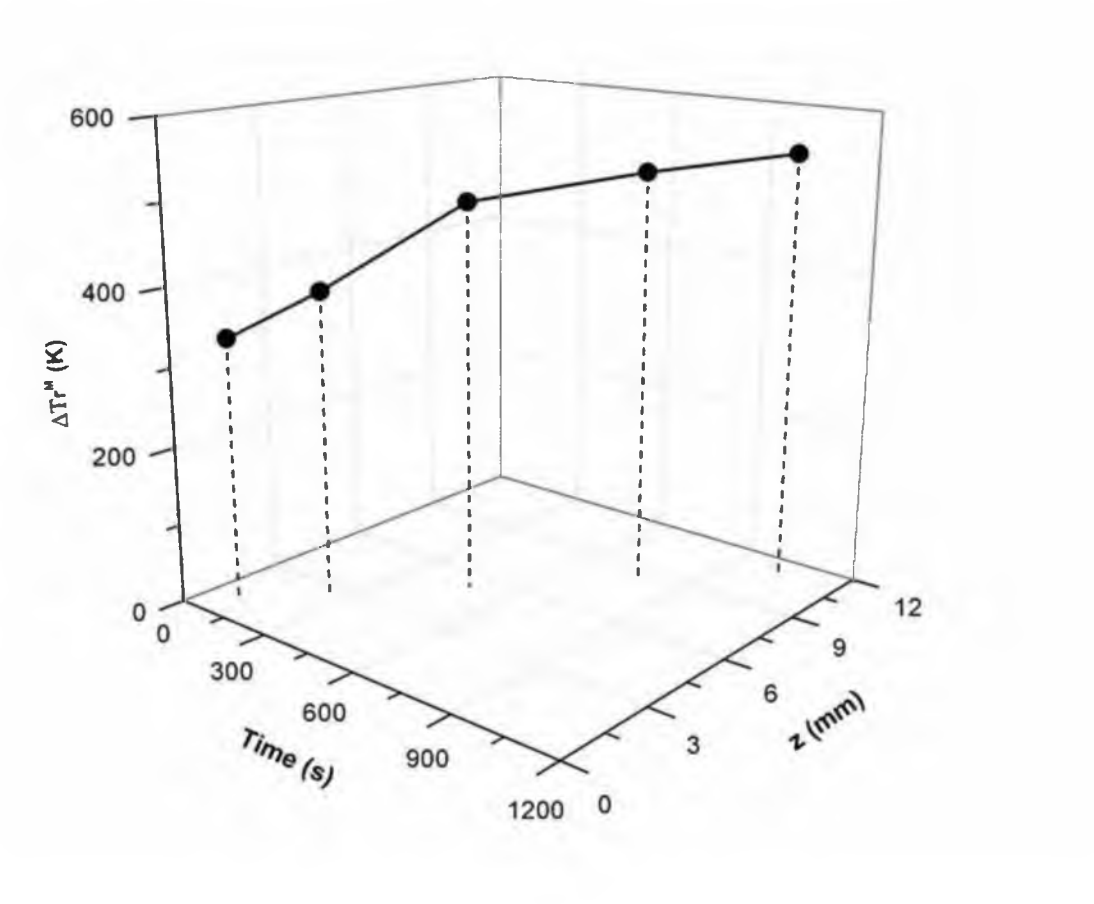

Figure 6.21 The simulated reference undercooling temperature ΔT_r^M as a function of growth time and distance to the top melt surface using T_M as the reference temperature.

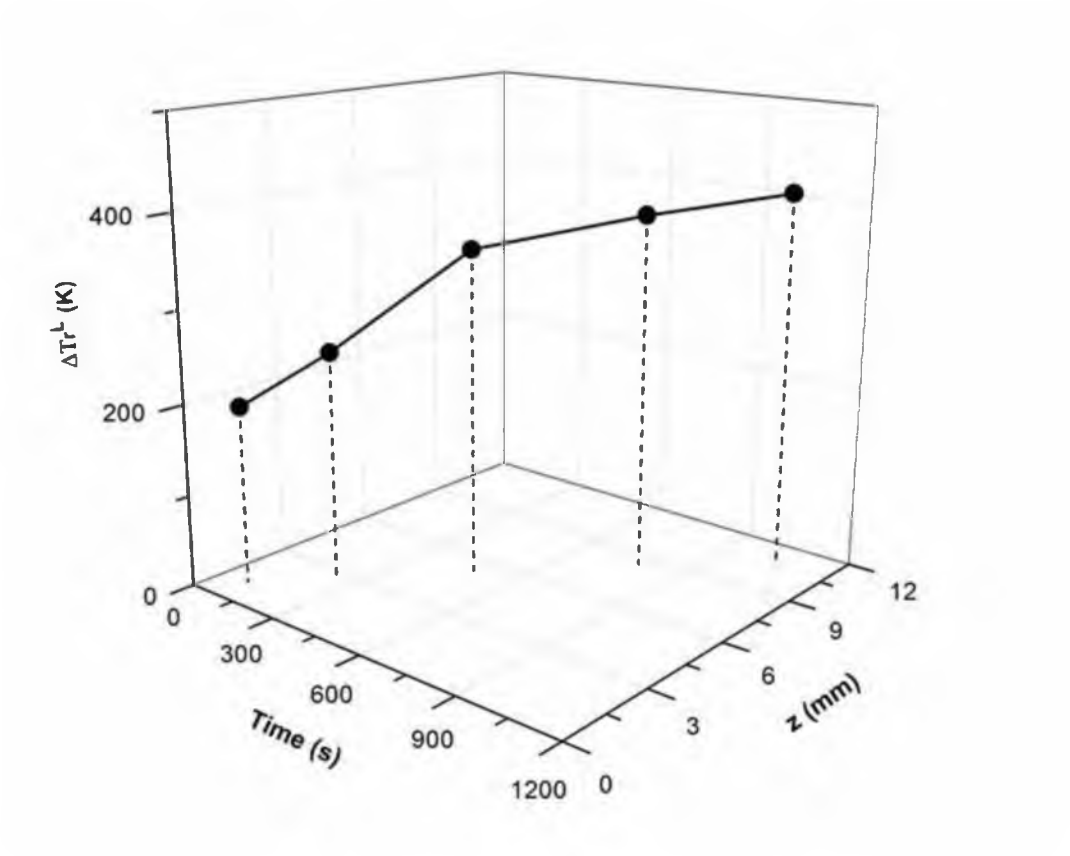

Figure 6.22 The simulated reference undercooling temperature ΔT_r^L as a function of growth time and distance to the top melt surface using T_L as the reference temperature.

some integers with the following suggested values:

$$n, p, q = 0, 1, 2, 3, 4. \tag{6.64}$$

Rearranging Equation (6.9) by moving the constants to one side, we have

$$\lambda_1 v^{p/4} (|G/T'|)^{q/4} \Delta T_r^{n/4} = Const. \tag{6.65}$$

or more conveniently,

$$\lambda_1^4 v^p (|G/T'|)^q \Delta T_r^n = Const. \tag{6.66}$$

After several tries with the constants, we obtained the following combination, which provides a good fit when p = n =1, q =3.

$$\lambda_1^4 v(|G/T'|)^3 \Delta T_r^M = 26.12 \tag{6.67}$$

where ΔT_r^M is the reference undercooling temperature with respect to T_M .

or

$$\lambda_1^4 v(|G/T'|)^3 \Delta T_r^L = 17.89 \tag{6.68}$$

where ΔT_r^L is the reference undercooling temperature with respect to T_L .

The detailed results are listed in Table 6.5 under the new model. The standard deviations for the two fits are calculated as 1.16 and 1.90, respectively. Apparently, ΔT_r^M yields better fit.

Although the new model has succeeded in the prediction of 2M-wollastonite growth, it is still not that convenient for direct application because of the interdependence

Table 6.5 Parameters used for the modeling of this study and the corresponding constants obtained using existing models and the new model

Experimental parameters		Modeling parameters					Constants of simulation models		
t (s)	z (μm)	v (μm/s)	λ_1 (μm)	ΔT_r^M (K)	$\lvert G\rvert$ (K/μm)	$\lvert T'\rvert$ (K/s)	Hunt-KF-Trivedi model	BK model	New model
90	1.01E3	11.70	8.13	335	14.57E-3	1.27	10.85	11.27	25.86
240	2.68 E3	11.51	7.96	389	5.15E-3	0.45	1.23	3.76	26.94
480	5.27 E3	11.15	7.35	494	2.50E-3	0.21	0.2	1.51	27.12
780	8.40 E3	10.42	7.25	527	1.52E-3	0.13	0.07	0.83	24.23
1050	10.80 E3	8.33	7.21	549	1.16E-3	0.09	0.03	0.50	26.47

Note: 1. The parameters have the following definitions: t is the growth time, z is the distance from cellular/dendrite growth front to the top melt surface. v is the growth rate, λ_1 is the primary arm spacing measured at the Trunk-Zone as discussed in Chapter 5, ΔT_r^M is the reference undercooling temperature using the melting point of pure wollastonite as the reference T_M as defined in (6.8), $\lvert G\rvert$ is the absolute temperature gradient $\left\lvert\frac{\partial T}{\partial z}\right\rvert$, T' is the absolute true cooling rate, it equals $\left\lvert\frac{\partial T}{\partial t}\right\rvert$.

2. Hunt-KF-Trivedi Model: $\lambda_1^4 G^2 v = Const.$

BK model: $\lambda_1^2 G v = Const.$

New model (this study): $\lambda_1^4 (G/T')^3 v \Delta T_r^M = Const.$

3. The smaller the differences among the constants, the better prediction of the model is.

of the growth rate and primary arm spacing in this model, as well as in other existing models. The immediate problem of using the new model is that we have to know either the growth rate or the primary arm spacing to predict the other one, which is still inconvenient. Therefore, in the last step, we will try to disconnect this interdependence, and build similar models to predict the growth rate or the primary arm spacing based on ΔT_r, G, and T' only, which have been simulated and are available.

With the above objectives, we propose the following two relationships

$$\lambda_1(|G/T'|)^{q/4}\Delta T_r^{n/4} = Const. \tag{6.69}$$

$$v^p(|G/T'|)^{-q/4}\Delta T_r^{n/4} = Const. \tag{6.70}$$

where the parameters remain the same as being defined previously, q and n are suggested having the values of 0, 1, 2, 3, or 4.

After plugging the experimental data into Equations (6.69) and (6.70), we are able to obtain the following combinations:

$$\lambda_1(|G/T'|)^{1/4}(\Delta T_r^M)^{1/4} = 64.7 \tag{6.71}$$

$$v(|G/T'|)(\Delta T_r^M)^{1/4} = 0.58 \tag{6.72}$$

The standard deviations for the two fits are 0.7 and 0.04, respectively.

6.5.2 Comparison with Existing Models

Before we compare the new model proposed in this study with other models, we shall first compare the simulation parameters either directly measured or calculated as a

whole, as shown in Figure 6.23.

As can be seen in Figure 6.23, the growth rate, primary arm spacing, and undercooling terms with a power exponent of ¼, which is the default exponent in all of the models including the one we proposed, do not change very significantly with increasing time. On the contrary, $\frac{\partial T}{\partial x}$ and $\frac{\partial T}{\partial t}$ both have significant time-dependence. This relatively large change is the main reason that contributes to the failure of fitting the experimental data to the older models. However, as also seen in this figure, the ratio of the $\frac{\partial T}{\partial x} / \frac{\partial T}{\partial t}$ or its reciprocal varies very slightly with increasing time; it is because of this reason that we include the ratio rather than just one of the two terms in our simulation, and in this way, we obtained a reliable constant, as presented in Table 6.5.

6.5.3 Comparison with Experimental Data

Once the new model has been determined, the next step is to verify the validation of this model. One way to achieve this is to predict some of the parameters using the corresponding model.

Figure 6.24 compares the measured and simulated growth rate with given λ_1. It is clearly seen that the one using ΔT_r^M as the reference undercooling temperature has a better prediction than the one using ΔT_r^L as the reference undercooling temperature, which agrees with the above-observed standard deviation calculation. However, both undercooling temperatures yield reliable results in the given measuring range.

Similarly, Figure 6.25 compares the simulated λ_1 with given v. Again, the one using ΔT_r^M as the reference undercooling temperature offers a better prediction than the

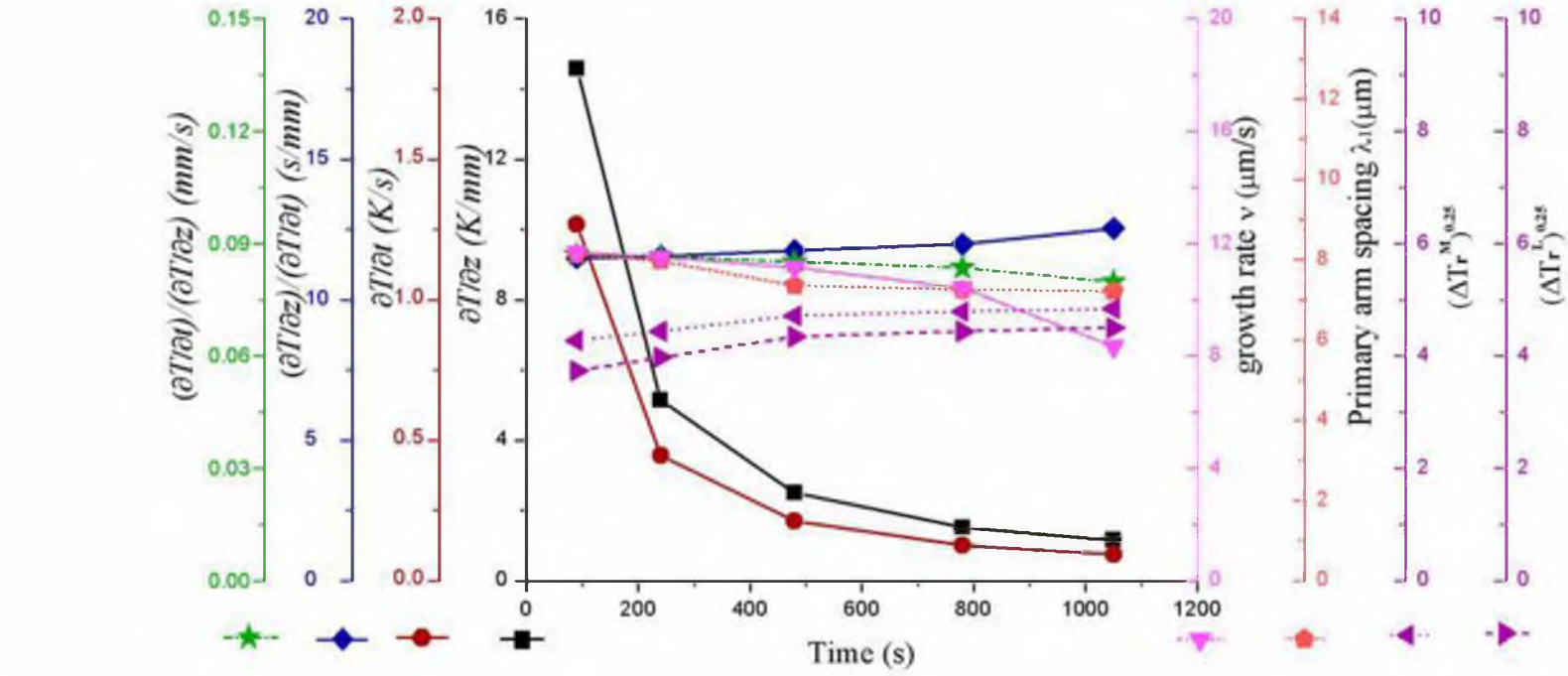

Figure 6.23. An overall comparison for the growth rate, primary arm spacing undercooling temperatures, temperature gradient, cooling rate, and the ratio between the last two as a function of cooling time.

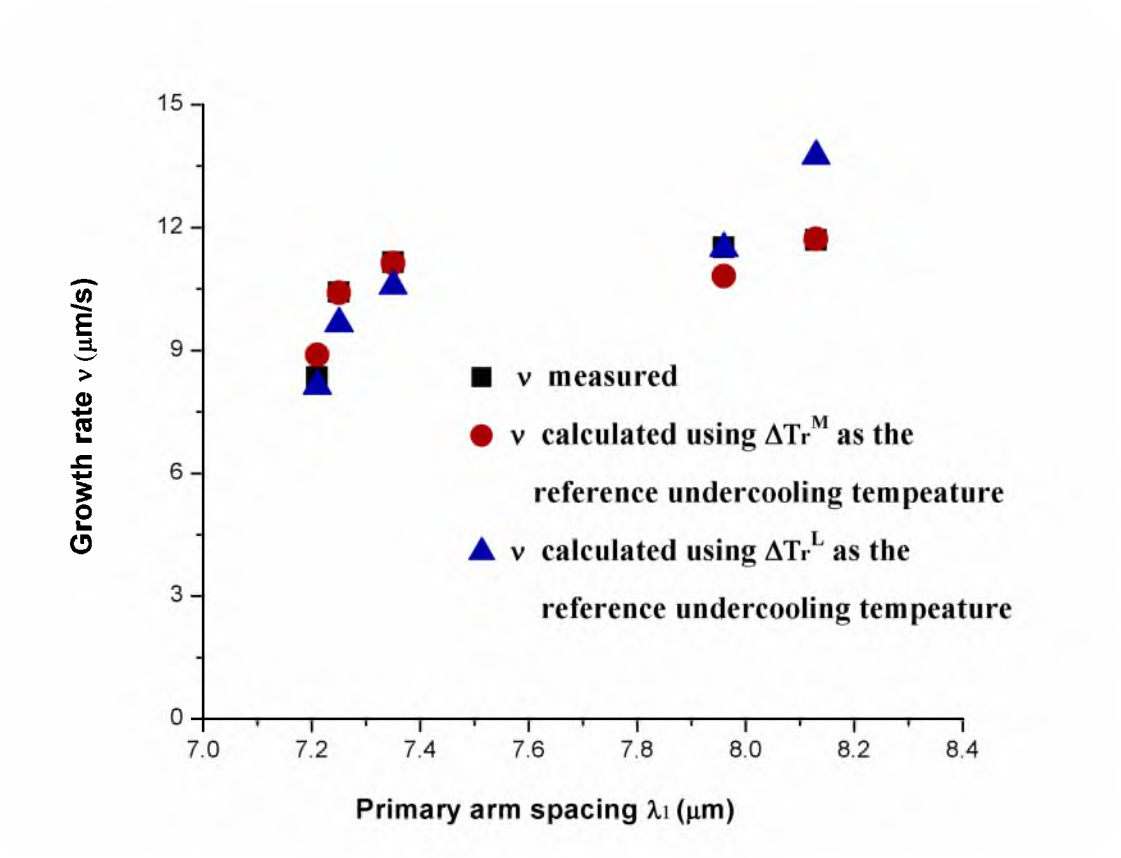

Figure 6.24 A comparison between measured and simulated growth rate with respect to the primary arm spacing. The simulated growth rate using ΔT_r^M as the reference undercooling temperature gives a better prediction than the one using ΔT_r^L as the reference undercooling temperature.

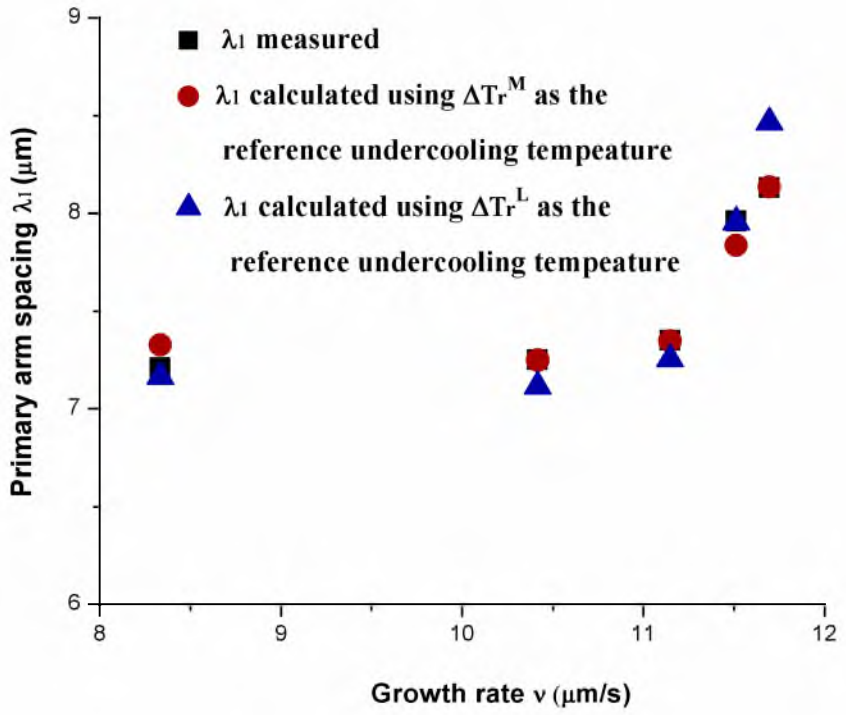

Figure 6.25 A comparison between measured and simulated primary arm spacing with respect to the growth rate. The simulated primary arm spacing using ΔT_r^M as the reference undercooling temperature has a better prediction than the one using ΔT_r^L as the reference undercooling temperature.

one using ΔT_r^L as the reference undercooling temperature. This difference could be likely caused by a relatively large error during the measurement of T_L. For systems where ΔT_r^M is much easier to obtain than ΔT_r^L, the former is recommended. For systems where both parameters are equally available, then we can plug both into the proposed model and choose the one that yields a series of constants with smaller standard deviation.

6.6. Conclusions

With the above discussion and explanations, the following conclusions regarding the cellular and dendritic growth of 2M-wollastonite from a ceramic alloy can be made as follows.

Various existing models on the prediction of cellular and dendritic growth have been compared through Table 6.5. A failure of fitting the experimental data into these models suggests a necessity of modifying or improving the existing models.

Based on the observation and comparison of existing models, we proposed a new model, as shown below.

$$\lambda_1 = c\left(\frac{k D \Delta T_0 T_L}{\Delta T_r}\right)^{n/4} v^{-p/4} \left(G/T\right)^{-q/4}$$

All the parameters have been defined previously. n, q, and p are some integers with the suggested values of: $n, p, q = 0, 1, 2, 3, 4$. Because of the difficulty of obtaining the constants in the above model, a more convenient format is written as

$$\lambda_1^4 v^p \left(G/T\right)^q \Delta T_r^n = Const$$

In order to verify the above model, one of the critical parameters is the

temperature distribution of a Melt-Crucible-Furnace cooling system. Based on mathematical calculations and computation software such as MatLab and Wolfram Mathematica, we successfully simulated the temperature profile of the melt as a function of dimensional parameters and time.

With the aid of a simulated temperature profile, the experimental data are fitted into the proposed model, and we are able to obtain a combination that provides a good fit when p = n =1, q =3, with the fact that the use of ΔT_r^M as the reference undercooling temperature has a better prediction than the use of ΔT_r^L as the reference undercooling temperature for this studied ceramic alloy system.

CHAPTER 7

CELLULAR AND DENDRITIC GROWTH UNDER UNSTEADY-STATESOLIDIFICATION: PART III. MODELING OF WOLLASTONITE GROWTH

7.1 Introduction

In Chapter 4, we introduced an effective way of producing acicular wollastonite particles using the Flux Growth process, where we observed an important characteristic microstructure pattern of wollastonite growth, i.e., the solidified crystals displayed a combination of oriented cellular and dendrite structures. Following that observation, we did further experiments in Chapter 5 to systematically study the cellular/dendrite structure in order to understand the growth behavior of such structures and to find the relationship between the mean aspect ratio and the primary arm spacing. We clearly found evidences for a strong relationship between the two parameters (Figure 5.26). However, because of the complexity of these molten oxides at high temperatures, we were unable to directly set up this correlation without the help of a simulation process, such as temperature simulation to obtain a real-time temperature and temperature gradient distribution at different locations, especially when we found that the existing models on cellular and dendritic growth are not sufficient or applicable to explain the experimental data that we have observed for wollastonite growth (Table 6.5). Because of this situation, simulation

and modeling of cellular and dendritic growth are studied in Chapter 6, where we proposed a new model for cellular and dendritic growth that applies mainly to unsteady-state high-temperature heat flow system and ceramic alloys, but it can reduce to other models under special conditions and thus is also applicable to metal and organic alloys under steady-state low temperature heat flow growth condition. Using the proposed model, we have simulated two important parameters that are related to wollastonite growth, which are growth rate (v) and primary arm spacing (λ_1), as a function of other parameters such as temperature gradient (G or $\frac{\partial T}{\partial x}$) , cooling rate (T' or $\frac{\partial T}{\partial t}$), and reference undercooling ΔT_r. All of these parameters have been defined previously in corresponding sections.

With the above-obtained experimental and simulation results, we are able to reach the next step which is also our final goal, where we will directly simulate the stages of wollastonite growth under a unidirectional or quasi-unidirectional heat flow condition, and predict the most important parameter for this study, the mean aspect ratio, as a function of growth time and raw material composition.

7.2 Simulation of Growth Front

The purpose of simulating the growth front is to monitor the solidification process at different time, so that we know how much time we need for a complete solidification.

In order to achieve this goal, the following relationship between growth rate and other parameters will be used.

$$v^p(|G/T|^{-})^{\phi 4}\Delta_r T^{n/4} = Co. \qquad (7.1)$$

where the parameters remain the same as being defined previously, q and n are suggested having the values of 0, 1, 2, 3 or 4. When used for wollastonite growth, the above equation becomes

$$\nu(|G/T'|)(\Delta T_r^M)^{1/4} = 0.58 \tag{7.2}$$

Rewriting Equation (7.2) to separate ν from other parameters.

$$\nu = \frac{0.58}{(|G/T'|)(\Delta T_r^M)^{1/4}} \tag{7.3}$$

The temperature profile corresponding to the system to be simulated has been determined previously as

$$T = 2113t^{-0.076}z^{9.8\times10^{-3}} \tag{7.4}$$

Differentiating Equation (6.59) with respect to z yields the tempeature gradient

$$G = \frac{\partial T}{\partial z} = 20.71t^{-0.076}z^{-0.99} \tag{7.5}$$

Differentiating Equation (6.59) with respect to t yields the true cooling rate

$$T' = \frac{\partial T}{\partial t} = -160.59t^{-1.076}z^{9.8\times10^{-3}} \tag{7.6}$$

Since pure wollastonite has a melting point of 1817 K, the reference undercooling is calculated as

$$\Delta T_r^M = 1817 - 2113t^{-0.076}z^{9.8\times10^{-3}} \tag{7.7}$$

In the above equations, v still has z dependence, i.e., the location of growth front. To remove this association, we can further solve z as a function of t using the data provided in Figure 6.13; the solved equation is

$$z = 0.0103t + 0.2173 \tag{7.8}$$

Substitute Equation (7.8) into Equations (7.4) to (7.7), we have

$$T = \frac{2113(0.2173 + 0.0103t)^{0.0098}}{t^{0.076}} \tag{7.9}$$

$$G = \frac{\partial T}{\partial z} = \frac{0.0207}{(0.2173 + 0.0103t)^{0.99} t^{0.076}} \tag{7.10}$$

$$T' = \frac{\partial T}{\partial t} = \frac{160.59(0.2173 + 0.0103t)^{0.0098}}{t^{1.076}} \tag{7.11}$$

$$\Delta T_r^M = 1817 - \frac{2113(0.2173 + 0.0103t)^{0.0098}}{t^{0.076}} \tag{7.12}$$

Then, substitute Equations (7.9) to (7.12) into Equation (7.3), and v becomes

$$v = \frac{4497.45(0.2173 + 0.0103t)^{0.9998}}{(1817 - \frac{2113(0.2173 + 0.0103t)^{0.0098}}{t^{0.076}})^{1/4} t} \tag{7.13}$$

Once v as a function of time is available, the thickness (L) of the solidified cellular/dendrite layer as a function of time can be calculate by the integration of small distance increment dL with respect to time.

Since $dL = v_t dt$, we thus have

$$L = \int_0^t v dt \tag{7.14}$$

The remaining unsolidified melt is simply given as

$$L_{left} = h - L \tag{7.15}$$

where h is the thickness of melt before solidification. In this study, we neglect the volume shrinkage of the melt as a function of temperature; thus, h equals the value measured after the melt has being cooled to room temperature. From repeating experiments, h was found to be 12.5 mm. By substituting h, Equations (7.13) and (7.14) into Equation (7.15), we have

$$L_{left} = 12.5 - 4497.45 \int_0^t \frac{(0.2173 + 0.0103t)^{0.9998}}{(1817 - \frac{2113(0.2173 + 0.0103t)^{0.0098}}{t^{0.076}})^{1/4} t} dt \tag{7.16}$$

To analytically solve the above equation is not an easy task; thus, we choose to solve it numerically, which has a little bit less accuracy but is much easier, and can sufficiently meet our requirements for this simulation process.

The final simulation work is computed using mathematical software named Mathematica. To facilitate the computation process and meanwhile provide a more intuitive and real simulation interface, the molten melt has the same dimensional relationship as that of an actual sample. As can be seen from Figure 7.1, initially, no melt crystallizes at time equals zero. At t = 200 seconds, the growth front has traveled about a

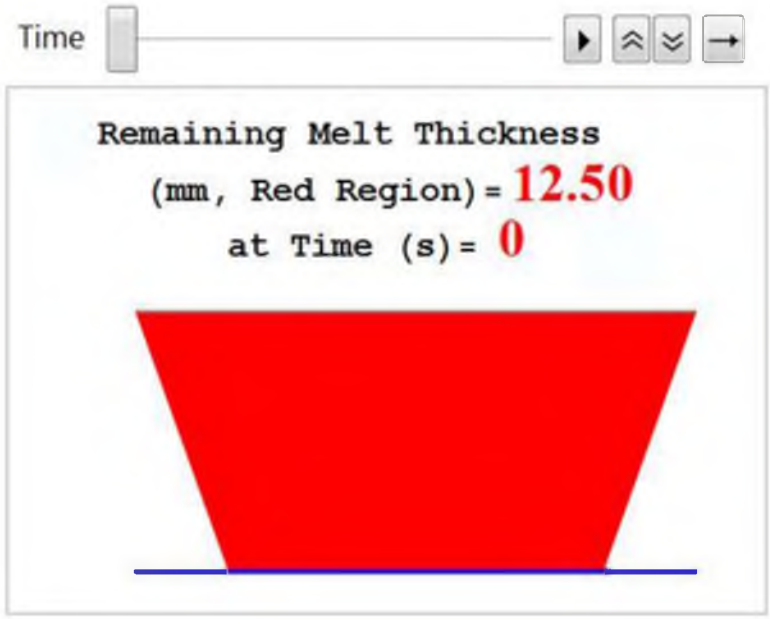

(a)

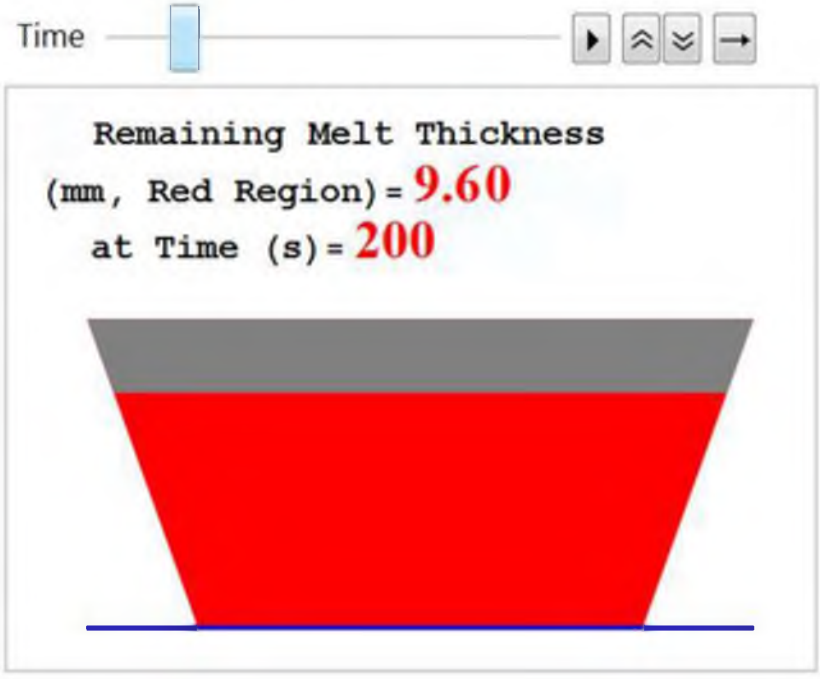

(b)

Figure 7.1 Simulated remaining melt thickness at time equals: (a) 0 second, and (b) 200 seconds, (c) 800 seconds, and (d) 1140 seconds. Red region indicates the unsolidified melt.

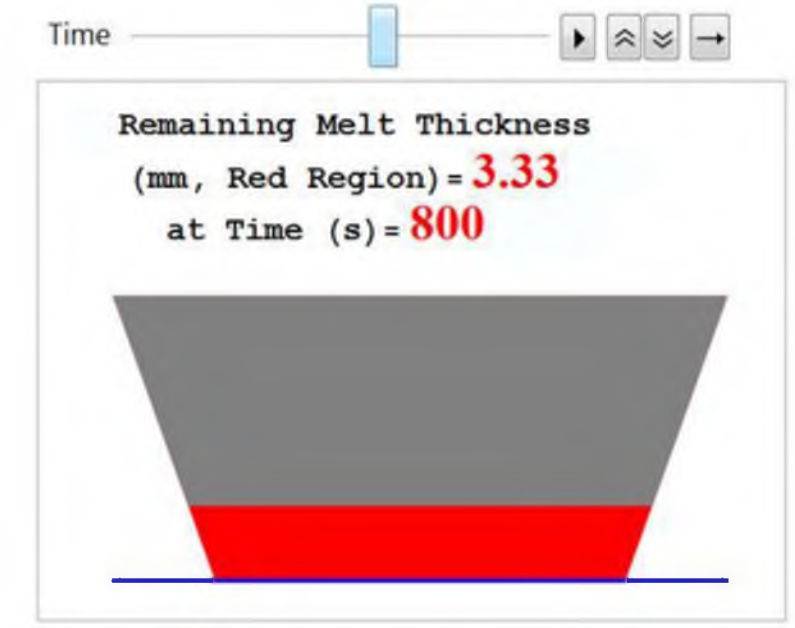

(c)

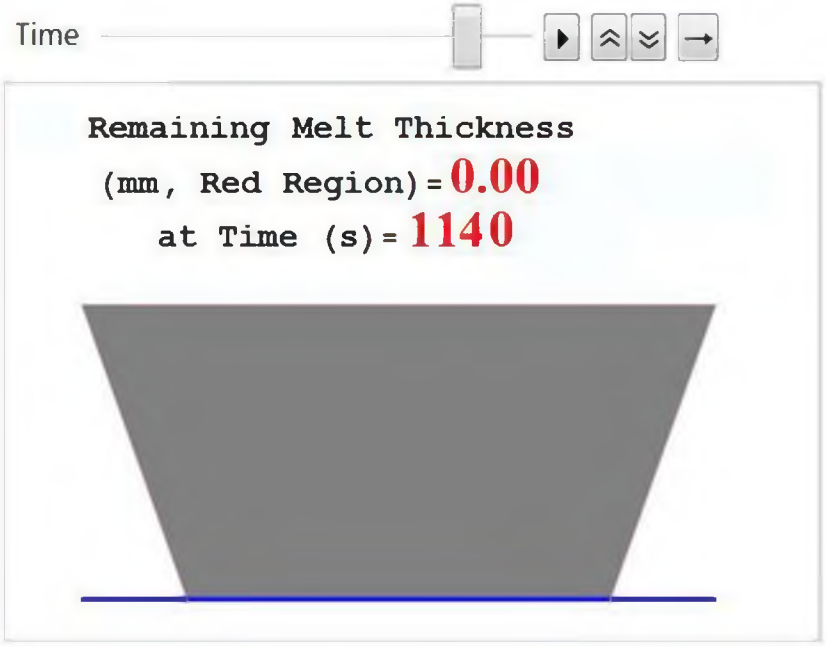

(d)

Figure 7.1 (Continued)

quarter of the total melt thickness. With increasing time, more melt solidifies (Figure 7.1c) and the remaining melt thickness becomes zero at t = 1140 seconds, as seen in Figure 7.1d, which indicates a complete solidification at this point.

To verify the simulated results, the simulated growth front is compared with that of experimental results, as shown in Figure 7.2. The growth front from experimental result at t =180 seconds is slightly higher than the simulated result. This is also true for time equals 300 seconds. However, beginning from 660 seconds, the simulated growth fronts match well with the experimental results, as seen in Figure 7.2c and d. Finally, the remaining melt thickness becomes slightly negative at t = 1200 seconds at which the actual sample presents a complete solidification. It is thus reasonable to conclude that the minimum time for a complete solidification should be within in 1140 seconds and 1200 seconds.

7.3 Simulation of Solidification Volume Fraction

In a way similar to the simulation of solidification thickness, solidification volume fraction or percentage as a function of time can also be simulated by replacing the integration element from a small control distance dL to a small control volume dV. As shown in Figure 7.3, in a truncated-cone shape solid object, for a point having a coordinate of (r, r, z), the relationship between r and z can be written as

$$r = \frac{r_1 - r_0}{h_1 - h_0} h + r_0 - \frac{r_1 - r_0}{h_1 - h_0} h_0 \tag{7.17}$$

where h_0 and h_1 are the z values, while r_0 and r_1 are the r values, of the points located at the bottom and top outer surface, respectively.

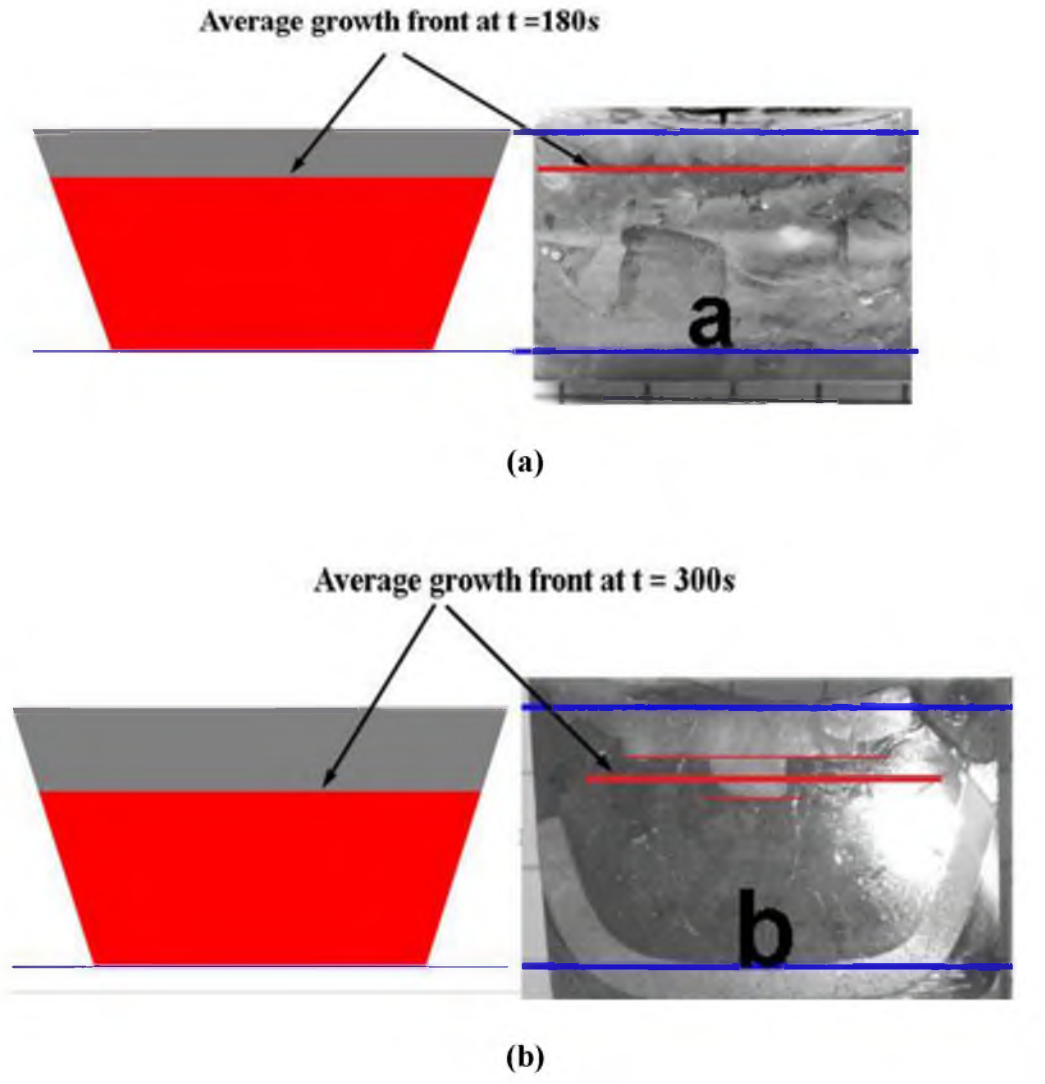

Figure 7.2 Comparison between simulated and measured growth front at time equals: (a) 180 seconds and (b) 300 seconds, (c) 660 seconds, (d) 900 s and (e) 1200 seconds.

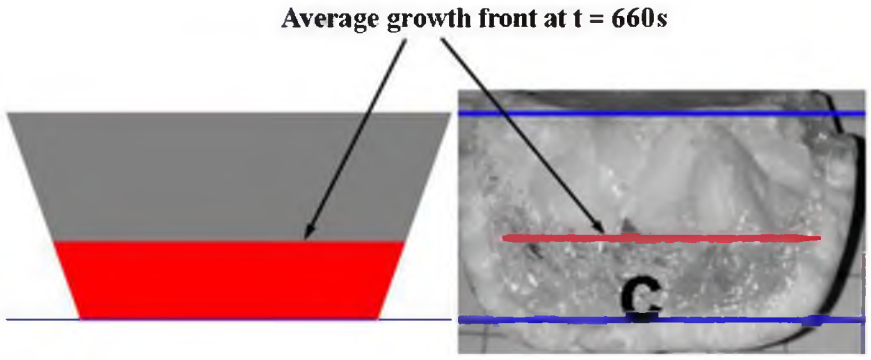

(c)

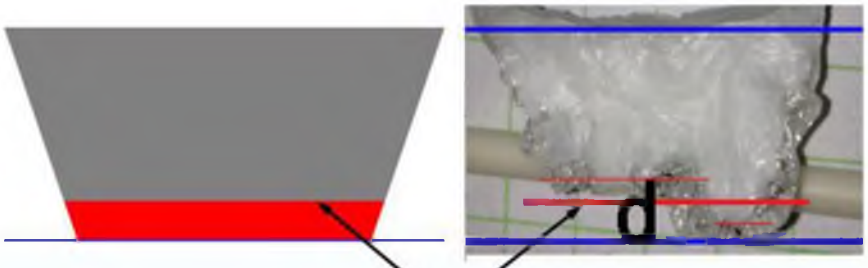

(d)

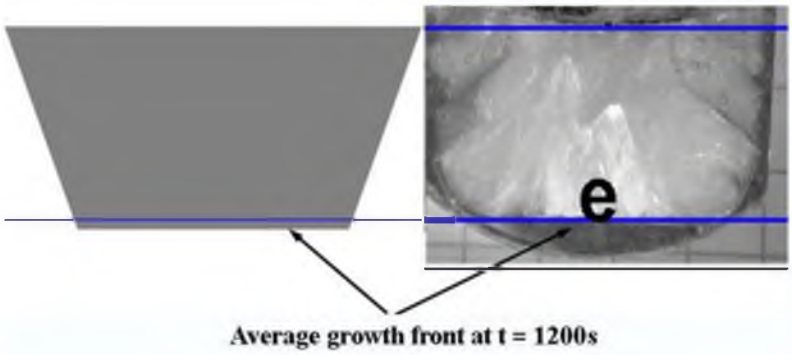

(e)

Figure 7.2 (Continued)

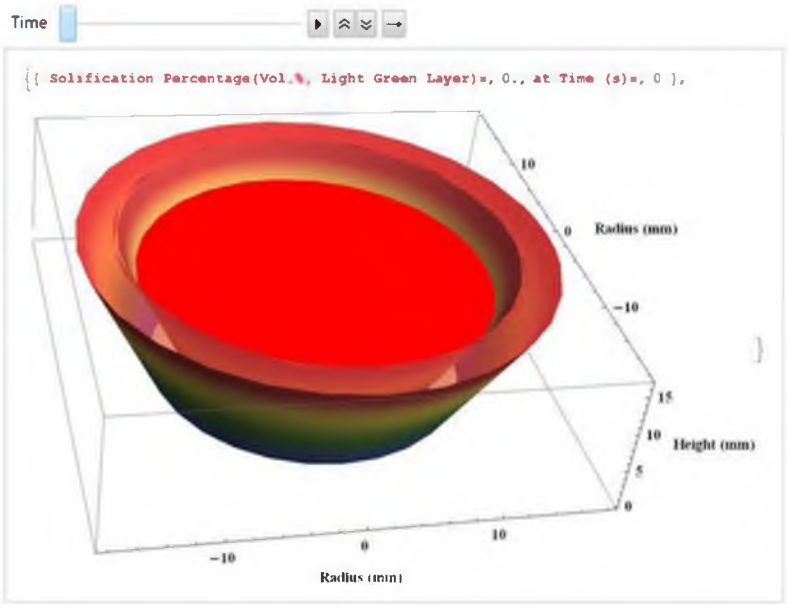

(a)

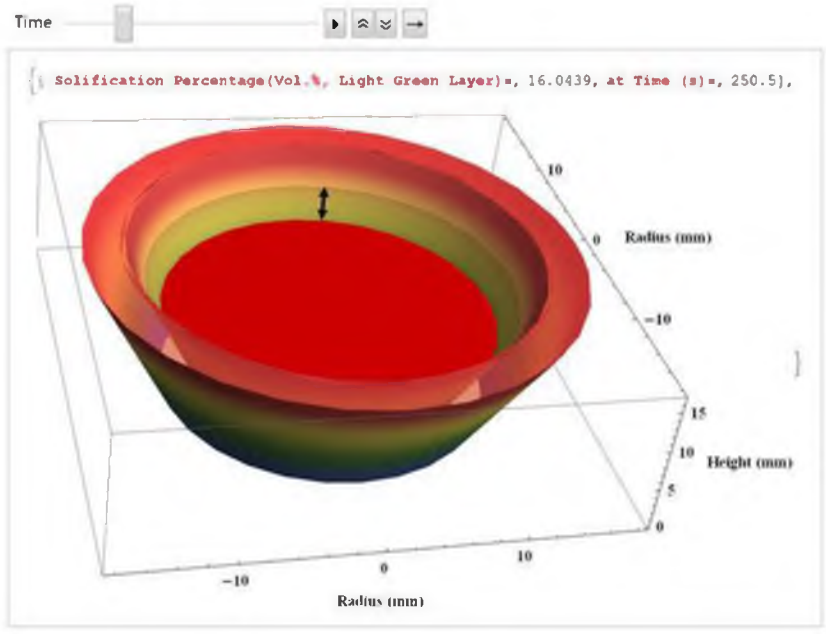

(b)

Figure 7.3 Simulated solidification volume percentages at time equals: (a) 0 second, (b) 250 seconds, (c) 503 seconds, (d) 700 seconds, (e) 1000 seconds, and (f) 1134 seconds.

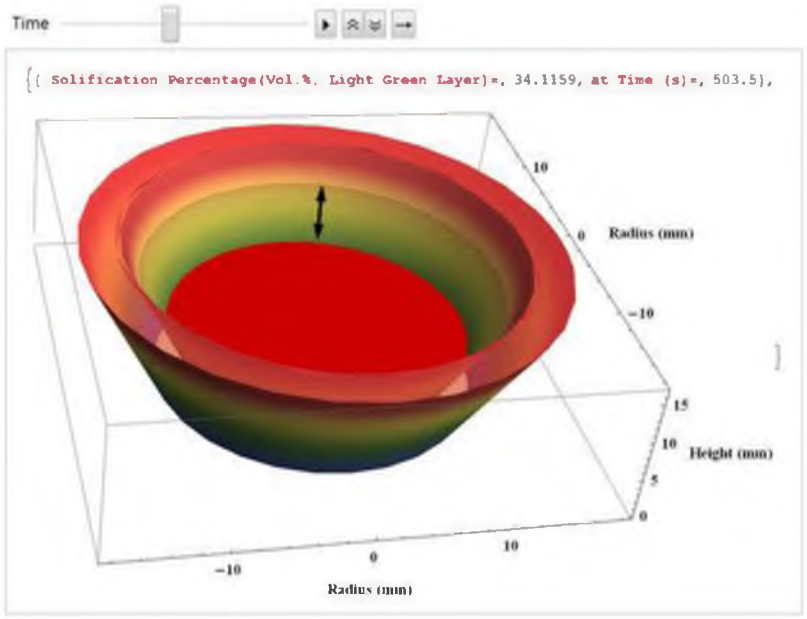

(c)

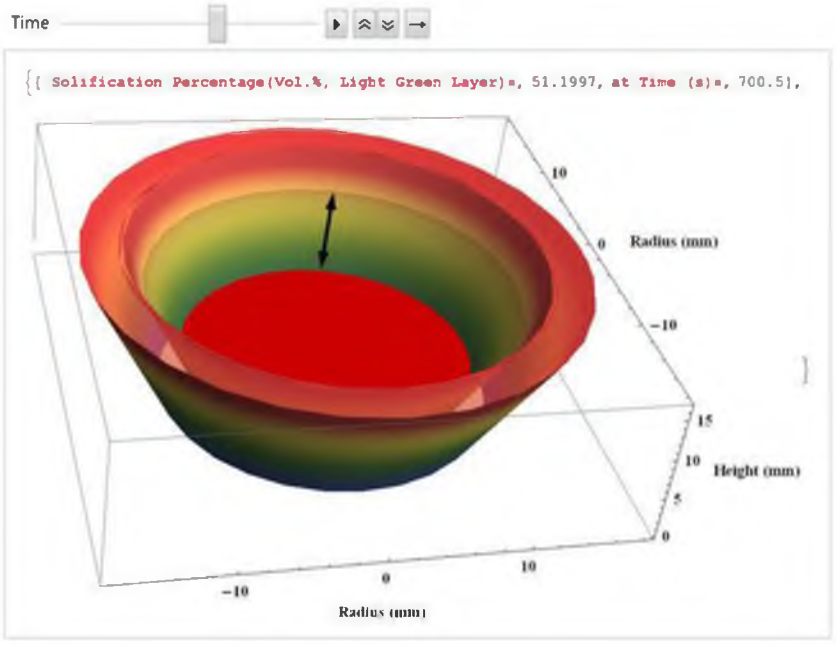

(d)

Figure 7.3 (Continued)

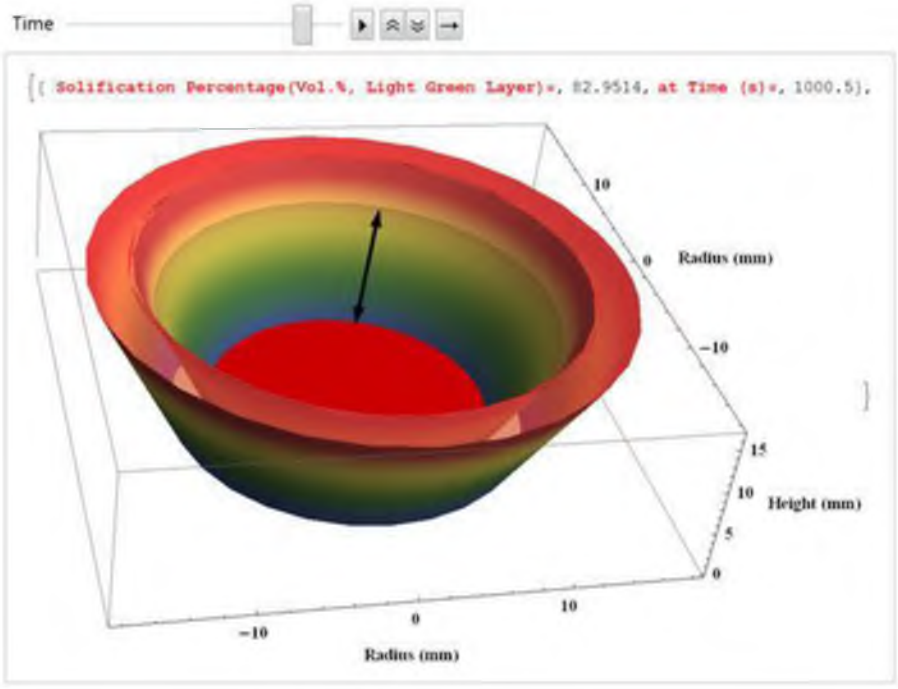

(e)

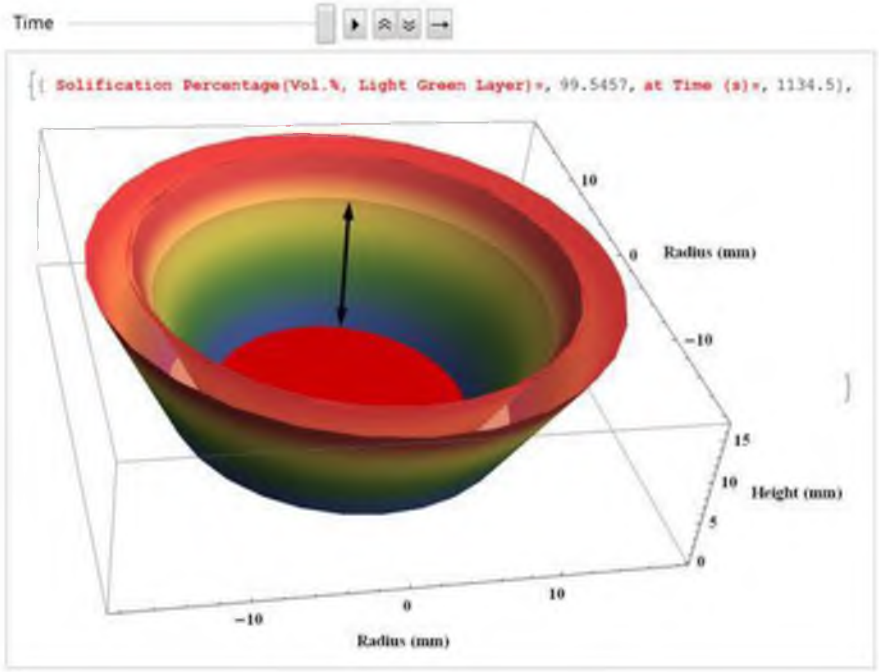

(f)

Figure 7.3 (Continued)

$$dV = \int_{L}^{L+dL} \int \pi r^2 dL \tag{7.18}$$

Assume the top surface is growing at a growth rate of v, and substitute Equation (7.17) into the above equation; it becomes

$$dV = \int_{t}^{t+dt} \pi\left(\frac{r_1 - r_0}{h_1 - h_0} h + r_0 - \frac{r_1 - r_0}{h_1 - h_0} h_0\right)^2 v dt \tag{7.19}$$

From the previous section, h as a function of time is obtained as

$$h = \int_{0}^{t} v dt \tag{7.20}$$

Rewrite Equation (7.20) as

$$dV = \int_{t}^{t+dt} \pi\left(\frac{r_1 - r_0}{h_1 - h_0} \int_{0}^{t} v dt + r_0 - \frac{r_1 - r_0}{h_1 - h_0} h_0\right)^2 v dt \tag{7.21}$$

Integrating Equation (7.21) from 0 to t yields

$$V = \int_{0}^{t} \pi\left(\frac{r_1 - r_0}{h_1 - h_0} \int_{0}^{t} v dt + r_0 - \frac{r_1 - r_0}{h_1 - h_0} h_0\right)^2 v dt \tag{7.22}$$

v as a function of time in the above equations has been solved previously as

$$v = \frac{4497.45(0.2173 + 0.0103t)^{0.9998}}{\left(1817 - \frac{2113(0.2173 + 0.0103t)^{0.0098}}{t^{0.076}}\right)^{1/4} t} \tag{7.23}$$

Plugging *v* into Equation (7.22), it becomes

$$V = \int_0^t \pi\left(\frac{r_1 - r_0}{h_1 - h_0}\int_0^t \left(\frac{4497.45(0.2173+0.0103t)^{0.9998}}{\left(1817 - \frac{2113(0.2173+0.0103t)^{0.0098}}{t^{0.076}}\right)^{1/4} t}\right)dt + r_0 - \frac{r_1 - r_0}{h_1 - h_0}h_0\right)^2 \left(\frac{4497.45(0.2173+0.0103t)^{0.9998}}{\left(1817 - \frac{2113(0.2173+0.0103t)^{0.0098}}{t^{0.076}}\right)^{1/4} t}\right)dt \quad (7.24)$$

Now, we see that solidification volume at any time is a function of time only. If we take 1138 seconds as the required solidification time as simulated from the previous section, and assign the measured values $h_0 = 0$, $h_1 = 12.5\,\text{mm}$, $r_0 = 9\,\text{mm}$, $r_1 = 13.5\,\text{mm}$, Equation (7.24) reduces to

$$V = \int_0^t \pi\left(\frac{13.5-9}{12.5}\int_0^t \left(\frac{4497.45(0.2173+0.0103t)^{0.9998}}{\left(1817 - \frac{2113(0.2173+0.0103t)^{0.0098}}{t^{0.076}}\right)^{1/4} t}\right)dt + 9\right)^2 \left(\frac{4497.45(0.2173+0.0103t)^{0.9998}}{\left(1817 - \frac{2113(0.2173+0.0103t)^{0.0098}}{t^{0.076}}\right)^{1/4} t}\right)dt \quad (7.25)$$

The total volume V_0 solidified at t = 1138 is calculated as

$$V_0 = \int_0^{1138} \pi\left(\frac{13.5-9}{12.5}\int_0^{1138} \left(\frac{4497.45(0.2173+0.0103t)^{0.9998}}{\left(1817 - \frac{2113(0.2173+0.0103t)^{0.0098}}{t^{0.076}}\right)^{1/4} t}\right)dt + 9\right)^2 \left(\frac{4497.45(0.2173+0.0103t)^{0.9998}}{\left(1817 - \frac{2113(0.2173+0.0103t)^{0.0098}}{t^{0.076}}\right)^{1/4} t}\right)dt \quad (7.26)$$

The solidification volume fraction is thus simply given as

$$f_V = \frac{V}{V_0} \tag{7.27}$$

The simulation process is then performed by using Mathematica again. Figure 7.4 presents the simulation results from Equation (7.27).

As can be seen from Figure 7.3, both the solidified layer and f_V increase with increasing time, and they are available by monitoring the movement of the solid-melt interface and by the dynamic number given on top of each graph. From previous simulation and experimental results, we have seen that growth rate decreases with increasing time; therefore, for a cylindrical crucible, the time required for a half solidification volume should be less than the half solidification time. However, as shown in Figure 7.3d, the solidification time is about 20% higher than the half solidification time when the solidification volume fraction is about 0.5, which directly proves the necessity for the simulation of solidification volume fraction, especially when we have large amounts of melt to solidify.

7.4 Simulation of Mean Aspect Ratio

With the simulation of solidification thickness and volume fraction, we are clear about the overall growth stages with respect to growth time and other growth conditions. In this section, we will continue to simulate the relationship between mean aspect ratio and growth conditions.

When other conditions are fixed such as molar ratio of SiO_2 to CaO, Li_2O addition, and crystallization time, B_2O_3 contents play a direct role on the mean aspect

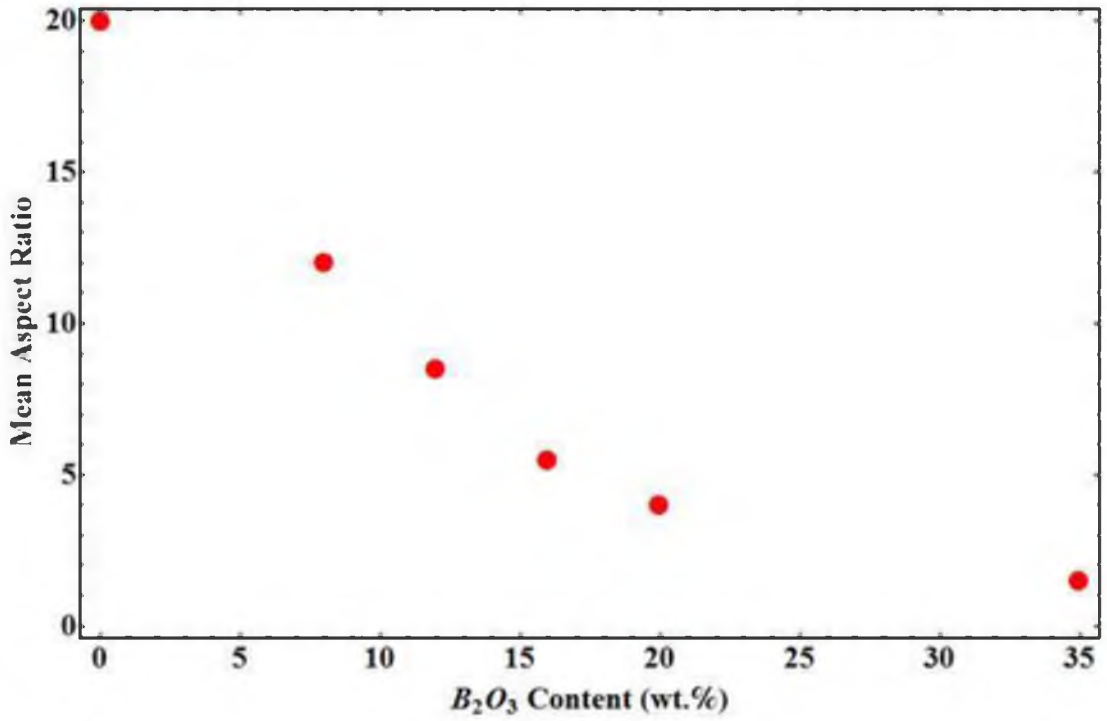

Figure 7.4 Experimental results on the relationship between mean aspect ratio and B_2O_3 contents.

ratios of final products, as seen in Figure 7.4.

Figure 7.4 shows that the mean aspect ratio decreases with increasing B_2O_3 content. Meanwhile B_2O_3 content can affect the primary spacing significantly, as seen in Figure 7.5. Therefore, it is easy to consider associating mean aspect ratio with primary arm spacing directly; this relationship is plotted in Figure 7.7.

Figure 7.6 indicates that the mean aspect ratio will be reduced at higher primary arm spacing. Apparently, the primary arm spacing is the most important parameter for the simulation of mean aspect ratio.

To understand the principle of the following modeling, it is necessary to look at a well-developed cellular structure pattern first, as shown in Figure 7.7.

In Figure 7.7, there are two critical parameters that will be used in this simulation. The first one is the primary arm spacing λ_1, the second is the radial fraction of wollastonite phase f_w. While the former has been extensively studied in previous sections, the latter is firstly mentioned here. The reason to introduce f_w is because of the observation in Figure 7.8, which shows the relationship between f_w and λ_1. As seen in this figure, f_w is not a fixed value with increasing λ_1; instead, it is decreasing almost linearly with λ_1. This linear relationship is fitted into the following equation.

$$f_w = 1 - 0.012\lambda_1 \tag{7.28}$$

By set $f_w = 0$, we obtain a $\lambda_1 = 80$ μm. The physical meaning of this result is that we cannot have very large λ_1, for example a few hundred micro meters, with very low volume fraction of wollastonite phase. Since λ_1 is directly affected by B_2O_3 content,

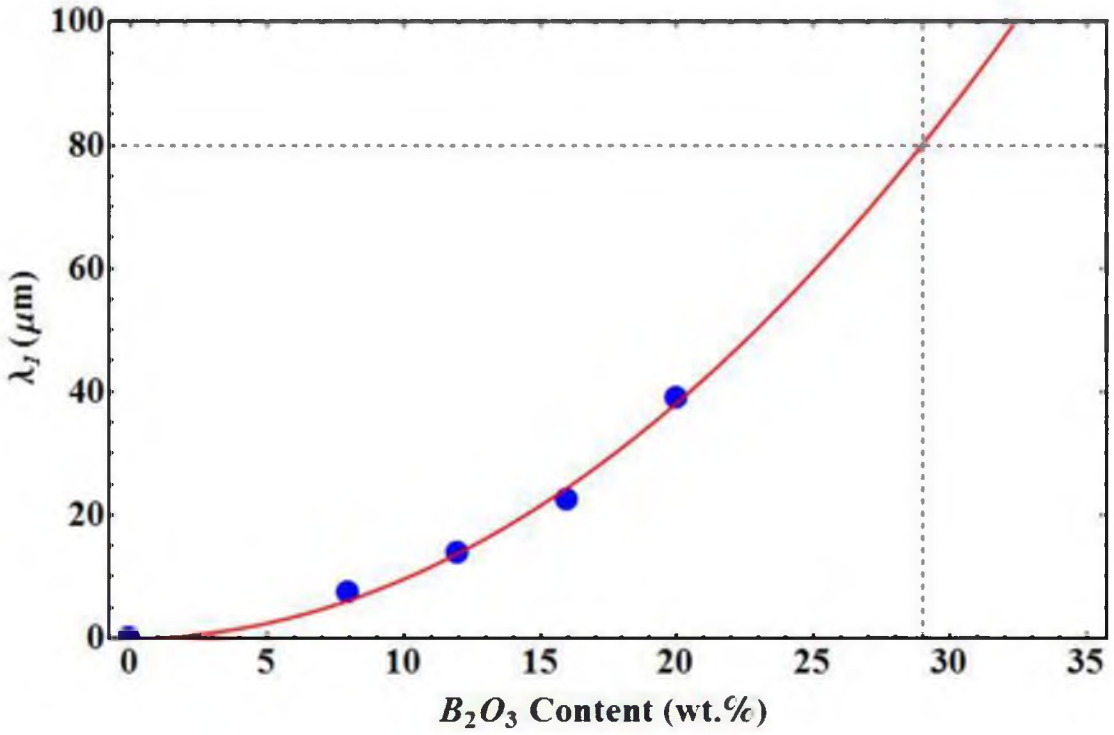

Figure 7.5 Experimental results on the relationship between primary arm spacing λ_1 and B_2O_3 contents.

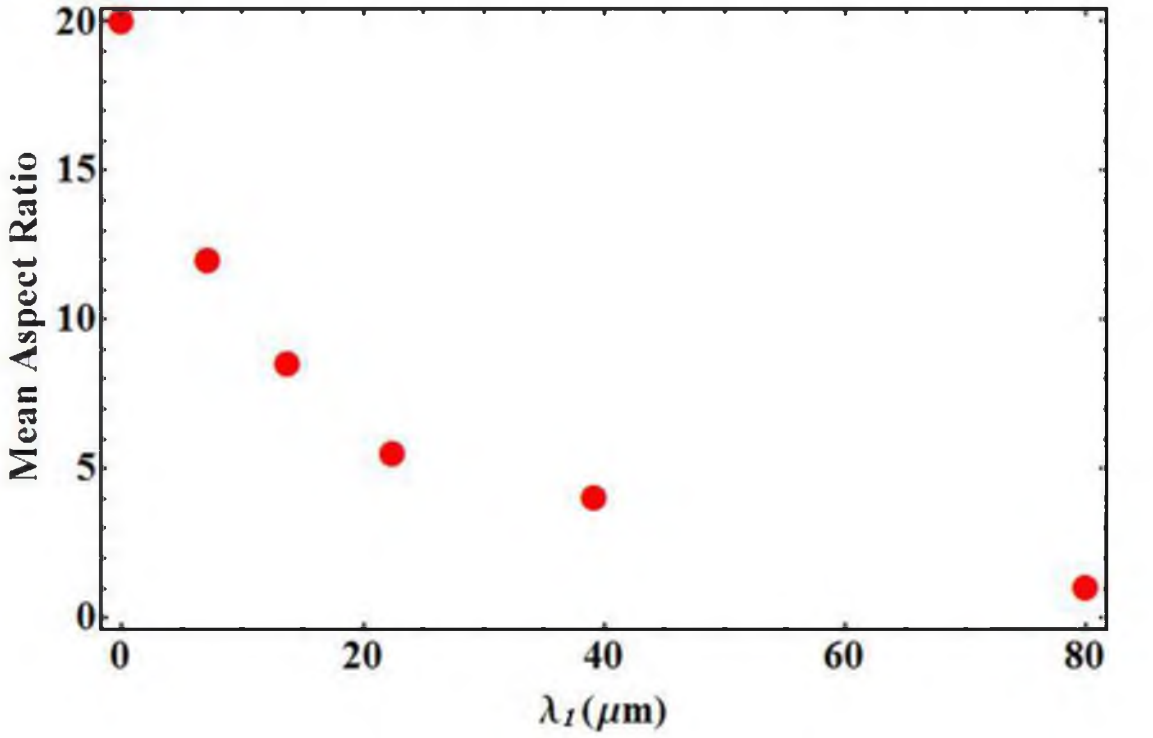

Figure 7.6 Experimental results on the relationship between mean aspect ratio and primary arm spacing λ_1.

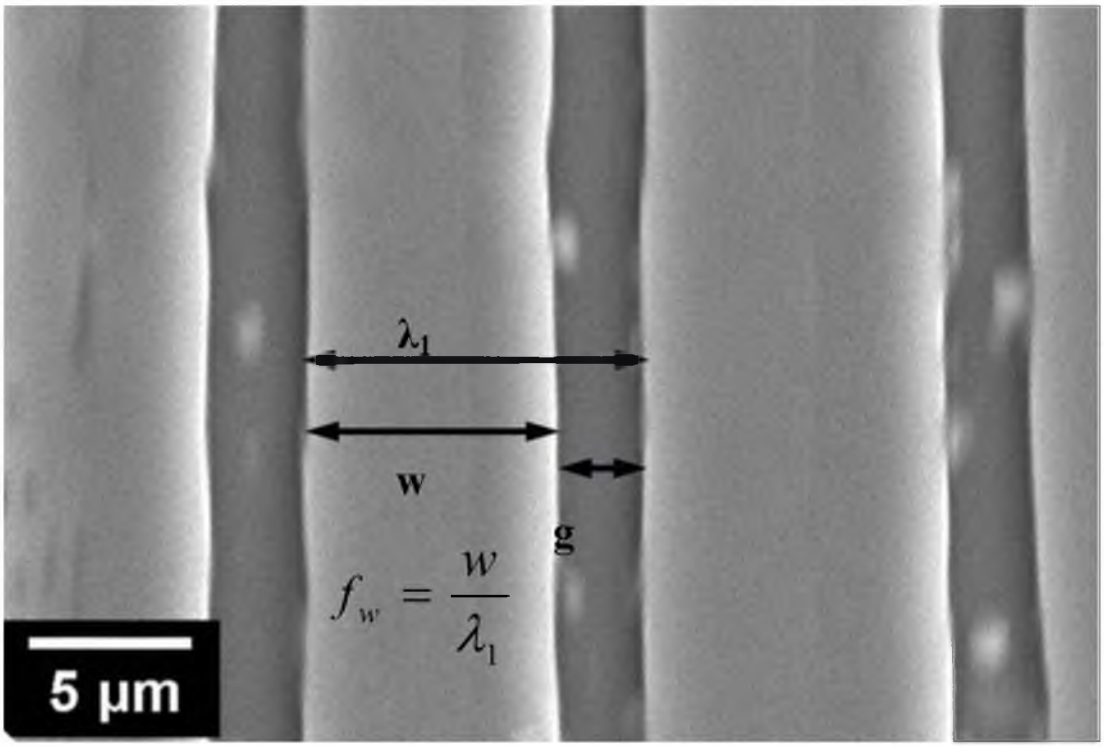

Figure 7.7 Illustration on the definition f_w using a well-developed cellular structure. Lighter phase is wollastonite.

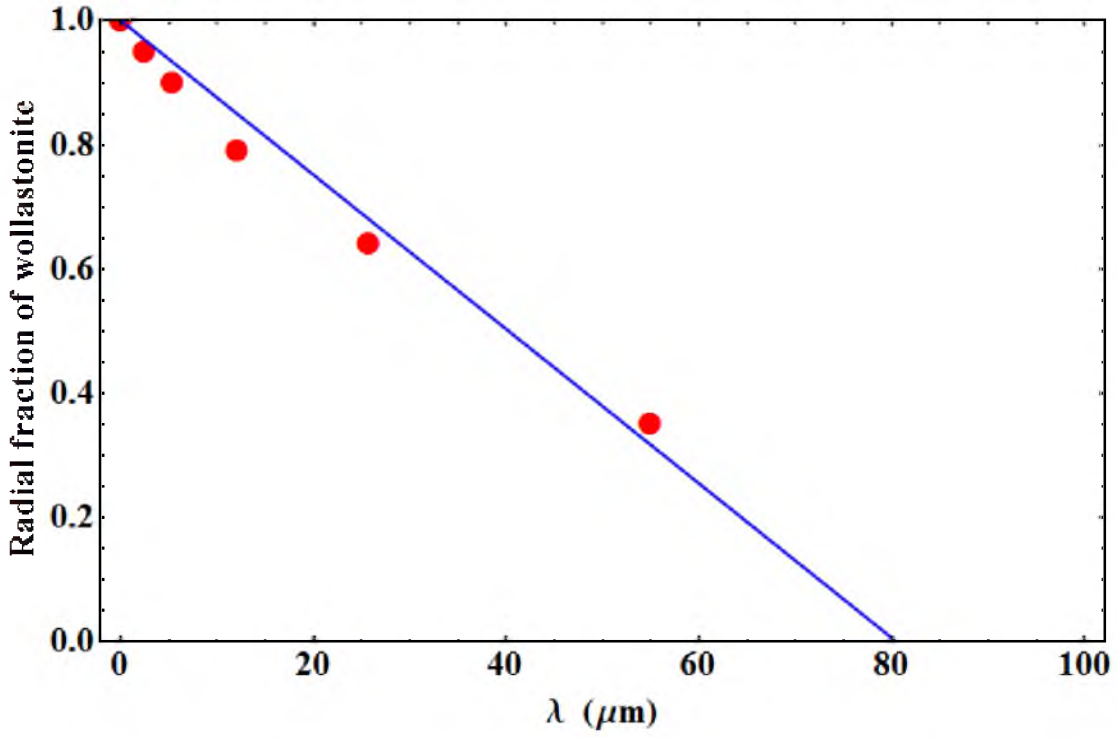

Figure 7.8 Relationship between f_w and primary arm spacing λ_1. The data points can be approximately fitted into a linear equation.

as seen in Figure 7.6, the experimental data are also fitted into a parabolic equation as follows.

$$\lambda_1 = 0.095\omega^2 \tag{7.29}$$

where ω is the B_2O_3 content in wt.%. From Equation (7.28), we have reached a conclusion that when λ_1 is greater than 80 μm, the wollastonite phase will disappear. By intersecting the fitted line and the horizontal line at λ_1 = 80 μm, the corresponding B_2O_3 content is about 29 wt.%, this result predicts that when ω is greater than 29 wt.%, wollastonite phase goes away. In Figures 5.21c and 5.23 in Chapter 5, we have seen that the cellular structure or individual wollastonite phases still exist when ω = 20, but they complete disappeared at ω = 35, which agrees with a maximum ω of 29 as predicted by Equations (7.28) and (7.29).

Based on Equation (7.28), the cellular growth pattern is then simulated as shown in Figure 7.9. As can be seen from this figure, when λ_1 is very small, such as λ_1 = 2 μm, nearly the whole volume is occupied by wollastonite. When λ_1 is very large, such as λ_1 = 78 μm, the wollastonite phase almost disappears. In the region between these two values, we see an increasing λ_1 along with decreasing wollastonite phase.

The simulated pattern is then compared with experimental results at some special λ_1 values, as shown in Figure 7.10.

With the help of Figures 7.9 and 7.10, we are now going to set up the model for the simulation of mean aspect ratio as a function of λ_1. Three assumptions will be used for this modeling.

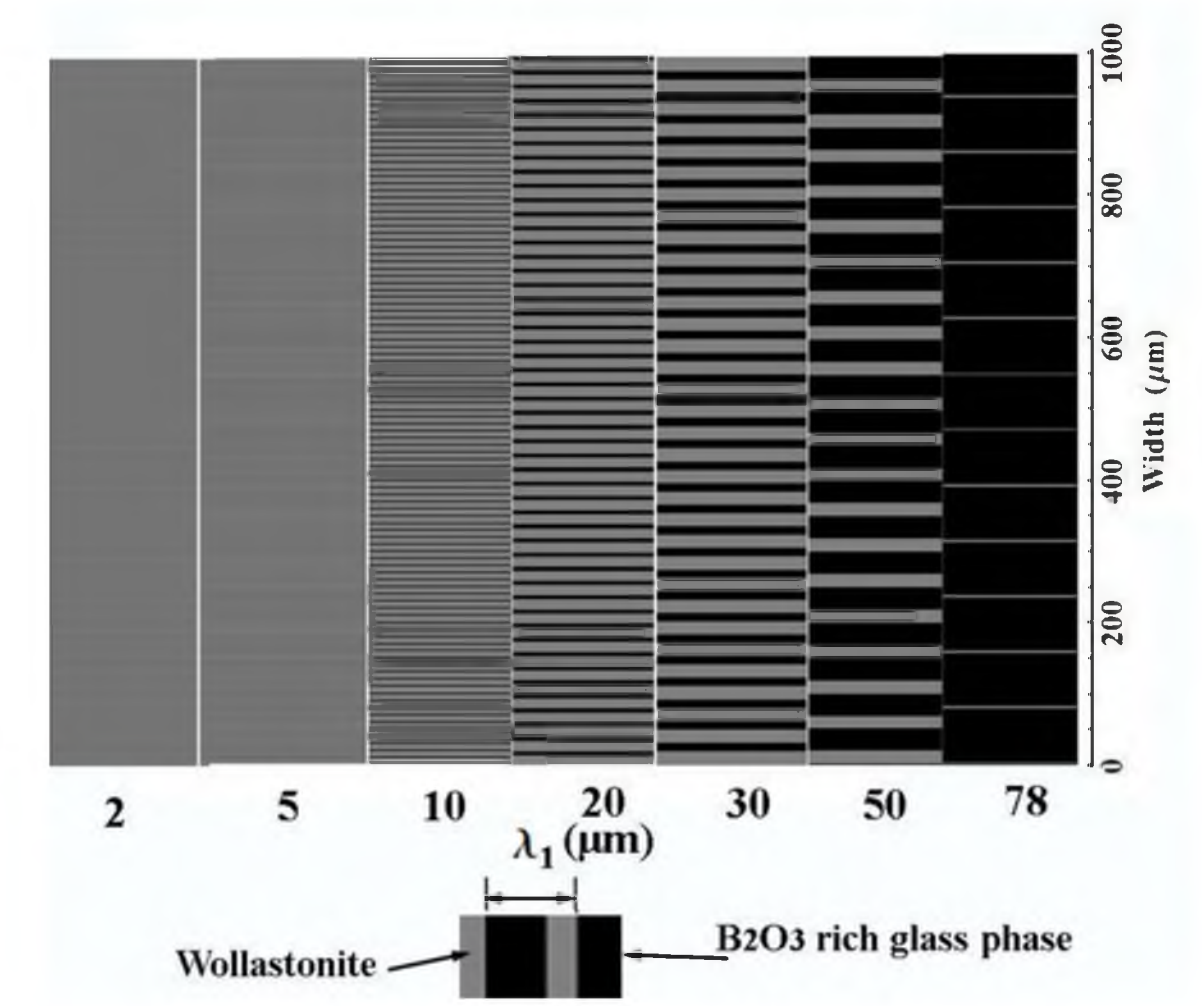

Figure 7.9 Simulated cellular structure pattern at various primary arm spacings. Lighter phase is wollastonite.

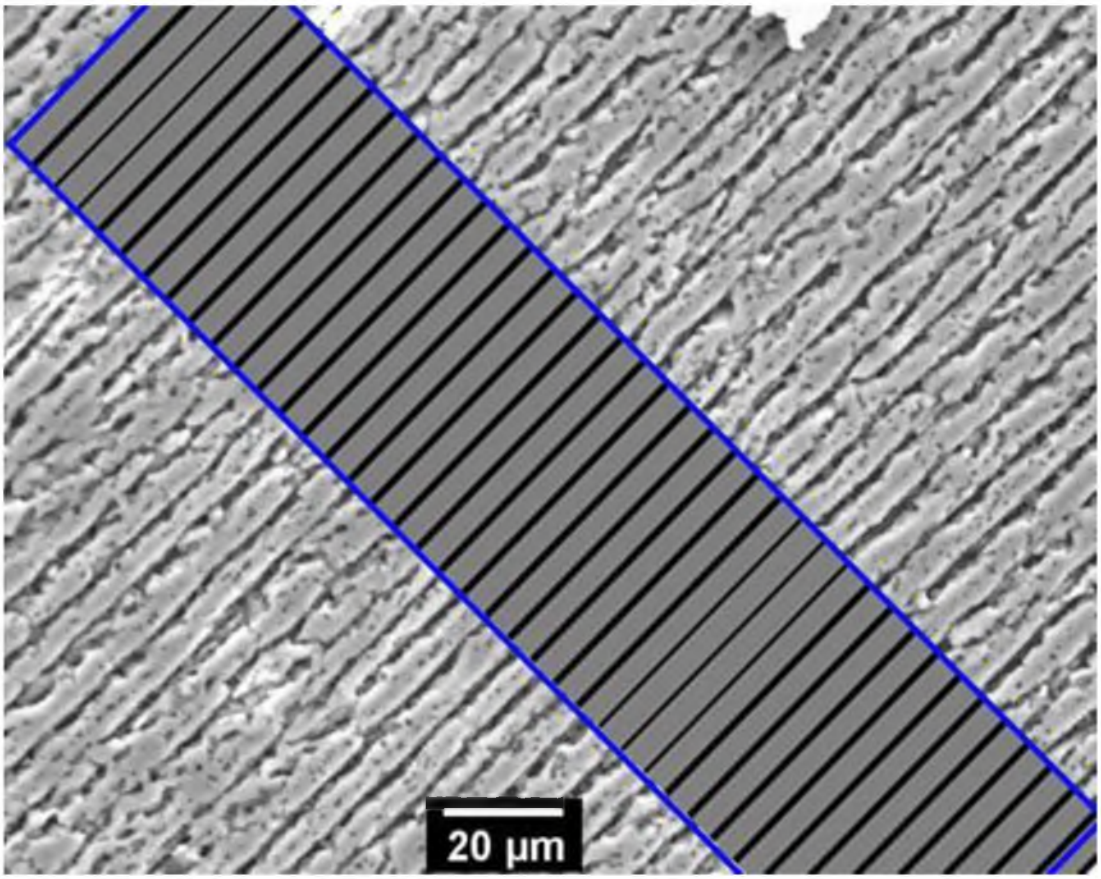

(a)

Figure 7.10 Comparison between simulated and experimentally observed cellular structure at: (a) $\lambda_1 = 5.4\,\mu m$ with $f_\omega = 0.9$, (b) $\lambda_1 = 12.2\,\mu m$ with $f_\omega = 0.79$, (c) $\lambda_1 = 25.7\,\mu m$ with $f_\omega = 0.64$, (d) $\lambda_1 = 30.7\,\mu m$ with $f_\omega = 0.5$, and (e) $\lambda_1 = 50\,\mu m$ with $f_\omega = 0.35$. Lighter phase is wollastonite in both simulated and measured patterns.

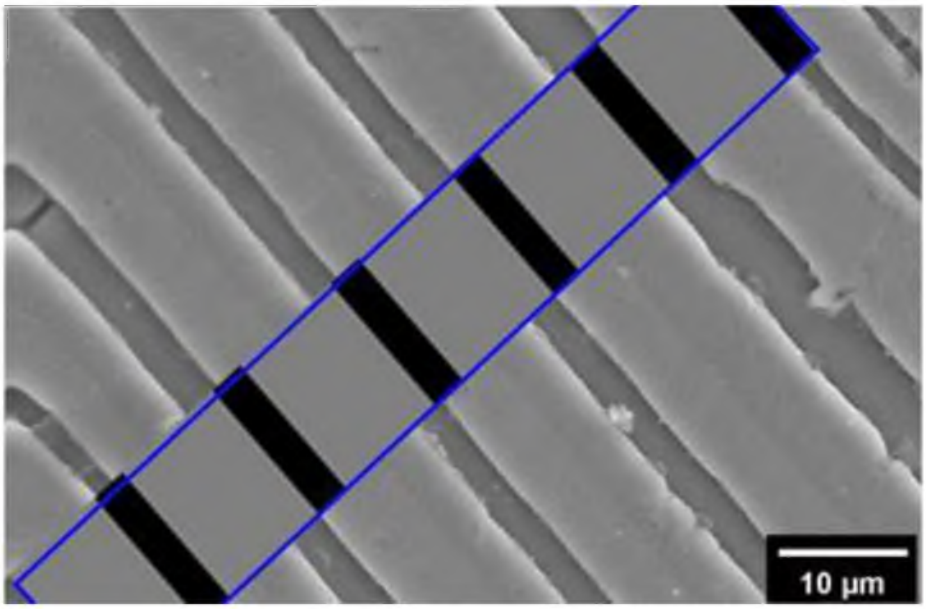

(b)

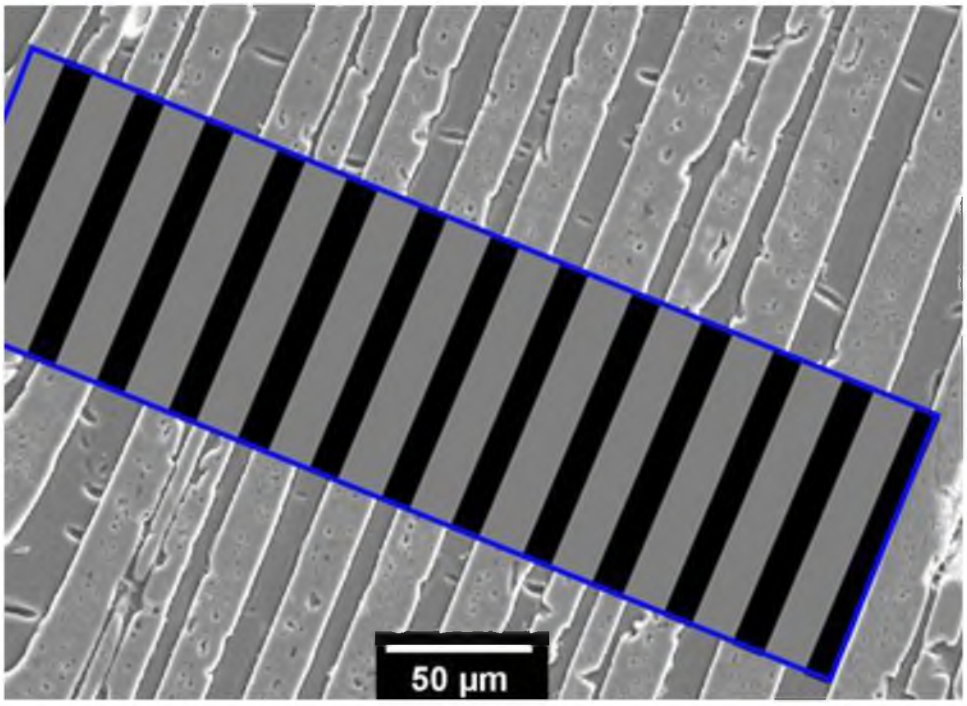

(c)

Figure 7.10 (Continued)

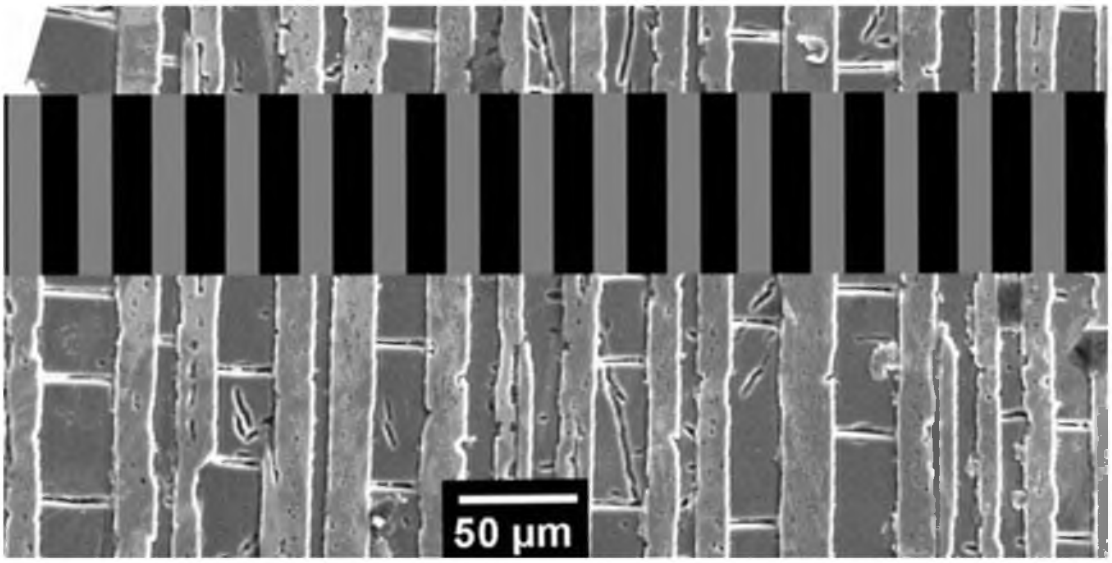

(d)

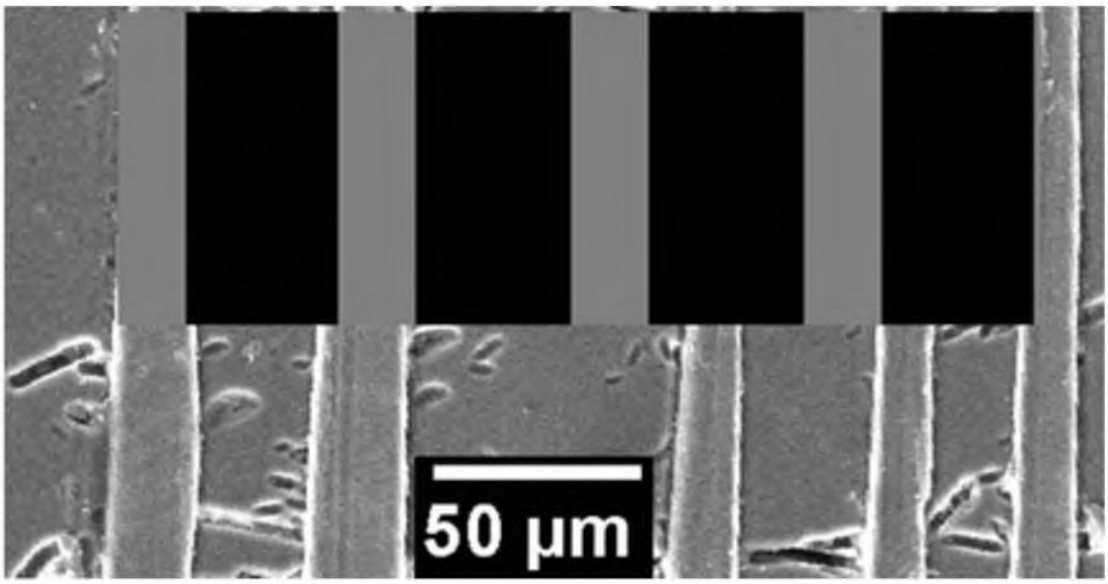

(e)

Figure 7.10 (Continued)

Assumption 1: Pure wollastonite ($\lambda_1 = 0$) breaks into particles having a mean aspect ratio (MAR) of AR^0. In this simulation, $AR^0 = 20{:}1$ is a good approximation based on experimental observation.

Assumption 2: Each sample with λ_1 greater than zero is made up of lots of individual units; such a unit is made of wollastonite phase of $\lambda_1 f_w$ and is balanced by glass phase of $\lambda_1(1-f_w)$. At smaller λ_1 values, for example $\lambda_1 = 1$ μm, each unit will not brick into particles of separated phase; instead, glass phase will still attach to wollastonite phase, but the overall AR will be reduced, it will change linearly with λ_1 until λ_1 reaches a critical value, which is defined as λ^*. This assumption is explained in Figure 7.11. The physical meaning of this λ^* can be understood as the average particle size in the width dimension, i.e., the minor axis of an acicular particle. The region between 0 and λ^* is defined as the linear cleavage zone. The corresponding AR of a sample having its λ_1 equals λ^* is defined as AR^*. In this simulation, AR^* is approximately half of AR^0, i.e., $AR^* = 10{:}1$. $\lambda^* = 10$ μm can approximately represent the average width size of produced acicular particles.

Assumption 3: When λ_1 is greater than λ_1^* but less than λ_1^∞, for example $\lambda_1 = 30$ μm, an aforementioned unit will begin to break into individual particles containing either wollastonite phase or glass phase. λ_1^∞ is defined as the maximum primary arm spacing when wollastonite phase fades away from the cellular pattern. This value is not a fixed value but varies across a large range nonlinearly with a very low radial fraction of wollastonite phase; however, practically speaking at these low f_w values, even λ_1^∞ has not reached a stable value, and the mean aspect ratio will not have significant changes

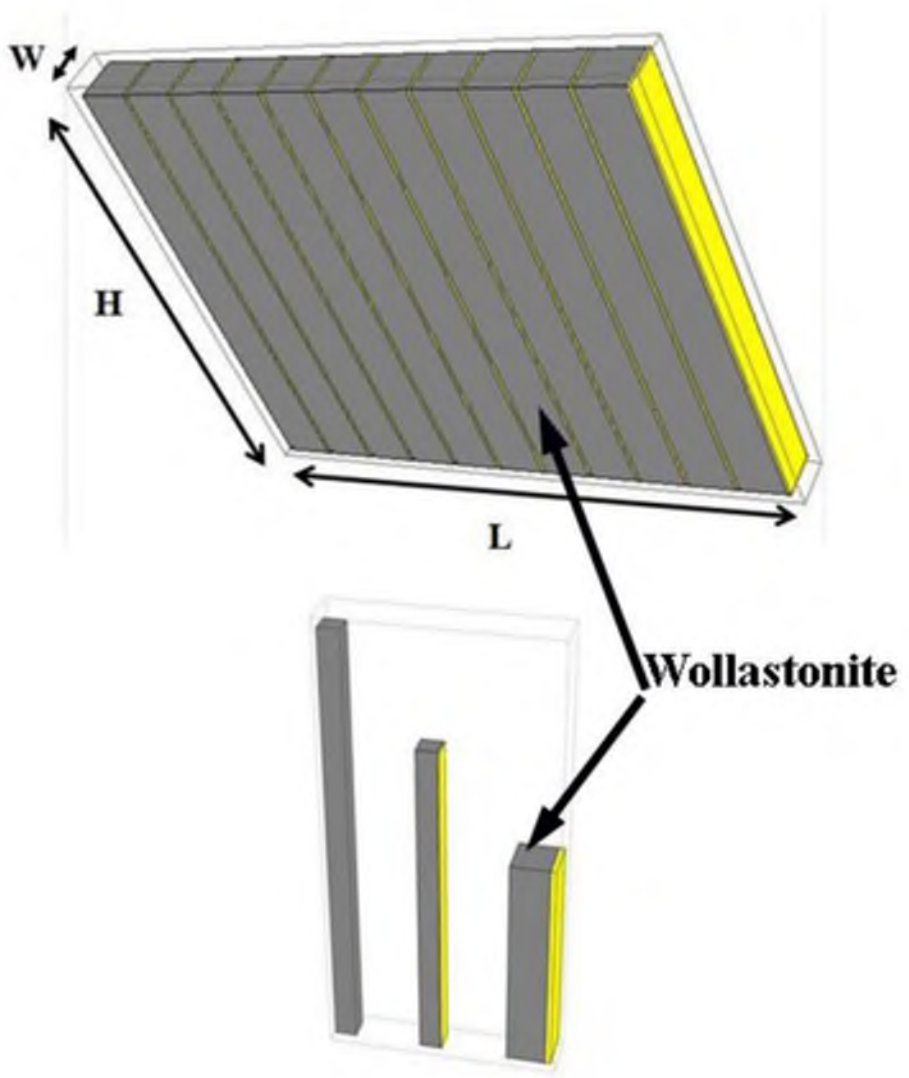

Figure 7.11 Illustration to show the linear cleavage property when λ_1 is less than λ_1^* where Assumption 2 applies. λ_1^* is the critical value at which glass phase separates from wollastonite phase. Under this assumption, at smaller λ_1 values, for example λ_1 = 1 μm, each unit will not brick into particles of separated phasel; instead, thin glass phase will attach to the wollastonite phase, but the overall mean aspect ratio will be reduced; it will change linearly with λ_1 until λ_1 reaches a critical value, which is defined as λ^*.

Therefore, the minimum λ_1^{∞} denoted as $\lambda_1^{\infty'}$ is used, which equals the intercept with horizontal axis of a linear fit in a f_w versus λ_1 plot beginning from the low λ_1 side, as shown in Figure 7.9. For this simulation, $\lambda_1^{\infty'}$ is approximately 80 μm. In the actual simulation, it is found that by increasing this number to a larger value such as a few hundreds micrometers does not change the overall trend in an effective way. Under ideal conditions, each wollastonite phase particle falling in this λ_1 range will have a mean minor axis of λ_1^* with a mean major axis of $AR^w\lambda_1^*$; each glass phase particle will also have a mean minor axis of λ_1^* with a mean major axis of $AR^g\lambda_1^*$. AR^w and AR^g represent the mean aspect ratios of a wollastonite particle and a glass particle, respectively. The corresponding illustration for this assumption is shown in Figure 7.12.

Since in Assumption 2, we have denoted the corresponding AR for particles with $\lambda_1 = \lambda_1^*$ equals AR^*, we shall simply set $AR^w = AR^*$ for continuity reason. For a pure glass phase, there is no special cleavage plane; therefor it should have an AR of nearly 1:1 and no greater than 2:1 for most cases considering also triangular shape particles. For this simulation, we choose AR^g =1.5 based on the observation of Figure 7.13, which shows the particle morphology of a sample consisting of nearly pure glass phase.

With the above assumptions, the mean aspect ratio is calculated as follows.

When $\lambda_1 \le \lambda_1^*$,

$$MAR = AR^0 + \frac{AR^* - AR^0}{\lambda^*}\lambda \tag{7.30}$$

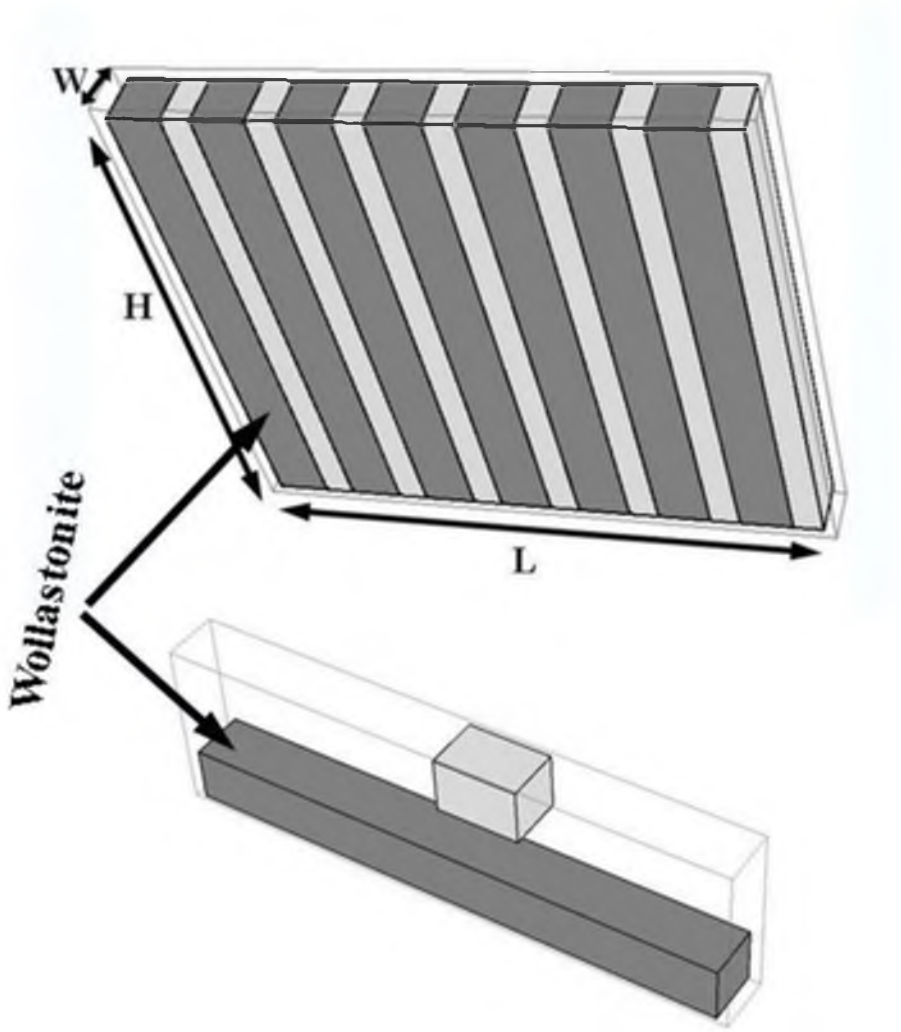

Figure 7.12 Illustration to show the nonlinear cleavage property when λ_1 is greater than λ_1^* but less than λ_1^∞ where Assumption 3 applies. Under this assumption, each wollastonite phase particle falling in this λ_1 range will have a mean minor axis of λ_1^* with a mean major axis of $AR^w\lambda_1^*$; each glass phase particle will also have a mean minor axis of λ_1^* but with a mean major axis of $AR^g\lambda_1^*$. AR^w and AR^g represent the mean aspect ratios of wollastonite particles and glass particles, respectively. λ_1^∞ is defined as the maximum primary arm spacing when wollastonite phase fades away from the cellular pattern.

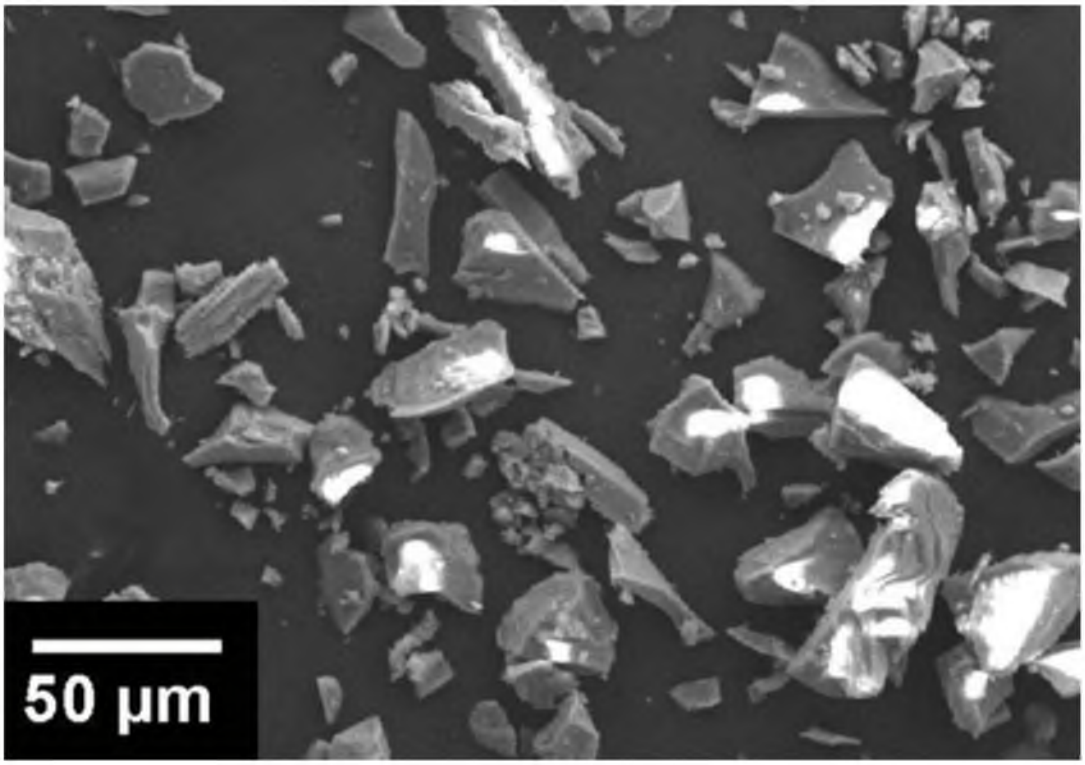

Figure 7.13 Determination of AR^g, which is the mean aspect ratio of glass phase particles based on the particle morphology of a sample consisting of nearly pure glass phase. For pure glass phase, there is no special cleavage plane; therefore it should have a MAR of nearly 1:1 and no greater than 2:1 for most cases considering also triangular shape particles. This figure suggests that AR^g for this simulation work is approximately 1.5.

When $\lambda_1^* < \lambda_1 \leq \lambda_1^{\infty'}$,

$$MAR = \frac{AR^w N_w + AR^g N_g}{N_w + N_g} \tag{7.31}$$

where N_w and N_g stand for the number of wollastonite and glass particles, respectively. They can be calculated as the cellular pattern.

$$N_w = \frac{LHWf_w}{(\lambda_1^* AR^w)\lambda_1^* W} \tag{7.32}$$

$$N_g = \frac{LHW(1-f_w)}{(\lambda_1^* AR^g)\lambda_1^* W} \tag{7.33}$$

where L, H, and W are the dimensions of a slab with certain λ_1 as illustrated in Figures 7.11 and 7.12. The numerators in the above two equations become the total volume of wollastonite and glass phase, respectively, and the denominators are the volume of a unit wollastonite and glass particle, respectively. It is worth mentioning that the actual elements of a cellular structure are some cylindrical or hexagonal rods; in this simulation, we assume they are perfect cuboids, but keep the radial fraction of the two different shapes the same.

Note that in Assumption 2 or Equation (7.30), we do not consider the small volume fraction of glass phase by assuming glass phase is acting as reducing the mechanical property of the wollastonite particles only without itself peeling off wollastonite phase where it attaches, which can be understood as if glass phase were also a part of additional "wollastonite" phase to make up a particle of the designated

width, except that this fictitious "wollastonite" does not contribute positively to the mean aspect ratio. To keep the continuity of the mean aspect ratio when λ_1 is greater than λ_1^*, the radial fraction of wollastonite phase needs to be adjusted by subtracting λ_1^* from the actual λ_1 so that it will decrease from 1 rather than the value corresponding to $\lambda_1 = \lambda_1^*$. The adjusted volume fraction is defined as

$$f_w' = 1 - 0.012(\lambda_1 - \lambda^*) \tag{7.34}$$

Equations (7.32) and (7.33) thus reduce to

$$N_w = \frac{LHf_w'}{AR^w(\lambda_1^*)^2} \tag{7.35}$$

$$N_g = \frac{LH(1-f_w')}{AR^g(\lambda_1^*)^2} \tag{7.36}$$

By substituting Equations (7.35) and (7.36) into Equation (7.31), and replacing f_w by f_w', the final mean aspect ratio can be expressed as a piecewise function as follows

$$MAR = \begin{cases} AR^0 - \dfrac{AR^* - AR^0}{\lambda_1^*}\lambda_1; & (0 < \lambda_1 \le \lambda_1^*) \\ \dfrac{1}{\dfrac{1-0.012(\lambda_1-\lambda^*)}{AR^w} + \dfrac{0.012(\lambda_1-\lambda^*)}{AR^g}}; & (\lambda_1^* < \lambda_1 \le \lambda_1^{\infty'}) \end{cases} \tag{7.37}$$

From Equation (7.37), we can see that when the constants AR^0, AR^*, AR^w,

AR^g, and λ_1^* are available, MAR is solvable as s function of λ_1 only. Now we insert the values we have determined previously: $AR^0 = 20$, $AR^* = AR^w = 10$, $AR^g = 1.5$, $\lambda_1^* = 10$ μm into the above equation; Equation (7.37) becomes

$$MAR = \begin{cases} 20 - \lambda_1; & (0 < \lambda_1 \le 10) \\ \dfrac{1}{0.032 + 0.0068\lambda_1}; & (10 < \lambda_1 \le 80) \end{cases} \tag{7.38}$$

The above equation is then calculated and plotted in Figure 7.14. In the same figure, the simulated results are also compared with the measured values. As can be seen from Figure 7.10, the simulated MAR matches well with the experimental results. Interestingly, we found that the reducing rate of the mean aspect ratio follows similarly to the half-life period pattern of a radioactive decay process. By taking AR^0 as the initial condition and λ_1 / λ_1^* as the index, MAR obeys approximately the following formula

$$MAR = AR^0 (\frac{1}{2})^{\lambda_1/\lambda_1^*} \tag{7.39}$$

Unlike Equation (7.38), the above equation is not separated into different regions. It simply predicts that the corresponding MAR for λ_1 equals 0, 10, 20, 30, 40, etc. will be 20, 10, 5, 2.5, etc., respectively. This trend is also provided as an alternative model in Figure 7.14. Compared with the experimental data and the first model, the half-life patterned model is able to predict well at small λ_1 region, but becomes off the points at the large λ_1 region. However, since the large λ_1 region yields very poor MAR, it is not very important and almost useless for the actual production; the half-life patterned model

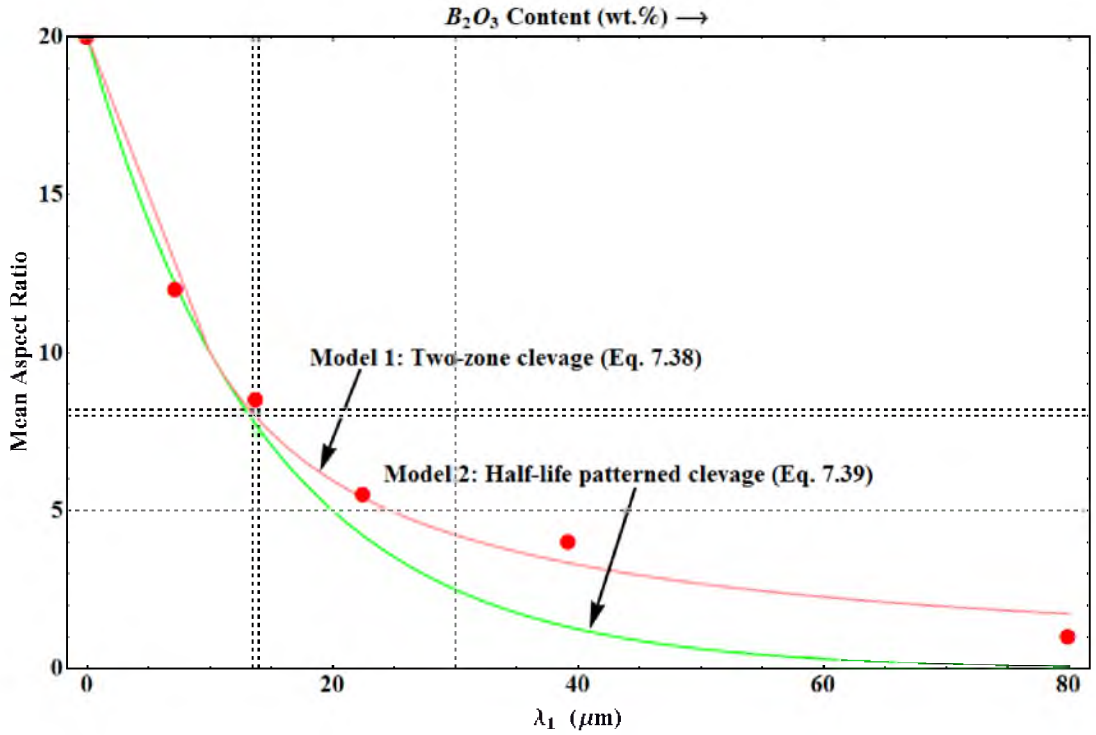

Figure 7.14 Comparison between simulated and measured mean aspect ratios as a function of primary arm spacing λ_1. Two models are provided to predict mean aspect ratio.

is still applicable for quick and approximate evaluation.

The singly dashed lines in Figure 7.14 indicate the general definition for high-aspect-ratio wollastonite particles. In most references [81, 82], HAR is defined as having a MAR of greater than 5:1. However, in some cases, where the definition is stricter, 8:1 is used for HAR [83]; this ratio is indicated by the doubly dashed lines. As pointed out by these references lines, the corresponding λ_1 for 5:1 and 8:1 are about 25 and 13 μm, respectively. This means that to produce HAR wollastonite particles using the Flux Growth process under this raw material composition, λ_1 should be controlled as less than 25 μm.

Once we have predicted MAR as a function of λ_1, now we can come back to the initial objective where we want to predict MAR directly from ω, the B_2O_3 content, without going through λ_1 measurement. This can be easily done by plugging $\lambda_1 = 0.095\omega^2$ into Equation (7.38) which yields

$$MAR = \begin{cases} AR^0 - 0.095\dfrac{AR^* - AR^0}{\lambda_1^*}\omega^2; & (0 < \omega \le \omega^*) \\ \dfrac{1}{\dfrac{1-1.14\times10^{-3}(\omega^2-(\omega^*)^2)}{AR^w} + \dfrac{1.14\times10^{-3}(\omega^2-(\omega^*)^2)}{AR^g}}; & (\omega^* < \omega \le \omega^{\infty'}) \end{cases} \tag{7.40}$$

where ω^* and $\omega^{\infty'}$ are ω values corresponding to λ_1^* and $\lambda_1^{\infty'}$, respectively. Under the same conditions as applied to λ_1-MAR simulation, Equation (7.40) can be reduced to

$$MAR = \begin{cases} 20 - 0.095\omega^2; & (0 < \lambda_1 \le 10) \\ \dfrac{1}{0.032 + 6.5\times10^{-4}\omega^2}; & (10 < \lambda_1 \le 29) \end{cases} \tag{7.41}$$

The above equation is then plotted in Figure 7.15. As expected, MAR decreases with increasing B_2O_3 content. The simulated results agree well with the measured values. From Equations (7.28) and (7.29), we have seen that when λ_1 is greater than 80 μm or ω is greater than 29 wt.%, those individual cellular structures or separated wollastonite phase will disappear, resulting in nearly pure glass phase cleavage property of very low MAR. This boundary condition is indicated by the marked arrow. To verify the validation of (7.41) at the regions where ω is greater than 29, it is extended to a larger value, such as 40 in this plot. We see that the measured MAR at 35 wt.% B_2O_3 falls closely to the extended curve, meaning the equation is also applicable at larger ω values even though the product is not that useful in this range. Similarly to Figure 7.14, the references lines corresponding to HAR=5:1 (singly dashed lines) and 8:1 (doubly dashed lines) are also provided. These reference lines suggest that the maximum B_2O_3 content for the generally defined HAR (5:1) and strictly defined HAR (8:1) are around 12 and 16 wt.%, respectively.

7.5. Conclusions

Based on experimental observations and appropriate assumptions, wollastonite growth and mean aspect ratio under the Flux Growth Process have been simulated as follows.

The growth front as a function of solidification time can be predicted using the following equation.

$$L_{ileft} = 12.5 - 4497.45\int_0^t \frac{(0.2173+0.0103t)^{0.9998}}{(1817-\frac{2113(0.2173+0.0103t)^{0.0098}}{t^{0.076}})^{1/4}t}dt$$

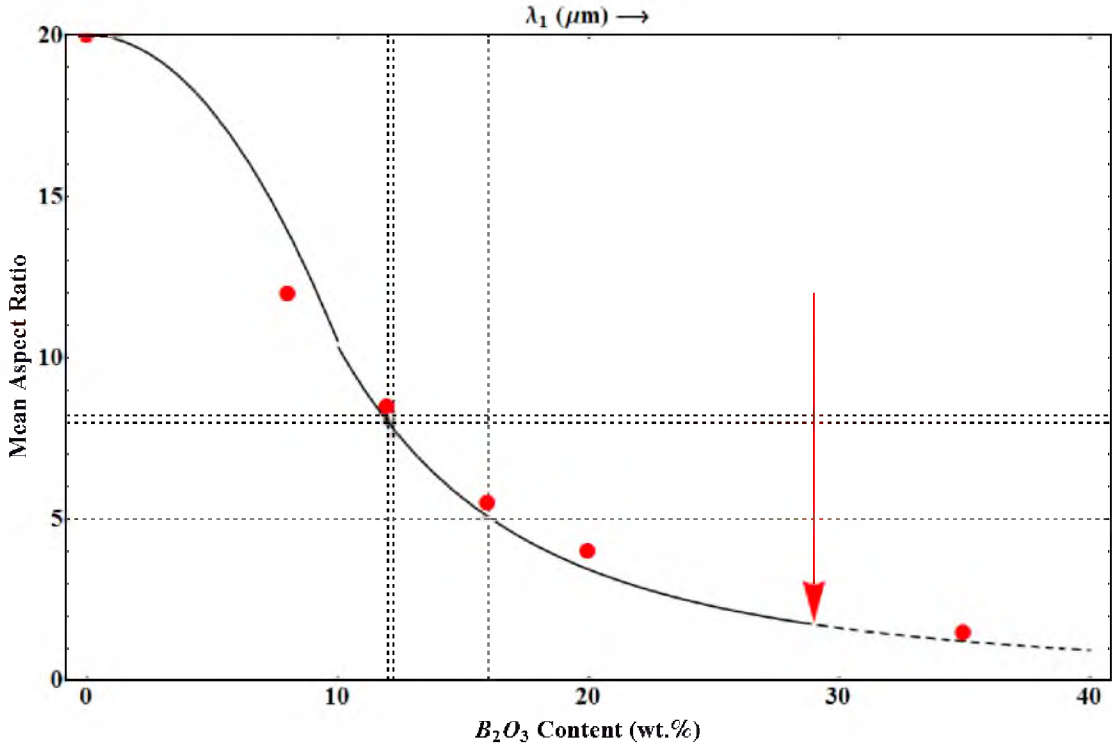

Figure 7.15 Comparison between simulated and measured mean aspect ratios as a function of B_2O_3 contents.

Solidification volume fraction as a function of time can be predicted by the following equations.

$$f = \frac{V}{V_0}$$

where

$$V = \int_0^t \pi\left(\frac{13.5-9}{12.5}\int_0^t \left(\frac{4497.45(0.2173+0.0103t)^{0.9998}}{\left(1817-\frac{2113(0.2173+0.0103t)^{0.0098}}{t^{0.076}}\right)^{1/4}t}\right)dt+9\right)^2 \left(\frac{4497.45(0.2173+0.0103t)^{0.9998}}{\left(1817-\frac{2113(0.2173+0.0103t)^{0.0098}}{t^{0.076}}\right)^{1/4}t}\right)dt$$

and

$$V_0 = \int_0^{1138} \pi\left(\frac{13.5-9}{12.5}\int_0^{1138} \left(\frac{4497.45(0.2173+0.0103t)^{0.9998}}{\left(1817-\frac{2113(0.2173+0.0103t)^{0.0098}}{t^{0.076}}\right)^{1/4}t}\right)dt+9\right)^2 \left(\frac{4497.45(0.2173+0.0103t)^{0.9998}}{\left(1817-\frac{2113(0.2173+0.0103t)^{0.0098}}{t^{0.076}}\right)^{1/4}t}\right)dt$$

Mean aspect ratio (MAR) as a function of either primary arm spacing λ_1 or B_2O_3 content ω can be simulated by the following two equations.

$$MAR = \begin{cases} AR^0 - \dfrac{AR^* - AR^0}{\lambda_1^*}\lambda_1; & (0 < \lambda_1 \le \lambda_1^*) \\ \dfrac{1}{\dfrac{1-0.012(\lambda_1-\lambda^*)}{AR^w} + \dfrac{0.012(\lambda_1-\lambda^*)}{AR^g}}; & (\lambda_1^* < \lambda_1 \le \lambda_1^{\infty'}) \end{cases}$$

$$MAR = \begin{cases} AR^0 - 0.095\dfrac{AR^* - AR^0}{\lambda_1^*}\omega^2; & (0 < \omega \le \omega^*) \\ \dfrac{1}{\dfrac{1-1.14\times10^{-3}(\omega^2-(\omega^*)^2)}{AR^w} + \dfrac{1.14\times10^{-3}(\omega^2-(\omega^*)^2)}{AR^g}}; & (\omega^* < \omega \le \omega^{cut}) \end{cases}$$

All the parameters in the above equations have been defined in corresponding sections.

CHAPTER 8

SUMMARY

Wollastonite is a versatile nonreusable material. While the current market relies greatly on natural wollastonite products, it is worthwhile to develop synthetic wollastonite to partially replace the natural resource.

Though current research has been done to synthesize wollastonite, it either failed to produce high-aspect-ratio wollastonite or did not produce acicular particles in an effective way. In order to produce high-aspect-ratio wollastonite effectively, we need to find either alternative methods or significant improvements on existing methods.

Wollastonite has various polymorphs and polytypes, among which the 2M-wollatonite has acicular cleavage property, but the study on the phase transformation temperature of this crystal structure is insufficient. In order to grow the right polymorph, a systematical study on the phase transformation temperature of wollastonite polymorphs and polytypes was studied. Compared with existing data, our results helped to clarify some inconsistences existing in order studies, and for the first time provided the direct information for the synthesis of 2M-wollasonite in the following way: 2M-wollastonite forms in an observable rate only when temperature exceeds 860^{o}C, and it transfers to α-wollastonite-4A around 1125^{o}C, the latter becomes amorphous when temperature is above 1500^{o}C.

Following the determination of phase transformation temperature, we developed

two different processes to produce high-aspect-ratio wollastonite powder.

The first process is the Partial Melting and Recrystallization (PMR) process. This process was found to be simple but effective to synthesize wollastonite powder without completely melting the raw materials. Using this process, we investigated the effects of additives on the preparation of acicular wollastonite particles. Through our studies, we found that B_2O_3 is a good additive to lower the melting point of the raw mixtures. Li_2O is a good additive that promotes the formation of acicular wollastonite particles.

The second process is called the Flux Growth (FG) process. It takes advantages of the heat transfer properties of the melt-crucible-furnace wall (MCF) system; a vertical temperature gradient is achieved to provide sites for the nucleation of 2M-wollatonite crystals. The solidified products contain nearly pure 2M-wollastonite crystals as the major component and amorphous glass phase as the minor part.

Both the PMR and FG processes yielded high-aspect-ratio particles. The crystals grown by the PMR process were small in size but large in number, and they grew randomly in the final products. The crystals grown by the FG process were aligned and they formed cellular and dendritic patterns. Such a growth behavior offers additional benefits for producing HAR wollastonite particles.

When the two processes were compared, the FG process surpasses the PMR process in terms of efficiency, and therefore, this process was studied in more detail. Unfortunately, existing models failed to explain the observed cellular and dendritic of 2M-wollastonite crystals; we thus did systematic experiments on this cellular and dendritic solidification system, and we propose a modified model as shown below

$$\lambda_1 = c\left(\frac{k\,D\Delta\,T_0\,\Gamma\,L_0}{\Delta T_r}\right)^{n/4} V^{-p/4} \left|G^{\,}/T\right|^{-q/4}$$

All the parameters have been defined previously. n, q, and p are some integers with the suggested values of: $n, p, q = 0, 1, 2, 3, 4.$

Using the above model, the growth front and solidification volume fraction as functions of temperature gradient and cooling rates were simulated. Finally, mean aspect ratio as a function of either primary arm spacing or B_2O_3 content was simulated.

REFERENCES

[1] V. L. Balkevich, F. S. Peres, A. Y. Kogos, A. B. Kliger, and M. A. Fishman, "Synthesizing wollastonite from natural siliceous carbonate compositions," *Glass Ceram.,* vol. 42, pp. 40-43, 1985.

[2] I. Kotsis and A. Balogh, "Synthesis of wollastonite," *Ceram. Int.,* vol. 15, pp. 79-85, 1989.

[3] H. X. Yang and C. T. Prewitt, "On the Crystal Structure of Pseudowollastonite ($CaSiO_3$)," *American Mineralogist,* vol. 84, pp. 929-932, 1999.

[4] T. Yamanaka and H. Mori, "The structure and polytypes of α-CaSiO3 (pseudowollastonite)," *Acta Crystallogr., Sect. B: Struct. Sci,* vol. 37, pp. 1010-1017, 1981.

[5] S. A. Nelson, "Silicate Structures and Structural Formula," *Available at http://www.tulane.edu/~sanelson/eens211/silicate_structures08.htm, Retrieved 8/22/2013.*

[6] C. Henmi, A. Kawahara, K. Henmi, I. Kusachi, and Y. Takeuchi, "The 3T, 4T and 5T polytypes of wollastonite from Kushiro, Hiroshima Prefecture, Japan," *Am. Mineral.,* vol. 68, pp. 156-163, 1983.

[7] K. F. Hesse, "Refinement of the crystal structure of wollastonite-2M (parawollastonite)," *Z. Kristallogr.,* vol. 168, pp. 93-8, 1984.

[8] D. A. Jefferson, J. M. Thomas, D. J. Smith, R. A. Camps, C. J. D. Catto, and J. R. A. Cleaver, "Individual silicate chains in wollastonite by high resolution electron microscopy," *Nature,* vol. 281, pp. 51-52, 1979.

[9] B. Phillips and A. Muan, "Phase Equilibria in the System CaO-Iron Oxide-SiO2 in Air," *J. Am. Ceram. Soc.,* vol. 42, pp. 413-423, 1959.

[10] M. He, R. Zhang, and H. Zhou, "Characterization and analysis of CaO-SiO_2-B_2O_3 ternary system ceramics " *Journal of Materials Science: Materials in Electronics,* vol. 22, pp. 389-393, 2011.

[11] N. Zhang, J. A. Molenda, J. H. Fournelle, W. L. Murphy, and N. Sahai, "Effects of pseudowollastonite (CaSiO3) bioceramic on in vitro activity of human mesenchymal stem cells," *Biomaterials,* vol. 31, pp. 7653-7665, 2010.

[12] A. Kartal and S. Akpinar, "Synthesis of Wollastonite by Using Various Raw Materials," *Key Engineering Materials,* vol. 264-268, pp. 2469-2472, 2004.

[13] Allen and White, "Polymorphic Forms of Calcium Metasilicates," *The American Journal of Science,* vol. 171, p. 101, 2010.

[14] R. L. Virta, "Wollastonite-A versatile industrial mineral," *U.S.Geol. Surv. Fact Sheet FS-002-01,* 2011.

[15] USGS, "2010 Minerals Yearbook - Wollastonite " *(Report, U. S. Department of the Interior, U. S. Geological Survey),* 2010.

[16] G. C. Hawley, "Wollastonite," *Mineral Engineering,* vol. 62, pp. 84-87, 2010.

[17] X. H. Huang and J. Chang, "Synthesis of nanocrystalline wollastonite powders by citrate-nitrate gel combustion method," *Mater. Chem. Phys.,* vol. 115, pp. 1-4, 2009.

[18] K. L. Lin, J. Chang, G. F. Chen, M. L. Ruan, and C. Q. Ning, "A simple method to synthesize single-crystalline β-wollastonite nanowires," *J. Cryst. Growth,* vol. 300, pp. 267-271, 2007.

[19] X. K. Li and J. Chang, "Synthesis of Wollastonite Single Crystal Nanowires by a Novel Hydrothermal Route," *Chemistry Letters* vol. 33, pp. 1458-1459, 2004.

[20] K. L. Lin, J. Chang, and J. X. Lu, "Synthesis of wollastonite nanowires via hydrothermal microemulsion methods," *Materials Letters,* vol. 60, pp. 3007-3010, 2006.

[21] M. S. Nizami, M. K. Farooq, K. Hussain, and M. Z. Iqbal, "Solid State Reaction Yielding a Mineral Utilizing Silica Obtained from an Agricultural Waste," *J. Mater. Sci. Technol.,* vol. 15, pp. 276-280, 1999.

[22] L. M. Saltevskaya, Z. A. Livson, and M. I. Ryshchenko, "Synthesis of wollastonite and its use in ceramic bodies," *Glass Ceram.,* vol. 31, pp. 114-117, 1974.

[23] S. B. Emrullahoğlu, Ö. F. Emrullahoğlu, and C. B. Emrullahoğlu, "Synthetic Wollastonite Production from Raw and Tailing Materials," *Key Eng. Mater.,* vol. 264-268, pp. 2485-88, 2004.

[24] Y. H. Yun, S. D. Yun, H. R. Park, Y. K. Lee, and Y. N. Youn, "Preparation of β-Wollastonite Glass-Ceramics," *J. Mater. Synth. Process.,* vol. 10, pp. 205-209, 2002.

[25] C. J. Jacob, "Synthesis of wollastonite from natural materials without fusion," *U. S. Patent No. 3,966,884,* 1976.

[26] S. Vichaphund, M. Kitiwan, D. Atong, and P. Thavorniti, "Microwave synthesis of wollastonite powder from eggshells," *Journal of the European Ceramic Society,* vol. 31, pp. 2435-2440, 2011.

[27] H. Ohsato and T. Sugimura, "Morphology of synthetic β-wollastonite and para-wollastonite," *J. Cryst. Growth,* vol. 74, pp. 656-658, 1986.

[28] M. Kume and T. Mizuno, "Glass composition suitable for production of fibrous wollastonite, method for producing said wollastonite, and wollastonite obtained thereby," *U. S. Patent No. 4,443,550,* 1984.

[29] A. Maries and P. S. Rogers, "Method For Making Aligned Fibrous Crystals," 1977.

[30] W. D. Kingery, H. K. Bowen, and D. R. Uhlmann, *Introduction to Ceramics*, Second ed.: John Wiley & Sons, Inc., 1975.

[31] K. L. Bartelmehs, "Silicate Structure Types," *Available at http://www.ccp14.ac.uk/ccp/web-mirrors/xtaldraw/crystal/silicate.htm, Retrieved 8/22/2013.*

[32] J. Tolliday, "Crystal Structure of β-Wollastonite," *Nature,* vol. 182, pp. 1012-1013, 1958.

[33] F. J. Trojer, "The crystal structure of parawollastonite," *Z. Kristallogr.,* vol. 127, pp. 291-308, 1968.

[34] Z. X. Ma, H. Li, G. S. Gai, and X. F. Hu, "The Present Situation and Conception of Milling Technology for Preparation of Needle-like Wollastonite Powder," *Bull. Chin. Ceram. Soc.,* pp. 42-45, 2000.

[35] S. J. Bennison and M. P. Harmer, "A History of the Role of MgO in the Sintering of alpha-Al2O3," *Sintering of Advanced Ceramics* vol. 7, 1990.

[36] J. Han, P. Q. Mantas, and A. M. R. Senos, "Densification and grain growth of Al-doped ZnO," *J. Mater. Res.,* vol. 16, 2001.

[37] G. Dhanaraj, K. Byrappa, V. Prasad, and M. Dudley (Eds), *Springer Handbook of Crystal Growth*: Springer, 2010.

[38] E. S. M., "Laser Ablation ICP-MS Analysis of Geological Materials Prepared as Lithium Borate Glasses," *Geostandards Newsletter,* vol. 27, pp. 147-162, 2003.

[39] H. P. Longerich, S. E. Jackson, and D. Gunther, "Laser Ablation Inductively Coupled Plasma Mass Spectrometric Transient Signal Data Acquisition and Analyte Concentration Calculation," *Journal of Analytical Atomic Spectrometry,* vol. 11, pp. 899-904, 1996.

[40] K. A. Jackson and J. D. Hunt, "Transparent compounds that freeze like metals,"

Acta Metallurgica, vol. 13, pp. 1212-15, 1965.

[41] E. Ustun, E. Cadirli, and H. Kaya, "Dendritic solidification and characterization of a succinonitrile-acetone alloy," *Journal of Physics: Condensed Matter,* vol. 18, pp. 7825-39, 2006.

[42] L. R. Morris and W. C. Winegard, "The cell to dendrite transition," *Journal of Crystal Growth,* vol. 6, pp. 61-6, 1969.

[43] K. Somboonsuk, J. T. Mason, and R. Trivedi, "Interdendritic spacing. I. Experimental studies," *Metallurgical Transactions A* vol. 15A, pp. 967-75, 1984.

[44] J. D. Hunt, Q. Han, and X. Wan, "Growth of a cellular/dendritic array," *J. Mater. Sci. Technol.,* vol. 13, pp. 161-172, 1997.

[45] M. H. Burden and J. D. Hunt, "Cellular and dendritic growth. I," *Journal of Crystal Growth,* vol. 22, pp. 99-108, 1974.

[46] D. A. Porter, K. E. Easterling, and M. Y. Sherif, *Phase Transformations in Metals and Alloys*, 2008.

[47] H. Fredriksson and U. Akerlind, *Solidification and Crystallization Processing in Metals and Alloys*: John Wiley & Sons, Ltd., 2012.

[48] R. Trivedi, "Growth of dendritic needles from a supercooled melt," *Acta Metallurgica,* vol. 18, pp. 287-96, 1970.

[49] C. M. Klaren, J. D. Verhoeven, and R. Trivedi, "Primary dendrite spacing of lead dendrites in Pb-Sn and Pb-Au alloys," *Metallurgical Transactions A* vol. 11A, pp. 1853-61, 1980.

[50] T. Okamoto and K. Kishitake, "Dendritic structure in unidirectionally solidified aluminum, tin, and zinc base binary alloys," *Journal of Crystal Growth,* vol. 29, pp. 137-146, 1975.

[51] J. A. Horwath and L. F. Mondolfo, "Dendritic growth," *Acta Metallurgica,* vol. 10, pp. 1037-1042, 1962.

[52] E. Cadirli, I. Karaca, H. Kaya, and N. Marasli, "Effect of growth rate and composition on the primary spacing, the dendrite tip radius and mushy zone depth in the directionally solidified succinonitrile-salol alloys," *Journal of Crystal Growth,* vol. 255, pp. 190-203, 2003.

[53] K. A. Jackson, *Liquid Metals and Solidification, ASM, Cleveland,* p. 174, 1958.

[54] O. L. Rocha, C. A. Siqueira, and A. Garcia, "Cellular/dendritic transition during unsteady-state unidirectional solidification of Sn-Pb alloys," *Materials Science and Engineering A* vol. 347, pp. 59-69, 2003.

[55] "Prediction of dendritic spacings in a directional-solidification experiment," *Phys. Rev.,* vol. 47, p. 2702, 1993.

[56] J. D. Hunt, *Solidification and Casting of Metals*. London: The Metals Society, 1979.

[57] W. Kurz and D. J. Fisher, "Dendrite growth at the limit of stability: tip radius and spacing," *Acta Metallurgica,* vol. 29, pp. 11-20, 1981.

[58] R. Trivedi, "Interdendritic spacing. II. A comparison of theory and experiment," *Metallurgical Transactions A* vol. 15A, pp. 977-82, 1984.

[59] D. Bouchard and J. S. Kirkaldy, "Prediction of dendrite arm spacings in unsteady- and steady-state heat flow of unidirectionally solidified binary alloys," *Metallurgical and Materials Transactions B,* vol. 28B, pp. 651-63, 1997.

[60] W. A. Tiller, K. A. Jackson, J. W. Rutter, and B. Chalmers, "The redistribution of solute atoms during the solidification of metals," *Acta Metallurgica,* vol. 1, pp. 428-437, 1953.

[61] J. W. Rutter and B. Chalmers, "A prismatic substructure formed during solidification of metals," *Canadian Journal of Physics,* vol. 31, pp. 15-39, 1953.

[62] ASM Handbook Volume 03: Alloy Phase Diagrams, ASM International, 1992.

[63] FactSage salt database, *Availabe at http://www.factsage.cn/fact/documentation /FTsalt/KCl-LiCl.jpg. Retrieved 8/22/2013.*

[64] J. S. Langer and H. Muller-Krumbhaar, "Theory of dendritic growth. I. Elements of a stability analysis," *Acta Metallurgica,* vol. 26, pp. 1681-7, 1978.

[65] J. Szekely, J. W. Evans, and H. Y. Sohn, *Gas-Solid Reactions*: Academic Press, 1976.

[66] T. L. C., *Heat Transfer*: Prentice Hall, Inc., 1993.

[67] R. B. Bird, W. E. Stewart, and E. N. Lightfoot, *Transport Phenomena*, 2001.

[68] L. D. Pye, A. Montenero, and I. Joseph, *Properties of Glass-Forming Melt*, 1st ed.: CRC Press, 2005.

[69] O. D. Gudovich and V. I. Primenko, "Calculation of the thermal capacity of silicate glasses and melt," *Soviet Journal of Glass Physics and Chemistry,* vol. 11, pp. 206-11, 1985.

[70] M. M. Ammar, K. H. El-Badry, M. R. Moussa, S. Gharib, and M. Halawa, "Thermal conductivity of some titania and lithia glasses," *Glass and Ceram. Bull.,* vol. 22, pp. 10-13, 1975.

[71] V. I. Primenko, "Theoretical method of determining the temperature dependence of the thermal conductivity of glasses," *Glass and Ceramics,* vol. 37, pp. 240-2, 1980.

[72] M. M. Ammar, S. Gharib, M. M. Halawa, K. El Badry, N. A. Ghoneim, and H. A. El Batal, "Thermal conductivity of some silicate glasses in relation to composition and structure," *Journal of Non-Crystalline Solids,* vol. 53, pp. 165-72, 1982.

[73] Y. V. Vavilov, V. E. Komarov, and N. A. Tabunova, "Calculation of the thermal conductivity of glasses," *Soviet Journal of Glass Physics and Chemistry,* vol. 8, pp. 326-30, 1982.

[74] L. van der Tempel, "Thermal conductivity of a glass. II. The empirical model," *Glass Physics and Chemistry,* vol. 28, pp. 147-52, 2002.

[75] R. P. Madding, "Temperature dependence of the graybody approximation to emissivity for some common materials," in *Thermosense XXIV conference*, 2002, pp. 37-43.

[76] R. Morrell, *Handbook of Properties of Technical and Engineering Ceramics*: Her Majesty's Stationary Office, 1987.

[77] G. Teodorescu, "Radiative emissivity of metals and oxidized metals at high temperature," *Auburn Theses and Dissertations, ,* 2007.

[78] Thermal Ceramics, "Insulating Fire Brick Products, Available at http://www.markbi.ro/files/Insulating%20Fire%20Brick%20Products.pdf., Retrieved 8/22/2013.

[79] Insulating fire bricks, *Availabe at http://www.traditionaloven.com/articles /81/insulating-fire-bricks, Retrieved 8/22/2013.,* 2013.

[80] H. Hasegawa, T. Kowatari, Y. Shiroki, H. Shibata, H. Ohta, and Y. Waseda, "Thermal Conductivity of Molten Silicate of Al_2O_3-CaO-Na_2O-SiO_2 Measured by Means of a Front Heating-Front Detection Laser Flash Method," *Metallurgical and Materials Transactions B* vol. Volume 43B, pp. 1413-9, 2012.

[81] NYCO Mineral. Inc., "A Value-added Functional Reinforcement," *Available at http://nycominerals.com/files/wollastonite-product-information.pdf.pdf, Retrieved 8/22/2013.*

[82] J. C. Salamone, *Concise Polymeric Materials Encyclopedia*, 1st ed.: CRC Press, 1998.

[83] Quarzwerke Group, "Wollastonite: Reinforcement, low thermal expansion," *Available at http://www.quarzwerke.com/home/maerkte_und_produkte/Range% 20of%20products/englHigh%20Performance%20Fillers/Wollastonite. Retrieved 8/22/2013.*